# Determination of k-factors of HVAC system components using measurement and CFD modelling

Shaun J. Smith Bsc



Thesis submitted to the University of Nottingham

for the degree of Doctor of Philosophy, March 1998

# Contents :

## Abstract

This thesis conforms conventional and advanced experimental techniques for the measurement of and mathematical prediction of velocity pressure-loss factors (k-factors) for fittings used in heating, ventilation and air-conditioning (HVAC) systems. After an extensive study of different tracer-gas experimental techniques, the constant injection method is applied to various duct fittings on a small scale HVAC system situated in a laboratory. The results are compared with those of experiments performed using a more conventional technique using a Pitot-static tube. The basis of the experimental procedure is to achieve an accurate method of measuring the mean air velocity within a duct. This allows an accurate estimate of the velocity pressure-loss factor to be obtained.

A wide variety of duct fittings are investigated experimentally and numerically including bends, transitions, branches, inlets, outlets and obstructions such as orifice plates, wire mesh and lateral pipe obstructions. Computational fluid dynamics (CFD) is applied to each duct fitting tested in the lab. A commercially available package FLUENT is used with a high powered computer to simulate the airflow through various duct fittings. The pressure loss and velocity vectors are predicted for each particular duct fitting and therefore a prediction for k-factors is obtained. k-factor predictions are compared with experimental results and

published data given in ASHRAE and CIBSE guides in order to assess the accuracy of CFD prediction.

It is shown that as an accurate method for prediction of k-factors in duct fittings, CFD is a useful tool for the design and development of HVAC systems. The application of CFD allows the designer to vary any duct component with ease to observe the effect on a particular duct fitting without incurring the expense of laboratory experimentation. It is also shown that values of current published k-factors are greatly over estimated leading to oversizing of HVAC system fans. Experimentally produced k-factors obtained using the tracer-gas method and CFD predictions are approximately 20% lower than current data available to HVAC system designers.

CFD may be applied to various applications in the field of heat-pumps and refrigeration systems. A detailed investigation is carried out here to compare CFD prediction and experimental results of several low pressure and high pressure ejectors commonly found in refrigerator absorption cycles. The compressible flow of refrigerants was modelled through an ejector to obtain a prediction of the entrainment ratio ( i.e. the ejector's ability to entrain a refrigerant from an evaporator using a hot main flow through a nozzle). These predictions were then

compared with experimental results and this indicated that CFD could serve as a useful tool in the design of refrigeration systems.

Application of CFD has also been studied in relation to the investigation of pressure loss through different types of evaporator/condenser coils found in heat pump systems; here the design of such coils is important to the operating efficiency. The pressure loss across heat-pipes found in ducted flows is also predicted using CFD; in this case the geometry and the thermal conditions play an important role in the overall pressure loss.

I would like to thank the Engineering and Physical Sciences Research Council (EPSRC) for their financial support for this project. I would like to thank my supervisors, Professor S. B. Riffat and Dr L. Shao for their continued support and assistance with my research work, and Dr G. Gan for his technical advice. I would also like to praise my wife Charlotte and my two children Samuel and Rosie for their unlimited patience during my studies.

# Nomenclature

Chapter 2 :

$C_0$ = tracer-gas sampling concentration at time zero [ppm]

$C_t$ = tracer-gas sampling concentration at time t [ppm]

F = air flow rate [$m^3/s$]

$F_t$ = air flow rate at time t [$m^3/s$]

$I_t$ = air exchange rate at time t [$h^{-1}$]

q = tracer-gas injection rate [l/s]

$q_t$ = tracer-gas injection rate at time t [l/s]

t = time [s]

V = internal duct volume [$m^3$]

Chapter 3 :

k = velocity pressure loss factor [Dimensionless]

$P_k$ = dynamic pressure [Pa]

$P_{kb}$ = dynamic pressure in the smaller of two different cross-section ducts [Pa]

v = duct mean air velocity [m/s]

$\Delta P_m$ = measured static pressure in duct [Pa]

$\Delta P_t$ = total pressure difference between two selected positions [Pa]

$\rho$ = air density [$kg/m^3$]

Chapter 4 :

$A_1$ , $A_2$ , $A_3$ ..... = polynomial coefficients

$C_{1\varepsilon}$ , $C_{2\varepsilon}$ , $C_{3\varepsilon}$ and R = software installed empirical constants [Dimensionless]

$C_\mu$ , $\sigma_\varepsilon$ and $\sigma_k$ = empirical constants = 0.09, 1.3 and 1.0, respectively

$c_p$ = specific heat capacity [J/kg.K]

$G_b$ = generation of turbulence due to buoyancy

$G_k$ = generation of turbulent kinetic energy

h = fluid mixture enthalpy [J/kg]

$J_j$ = diffusion flux of species j

k = turbulent kinetic energy [$m^2/s^2$]

$k_c$ = user defined empirical constant [Dimensionless]

$k_e$ = effective conductivity [W/m.K]

$k_m$ = molecular conductivity [W/m.K]

$k_t$ = thermal conductivity [W/m.K]

M = molecular weight of fluid [Dimensionless]

$M_i$ = molecular weight of species i [Dimensionless]

$m_i$ = mass fraction for species i [Dimensionless]

n = user defined empirical constant [Dimensionless]

P' = local relative (guage) pressure [Pa]

$P_{op}$ = operating pressure [Pa]

R = universal gass constant [J/mol.K]

$\dot{S}$ = local strain rate of the fluid [$s^{-1}$]

$S_h$ = Source term for additional heat sources.

T = temperature [K]

T* = function of reduced collision integral [K.s]

$T_n$= temperature at iteration n [K]

$T_{n+1}$= temperature at iteration n+1 [K]

$u_i$ and $u_j$ = velocity component [m/s]

$X_i$, = mole fraction of species i [Dimensionless]

$x_i$ and $x_j$ and $x_k$ = Cartesian co-ordinates [m]

$\alpha_k$ and $\alpha_\varepsilon$ = inverse effective Prandtl numbers for k and ε, respectively

Δs = displacement vector from cell centroid and face centroid

$\delta_{ij}$ = Kronecker delta

ε = dissipation rate of turbulent kinetic energy [$m^2/s^3$]

$\phi$ = averaged value of a general variable

$\phi_e$ = cell face value of any particular variable

$\phi_{i'j'}$ = function of species component viscosity and species mole fraction

$\phi_p$ and $\nabla\phi_p$ = value and gradient of node P

Γ = diffusion coefficient [Dimensionless]

$\mu$ = fluid viscosity [$Ns/m^2$]

$\mu_{eff}$ = effective viscosity [$Ns/m^2$]

$\mu_i$, = component viscosity of species i [$Ns/m^2$]

$\mu_t$ = turbulent viscosity $Ns/m^2$]

$\rho$ = fluid density [$kg/m^3$]

$\rho_n$= fluid density at iteration n [$kg/m^3$]

$\rho_{n+1}$= fluid density at iteration n+1 [$kg/m^3$]

$\rho_i$ = fluid density for species i [$kg/m^3$]

$\sigma$ = Lennard-Jones parameter [Angstrom]

$\sigma_h$ = turbulent Prandtl number [Dimensionless]

$\Omega_\mu$ = reduced collision integral, a function of T*

Chapter 5 :

$C_f$ = loss coefficient correction factor [Dimensionless]

$k_o$ = loss coefficient for interacting duct fittings [Dimensionless]

$k_1$ and $k_2$ = component loss coefficients for interacting duct fittings [Dimensionless]

Re = Reynolds number [Dimensionless]

v = mean duct air velocity [m/s]

$\nu$ = kinematic air viscosity [$m^2/s$]

Chapter 6 :

k = duct fitting loss coefficient [Dimensionless]

v = mean duct velocity [m/s]

$\Delta P$ = total pressure loss [Pa]

Appendix 3 :

Co = loss coefficient for one bend in S-shaped coil [Dimensionless]

D = coil pipe diameter [m]

Dc = spiral coil diameter [m]

f = friction coefficient [Dimensionless]

$f_v$ = vapour friction coefficient [Dimensionless]

$G_r$ = mass velocity of refrigerant [$kg/s.m^2$]

$k_r$ = roughness value [mm]

$L_c$ and $L_s$ = total length of spiral and S-shaped coil, respectively, without upstream and downstream pipes [m]

Re = fluid Reynolds number [Dimensionless]

$X_t$ = function of vapour/liquid mixture

x = quality of mixture [Dimensionless]

$\Delta P_f$ = frictional pressure loss [Pa]

$\Delta Pgc$ = geometric pressure loss for spiral coil [Pa]

$\Delta Pgs$ = geometric pressure loss for S-shaped coil [Pa]

$\Delta P_m$ = pressure loss due to momentum change within the liquid/vapour mix [Pa]

$\mu_v$ and $\mu_L$ = vapour and liquid viscosity, respectively [Pa.s]

$\rho_v$ and $\rho_L$ = density of refrigerant vapour and liquid, respectively [kg/m$^3$]

$\xi$ = void fraction [Dimensionless]

# List of Equations :

3.3 Fluid friction coefficient for an S-shaped coil for single phase flow.

3.4 Pressure loss due to friction in bothe types of coil in single phase.

3.5 Total pressure loss through coils for single phase flow.

3.6 Pressure loss due to momentum for two phase fluid in an S-shaped coil.

3.7 Void fraction for equation 3.5 .

3.8 Pressure loss due to friction through coils with two phase fluid.

3.9 Pressure loss due to friction for vapour in a coil.

3.10 Function of vapour/liquid mixture

3.11 Fluid friction coefficient for vapour in a coil.

3.12 Total pressure loss through S-shaped and spiral coils.

Appendix 4

4.1 Fluid pressure loss.

# List of Tables :

# List of Plates :

# List of Figures :

Chapter 5

# Chapter 1

# Introduction

# 1.0 Introduction

Energy use, thermal comfort and air quality in mechanically ventilated buildings is mainly dependent on the performance of HVAC systems. The parameters governing the design of such systems may be predicted using pressure loss factors (k-factors) available in reference guides such as ASHRAE (1) and CIBSE (2). The data available to designers however include large discrepancies resulting in inaccurate sizing of fans used in HVAC systems leading to energy wastage. These discrepancies were such to cause the BSRIA (3) handbook to be removed from publication.

Several factors may contribute to inefficiencies of mechanical ventilation systems. These include poor insulation, bad geometrical designs leading to large pressure losses and over estimation of pressure loss factors leading to exaggeration of fan requirements. Poorly designed and maintained ventilation systems have high operating costs and poor efficiency in terms of systems ability to remove pollutants and contaminants. Increasing the ventilation rate in order to meet efficiency requirements inevitably results in the removal of warm clean air as well as the polluted air. This creates a somewhat draughty and uncomfortable working environment, the physical implications of which include poor air quality and therefore a reduction in physical health.

It is essential to have a full knowledge of the ventilation requirements for each building, which depends on many factors for example, number of occupants and contaminant sources. The CIBSE have published standards for engineers which serve as an aid for the design of ventilation systems, however this thesis suggests reasons why such data might be greatly over estimated in some cases as much as 300 %. This clearly shows the need to establish a method of measurement and prediction that is simple to use and provides a high degree of accuracy. This may be achieved using modern experimental techniques or computational methods using CFD software such as FLUENT (4).

Traditionally measurements of airflow in HVAC systems have been carried out using conventional methods for measuring the duct mean velocity, with instruments such as the Pitot-static tube, vane anemometers and hot-wire anemometers. Due to their requirement for a long upstream and downstream duct length to produce a fully developed flow, it is sometimes difficult to obtain accurate measurements using conventional equipment. This is because with HVAC systems found in industry long straight duct lengths are rarely found both before and after each duct fitting. Errors may also arise due to placing the instrumentation directly in the airflow impeding it to some extent.

Tracer-gas techniques allow us to make accurate duct mean velocity measurements based on the injection rate and the concentration after the tracer-gas has mixed with the air. These methods do not obstruct the air flow and unlike conventional methods which take a velocity measurement at a single point, tracer-gas techniques give us a duct mean velocity reading over the entire duct cross-section. The versatility of tracer-gas methodology permits accurate airflow measurements to be performed in situations where traditional instrumentation cannot be employed. The application of tracer-gas measurements in buildings has been investigated (5-9) but only a few researchers have applied tracer-gas measurements to HVAC systems (10-13) . The physical properties of tracer-gases such as being colourless, odourless and existing at an infinitesimally low concentration in the atmosphere, make them suitable for measurements in HVAC systems, the principle being that they are easily identifiable for analysis after being mixed with air.

A cost-effective way of examining a large group of HVAC system configurations is by CFD prediction. Once CFD has been justified with experimental results it naturally follows that data based on a variation of a previous model can be found. Various CFD codes such as FLUENT provide a variety of computational models, grid structures and solving schemes that allow accurate prediction of duct fitting characteristics.Other CFD codes such as FlowVent (14) are specialised and are

restricted to certain applications. However the application of CFD is not restricted to ducted flows, but can give accurate prediction of fluid flow for a variety of situations, for example compressible flows in ejectors, crystal growth, coal combustion and thermal transport.

The objectives of this investigation are to compare previously available k-factors found in reference manuals with experimental results using conventional and advanced techniques for measuring the mean duct air velocity. The second part of this investigation is to compare experimental results with CFD prediction of k-factors for numerous HVAC components and to expand on the limited variations of k-factors found in reference manuals with a comprehensive data collection of k-factors obtained using CFD prediction.

Chapter 2

# Review of airflow measuring instrumentation

## 2.0 Review of airflow measuring instrumentation

There are several main sources of k-factor data available to HVAC system designers, the most common are the CIBSE and ASHRAE handbooks discussed in the previous chapter. However with incomplete data, innacurate data and data obtained being as much as 50 years old, it was inevitable that in 1983 ASHRAE held its annual meeting to discuss the accuracy of its published k-factor data in their handbook. Other sources of data include the Russian translated handbook by Idelchik (15) . Over the last 20 years with the introduction of newer duct components with cheaper manufacturing techniques there has been a clear need for a revised and comprehensive research program in this HVAC field.

Results of recent research have produced a revised set of ASHRAE k-factor data by Brooks (16) and the release of the American standards (17) of measuring pressure loss and mean duct velocity for obtaining k-factor data. These standards however still incorporate the use of conventional instrumentation for the measurement of air velocity such as orifice plates and Venturi meters which are time consuming and very expensive to include in a comprehensive experimental investigation.

## 2.1 Review of airflow instrumentation and techniques

With advancement of technology, there appears to be a wide variety of airflow measurement devices and instrumentation available to engineers and the scientific community. This poses the notion of measurement accuracy, however it is necessary to have different measuring devices suitable for different applications. Airflow instrumentation ranges from the most commonly used measuring device, the Pitot-static tube, to the more complex ultrasonic flowmeter. Various flow meters are described in more detail in Streeter (18).

### 2.1.1 Pressure differential technique

Although there are many types of flow measuring device, the two main types of flowmeter are based on two separate theories. The pressure differential method includes restricting the flow in a duct or a pipe with the measuring device. This causes a change in fluid velocity and therefore a change in pressure across the measuring device. Such airflow meters include the orifice plate, the venturi tube, the Dall flow tube, the flow nozzle and the Pitot-static tube. The pressure change is inversely proportional to the volume flow rate squared. This method requires fully developed flow upstream and consequently a long upstream duct length is needed. Measurements taken using restriction of flow are accurate because there

are no moving parts, however the flow is effected with a reduction in total pressure.

### 2.1.2 Thermal measuring devices

The thermal method of measuring airflow is based on the relation between the rate of loss of heat from a heated body and the speed of flow of a fluid in which the measuring device is immersed. This method has been extensively researched and attention has mainly been concentrated on the use of electrically heated wires as anemometers. The laws governing the convective cooling of a hot cylindrical wire by a fluid stream are now well established, and the device is widely used for flow measurements when pressure tubes are inappropriate. Heated-body methods pose several distinct advantages, particularly their high sensitivity at low rates of flow. In the case of the hot wire, the wire itself has to have a very small diameter which consequently results in it being fragile and its characteristics are seriously affected by dust deposition, oil or other surface contamination. Other errors in measurements may arise due to the impedance of flow with the probe being placed directly into the flow. Thermal method measuring devices include the hot-wire anemometer, the hot-grid anemometer and the sinusoidal heated hot-wire anemometer.

## 2.2 Conventional airflow measurement instrumentation

There are a wide variety of airflow measurement devices in use today, but only the most common ones will be described here.

### 2.2.1 Pitot-static tube

Figure 2.1 shows a diagrammatic arrangement of a standard Pitot-static tube. The design proportions are labelled for optimum performance, where **d** is set as the external diameter.

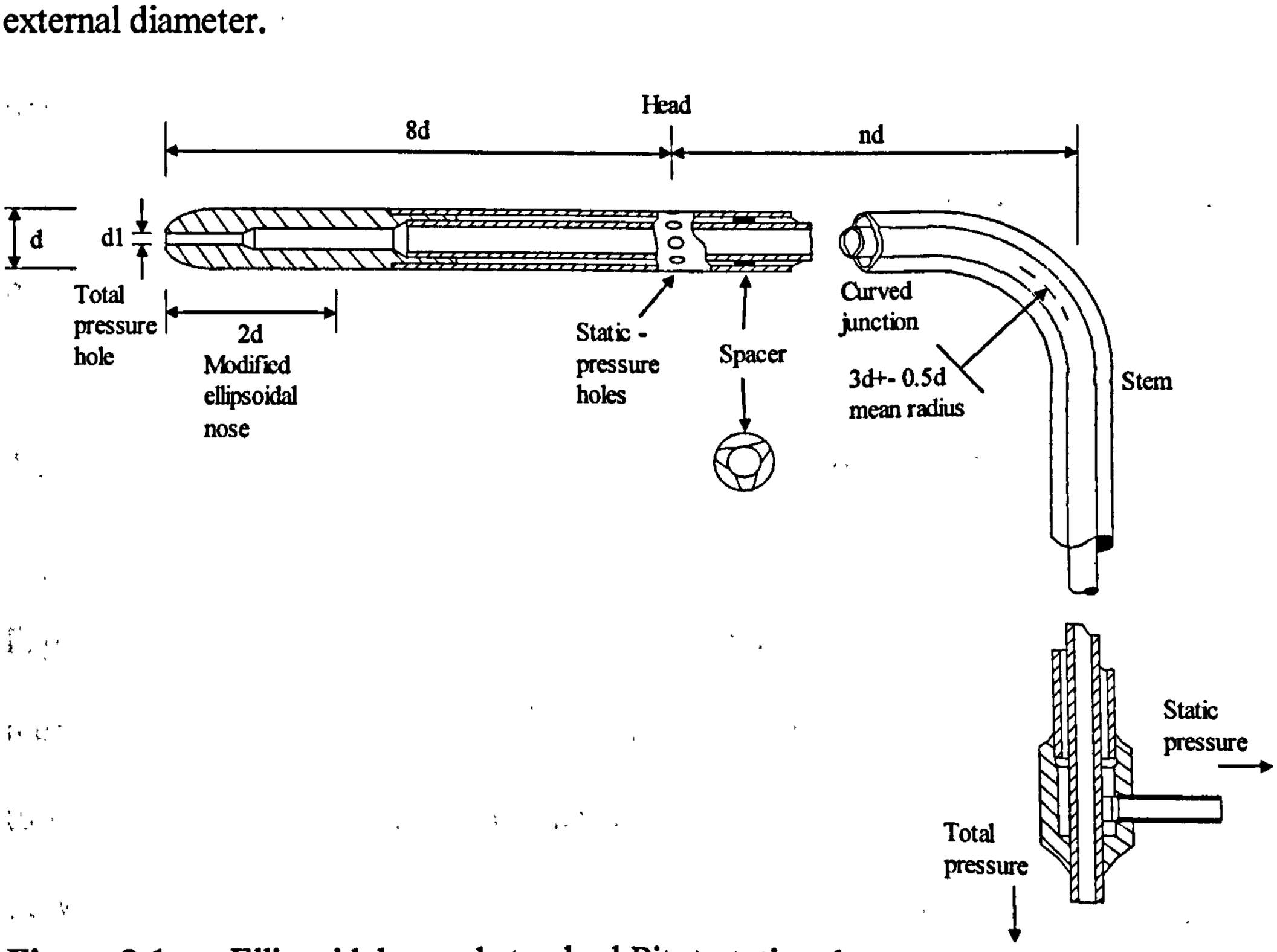


**Figure 2.1** Ellipsoidal-nosed standard Pitot-static tube.

In general, the Pitot-static tube consists of two concentric tubes; the inner tube transmits the impact pressure while the annular space between the two tubes transmits static pressure. The static pressure taps are situated well back from the tube's front face to prevent interaction from eddy currents. The advantages of using Pitot-static tubes are that they are easy to use and apply to numerous experimental tests making them very cost effective. The primary disadvantage of using a Pitot-static tube to measure the mean airflow is that it is limited to only single point measurements. In addition, Pitot-static tubes are very susceptible to fouling by foreign matter in the fluid medium. This is why stringent experimental techniques have to be employed when using such instrumentation. With sensitive pressure measuring devices such as a micro-manometer, the measurement uncertianty of Pitot-static tubes is given around ±5 % with a typical flow velocity of between 3 and 20 m/s.

#### 2.2.1.1 Experimental implimentation of the Pitot-static tube

Figure 2.2 shows a typical setup for the use of a Pitot-static tube in measuring the mean air velocity in a ventilation duct. This comprises of placing the Pitot-static tube through a sealed hole within the duct wall in a position opposing the air flow. The Pitot-static tube is then connected via two equal lengths of flexible tube to a micro-anemometer. The typical dimensions and details of which are given in

the next chapter. The measurement of total pressure is made by the hole at the front of the probe and the holes at the side measure the static pressure. The difference in these two measurements ( i.e. the velocity pressure ) are recorded by the micro-anemometer which is correlated to give a reading in velocity. As this is only representative of a single data point then a traverse is needed and an average value calculated. The use of a Pitot-static tube traverse for the measurement of duct mean air velocty is given in the next chapter.

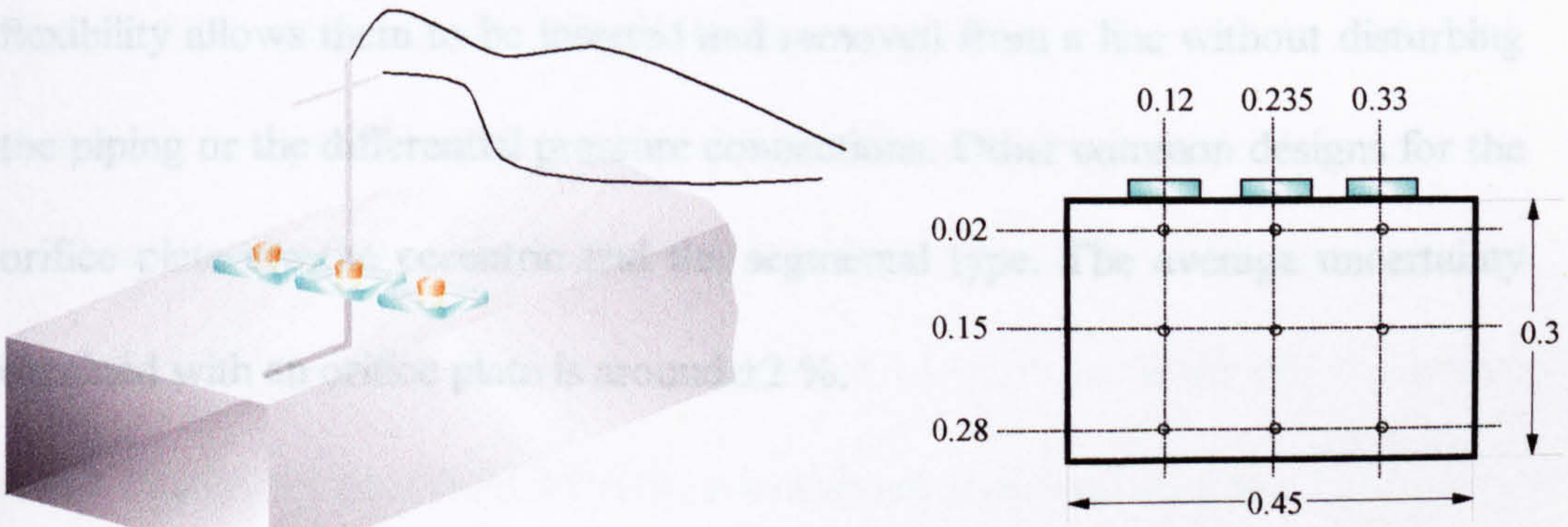


**Figure 2.2** Setup of Pitot-static tube used in mean air velocity measurement.

### 2.2.2 Orifice plate

The differential pressure between the upstream and downstream sides of the unit is measured with pressure taps located on either side of the orifice plate. The most common design for the orifice is a circular hole in a diaphragm, which is mounted concentrically between the flanges of the flow pipe. The difference in pressure caused by changes in flow rates is a measure of the flow and is used to calculate mean flow velocity. The advantage of orifice plates is that their flexibility allows them to be inserted and removed from a line without disturbing the piping or the differential pressure connections. Other common designs for the orifice plate are the eccentric and the segmental type. The average uncertainty obtained with an orifice plate is around ±2 %.

### 2.2.3 Hot-wire

The sensing element at the end of the probe is kept at a constant temperature using an electric current. Exposed to the air flow the resulting temperature drop or the electrical current required to keep the element at a constant temperature is measured and is calibrated to relate to the air flow velocity at a single point. Due to the fragility of the wire, extensive work has been carried out in the area of

thermal related measuring devices. Work in this field is focused at reduction of wire contaminant and fragility when subjected to high velocity dirty flows.

The next step in hot-wire technology is the shielded hot-wire. Increasing the effective diameter of the measuring probe whilst keeping the wire diameter the same, results in greatly reduced fluctuations in measurement accuracy due to dust and contaminant deposition commonly experienced when using the unshielded hot-wire anemometer. With periodic cleaning, the shielded anemometer gives highly satisfactory results with calibration remaining constant for indefinite periods as compared to only hours with the unshielded types. The instrument is much more robust than the ordinary type with a wire of the same diameter, and the effect of variations of air temperature, of as much as 30 or 40° C, is very small. Finally, the sensitivity of such an instrument is around ±0.5 %.

### 2.2.4 Other air flow measuring devices

Figure 2.5 shows several other types of airflow measuring devices.

With such a large variety of airflow measuring devices available, careful consideration can be given to the choice of device depending on the application

and accuracy required. The simple but very crude measurement can be made by releasing visual tracers, e.g., particle beads or paper streamers directly into the flow and timing their movement. Other airflow measuring devices which have been widely used are the Venturi tube, three cup anemometer, Savonius rotor, rotating vane anemometer, hot film anemometer and the laser-Doppler anemometer. The accuracy of some of these devices, such as the Venturi tube are very high, however it may become difficult to use in applications where space is limited. If a high degree of accuracy is not needed then a cheap, simple-to-use flow meter might be more appropriate, e.g., the static Pitot-static tube or the vane anemometer. Other very expensive techniques such as the laser-Doppler anemometer would be employed when a large number of measurements and extreme accuracy are required.

## 2.3 Tracer-gas techniques used for airflow measurement

A relatively new technique usually incorporated in the measurement of airflow in buildings can be used to take many experimental measurements within HVAC systems. By releasing a traceable gas into an airflow upstream of a duct it is possible to measure its concentration downstream and relate this to the mean duct velocity. The theory of tracer-gas calculations is given in chapter 3.4 .

### 2.3.1 Tracer-gas specifications

Various tracer gases are used in experimental studies and the type of tracer used depends on the application. In general, for a tracer gas to be suitable there are several conditions which must be fulfilled.

- The tracer-gas must be non-toxic and safe to use in open laboratory conditions. There also must be no danger to other equipment and laboratory materials.
- The tracer-gas must be completely independent and non-reactive with the surrounding air, to provide accurate measurements.
- The tracer-gas must exist at infinitesimally low concentrations in the ambient air so that it is distinctive and easily measurable using a particular experimental technique and instrumentation.
- The tracer-gas should be commercially available and it must have similar physical properties to air.

No single tracer-gas satisfies all of these requirements completely, however several tracers are in common use today, these include sulphur hexafluoride [$SF_6$] , nitrous oxide [$N_2O$] , carbon dioxide [$CO_2$] and various perfluorocarbon (PFT)

tracers. Extensive work has been done with the development of PFT tracers by Sateri (19) and Dietz et. al. (20) . PFT tracers are suitable for use in experiments in large buildings as they are easy to use and cheap to apply.

### 2.3.2 Injection requirements

There has been much investigation into tracer-gas injection, however the most important requirement is that the ducted airflow mixes with the tracer-gas as much as possible so that sampling provides an accurate measurement. Figure 2.3 shows a diagrammatic arrangement of an injection array as used in circular and square cross-section ducts. The 4 mm diameter copper tubes are wired together and arranged so that an even injection of tracer-gas is delivered into the duct. Each tube has 1 mm diameter holes drilled in a line and the injection is in the opposite direction to the airflow to aid the tracer-gas/air mixing.

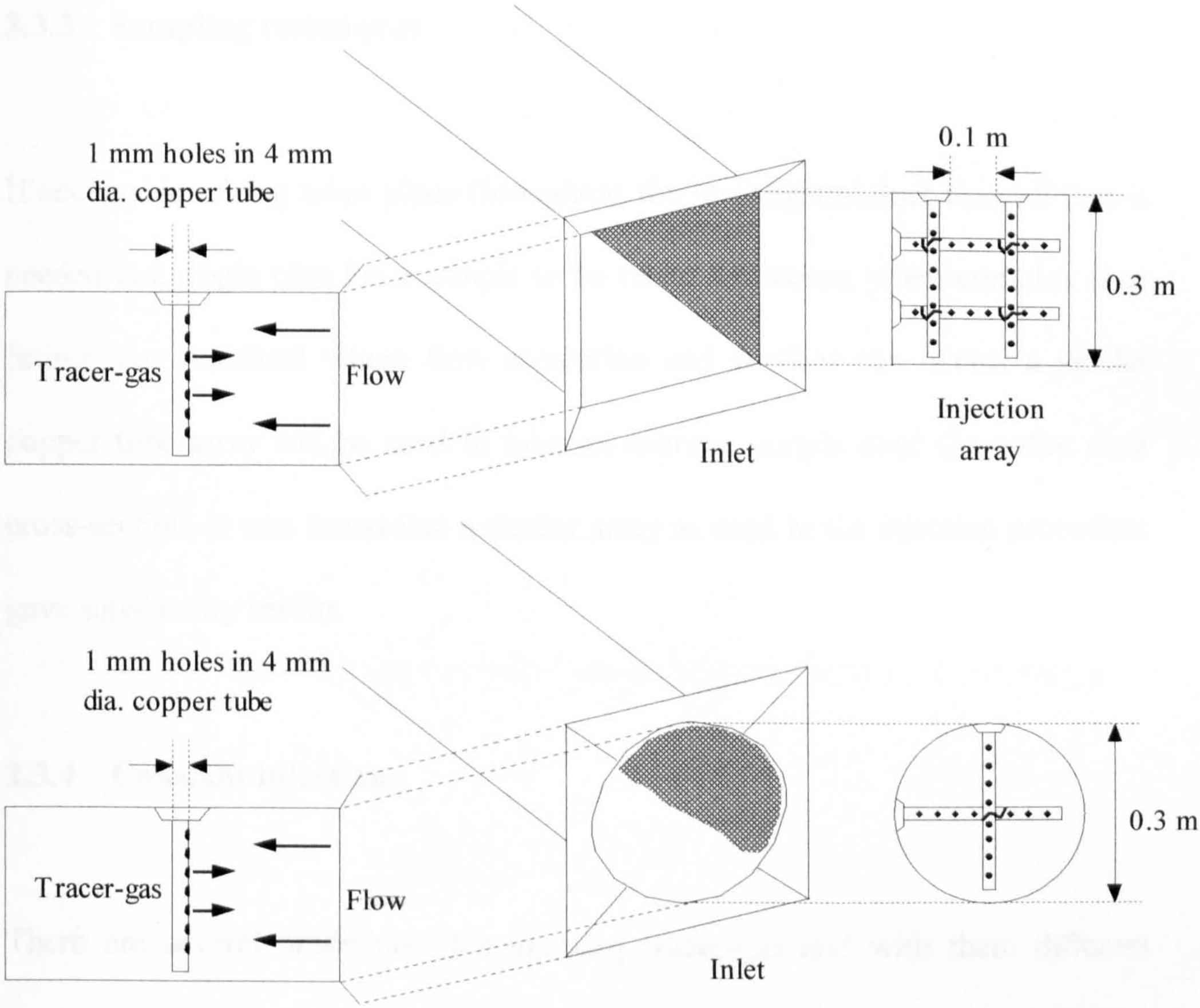


**Figure 2.3** Tracer-gas injection array for circular and square cross-section duct.

With highly turbulent flows and the introduction of honeycomb inlets it was found that very satisfactory mixing takes place at relatively low inlet lengths, between 5 and 10 duct diameters.

### 2.3.3 Sampling techniques

If acceptable mixing takes place throughout the investigated duct then all that is needed is a single pipe for a sample to be taken. However, when complex duct fittings are examined where flow separation and vortices can occur, a similar copper tube array can be used to take an average sample over the entire duct cross-section. It was found that a similar array as used in the injection procedure gave satisfactory results.

### 2.3.4 Constant injection

There are several procedures for injecting tracer-gas and with them different theories. The general experimental technique is described in chapter 3.3.2 . The constant injection method involves keeping tracer-gas injection at a constant rate and taking the sample averaged over a certain time limit, e.g., every 10 seconds.

In this method, the tracer-gas term of the mass balance equation is set at a constant value; in practice this is achieved by using a mass flow controller. Assuming that the background tracer-gas concentration is zero, the mass balance equation is given as :

$$V\frac{dC_{(t)}}{dt} = -F_{(t)}C_{(t)} + q_{(t)} \tag{2.1}$$

If equation 2.1 is solved with respect of tracer-gas concentration, it becomes :

$$C_{(t)} = \frac{q}{F} + \left[C_{(0)} - \frac{q}{F}\right]e^{-\frac{F_{(t)}}{v}t} \tag{2.2}$$

The air exchange rate in the duct is given as :

$$I_{(t)} = \frac{F_{(t)}}{V} \tag{2.3}$$

Equation 2.2 can be simplified by assuming that the initial tracer-gas concentration $C_{(0)}$ is zero, and therefore becomes :

$$C_{(t)} = \frac{q}{F}\left[1 - e^{-It}\right] \qquad (2.4)$$

It can be seen that after a considerable amount of time if the air exchange rate, I, is constant, then the exponential term in equation 2.4 disappears and the resulting equation is :

$$F = \frac{q}{C_{(t)}} \qquad (2.5)$$

Therefore the concentration of sampled tracer-gas (**C**) is inversely proportional to the airflow rate (**F**), for any given constant injection rate (**q**).

### 2.3.5 Other tracer-gas methods

There are several techniques of tracer-gas implementation. However, for the purpose of this investigation it was found that the constant injection method gave very satisfactory results.

### 2.3.5.1 Pulse injection

This technique involves using a large syringe to inject a predetermined amount of tracer-gas into the HVAC system and storing time dependant-samples of air in sealed bags. These samples are then analysed, usually within another establishment, to determine the concentration of tracer gas present.

The problem with this method is that it is difficult to ensure a precise measurement of tracer gas being injected, and that depletion in the sample may cause errors in the result if a long period of time lapses between collecting the sample and analysing it. It is also much easier to maintain a constant injected flow rate of tracer gas than it is to exactly measure a small amount injected.

### 2.3.5.2 Concentration decay

If the operational fan is switched off in an HVAC system then a time-dependant amount of tracer gas is injected into the system and allowed to mix, usually with the aid of small desktop fans. The main fan is then switched on and the tracer-gas concentration is monitored using a gas analyser, similar to the sampling method used in the constant injection technique.

However, errors can occur because of inadequate mixing often found when using this technique. The concentration decay method is more useful for measuring ventilation rates within whole buildings because natural air movements occurring within rooms lead to better mixing.

### 2.3.5.3 Constant concentration

By taking equation 2.5, if we varied the injection flow rate (**q**) such that a constant concentration (**C**) is maintained, then the air flow rate (**F**) would be directly proportional to the tracer-gas injection rate with a constant (**1/C**).

The problem with this technique is that due to small fluctuations in the analysed tracer-gas concentration, it proves very difficult to maintain the sampled concentration at a constant level. This could be assisted by the use of highly sophisticated computer controlled injection devices, however this would be very expensive.

## 2.4 Conventional techniques vs. tracer-gas

Tracer-gas techniques are simple to employ and have many advantages over more conventional air flow measuring devices, such as the Pitot-static tube, the hot-wire anemometer and the vane anemometer. These advantages include the following :

- The duct length can be reduced to a minimum without the requirement for fully developed flows. However a duct length allowing sufficient tracer-gas/air mixing is required.
- Tracer-gas techniques are not limited by the complexity of the duct configurations. A single point measurement can be taken because if sufficient mixing is obtained the result represents an average air flow velocity over the entire duct cross-section whilst a measurement taken using conventional measuring devices and probes represents a value at one single point.
- A wide range of airflow rates can be measured using tracer-gas techniques. This is not possible with the Pitot-static tube, which has significant inaccuracies when the velocity is less than 3 m/s.

- Tracer-gas techniques can be used to measure the air-tightness of a section of ductwork within an HVAC system.

## 2.5 Error analysis of airflow measurement

Before measurements can be taken with either conventional airflow measuring devices or sophisticated modern techniques, it is important to establish the error range within which one is working . Errors and measurement corrections have been discussed by other researchers such as Munson (21), however basically the three main measurement errors applied to the Pitot-static tube and the hot wire anemometer are as follows :

- reading error
- measuring instrument error
- experimental technique error, with the addition of the error due to rogue values, e.g. deviations in the data from a linear relationship.

Measurement errors for the tracer-gas experiments are evaluated in a similar way to the Pitot-static tube and the hot wire anemometer with the addition of error ranges being present for the tracer-gas injection and for the sampling measurements.

## 2.6 Review of CFD for the prediction of k-factors

Limited work has been carried out in the investigation of CFD as a tool for the prediction of k-factors for HVAC systems. Shao and Riffat (22) looked at the accuracy of using CFD for this application and Lin (23) has looked into a simplified HVAC duct, all using different CFD codes. The successes and failures of CFD for the prediction in HVAC applications has been discussed by Chen (24) where the issues of turbulence modelling and modelling technique are addressed.

## 2.7 Summary

The wide selection of airflow measuring devices that have been used for many years and are being continuously used today prove to show differing degrees of accuracy and application. It is evident however that as more advanced techniques are being incorporated to measuring the mean duct airflow rate in HVAC systems, then there is a clear need for the detailed and comprehensive comparison of all measuring devices from which standards and characteristics of application may be obtained.

Chapter 3

# Experimental Measurement Of Velocity Pressure Loss Factors in HVAC Systems

# 3.0 Experimental measurement of velocity pressure loss factors in HVAC systems

This section introduces the application of using experimental techniques to measure the pressure loss across various duct fittings and different techniques for measuring the duct mean air velocity. Two main techniques of measuring the mean air velocity within the duct are employed and a comparison is made between experimental results, published data and CFD prediction. The results of this investigation yield a log of k-factors produced for a wide variety of duct fittings that are both common and uncommon to designers of HVAC systems, which is given in appendix 2.

## 3.01 Literature search

Much work has been carried out in the area of flow resistance in ductwork and airflow measurment using various conventional instrumentation, however extensive work using tracer-gas methods has been carried out by Shao and Riffat (25). Other work carried out by Cheong (26) shows results for the experimental investigation and comparison of different tracer-gas techniques for the measurment of airflow rates in ducted systems.

## 3.1 Experimental theory

The experimental procedure yielded results of static pressure drop, sampled $SF_6$ concentration and Pitot-static tube mean airflow velocity. During the experiments average values for $SF_6$ concentration and duct mean velocity were obtained.

### 3.1.1 Velocity pressure loss factor (k-factor)

The k-factor is a dimensionless value of the attenuation of a particular duct fitting. A straight duct has a k-factor of zero whilst it does restrict the airflow because of the resistance between the air and the walls of the duct. Although a particular duct fitting also has a pressure loss due to resistance, the effect of this may be omitted in these experiments because we are measuring the pressure gradient along the duct fitting and the effect of resistance will be the same before and after the fitting. This is based on the material of the ductwork having the same degree of roughness and properties throughout. The material used for the ductwork in the experiments was galvanised steel.

### 3.1.1.1 Pressure distribution

During the experiments the static pressure difference was measured across the duct fitting at calculated distances to the fitting in the upstream flow, and from the fitting in the downstream flow. The resulting k-factor for any given fitting can be calculated using :

$$k = \frac{\Delta P_t}{P_k} \tag{3.1}$$

where $\Delta P_t$ is the total pressure difference across the duct fitting and $P_k$ is the dynamic pressure in the duct calculated by using :

$$P_k = \frac{1}{2}\rho v^2 \tag{3.2}$$

where $\rho$ is the air density ( i.e. 1.2 kg/m$^3$ at STP) and v is the mean air velocity in the duct. Where the duct cross-sectional area is constant across the duct fitting, the total pressure difference $\Delta P_t$ is given as the static pressure difference $\Delta P_s$ because the mean air velocity remains constant. However where the cross-section

area is not constant across the duct fitting such as a diffuser or a contraction, then the total pressure difference $\Delta P_t$ has to be normalised by using :

$$\Delta P_t = \Delta P_m + \Delta P_{kb} \tag{3.3}$$

where $\Delta P_m$ is the measured static pressure difference and $\Delta P_{kb}$ is the difference in dynamic pressures in the upstream and downstream ducts. For duct fittings such as branches, two k-factors are obtained, one for the branch section and one for the main flow. The total pressure difference is calculated using equation 3.3 and the upstream and downstream duct lengths are treated the same as a transition because the duct mean velocity changes.

Figure 3.1 shows a plot of the division of total pressure difference and dynamic pressure (i.e. $\Delta P_t/P_k$ ) against the distance from the duct fitting given as negative upstream and positive downstream.

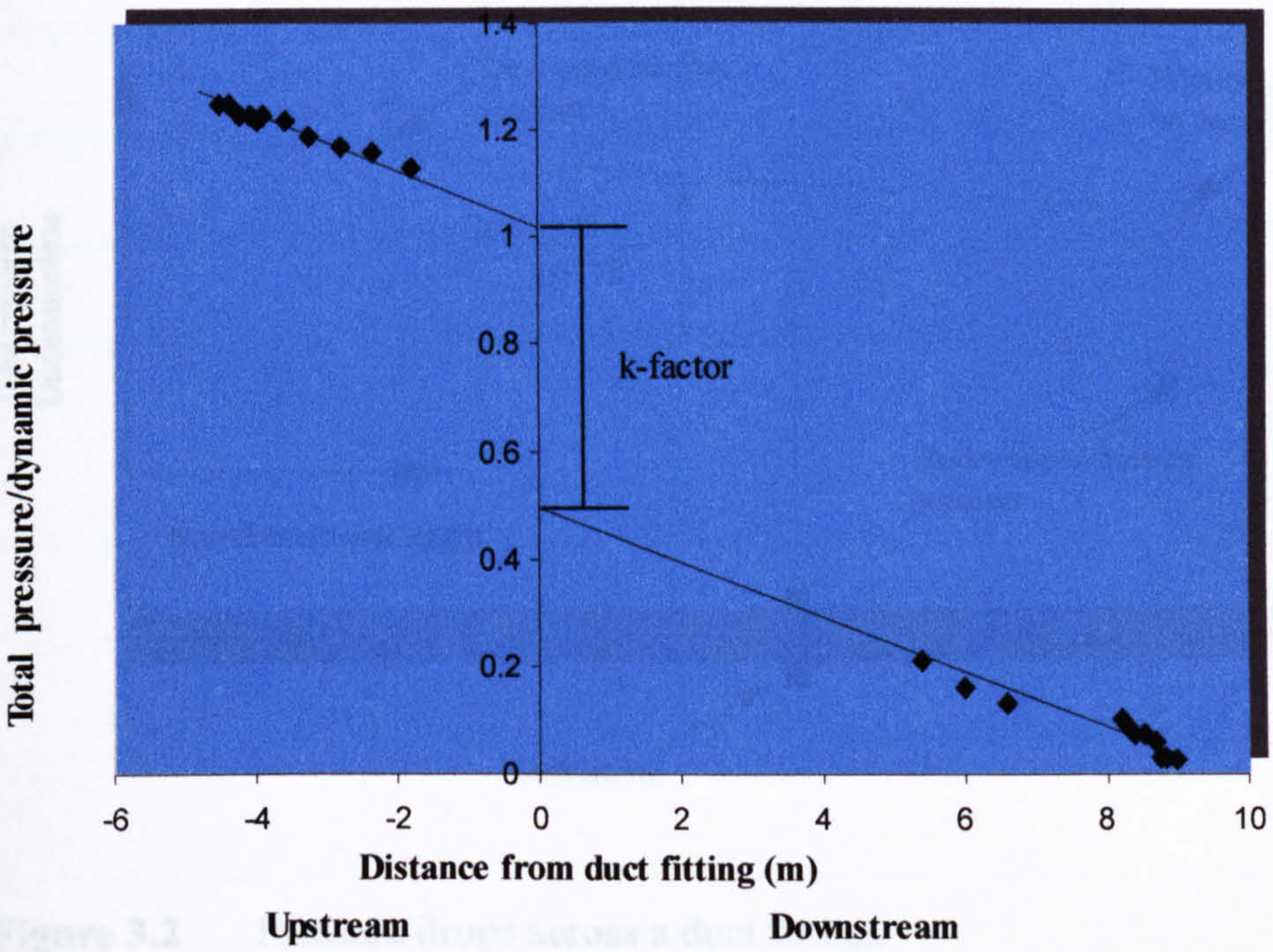


**Figure 3.1** Pressure distribution plot.

It can be seen from figure 3.1 that each distribution is a measure of the k-factor before and after the duct fitting, therefore if each tangent is traced back to the zero point where the duct fitting is represented then this difference is the k-factor for that particular duct fitting. It should be noted that for constant cross-section ducts both tangents should be parallel however due to small fluctuations in the airflow, in practice the tangents are not exactly parallel. Figure 3.2 shows the normalised total pressure across a duct fitting.

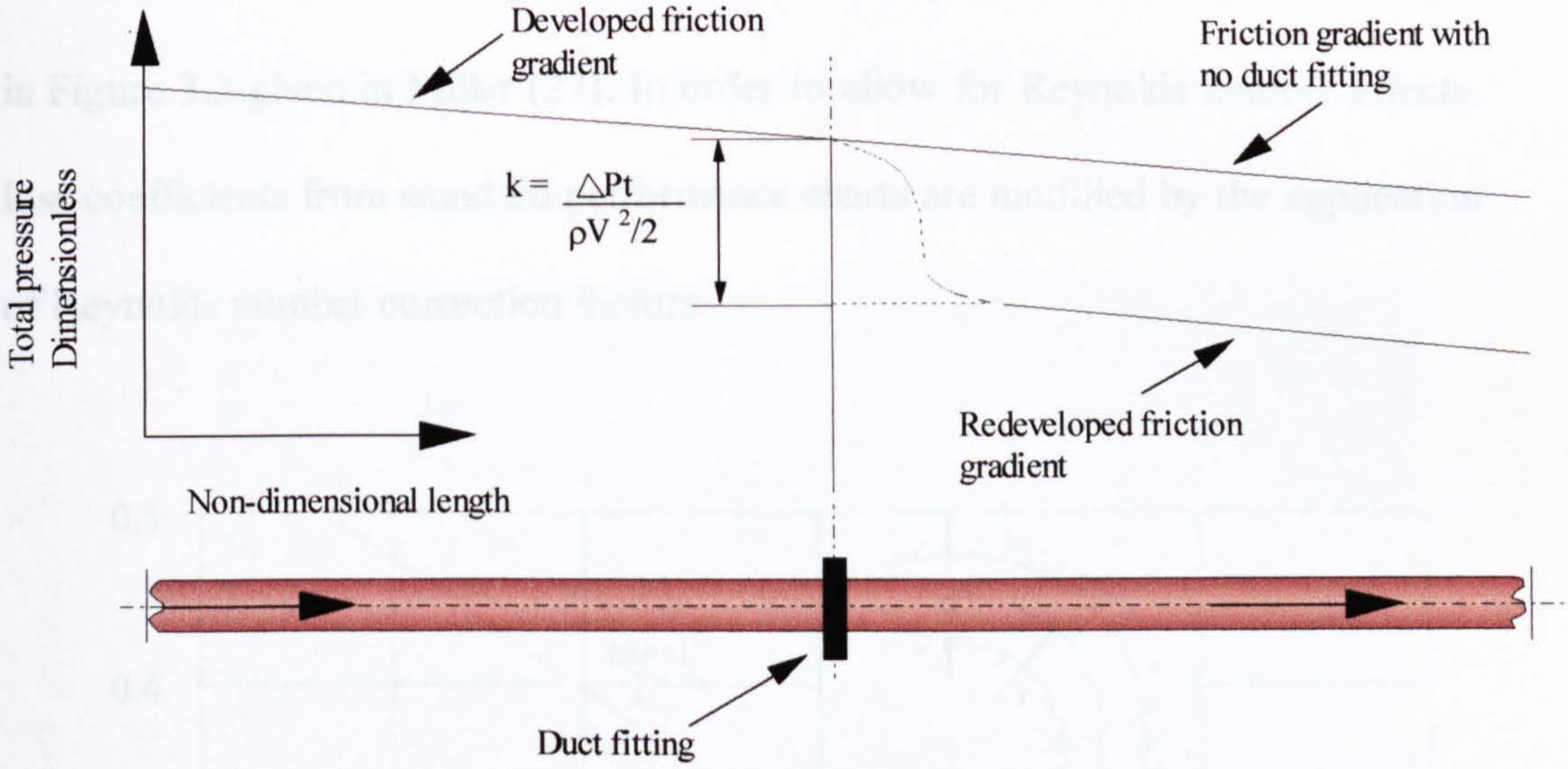


**Figure 3.2** Pressure drops across a duct fitting.

### 3.1.1.2 Pressure difference and Reynolds number

The pressure distribution method excludes the Reynolds number from the calculations by obtaining the k-factor from a single airflow velocity. Although it is known that the Reynolds Number affects the k-factor at very low velocities, it is not always possible in industry and in the research laboratory to involve experiments at various airflow velocities. Therefore, in some applications it is preferred that if possible long duct lengths are used and the pressure distribution at one airflow velocity is measured.

k-Factors for 90° bends vary considerably with Reynolds number as can be seen in Figure 3.3 given in Miller (27). In order to allow for Reynolds number effects, loss coefficients from standard performance charts are modified by the application of Reynolds number correction factors.

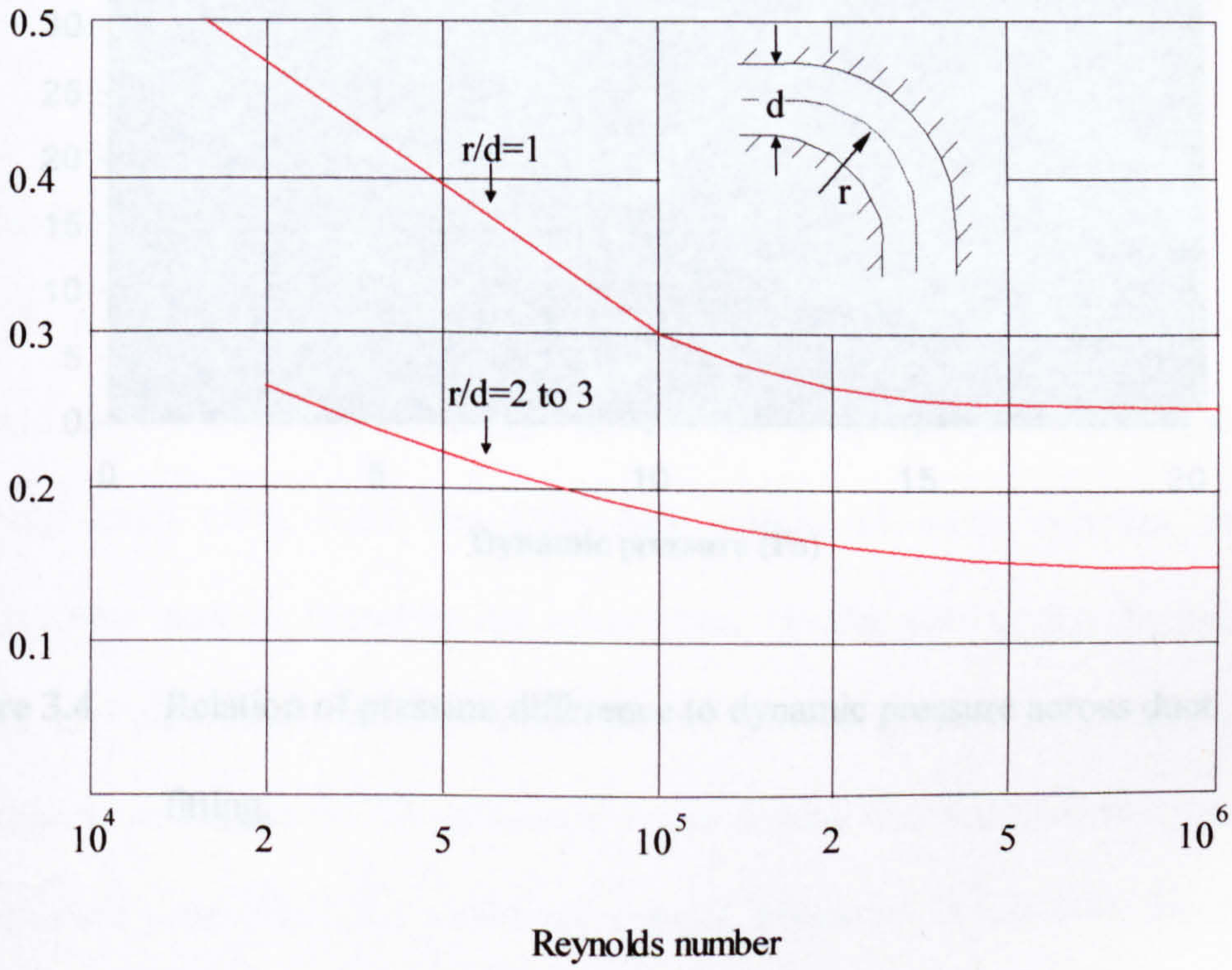


**Figure 3.3** Effect of Reynolds number on 90° bend loss coefficients. (Taken from Miller).

Another method of the pressure difference technique involves plotting the total pressure difference, $\Delta P_t$ , against the corresponding dynamic pressure, $P_k$, through a particular duct fitting. Figure 3.4 shows this plot where the gradient of

the resulting line is the k-factor. This method is however applicable only at high duct mean velocities to exclude the effect of the Reynolds Number.

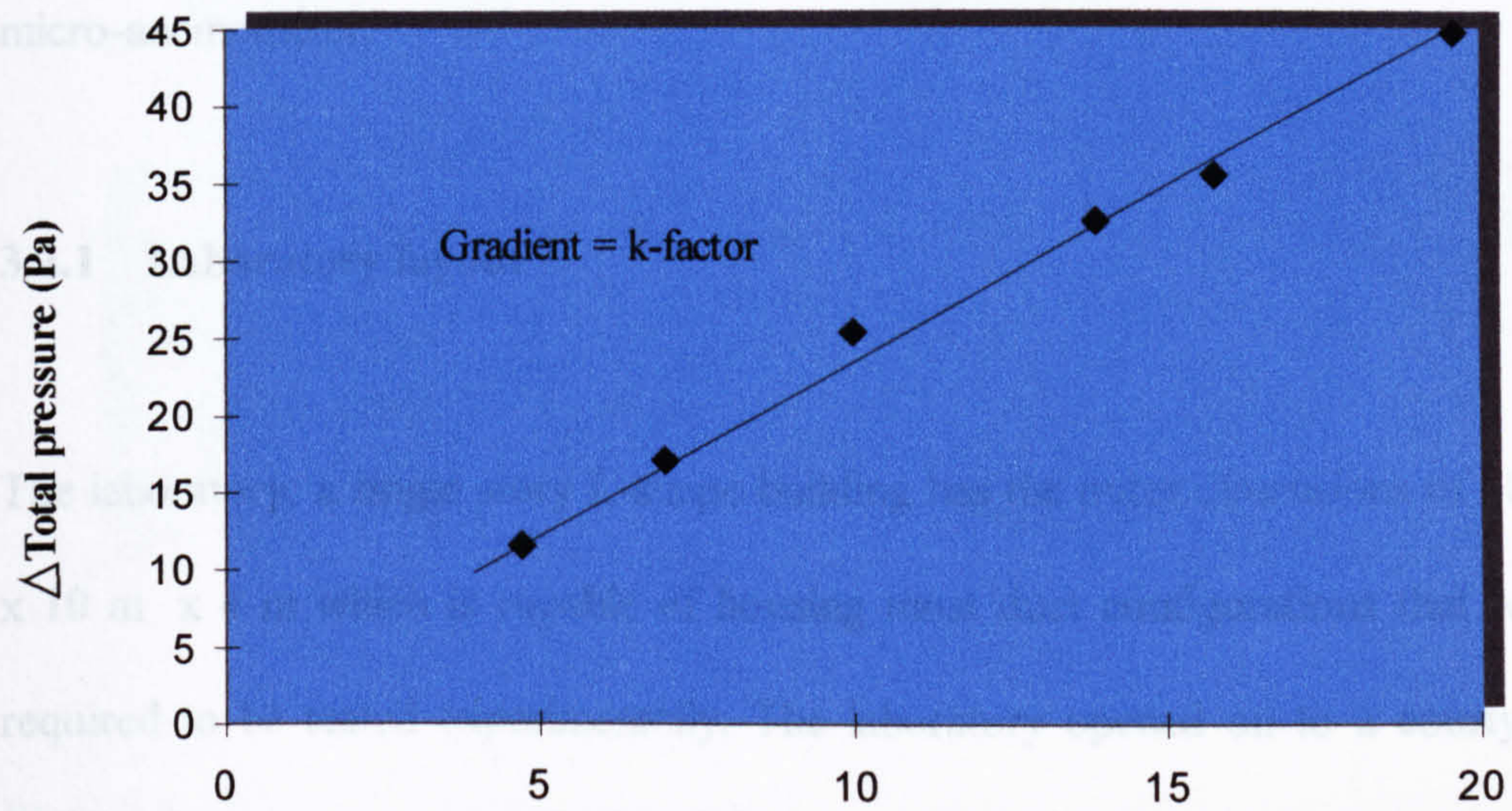


**Figure 3.4** Relation of pressure difference to dynamic pressure across duct fitting.

## 3.2 Rig construction

The experimental rig consisting of the system fan, instrumentation and the investigated duct fittings was constructed within the laboratory designed for experimental procedure of this kind. The duct work is set out with long upstream and downstream lengths for fully developed flow, and the instrumentation

adapted for each experiment to inject tracer-gas upstream and to sample the concentration downstream so that an accurate velocity measurement could be calculated. Velocity measurements were also taken using a Pitot-static tube and a micro-anemometer.

### 3.2.1 Laboratory layout

The laboratory, a single story L-shape building has the outer dimensions of 10 m x 10 m x 4 m which is capable of housing most duct configurations that were required to be tested experimentally. The laboratory opened on to a courtyard allowing much more room for long duct lengths of more complex duct arrangements such as branches and y-junctions. Having part of the ductwork outside and part inside the laboratory did not provide problems in tracer-gas experiments so long as the fan outlet was a considerable distance from the tracer-gas injection point. Plate 3.1 shows the general laboratory layout with the fan, instrumentation and ductwork.

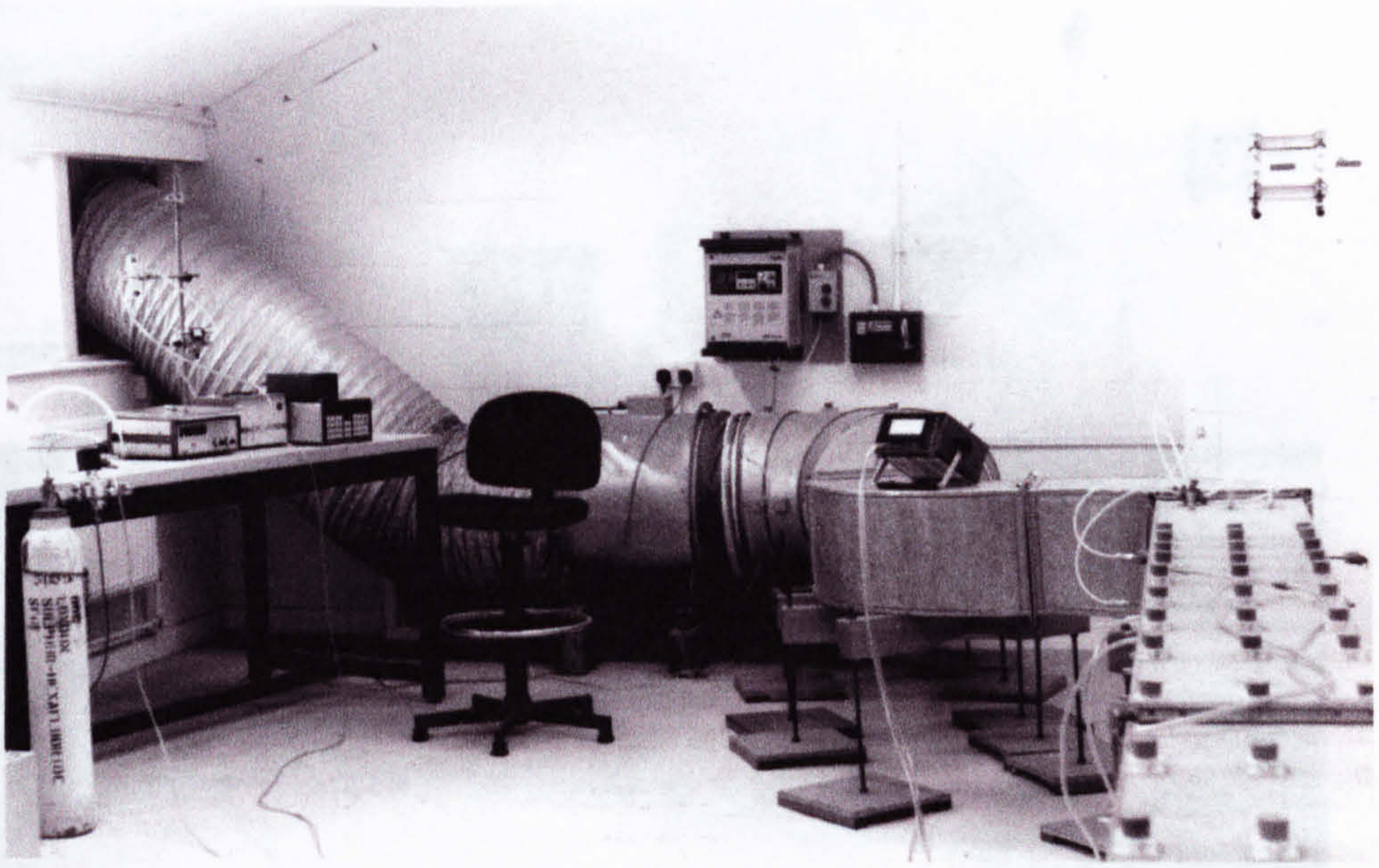

**Plate 3.1** Laboratory layout

### 3.2.2 Investigated duct fittings

The wide variety of duct fittings in this investigation involve fittings covered by ASHRAE and CIBSE with the addition of many components that are in common use today in HVAC systems. Plate 3.2 shows a sample of duct fittings in the laboratory including a y-junction, a diffuser and a multi-branch.

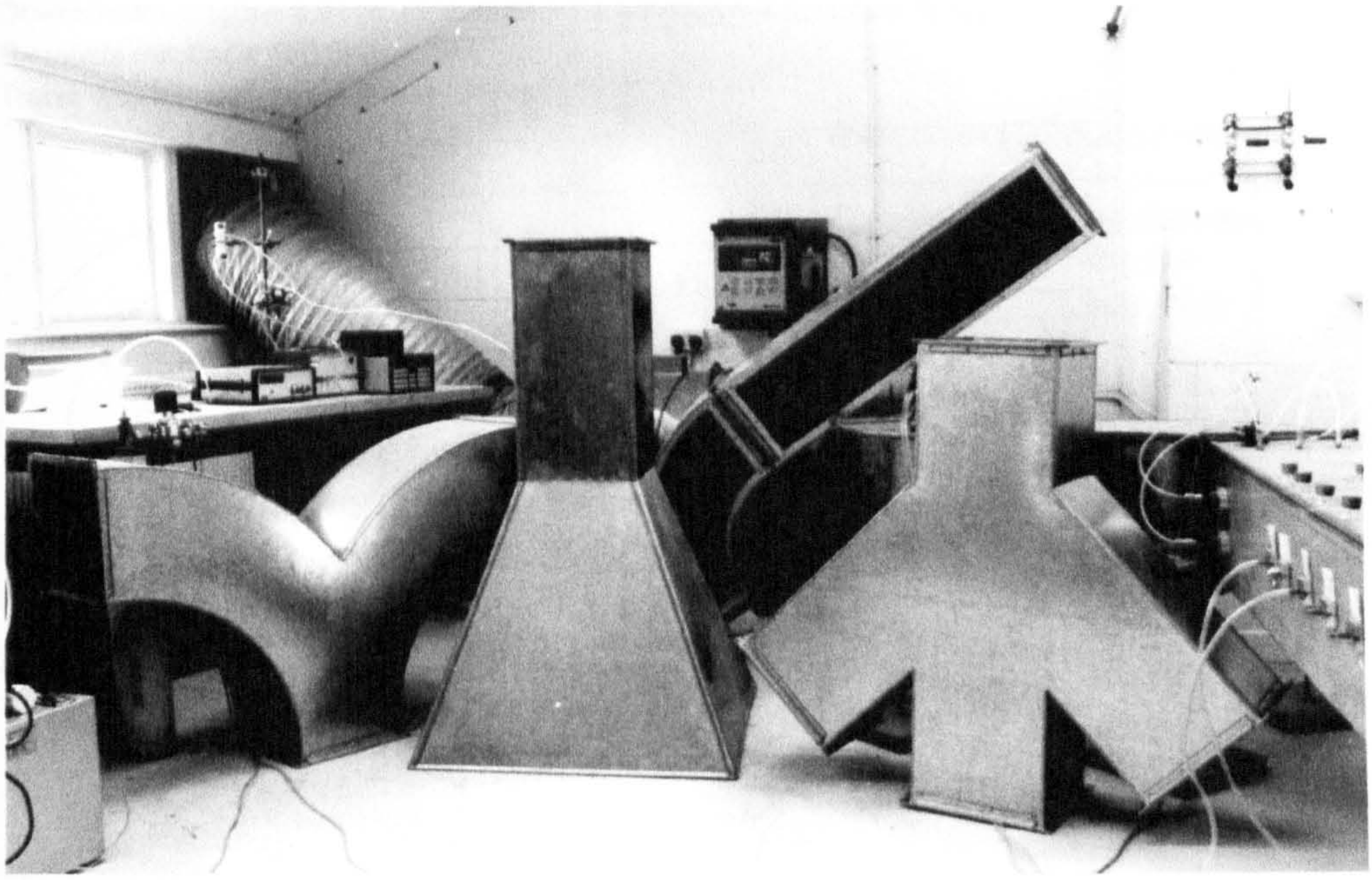

**Plate 3.2** Investigated duct fittings

Figures 3.5 to 3.19 show the dimensions of the experimental investigations with the operating conditions used.

Rectangular 90 degree smooth bend :
Upstream length = 5.375 m, Pitot-static tube traverse = 1.0 m from fitting.
Downstream length = 5.81 m, Pitot-static tube traverse = 4.0 m from fitting.
Reynolds number = 150,829.
Tracer-gas injection rate = 0.8 l/min

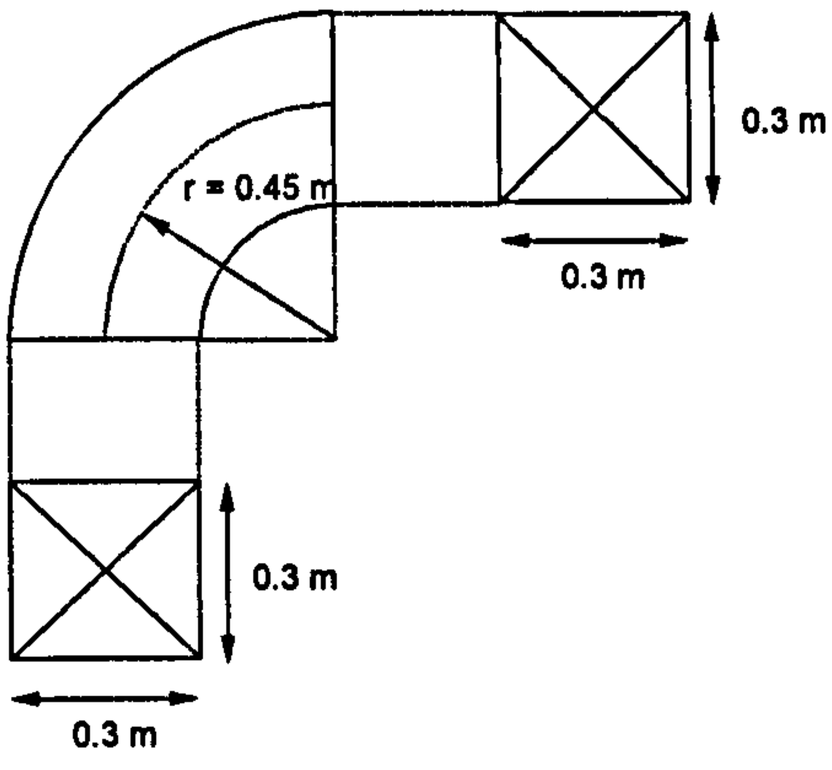


Static pressure tapping positions :

| Upstream distance from fitting : | Downstream distance from fitting : |
|---|---|
| 1.53 | 1.455 |
| 1.375 | 1.780 |
| 1.23 | 2.235 |
| 1.075 | 2.685 |
| 1.00 | 3.23 |
| 0.85 | 3.835 |
| 0.70 | 4.435 |
| 0.625 | 5.035 |
| 0.55 | |
| 0.40 | |
| 0.25 | |
| 0.15 | |
| 0.08 | |

**Figure 3.5** Experimental dimensions for rectangular 90 ° bend.

Rectangular u-bend :
Upstream length = 5.375 m, Pitot-static tube traverse = 1.0 m from fitting.
Downstream length = 5.81 m, Pitot-static tube traverse = 4.0 m from fitting.
Separation x varied as (0, 0.5 and 1.2) m in length.
Reynolds number = 149,171.
Tracer-gas injection rate = 1.4 l/min

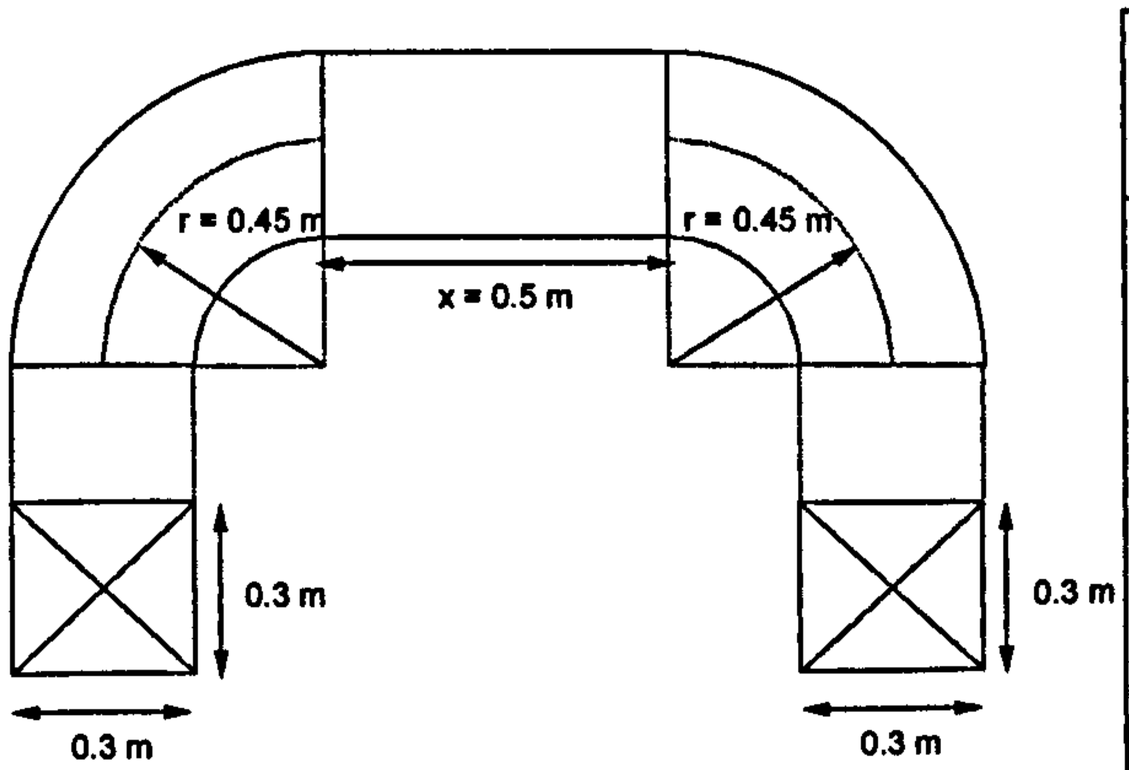


Static pressure tapping positions :

| Upstream distance from fitting : | | Downstream distance from fitting : |
|---|---|---|
| 4.53 | 1.20 | 1.455 |
| 4.435 | 1.05 | 1.780 |
| 4.285 | 0.90 | 2.235 |
| 4.135 | 0.745 | 2.685 |
| 3.985 | 0.65 | 3.23 |
| 3.905 | 0.58 | 3.835 |
| 3.755 | | 4.435 |
| 3.605 | | 5.035 |
| 3.535 | | |
| 3.455 | | |
| 3.305 | | |
| 3.155 | | |
| 3.055 | | |
| 2.98 | | |
| 1.505 | | |
| 1.35 | | |

**Figure 3.6** Experimental dimensions for a rectangular U-bend.

Rectangular expansion :
Upstream length = 3.606 m, Pitot-static tube traverse = 1.0 m from fitting.
Downstream length = 4.22 m, Pitot-static tube traverse = 4.0 m from fitting.
Reynolds number = 116,022.
Tracer-gas injection rate = 1.4 l/min

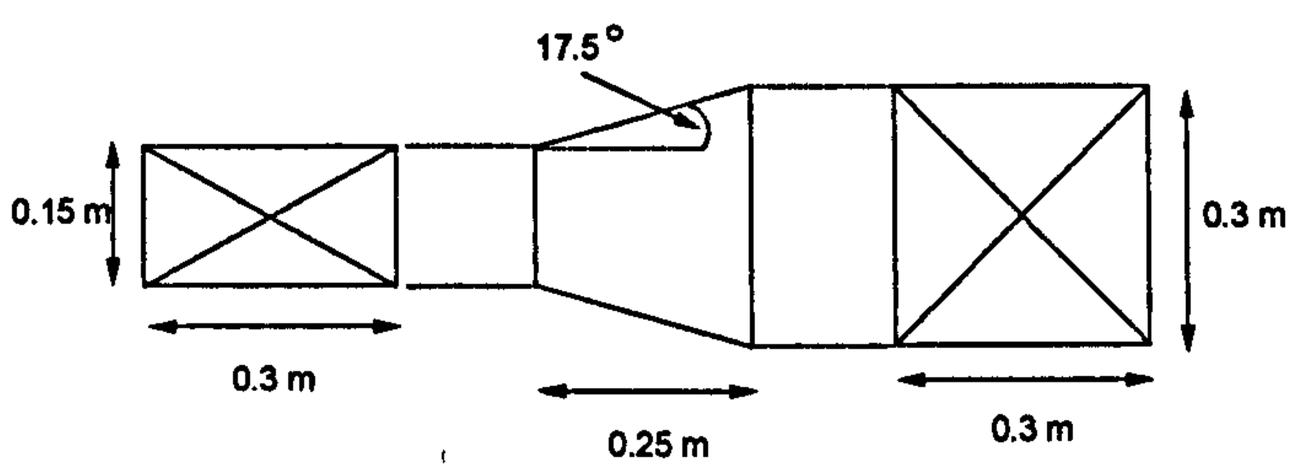


Static pressure tapping positions :

| Upstream distance from fitting : | Downstream distance from fitting : |
|---|---|
| 1.05 | 4.00 |
| 0.855 | 4.325 |
| 0.705 | 4.78 |
| 0.405 | 5.23 |
| 0.25 | 5.775 |
| 0.15 | 6.38 |
| 0.075 | 6.98 |
| | 7.58 |

**Figure 3.7** Experimental dimensions for a rectangular expansion.

Rectangular contraction :
Upstream length = 4.22 m, Pitot-static tube traverse = 1.0 m from fitting.
Downstream length = 3.606 m, Pitot-static tube traverse = 3.0 m from fitting.
Reynolds number = 166,667.
Tracer-gas injection rate = 2.7 l/min

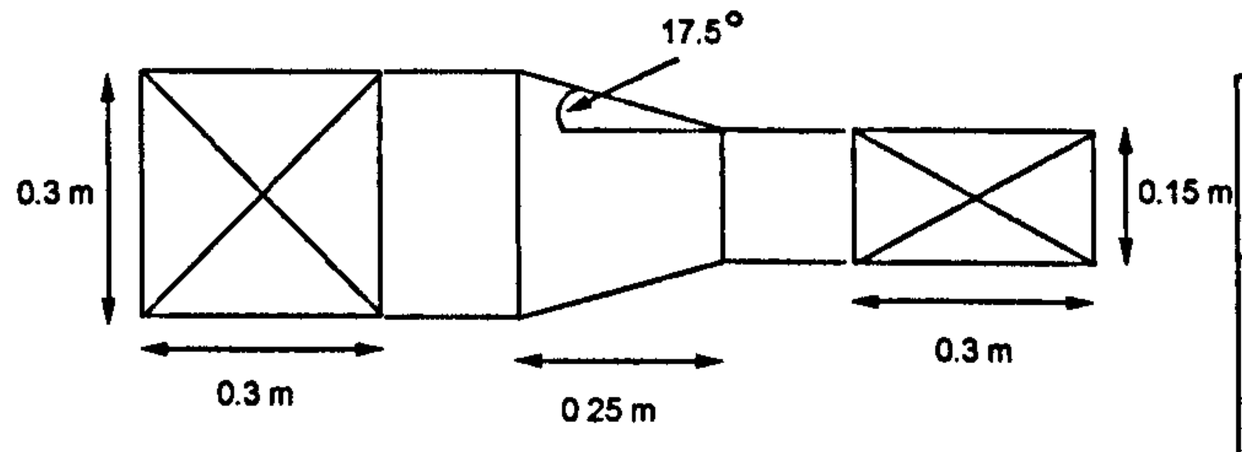


Static pressure tapping positions :

| Upstream distance from fitting : | | Downstream distance from fitting : |
|---|---|---|
| 3.23 | 1.35 | 3.535 |
| 3 075 | 1.2 | 3.46 |
| 2 93 | 1.05 | 3.36 |
| 2.78 | 0.9 | 3.205 |
| 2.555 | 0.745 | 2.91 |
| 2 405 | 0.65 | 2.76 |
| 2.33 | 0.58 | 2 61 |
| 2.255 | | |
| 2.105 | | |
| 1.955 | | |
| 1 855 | | |
| 1.78 | | |
| 1.505 | | |

**Figure 3.8** Experimental dimensions for rectangular contraction.

Rectangular expansion and u-bend :
Upstream length = 3.606 m, Pitot-static tube traverse = 1.0 m from fitting.
Downstream length = 7.002 m, Pitot-static tube traverse = 5.0 m from fitting.
Reynolds number = 155,556.
Tracer-gas injection rate = 1.37 l/min

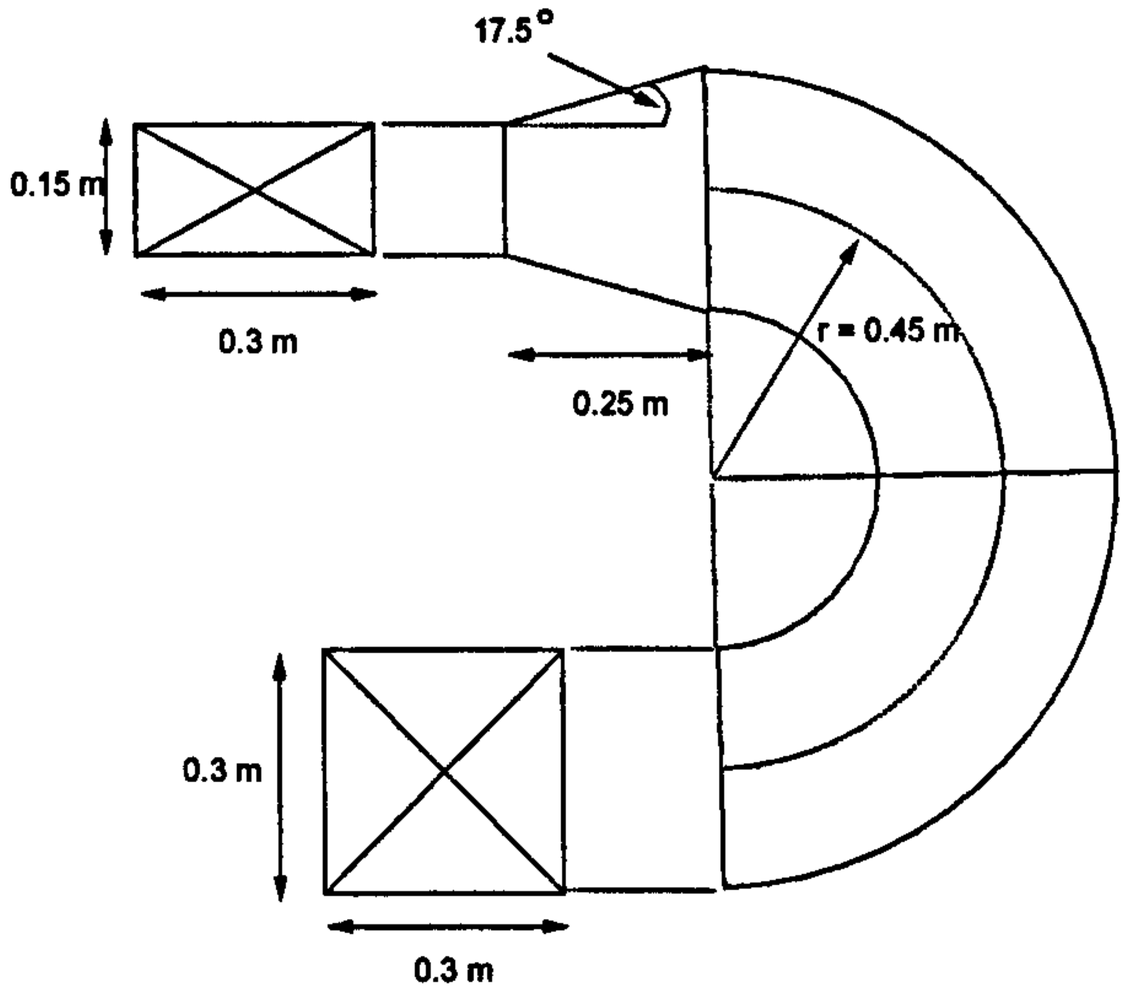


Static pressure tapping positions :

| Upstream distance from fitting : | Downstream distance from fitting : |
|---|---|
| 1.0 | 2.66 |
| 0.85 | 2.985 |
| 0.705 | 3.435 |
| 0.55 | 3.89 |
| 0.405 | 4.435 |
| 0.25 | 5.04 |
| 0.15 | 5.64 |
| 0.075 | 6.24 |

**Figure 3.9** Experimental dimensions for a rectangular expansion and U-bend.

Rectangular contraction, expansion and u-bend :
Upstream length = 4.22 m, Pitot-static tube traverse = 1.0 m from fitting.
Downstream length = 7.002 m, Pitot-static tube traverse = 5.0 m from fitting.
Reynolds number = 116,667.
Tracer-gas injection rate = 1.37 l/min

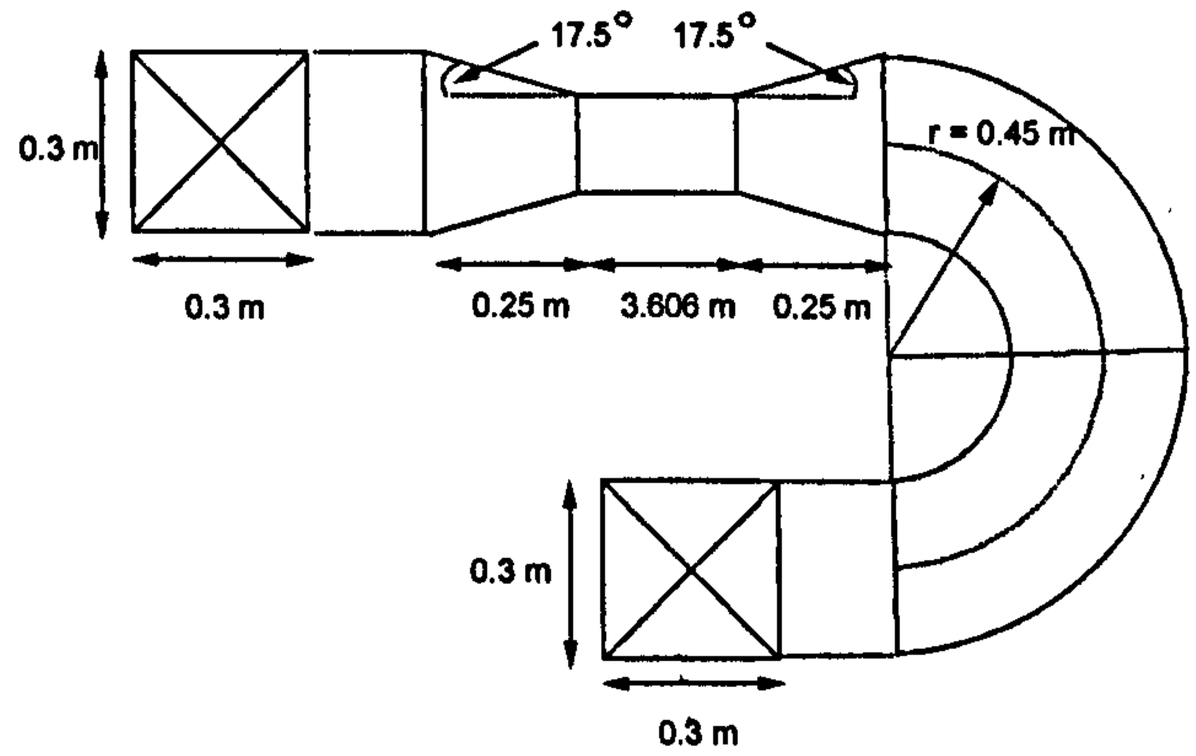


Static pressure tapping positions :

| Upstream distance from fitting : | | Downstream distance from fitting : |
|---|---|---|
| 3.23 | 1.2 | 2.66 |
| 3.075 | 1.05 | 2.985 |
| 2.93 | 0.9 | 3.435 |
| 2.78 | 0.745 | 3.89 |
| 2.555 | 0.65 | 4.435 |
| 2.405 | 0.58 | 5.04 |
| 2.33 | | 5.64 |
| 2.255 | | 6.24 |
| 2.105 | | |
| 1.955 | | |
| 1.855 | | |
| 1.78 | | |
| 1.505 | | |
| 1.35 | | |

**Figure 3.10** Experimental dimensions for a rectangular contraction, expansion and U-bend.

Rectangular damper plate :
Damper angle varied for (10, 20, 45, and 60) degrees.
Upstream length = 2.605 m, Pitot-static tube traverse = 1.0 m from fitting.
Downstream length = 7.82 m, Pitot-static tube traverse = 5.0 m from fitting.
Reynolds number = 63,333.
Tracer-gas injection rate = 1.56 l/min

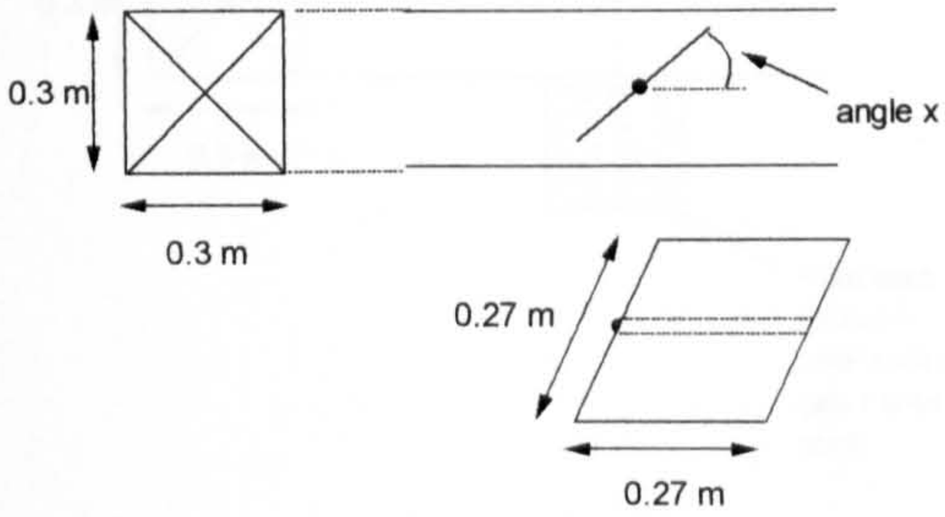


Static pressure tapping positions :

| Upstream distance from fitting : | Downstream distance from fitting : |
|---|---|
| 1.83 | 0.89 |
| 1.68 | 0.955 |
| 1.53 | 1.055 |
| 1.155 | 1.205 |
| 0.93 | 1.355 |
| 0.855 | 1.505 |
| 0.705 | 1.655 |
| 0.555 | 1.805 |
| 0.38 | 2.78 |
| | 3.38 |
| | 3.98 |
| | 4.585 |
| | 5.13 |
| | 5.585 |
| | 6.035 |
| | 6.36 |

**Figure 3.11** Experimental dimensions for a rectangular damper plate.

Rectangular wire mesh :
Mesh free area ratio varied for (0.35, 0.4 and 0.5).
Upstream length = 2.305 m, Pitot-static tube traverse = 1.0 m from fitting.
Downstream length = 7.520 m, Pitot-static tube traverse = 5.0 m from fitting.
Reynolds number = 115,000.
Tracer-gas injection rate = 1.95 l/min

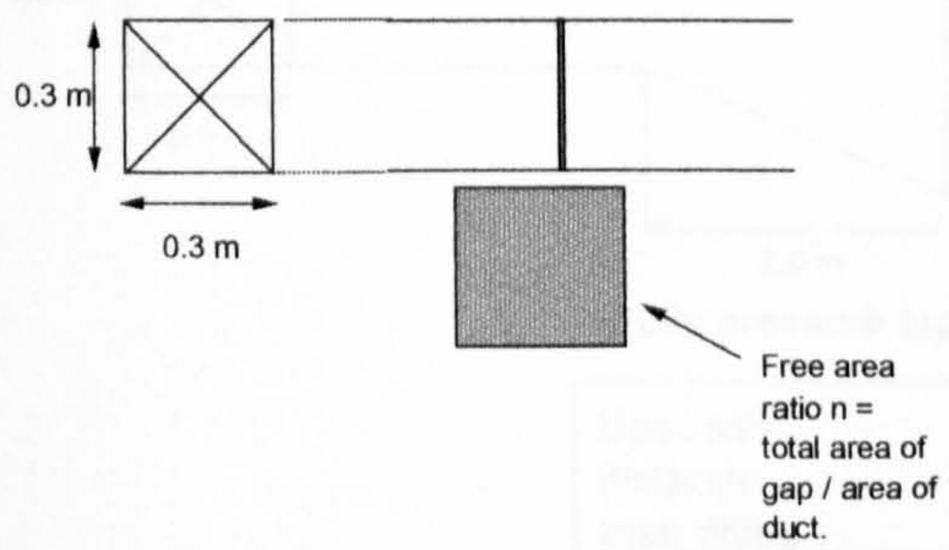


Static pressure tapping positions :

| Upstream distance from fitting : | Downstream distance from fitting : |
|---|---|
| 1.53 | 0.585 |
| 1.33 | 0.655 |
| 1.23 | 0.755 |
| 0.855 | 0.905 |
| 0.63 | 1.055 |
| 0.555 | 1.205 |
| 0.405 | 1.355 |
| 0.255 | 1.505 |
| 0.08 | 2.48 |
| | 3.08 |
| | 3.68 |
| | 4.285 |
| | 4.83 |
| | 5.285 |
| | 5.735 |
| | 6.06 |

**Figure 3.12** Experimental dimensions for a rectangular wire mesh obstruction.

Rectangular perforated sheet :
Mesh free area ratio varied for (0.2, 0.3, 0.4 and 0.5).
Upstream length = 2.305 m, Pitot-static tube traverse = 1.0 m from fitting.
Downstream length = 7.520 m, Pitot-static tube traverse = 5.0 m from fitting.
Reynolds number = 111,667.
Tracer-gas injection rate = 1.95 l/min

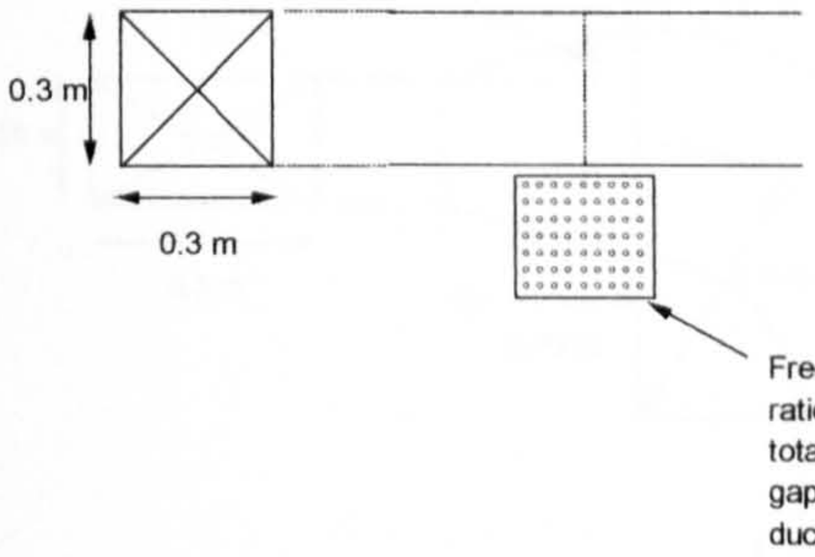


Static pressure tapping positions :

| Upstream distance from fitting : | Downstream distance from fitting : |
|---|---|
| 1.53 | 0.585 |
| 1.33 | 0.655 |
| 1.23 | 0.755 |
| 0.855 | 0.905 |
| 0.63 | 1.055 |
| 0.555 | 1.205 |
| 0.405 | 1.355 |
| 0.255 | 1.505 |
| 0.08 | 2.48 |
| | 3.08 |
| | 3.68 |
| | 4.285 |
| | 4.83 |
| | 5.285 |
| | 5.735 |
| | 6.06 |

**Figure 3.13** Experimental dimensions for a rectangular perforated sheet obstruction.

Rectangular exit diffuser :
Upstream length = 9.403 m, Pitot-static tube traverse = 2.0 m from fitting.
Reynolds number = 111,667.
Tracer-gas injection rate = 1.56 l/min

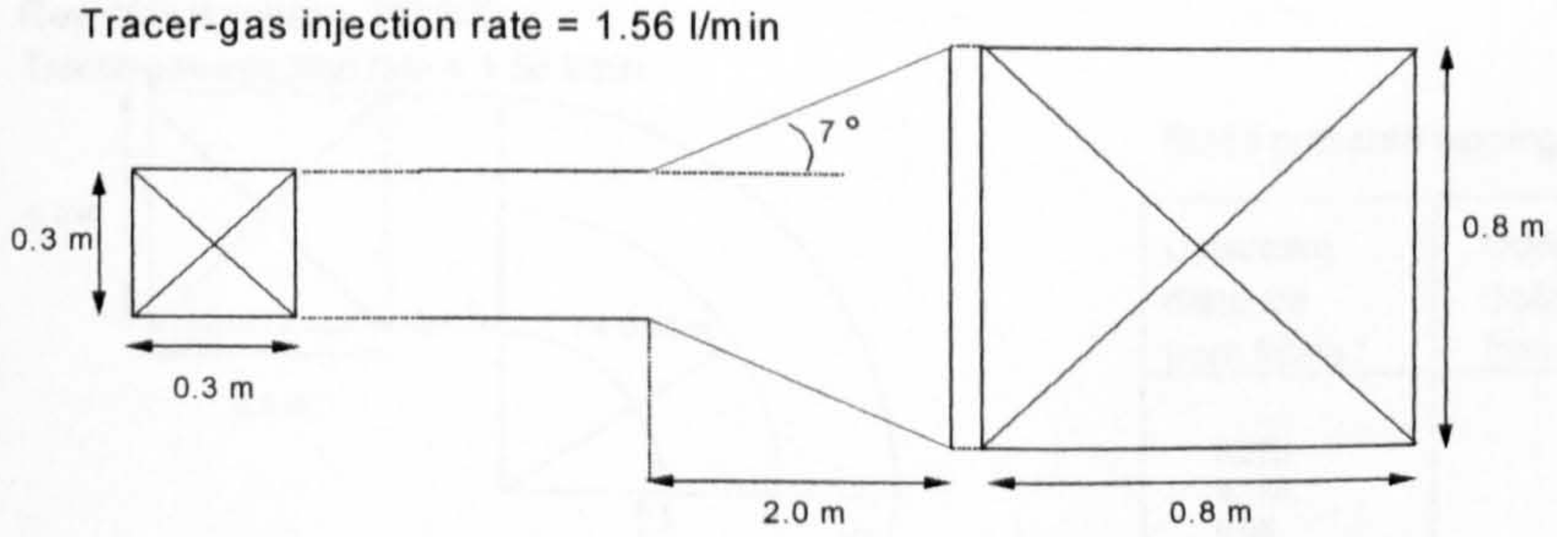


Static pressure tapping positions :

| Upstream distance from fitting : | | |
|---|---|---|
| 8.723 | 7.498 | 3.918 |
| 8.478 | 7.348 | 3.313 |
| 8.323 | 7.248 | 2.763 |
| 7.948 | 7.173 | 2.313 |
| 7.723 | 5.118 | 1.858 |
| 7.648 | 4.518 | 1.533 |

**Figure 3.14** Experimental dimensions for a rectangular exit diffuser.

Rectangular expansion and 90 degree bend :
Upstream length = 3.606 m, Pitot-static tube traverse = 1.0 m from fitting.
Downstream length = 7.002 m, Pitot-static tube traverse = 5.0 m from fitting.
Reynolds number = 122,222.
Tracer-gas injection rate = 1.56 l/min

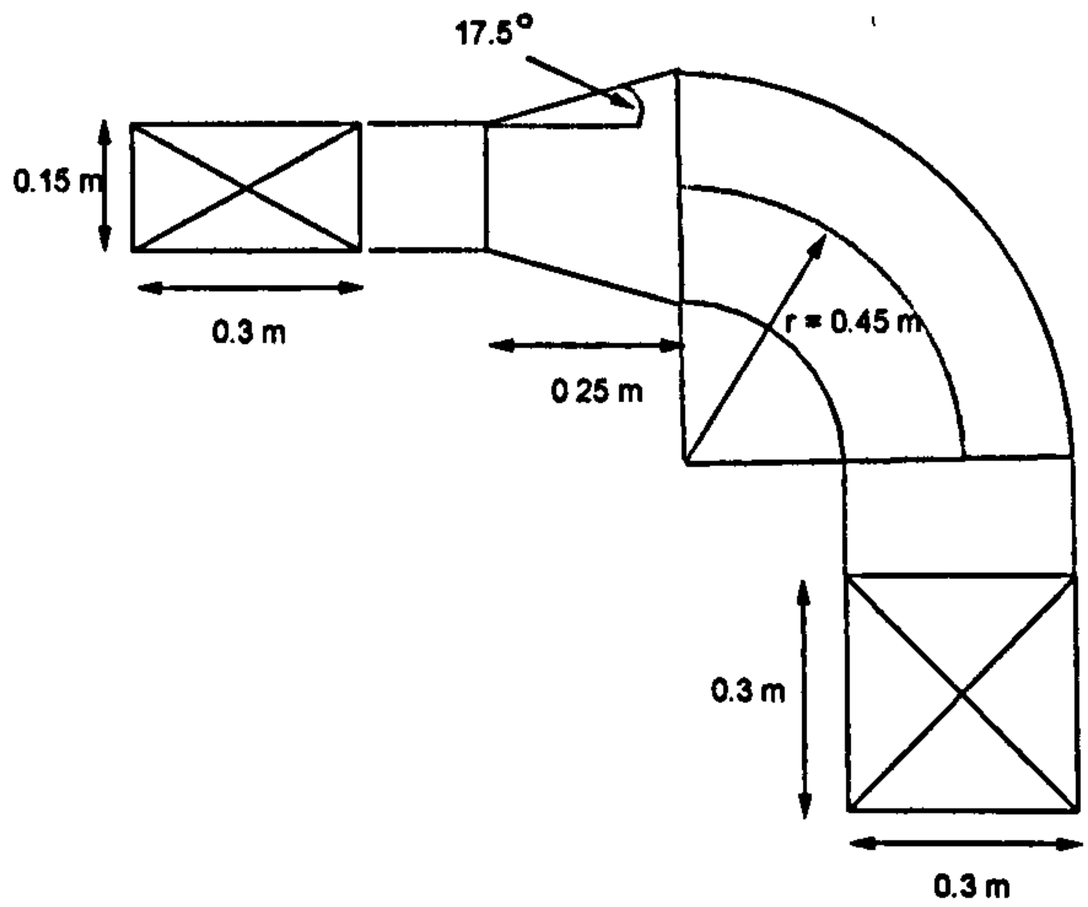


Static pressure tapping positions :

| Upstream distance from fitting : | Downstream distance from fitting : |
|---|---|
| 2.255 | 5 375 |
| 2.155 | 5.70 |
| 2.00 | 6 155 |
| 1.70 | 6 605 |
| 1 405 | 7.15 |
| | 7.50 |
| | 7.675 |
| | 7.825 |
| | 7.975 |
| | 8 05 |
| | 8.125 |
| | 8.275 |
| | 8.425 |
| | 8 575 |

**Figure 3.15** Experimental dimensions for a rectangular expansion and 90° bend.

Rectangular 90 degree bend and contraction :
Upstream length = 7.022 m, Pitot-static tube traverse = 1.0 m from fitting.
Downstream length = 3.606 m, Pitot-static tube traverse = 5.0 m from fitting.
Reynolds number = 108,889.
Tracer-gas injection rate = 1.56 l/min

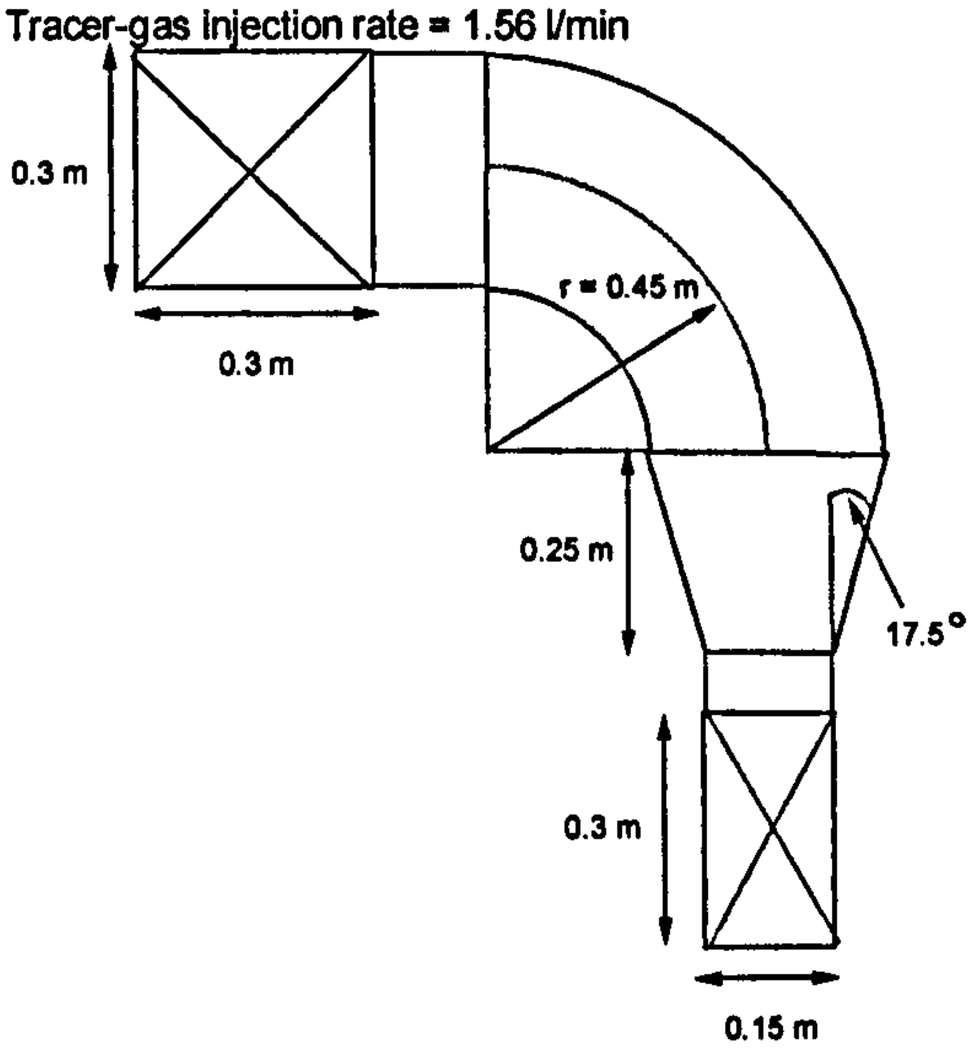


Static pressure tapping positions :

| Upstream distance from fitting : | Downstream distance from fitting : |
|---|---|
| 8.275 | 1 405 |
| 8.125 | 1.70 |
| 8 05 | 2.00 |
| 7.975 | 2.155 |
| 7.825 | 2.255 |
| 7.675 | 2.61 |
| 7.50 | 2.91 |
| 7.15 | 3.21 |
| 6.605 | 3.36 |
| 6 155 | 3 46 |
| 5 70 | |
| 5 375 | |

**Figure 3.16** Experimental dimensions for a rectangular 90° bend and contraction.

Rectangular 90 degree bend and damper plate :
Damper angle varied for (10, 20 and 30) degrees.
Upstream length = 5.605 m, Pitot-static tube traverse = 1.0 m from fitting.
Downstream length = 7.82 m, Pitot-static tube traverse = 5.0 m from fitting.
Reynolds number = 83,333.
Tracer-gas injection rate = 1.56 l/min

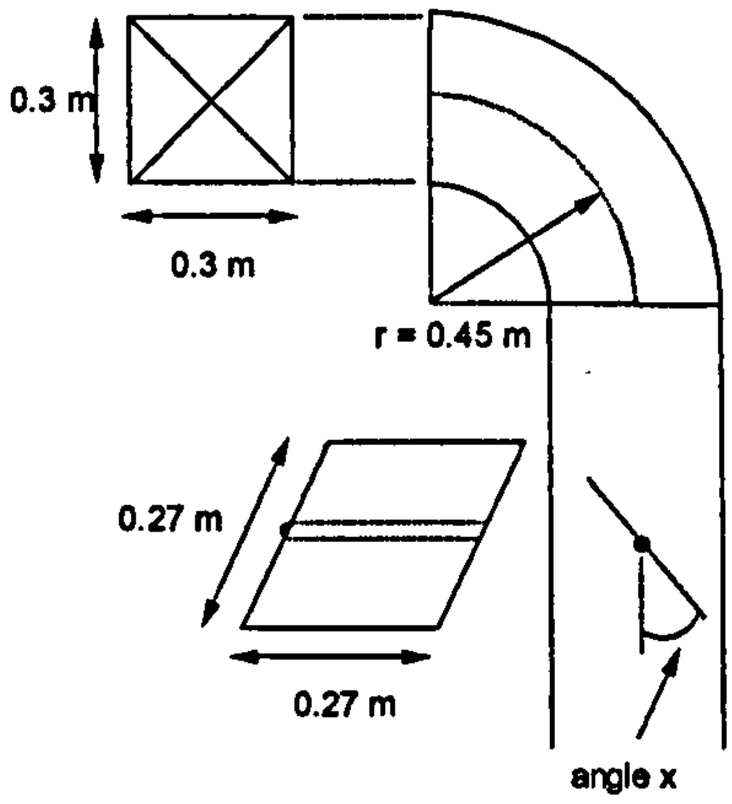


Static pressure tapping positions :

| Upstream distance from fitting : | Downstream distance from fitting : |
|---|---|
| 8.98 | 1.785 |
| 8.83 | 2.33 |
| 8.755 | 2.785 |
| 8.68 | 3.24 |
| 8.53 | 3.565 |
| 8.38 | 3.89 |
| 8.28 | 3.965 |
| 8.205 | 4.06 |
| 6.595 | 4.215 |
| 5.995 | 4.365 |
| 5.395 | 4.51 |
| | 4.66 |
| | 4.815 |

**Figure 3.17** Experimental dimensions for a rectangular 90° bend and damper plate.

Rectangular smooth T-branch :
Staight lengths = 5.0 m, Pitot-static tube traverse = 1.0 m from fitting.
Branch length = 6.1 m, Pitot-static tube traverse = 5.0 m from fitting.
Reynolds number = 100,000.
Tracer-gas injection rate = 1.17 l/min
Static pressure tappings placed at 0.6 m upstream and 3.0 m downstream from fitting.

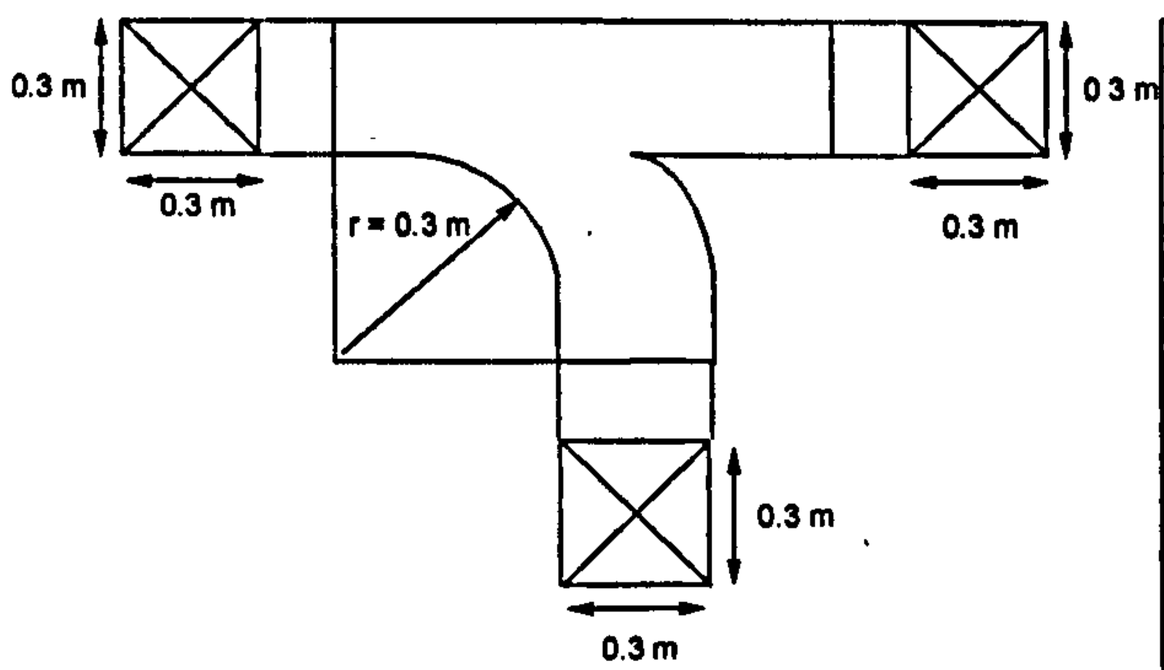


Varied velocity ratio :

| Diverging Main flow ratio : | Diverging Branch flow ratio : |
|---|---|
| 0.58 | 0.51 |
| 0.54 | 0.45 |
| 0 52 | 0 44 |
| | 0 47 |
| | 0 48 |
| | 0.50 |
| **Converging Main flow ratio :** | **Converging Branch flow ratio :** |
| 0.43 | 0.79 |
| 0.44 | 0.80 |
| 0.46 | 0.82 |

**Figure 3.18** Experimental dimensions for a rectangular Wye-branch.

Rectangular to circular extract hood :
Downstream length = 3.60 m, Pitot-static tube traverse = 3.0 m from fitting.
Reynolds number = 71,944.
Tracer-gas injection rate = 0.82 l/min

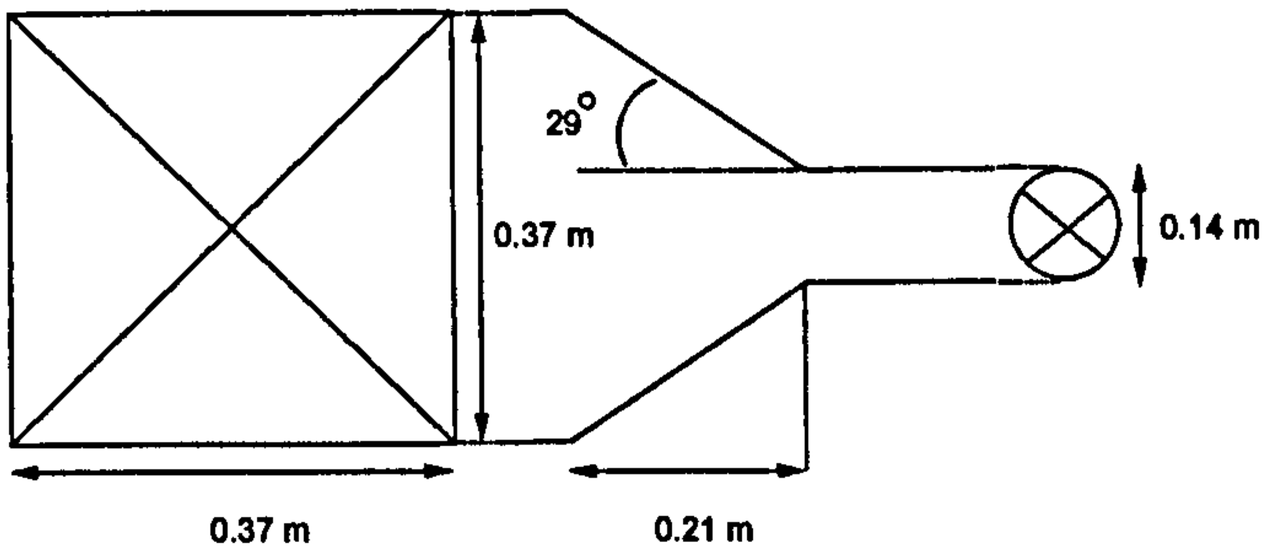


Static pressure tapping positions :

| Downstream distance from fitting : |
|---|
| 1.54 |
| 1.785 |
| 2.02 |
| 2.185 |
| 2.36 |
| 2.58 |
| 2.755 |
| 3.01 |
| 3.22 |
| 3.465 |

**Figure 3.19** Experimental dimensions for a rectangular to circular inlet extract hood.

The experimental designs for tested duct fittings in Figures 3.5-3.19 have been the basis for the CFD investigation. The CFD modelling was based on identical duct fittings tested in the laboratory except with slight geometrical variations such as aspect ratio and branch angles. Certain experimental characteristics are carried through to the CFD modelling to ensure a realistic prediction, and are given as follows :

- Upstream and downstream duct lengths kept between 20 and 30 hydraulic diameters to ensure flow development and re-development.

- Inlet air velocity is the same as measured in the experimental tests.
- A high density of grid cells are used in the near wall regions to ensure the prediction of the boundary layer thickness.

The velocity profile over the cross-section within a CFD model can be observed at different stages in the model to obtain the point where the profile does not change. It is at this point that the CFD prediction has determined the point of fully developed flow.

## 3.3 Experimental instrumentation

Figure 3.20 shows a schematic arrangement of the experimental apparatus as used in the tracer-gas experiments. The instrumentation is divided up into the tracer-gas injection and sampling sections. The apparatus is designed so that it may be adapted to suit any duct fitting to be investigated. The injection array is inserted into a length of duct that may be fitted anywhere within a duct configuration so that tracer-gas injection may be applied at various positions.

The instrumentation specifications are detailed as :

**System fan**

Type : Axial fan made by Elta Fans Ltd

Max RPM : 2880

Power rating : 4 kW

Impeller diameter : 700 mm

Controller : Sami ministar made by ABB

(Asea Brown Boveri)

**Pump**

Type : L2-C made by Capex Ltd

Max output : 5 l/min

**Gas analyser**

Type : Binos 1001 made by Rosemount Ltd

Sampling range : 0-500 ppm and 500-5000 ppm of $SF_6$

Averaged time range : 10 second intervals

Accuracy ± 3 %.

**Mass flow controller**

Type : El-Flow

Bronkhorst Hi-Tech Ltd

Max flow rate : 3.9 l/min of $SF_6$

**Flow meter**

Type : Platon

Range : 0-5 l/min with dust filter

**Micro-anemometer**

type : EDM 2500 made by Airflow Ltd

Range : 1-2500 Pa (0-30 m/s), Accuracy ±5 %

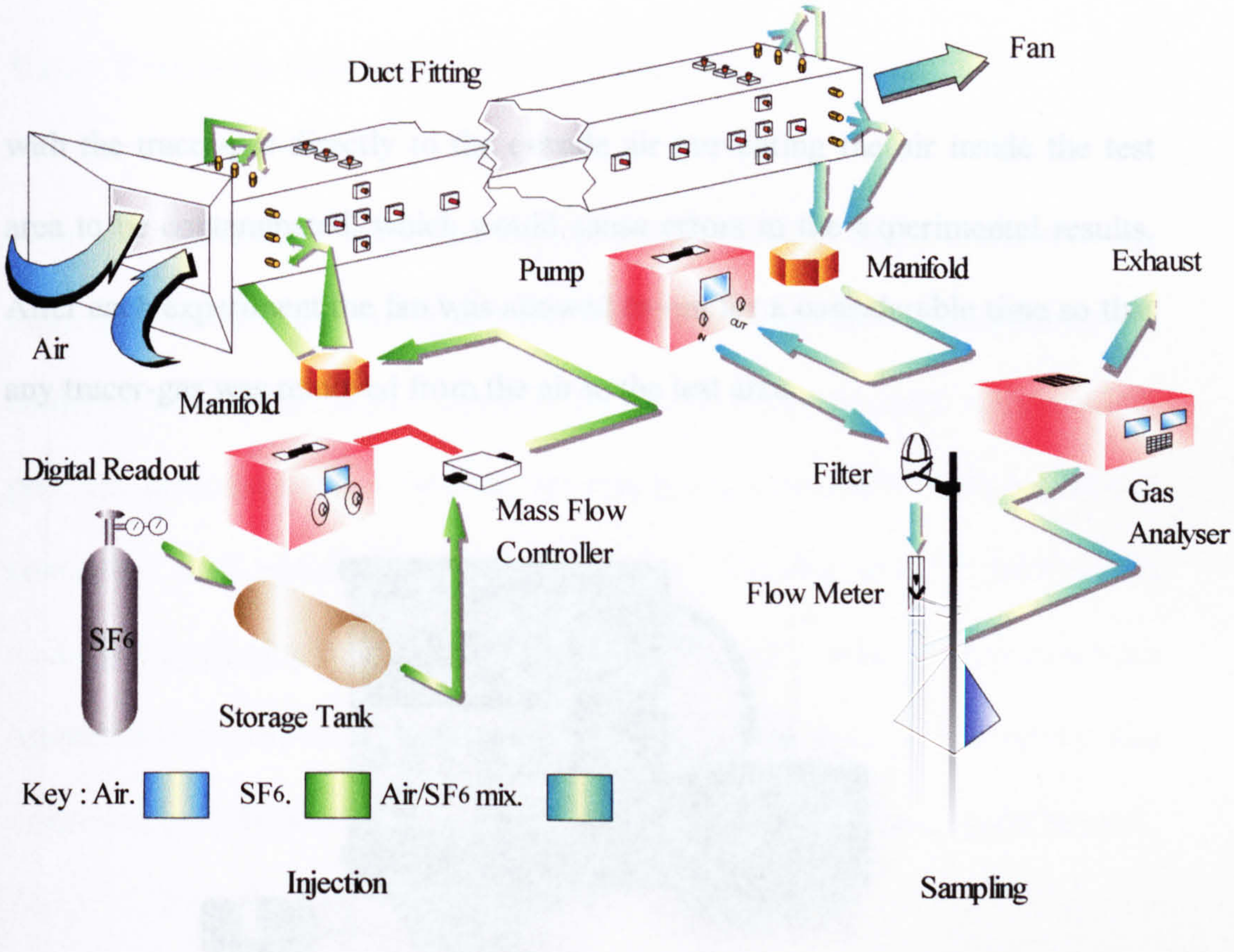


**Figure 3.20** Experimental instrumentation

### 3.3.1 Fan operations

The maximum power of the fan is 4 kW, and is sufficient to produce air velocities in the range of 0.5 m/s to 30 m/s which are used in HVAC systems. Plate 3.3 shows the general arrangement of the fan control panel. From this the voltage to the axial fan can be controlled and various airflow rates can be produced. Plate 3.3 also shows the flexible circular duct expelling the exhaust air

with the tracer-gas directly to the outside air preventing the air inside the test area to be contaminated, which would cause errors in the experimental results. After each experiment the fan was allowed to run for a considerable time so that any tracer-gas was removed from the air in the test area.

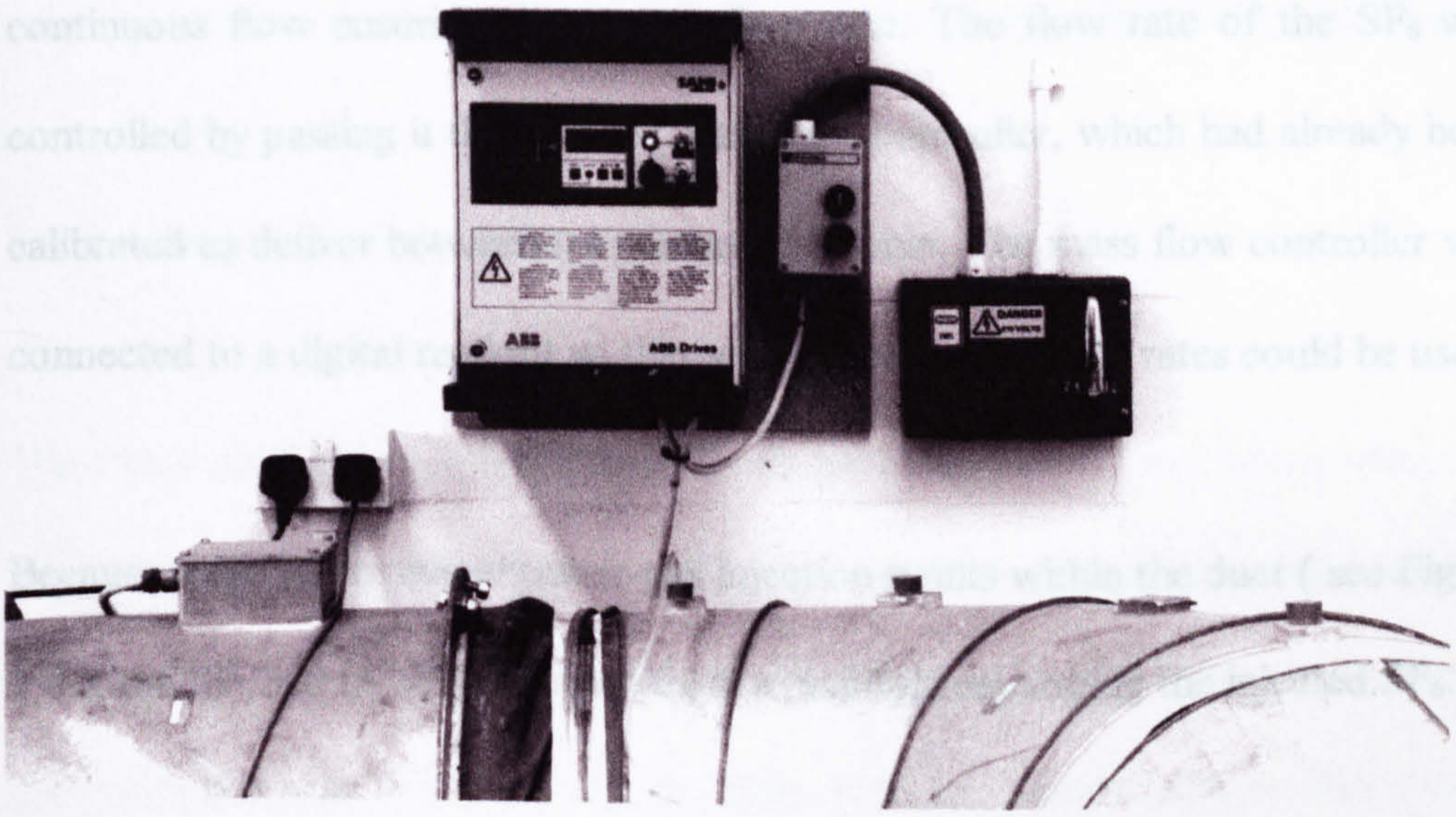


**Plate 3.3** Fan control panel

### 3.3.2 Tracer-gas injection

With the experimental apparatus arranged as is seen in figure 3.20, with the tracer-gas injection and sampling points determined the tracer-gas measurement could be taken. The sulphur hexaflouride ( $SF_6$ ) was released with constant pressure from the storage cylinder into the storage tank. The tank provided a continuous flow ensuring a constant flow rate. The flow rate of the $SF_6$ was controlled by passing it through the mass flow controller, which had already been calibrated to deliver between 0 l/min and 3.9 l/min. The mass flow controller was connected to a digital readout so that various tracer-gas flow rates could be used.

Because there were several tracer-gas injection points within the duct ( see Figure 2.6 ), the $SF_6$ had to be distributed from a manifold separating the injected $SF_6$.

### 3.3.3 Tracer-gas sampling

In order to achieve an accurate measurement of sampled $SF_6$, the upstream and downstream duct lengths have to be long enough to ensure adequate tracer-gas / air mixing which is explained in section 2.2.2 . However with highly turbulent flows mixing is easily obtained.

The sampled air is pumped out of the downstream duct at several points across the duct cross-section to ensure an even sample. The air is collected and controlled through a manifold at a rate of 2 l/min, which is required by the gas analyser. The sampled air is filtered so as not to allow dust and small particulates into the $SF_6$ gas analyser causing damage to the inner parts and also cause significant errors in the results. Finally, after $SF_6$ analysis, the sampled air is returned to the duct downstream of the fan where it is expelled to the outside air.

### 3.3.4 Duct mean velocity measurement

The mean air velocity within the duct for each experiment was taken using the conventional Pitot-static tube in conjunction with the micro-anemometer and the constant-injection tracer-gas technique. For the rectangular duct cross section used with dimensions 0.3 m x 0.3 m , three velocity measurement positions were used across the cross section with three different positions using different depths by which the Pitot-static tube was inserted. This meant a total of nine measurement points could be made and averaged to obtain the mean duct air velocity.

### 3.3.4.1 Pitot-static tube

The standard slim design of the Pitot-static tube as shown in Figure 2.1 is shaped in a 90° bend so that it may be inserted into the duct opposing the airflow. A series of 25 mm holes were drilled in the standard straight pieces of duct used for the upstream and downstream flows at distances of about ten diameters from the duct inlet and the duct fitting. A rubber bung was then seated within a sealed Perspex sleeve over the hole. Plate 3.4 shows how the Pitot-static tube, with rubber bung added, was placed through the hole in order to take a measurement. The holes were made along the length of the duct and across the cross-section so that an average measurement could be made. Taking in to account the micro-anemometer accuracy and the error allowed for taking measurements along with the average best fit accuracy when plotting the experimental results, the average accuracy for Pitot-static tube measurements is about ±6 %.

**Plate 3.4** Pitot-static tube velocity measurement position.

### 3.3.4.2 Tracer-gas

The $SF_6$ gas analyser gives a reading of tracer-gas in parts per million which is related to the velocity of the air in the duct through the $SF_6$ injection rate and the duct cross-sectional area, as is described in section 2.2.4 . Taking in to account the accuracy of the BINOS gas analyser and the best average best fit accuracy, the overall accuracy for tracer-gas measurements is about ±8 %. Unlike the velocity measurements taken with the Pitot-static tube which takes a single reading at a specific point, tracer-gas measurements are representative over the entire duct cross-section giving a more positive result.

## 3.4 Experimental procedure for single fittings and fittings interaction

With upstream and downstream duct lengths in the order of 20 diameters which is sufficient for fully developed flow and flow recovery, a wide variety of duct fittings were tested. The fittings such as a branch included either multiple upstream flows or downstream flows depending on the flow direction. In most cases the fitting was reversed so that the reverse characteristics could be tested. Multiple duct fittings in close proximity were also investigated and during the experiment were treated as a single fitting and as two separate fittings with a varied distance between them.

### 3.4.1 Static pressure measurement

For the calculation of velocity pressure loss factors (k-factors), the static pressure along the duct lengths before and after the fitting had to be measured. This was done by drilling 2 mm holes along the length of the duct. Attached to these holes were 4 mm copper tubes with a 2 mm inner diameter, to which could be connected to a micro-anemometer via flexible tubes so that a measurement of the pressure drop between two positions could be made. Figure 3.21 shows that the static pressure tapping flushes with the inner part of the duct so that it is the static pressure being measured but not the dynamic pressure.

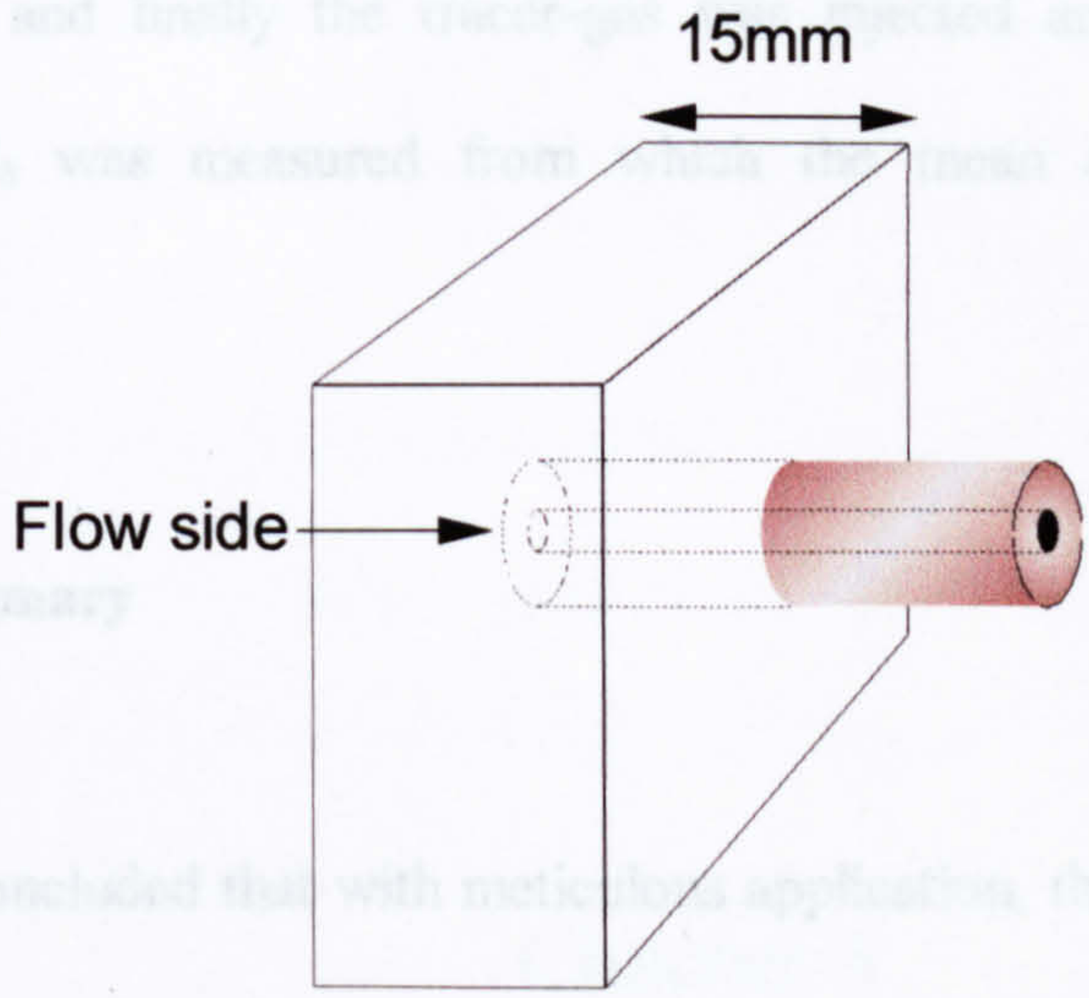


**Figure 3.21** Static pressure tapping.

### 3.4.2 Tracer-gas measurement

Accuracy of tracer-gas measurements depends greatly on how sealed the ductwork is. If the joints between duct fittings and tracer-gas pipe connections are not sealed properly then tracer-gas can leak into the test area and cause serious errors in the results. In this investigation the ductwork was sealed with sponge-foam tape whilst the brass connections for the $SF_6$ injection and sampling were sealed using standard thread sealant. In all experiments including single duct fittings and multiple interacting duct fittings, the mean airflow was first recorded using the Pitot-static tube, then the static pressure drop was measured across the

duct fitting and finally the tracer-gas was injected and the concentration of sampled $SF_6$ was measured from which the mean duct velocity could be calculated.

## 3.5 Summary

It may be concluded that with meticulous application, the tracer-gas method can be used to accurately measure the mean duct velocity. A comprehensive experimental investigation may be employed to obtain an effective comparison of velocity pressure loss and airflow measurements between conventional techniques and modern methods. It may be deduced that the application of the tracer-gas techniques becomes extremely diverse for the measurement of airflow rates from HVAC systems to experiments involving entire buildings.

Chapter 4

# Computational Fluid Dynamics Applied to HVAC Systems

# 4.0 Computational fluid dynamics applied to HVAC systems

In this work, FLUENT is used to predict k-factors of HVAC systems. FLUENT is a general purpose computer program for modelling fluid flow, heat transfer, and chemical reaction. An up-to-date modelling technique is used in FLUENT which is accessible by the user in either the text input or the graphical interface input form. When required, FLUENT can be interfaced with other CFD programs such as NECTON, FLUENT/UNS (Unstructured) and RAMPANT. Where complex geometries are to be modelled, a pre-processor can be used to create a body fitted grid to acquire the degree of accuracy needed. Pre-processors may include PREBFC and AutoCAD.

## 4.1 CFD software / hardware

The CFD software used in this investigation is FLUENT, with the addition of PRE-PREBFC as a pre-processor to create body fitted grids enabling the use of smooth and curved geometries. FLUENT can be used to create grids based on Cartesian co-ordinates, however for complex geometries require a larger number of grid cells to achieve the same degree of accuracy when using the pre-processors. Figure 4.1 shows the accuracy of a curve represented by FLUENT and the pre-processor PREBFC.

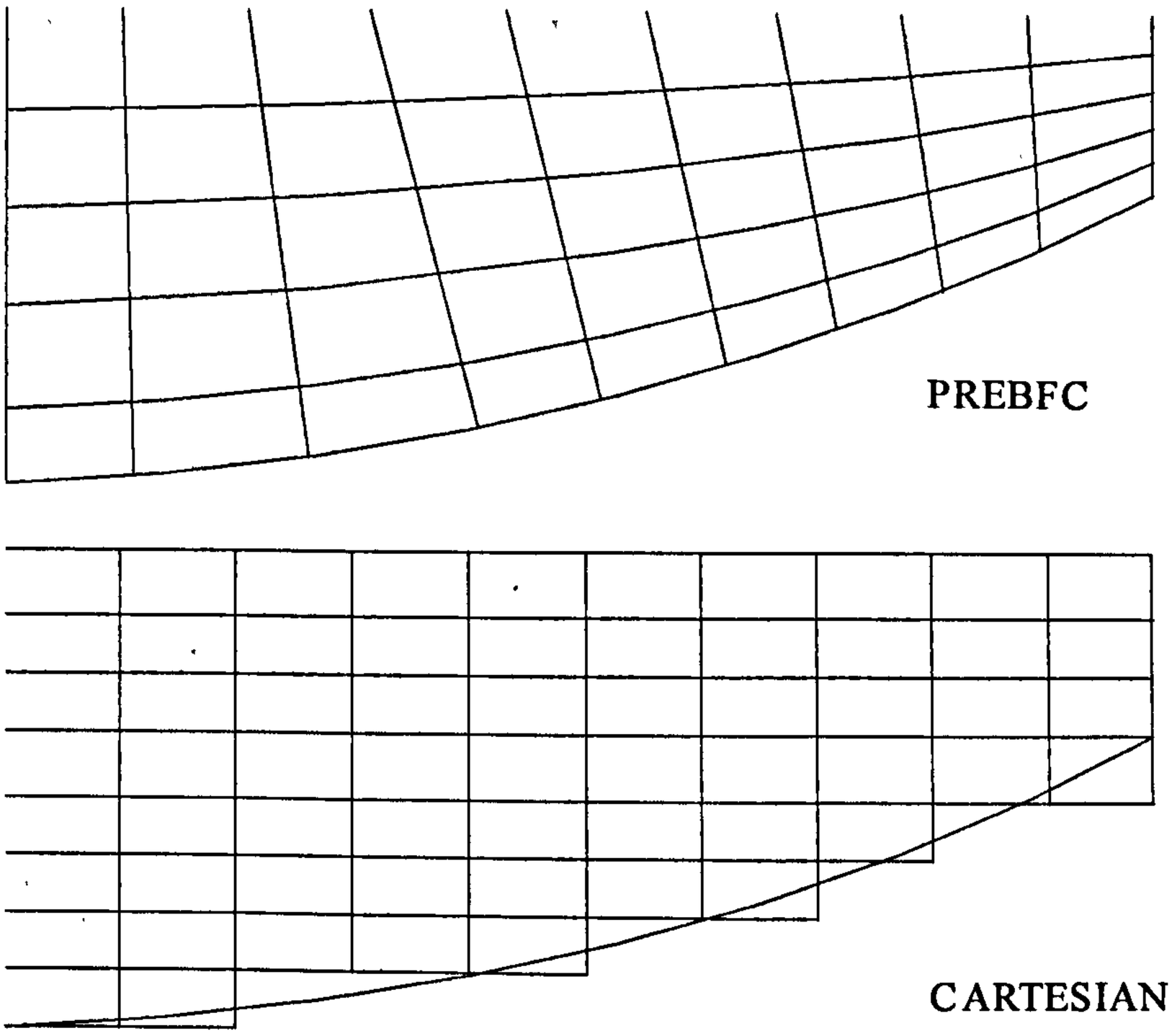


**Figure 4.1** Grid accuracy comparison between FLUENT and PREBFC.

Other software used in this investigation is the FLUENT/UNS unstructured version as is described in section 4.3.2.2 . Throughout this investigation several versions of FLUENT have been upgraded as newer versions were available. FLUENT versions 4.2; 4.25; 4.3; 4.4 and FLUENT/UNS version 4.3 have been used.

All the CFD software is run using a Silicon Graphics Indy (8-bit) MIPS R4600 Workstation. The computer memory required to run vast modelling batch-jobs is

a 64 Mbytes RAM memory with a 134 MHertz A2 Audio Processor. The large amount of data files accumulated during extensive CFD investigations are stored on two computer hard disks summing up to 2.5 Gbytes of disk space.

## 4.2 Practical application

The ability to predict fluid flow, heat transfer and chemical reaction allow a wide variety of practical applications using CFD simulation. A few examples of CFD application are described below.

- aerodynamic design modelling the shock waves on the cross-section of an airfoil.
- combustion design and engineering, including gaseous combustion, liquid fuel combustion, and coal combustion.
- architectural design, modelling the external and internal air flow rates for ventilation and HVAC system design.
- materials processing, with crystal growth including a mushy zone intermediate state.
- dispersed second phase of particles, bubbles or droplets for Lagrangian trajectory calculations, effects of heating and cooling, and for changing of a single state medium.

## 4.3 CFD simulation procedure

Before any CFD model can be considered, an extensive preliminary investigation has to be undertaken to ascertain the viability of using CFD. When planning a CFD model the following has to be taken into account :

- **Definition of modelling goals :** What specific results are required from the CFD model and how will they be used ? What degree of accuracy is required from the model ?
- **Determination of computational model :** Can the model be an isolation of a small portion of the physical system? What are the bounds of the model and the boundary conditions involved? Will a 2D or a 3D model be required and what grid topology is needed?
- **Application of physical models :** Is the flow inviscid, laminar or turbulent? Is heat transfer important? Is the flow steady or unsteady? Are there any other governing physical processes involved such the compressible effect ?.
- **Solution procedure :** This issue is one that is best decided during the actual solution iterative process because the best way of determining the solution convergence is to observe the solution. Considerations must be given to the solution convergence rate, solution stability and the CPU run time.

The basic modelling approach is outlined in Figure 4.2.

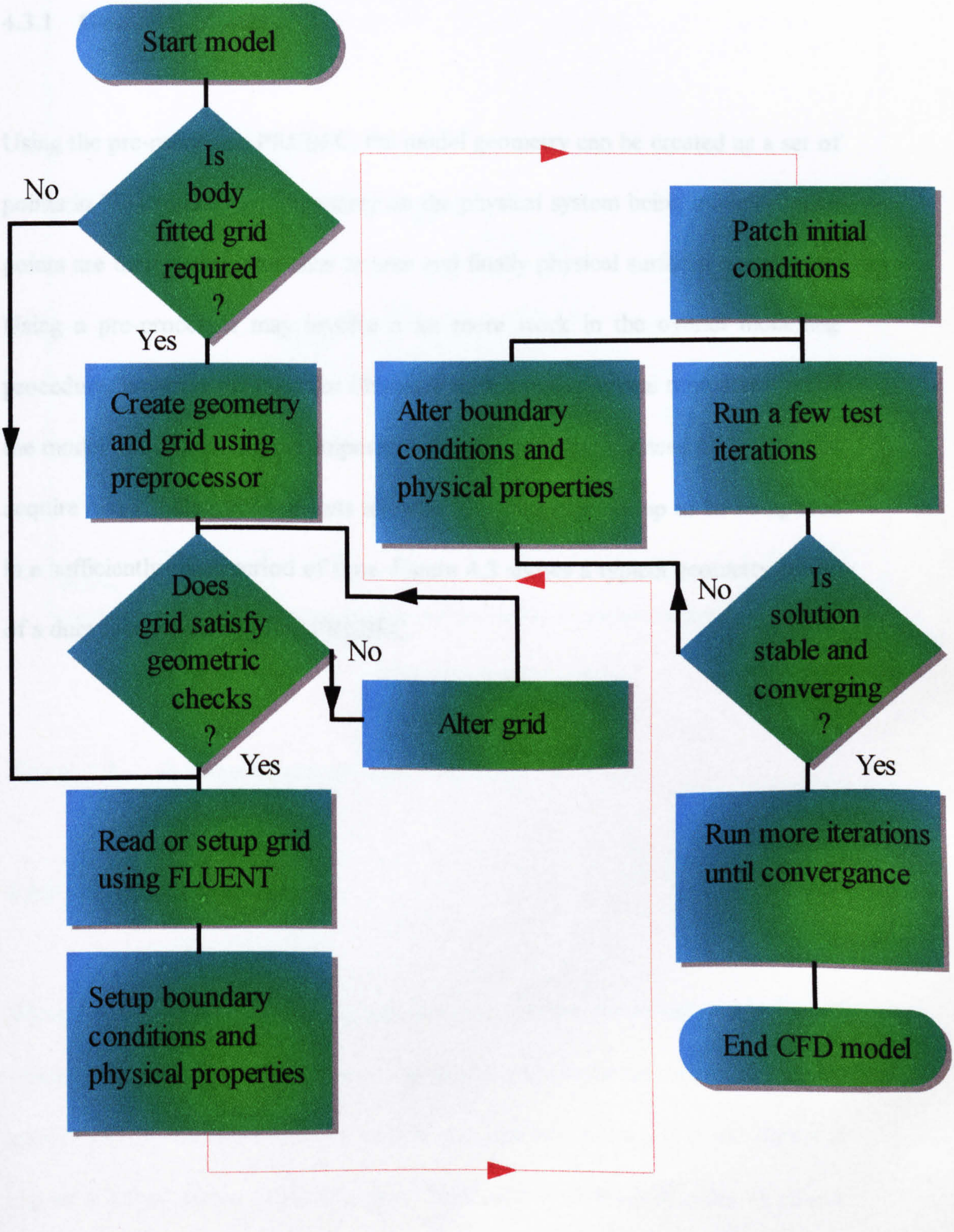


**Figure 4.2** CFD modelling approach.

### 4.3.1 Geometry set-up

Using the pre-processor PREBFC, the model geometry can be created as a set of points in 3D or 2D space depending on the physical system being modelled. The points are then joined with lines or arcs and finally physical surfaces are created. Using a pre-processor may involve a lot more work in the overall modelling procedure, however the need for obtaining an accurate physical representation of the model in question is more important. However the experienced CFD user will acquire many skills and short-cuts allowing the geometry set-up to be completed in a sufficiently short period of time. Figure 4.3 shows a typical geometry set-up of a duct fitting created using PREBFC.

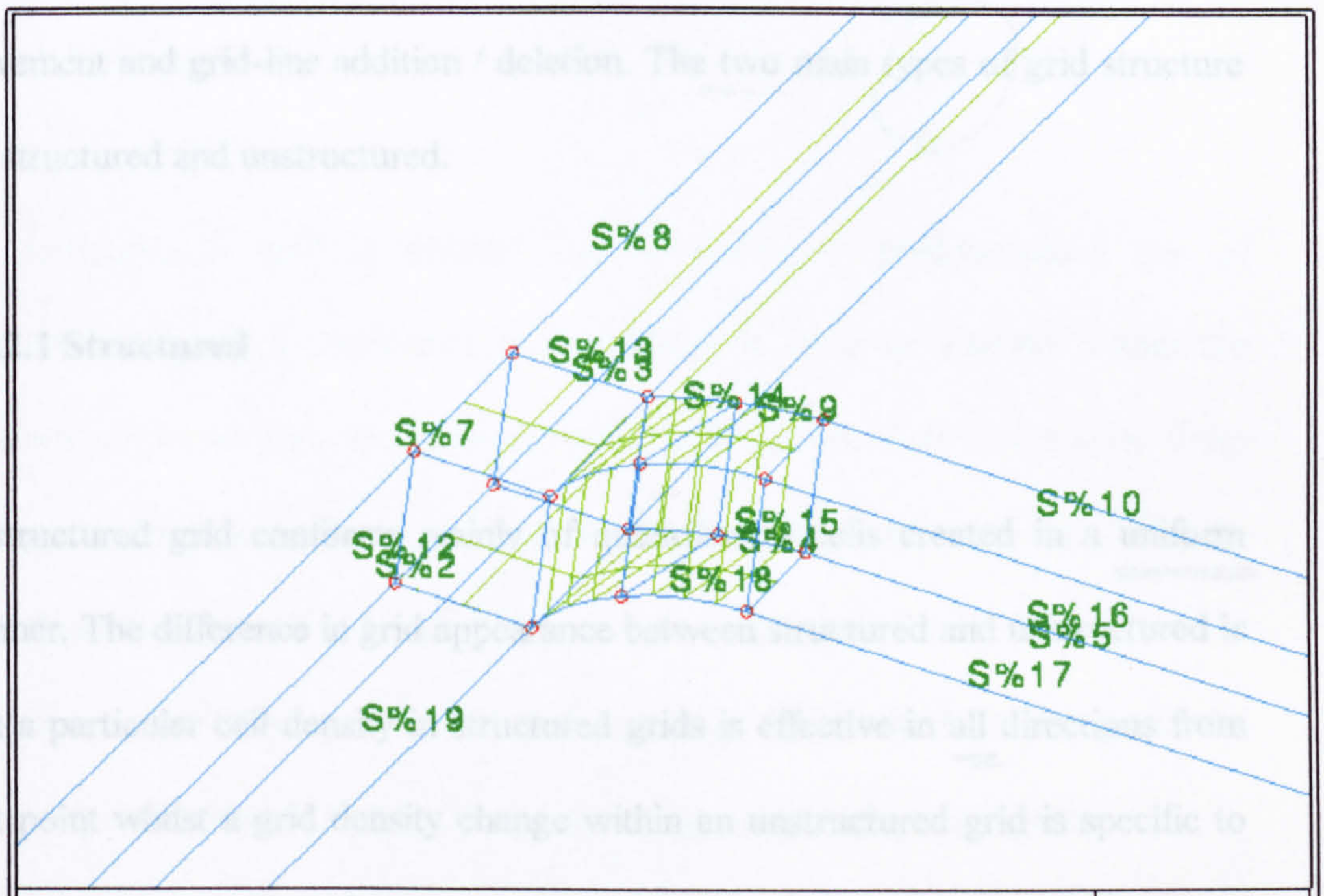


**Figure 4.3** A geometry set-up using PREBFC.

### 4.3.2 Grid topology

When the Cartesian or body-fitted grid has been created, the model grid is formed which is broken down into many individual computational cells. Many grid alterations may be made before a satisfactory grid is obtained. It is mentioned in Figure 4.2 that several automatic grid checks are performed in order to reduce computation instability. The range of grid alterations may include grid-line

movement and grid-line addition / deletion. The two main types of grid structure are structured and unstructured.

### 4.3.2.1 Structured

A structured grid conforms mainly of quadrilateral cells created in a uniform manner. The difference in grid appearance between structured and unstructured is that a particular cell density in structured grids is effective in all directions from that point whilst a grid density change within an unstructured grid is specific to that point. An example of a structured grid is shown in Figure 4.4 .

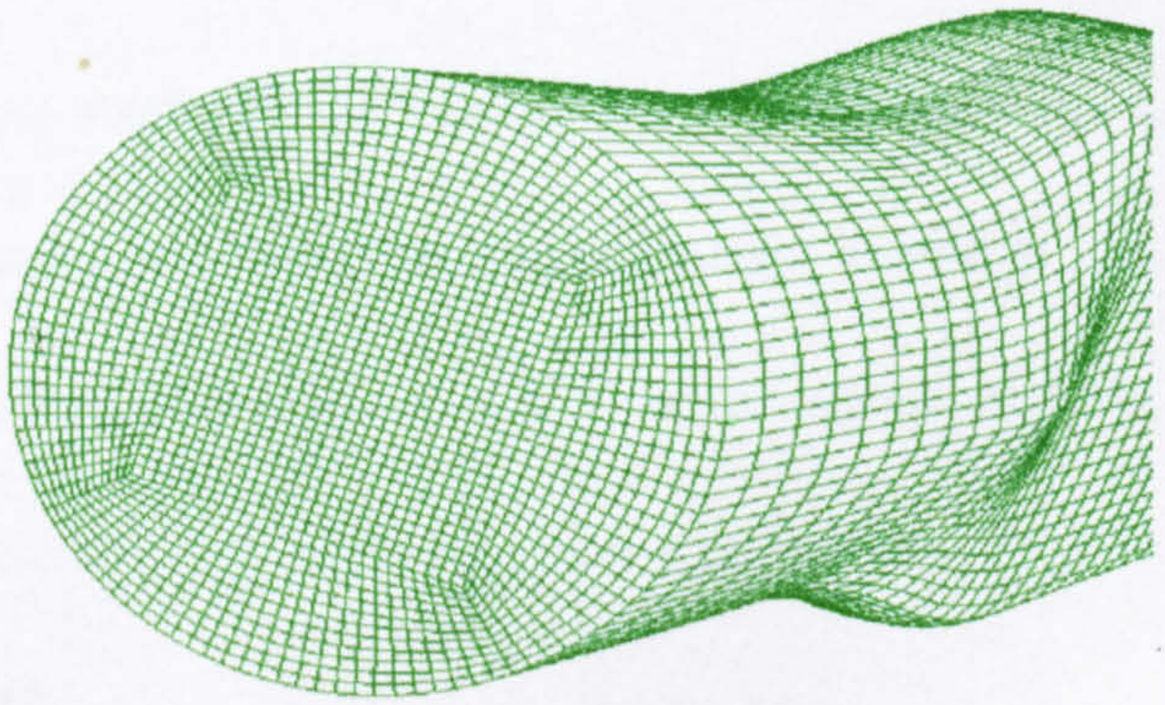

**Figure 4.4** Duct transition using structured grid format.

### 4.3.2.2 Unstructured

An unstructured grid is created by connecting a predetermined set of computational nodes distributed in a uniform or irregular manner within the geometry. Internal data structures are used to assign an order to the cells, faces and grid points in a mesh and to maintain contact between adjacent cells. They do not, therefore, require i,j,k indexing to locate neighbouring cells. This gives the user more flexibility to use the grid topology best suited to the particular geometry that poses as a restriction when using structured grids. Typical cell types are shown in Figure 4.5 .

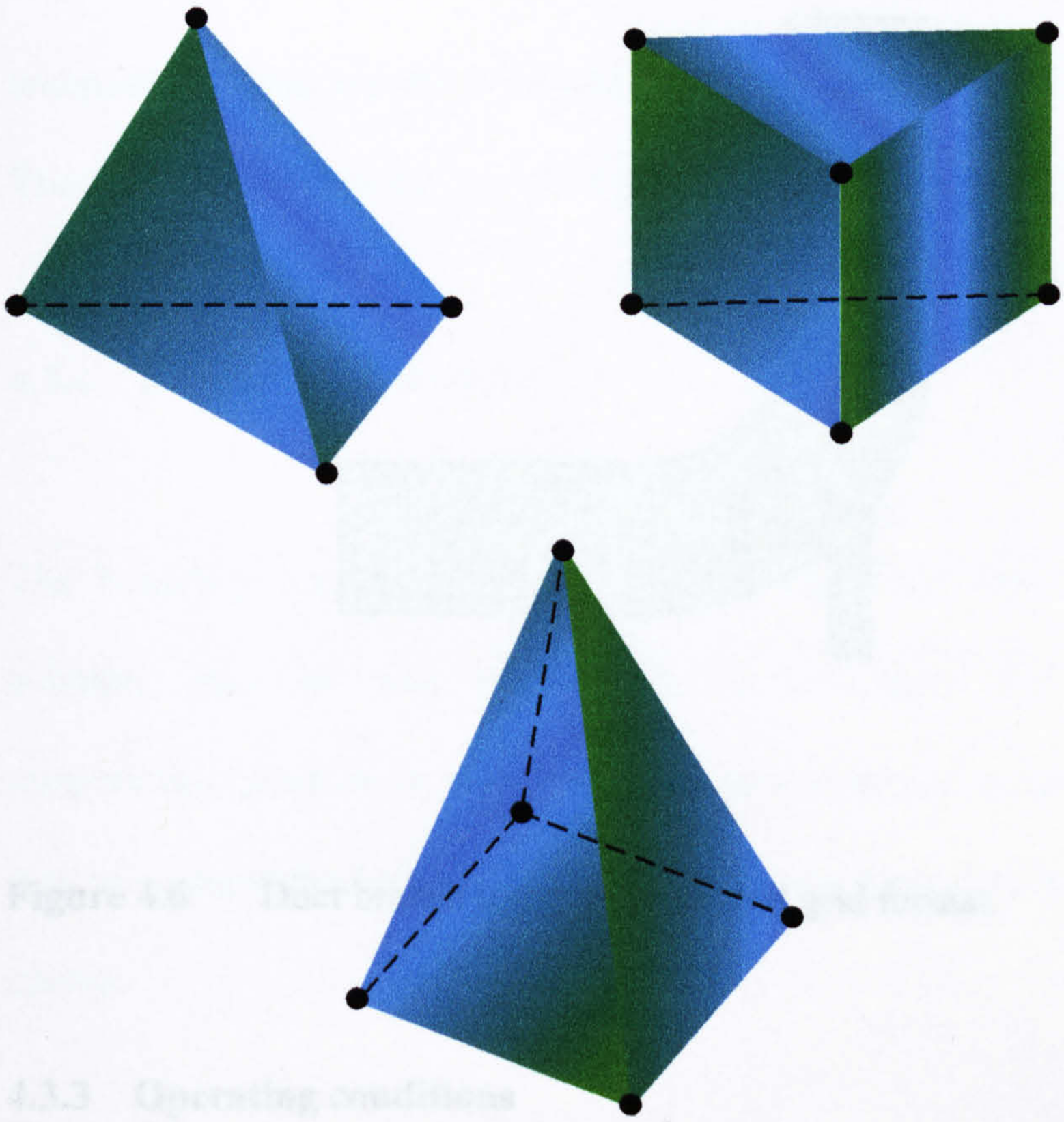

**Figure 4.5** Unstructured cell types.

Figure 4.6 shows examples of unstructured grids. In some cases the modelling geometry may require a structured grid to best represent its surfaces whilst the modelling boundary may require a large open space with an unstructured grid. Hybrid grid structures are used for such applications, for example a triangular / quadrilateral grid.

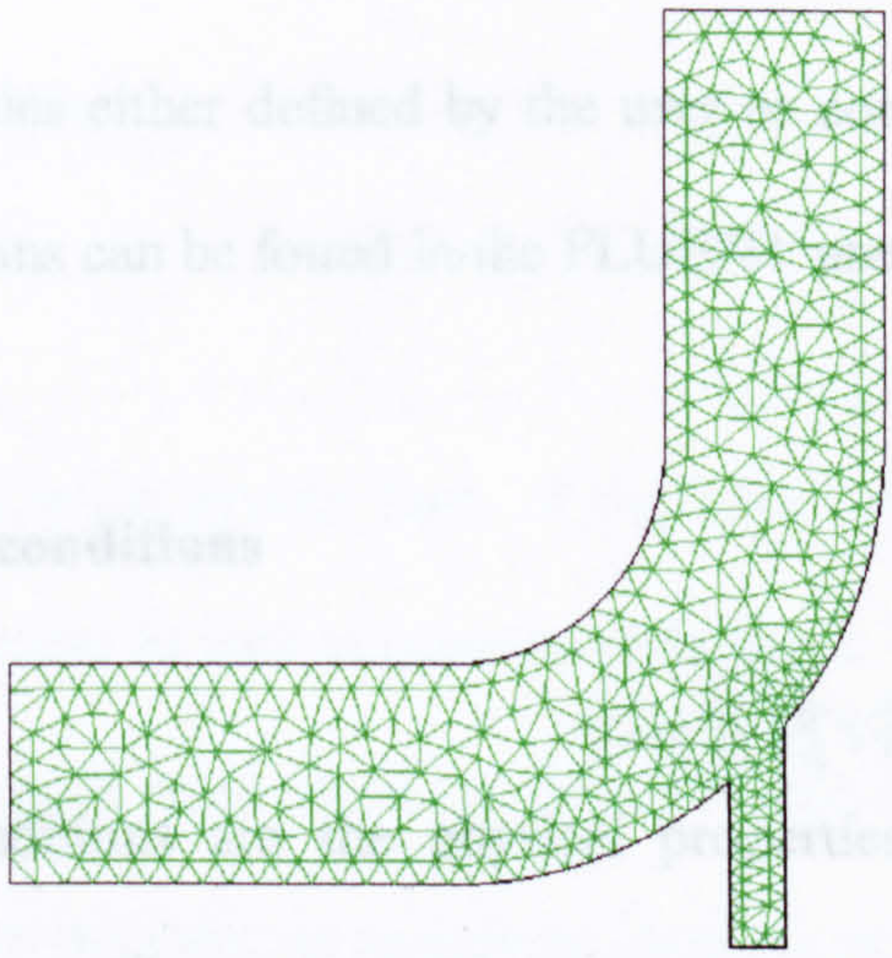

**Figure 4.6** Duct branch using unstructured grid format.

### 4.3.3 Operating conditions

The operating conditions of any CFD model invlove the use of model equations, physical constants and the fluid properties, which all have to be defined by the user. However FLUENT/UNS includes a large database of fluid properties which have predetermined physical values for variables such as density, viscosity and thermal conductivity.

Properties may be temperature and/or composition dependent, with temperature dependence based on a polynomial or piecewise-linear function and individual

component properties either defined by the user or computed via kinetic theory. The general equations can be found in the FLUENT user guide manual (28).

### 4.3.4 Boundary conditions

The boundary conditions are the physical properties that govern the model solution, such as wall temperature or movement and fluid inlet/outlet temperature, pressure or velocity. These properties are entered by the user and may be changed throughout the solution if for any reason the boundary conditions change.

### 4.3.5 Solution procedure and governing equations

There are several turbulent theories and therefore governing equations within FLUENT that can be used where each of them are more suitable to certain applications than others. The governing equations of fluid flow adapted for FLUENT which were used in this investigation are given as basic conservation equations of mass and momentum :

$$\frac{\partial \rho}{\partial t} + \frac{\partial}{\partial x_i}(\rho u_i) = S_m \tag{4.1}$$

Where equation 4.1 is the general form of the mass conservation equation and is valid for incompressible as well as compressible flows. The source $S_m$ is the mass added to the continuous phase from the dispersed second phase. Conservation of mementum in the ith direction in an inertial (non-accelerating) reference frame, is given as :

$$\frac{\partial}{\partial t}(\rho u_i) + \frac{\partial}{\partial x_j}(\rho u_i u_j) = -\frac{\partial p}{\partial x_i} + \frac{\partial \tau_{ij}}{\partial x_j} + \rho g_i + F_i \tag{4.2}$$

where p is the static pressure, $\tau_{ij}$ is the stress tensor and $g_i$ and $F_i$ are the gravitational acceleration and external body forces in the i direction, respectively.

The stress term τij is given by :

$$\tau_{ij} = \left[\mu\left(\frac{\partial u_i}{\partial x_j} + \frac{\partial u_j}{\partial x_i}\right)\right] - \frac{2}{3}\mu\frac{\partial u_i}{\partial u_j}\delta_{ij} \tag{4.3}$$

### 4.3.5.1 Solution models

In the standard k-ε model, Reynolds stressses are modelled using the Boussinesq hypothesis (29) :

$$\overline{\rho u_i' u_j'} = \rho \frac{2}{3} k \delta_{ij} - \mu_t \left( \frac{\partial u_i}{\partial x_j} + \frac{\partial u_j}{\partial x_i} \right) + \frac{2}{3} \mu_t \frac{\partial u_i}{\partial x_i} \delta_{ij} \qquad (4.4)$$

The turbulent viscosity, $\mu_t$ , is computed from a velocity scale ($k^{1/2}$) and a length scale ($k^{3/2}$)/ε which are predicted at each point in the flow via solution of transport equations for k and ε :

$$\frac{\partial}{\partial}(\rho k) + \frac{\partial}{\partial x_i}(\rho u_i k) = \frac{\partial}{\partial x_i} \frac{\mu_t}{\sigma_k} \frac{\partial k}{\partial x_i} + G_k + G_b - \rho \varepsilon \qquad (4.5)$$

and

$$\frac{\partial}{\partial}(\rho \varepsilon) + \frac{\partial}{\partial x_i}(\rho u_i \varepsilon) = \frac{\partial}{\partial x_i} \frac{\mu_t}{\sigma_\varepsilon} \frac{\partial \varepsilon}{\partial x_i} + C_{1\varepsilon} \frac{\varepsilon}{k} \left( G_k + (1 - C_{3\varepsilon}) G_b \right) - C_{2\varepsilon} \rho \frac{\varepsilon^2}{k}$$

..... (4.6)

where $G_k$ is the generation of k and is given by :

$$G_k = \mu_t \left( \frac{\partial u_j}{\partial x_i} + \frac{\partial u_i}{\partial x_j} \right) \frac{\partial u_j}{\partial x_i} \tag{4.7}$$

and $G_b$ is the generation due to buoyancy :

$$G_b = -g_i \frac{\mu_t}{\rho \sigma_h} \frac{\partial \rho}{\partial x_i} \tag{4.8}$$

where $\sigma_h$ is the turbulent Prandtl number, $\frac{\mu_t C_p}{k_t}$ .

The turbulent viscosity is then related to k and ε by the expression:

$$\mu_t = \rho C_\mu \frac{k^2}{\varepsilon} \tag{4.9}$$

The coefficients $C_{1\varepsilon}$ , $C_{2\varepsilon}$ , $C_\mu$ , $\sigma_k$ and $\sigma_\varepsilon$ are empirical constants which have the following empirically derived values :

$C_{1\varepsilon} = 1.44$, $C_{2\varepsilon} = 1.92$, $C_\mu = 0.09$, $\sigma_k = 1.0$, $\sigma_\varepsilon = 1.3$ .

For CFD models where the prediction of heat transfer is required, FLUENT solves the energy equation in the form of a transport equation for the static enthalpy, h :

$$\frac{\partial}{\partial t}(\rho h)+\frac{\partial}{\partial x_i}(\rho u_i h)=\frac{\partial}{\partial x_i}(k_m+k_e)\frac{\partial T}{\partial x_i}-\frac{\partial}{\partial x_i}\sum h_j J_j+\frac{Dp}{Dt}+\tau_{ik}\frac{\partial u_i}{\partial x_k}+S_h \quad (4.10)$$

Where $k_m$ is the molecular conductivity, $k_e$ is the effective conductivity due to turbulent transport ($k_e=\mu_t/P\tau_t$), $J_j$ is the diffusion flux of species j, and the source term $S_h$ includes heat of chemical reaction, any interphase exchange of heat, and any other volumetric heat sources defined by the user. The enthalpy is defined as :

$$h=\sum_j m_j h_j \quad (4.11)$$

Where $m_j$ is the mass fraction of species j and :

$$h_j=\int_{T_{ref}}^{T} c_{pj}\,dT \quad (4.12)$$

### 4.3.5.2 Discretisation schemes

To obtain a higher degree of accuracy in the CFD prediction FLUENT uses a control volume based technique to convert the differential conservation equations to algebraic equations which can be solved numerically. The purpose of a discretisation scheme is to interpolate face values from cell centres which can be done using the power-law scheme (30) , the second-order upwind scheme (31) or the QUICK scheme (32).

The power-law scheme interpolates face values using the exact solution to a one-dimensional convection-diffusion equation :

$$\frac{\partial}{\partial x}(\rho u \phi) = \frac{\partial}{\partial x}\Gamma\frac{\partial \phi}{\partial x} \qquad (4.13)$$

where the diffusion coefficient, $\Gamma$, and the term, $\rho u$, are constant across the interval $\Delta x$.

The second-order upwind scheme computes face values using a Taylor series expansion about the cell centroid :

$$\phi_e = \phi_p + \nabla\phi_p . \Delta s \tag{4.14}$$

where $\phi_p$ and $\nabla\phi_p$ are the values at the node P, and its gradient, and Δs is the displacement vector from the cell centroid to the face centroid. This formulation requires the determination of the gradient $\nabla\phi$ in each cell.

When the flow is at an angle to the grid and a higher numerical accuracy is required, the QUICK scheme can be used. This scheme provides a blending, based on local flow conditions, of second-order upwind and central differencing to calculate face values. The interpolation can involve values from two cells upstream of the face and the cell downstream. The QUICK scheme involves a quadratic interpolation in which the face value is based on the adjacent nodal values and on an additional neighbour node.

### 4.3.5.3 Underelaxation and multigrid

With increased CPU run time and solution instability ( consequences of using higher order schemes ), and due to the non-linear nature of the flow equations, the common options FLUENT provides to help increase solution convergence rate are underelaxation and multigrid.

Due to the nonlinearality of the equation set being solved by FLUENT, the substitution of the "improved" values in each iteration for each variable can cause solution divergence. This can be counteracted by underelaxation which reduces the change in the value of each variable produced during each iteration. In a simple form, the new value of each variable $\phi_p$ at node P depends upon the old value, $\phi_{p,old}$ , the computed change in $\phi_p$ , $\Delta\phi_p$ , and the underelaxation factor, $\alpha$ , as follows :

$$\phi_p = \phi_{p,old} + \alpha\Delta\phi_p \tag{4.15}$$

FLUENT uses a multigrid scheme to accelerate the convergence of the standard line solver, using additive correction to compute corrections on a series of coarser grid levels. The use of this multigrid scheme can greatly reduce the number of iterations and the CPU time required to obtain a converged solution, particularly when the FLUENT model contains a large number of control volumes and/or control volumes which are of large aspect ratio.

### 4.3.5.4 Solution convergence and divergence

The definition of convergence as given by FLUENT is when all governing equations are balanced at each point in the solution domain and that generally all residual values are in the order of $1x10^{-3}$ for each cell with the exception of the enthalpy residual with heat transfer models which needs to be of the order of $1x10^{-6}$ .

However, if a particular solution is being monitored using the residual history plot, then convergence can be observed when the solution does not change over a particular number of iterations. An option within FLUENT allows the user to observe graphically the model solution and the residual amounts. Figure 4.7 shows a history log plot of the normalised residual values for a particular model solution. Normalisation of the residual sum is accomplished by dividing by the maximum redisdual value after a predetermined amount of iterations which is set within the CFD code. It can be seen in Figure 4.7 that after 100 iterations, although the graphical representation is typical of that of a converging solution, the solution for dissipation rate, turbulent energy and the u, v-velocity components fail to meet the stated convergance critrerion of $1x10^{-3}$ . This is proceeded by increasing the underelaxation factors for these variables and then running more iterations.

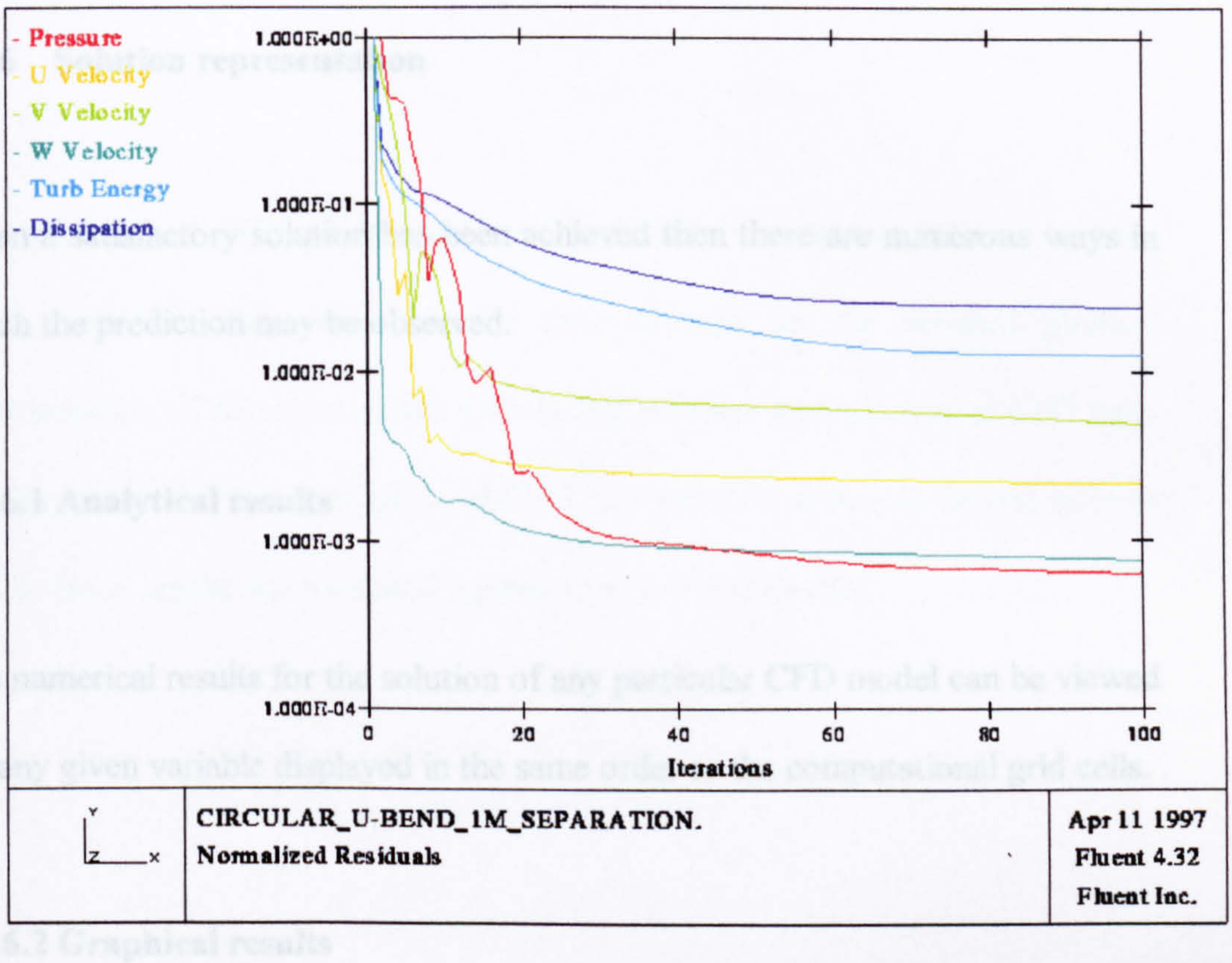


**Figure 4.7** Residual history plot.

FLUENT automatically reports any divergence in the solution over a certain amount predetermined within the FLUENT code. Solution divergence can be caused by incorrect user input or poor grid structure such as grid skewness and large cell aspect ratio.

### 4.3.6 Solution representation

When a satisfactory solution has been achieved then there are numerous ways in which the prediction may be observed.

#### 4.3.6.1 Analytical results

The numerical results for the solution of any particular CFD model can be viewed for any given variable displayed in the same order as the computational grid cells.

#### 4.3.6.2 Graphical results

The most suitable method of analysing a CFD solution using FLUENT is in graphical format. This option ranges from simple graphical plots of any variable in any direction through the model, to more complex graphical representations such as contour slices, velocity vectors and streamline functions. Contour slices can provide a picture of variable ranges within several slices of the model and streakline functions provide an animated view of the general outline of the fluid flow within the model.

## 4.4 Summary

The accuracy of CFD prediction depends on the boundary conditions and the closure of fluid flow equations. It also depends on the detailed physical representation of actual modelled system that requires an experienced CFD user. It is important that the application of CFD prediction of airflow in ducted systems is fully investigated and validated against experimental results.

Chapter 5

# Experimental and CFD Results On Pressure Loss in HVAC Systems

# 5.0 Experimental and CFD results on pressure loss in HVAC systems

This chapter compares the data obtained experimentally with predictions from CFD analysis. Furthermore, k-factors are compared with data available to HVAC system designers, such as ASHRAE and CIBSE handbooks. The validity of using CFD to predict k-factors is shown by direct comparison with experimental results so that further CFD analysis can be made.

## 5.1 Flow development

Figure 5.1 shows the various stages of flow development in a straight pipe. If the flow at the contraction inlet is laminar then it quickly becomes turbulent in region 1, assuming that the Reynolds number is increased above the value of 2000. The boundary layer (i.e. the volume of near zero velocity fluid caused by viscous forces with the fluid being in contact with the wall), is allowed to develop in region 2. In region 3 for ducts with constant cross-section, the average flow velocity over the pipe cross-section becomes constant with a fully developed flow profile.

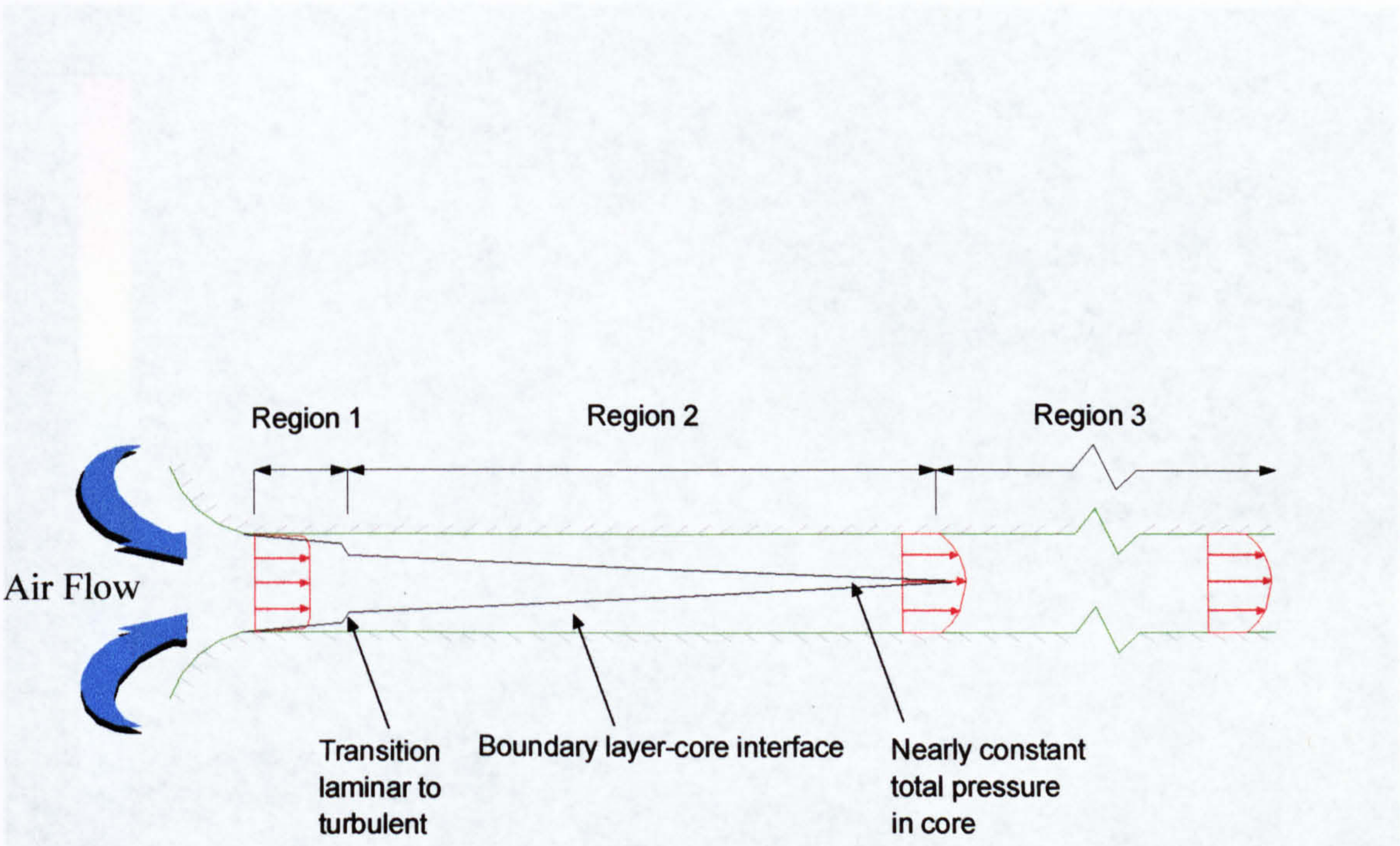


**Figure 5.1** Boundary layer development after a smooth contraction.

Figure 5.2 shows a CFD prediction of a fully developed air-flow profile showing the requirement for a high density of grid cells close to the duct wall. This profile takes in the order of 20-30 duct diameters to develop.

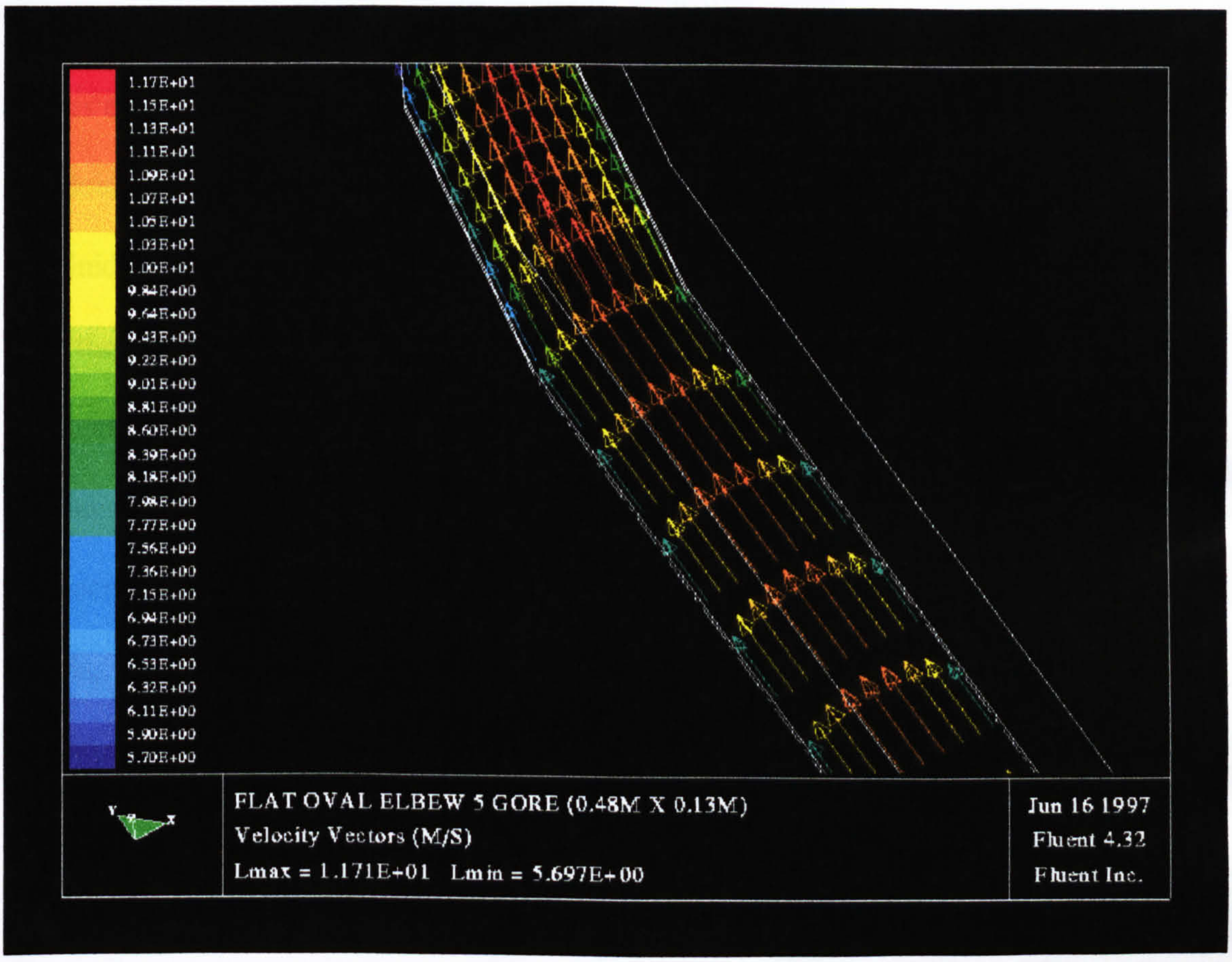


**Figure 5.2** CFD prediction of a fully developed velocity vector profile.

## 5.2 Turning flow

When the flow is turned, static pressure and velocity distributions change, two adverse gradients are created, secondary flows are generated and curvature affects the turbulence structure of the flow. Non-uniform energy distributions are involved in flows through bends because of the velocity profile ranging from zero

at the wall to a maximum at the centre. This change in direction of the fluid causes energy losses. An ideal flow situation can be seen in Figure 5.3. Whenever the fluid flows in a curved path there must be a force acting radially inwards on the fluid to provide the inward acceleration. There is thus an increase of pressure near the outer wall of the bend , starting at point A and rising to a maximum at point B. There is also a reduction of pressure near the inner wall giving a minimum pressure at C and a subsequent rise from C to D. Between A and B and between C and D the fluid therefore experiences an adverse pressure gradient, that is, the pressure increases in the direction of the flow. Unless the radius of curvature is very large, separation occurs on the inside wall just after the bend leading to energy losses in turbulence. The magnitude of these losses depends mainly on the radius of curvature of the bend.

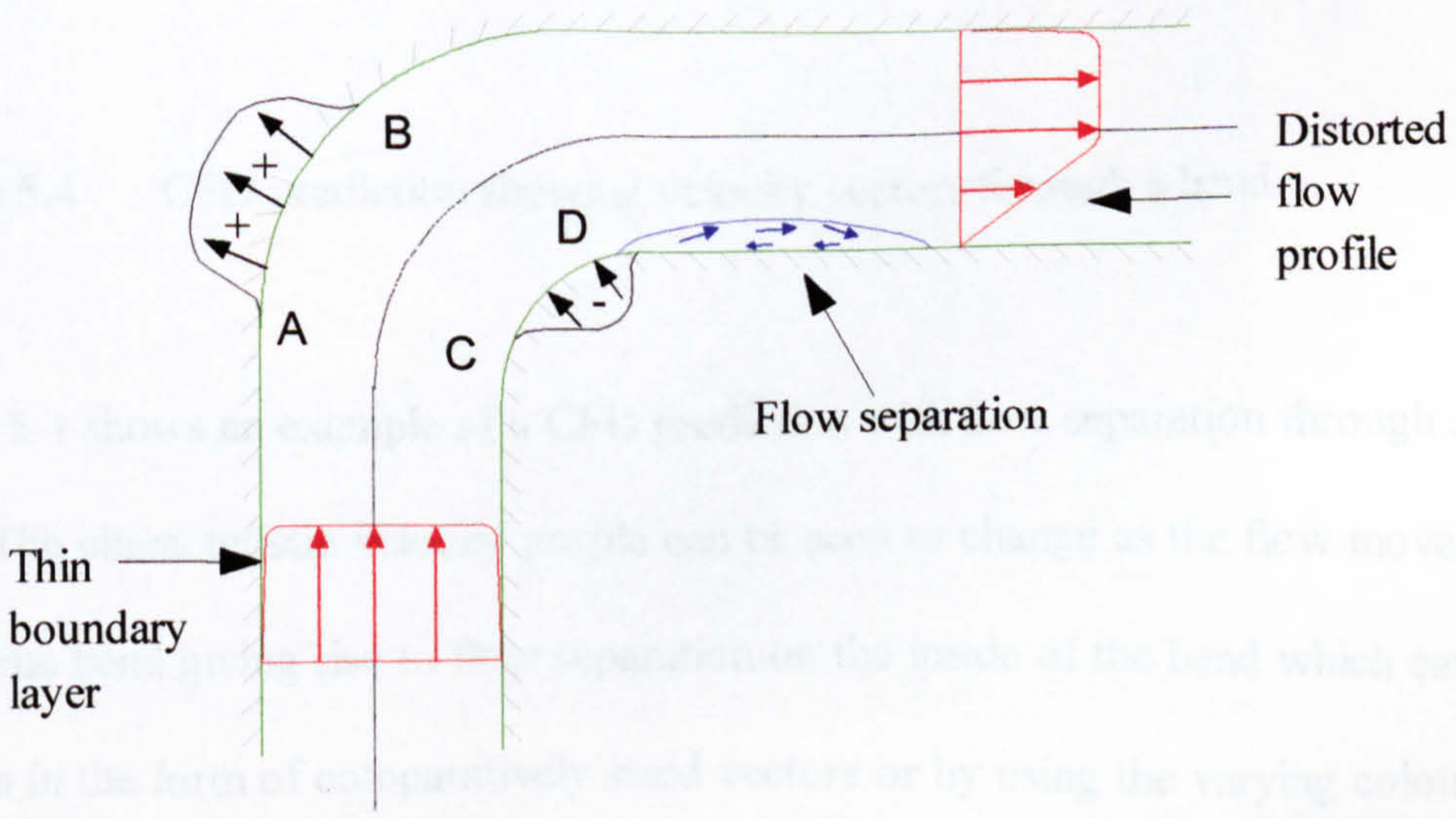


**Figure 5.3** Ideal flow through a bend.

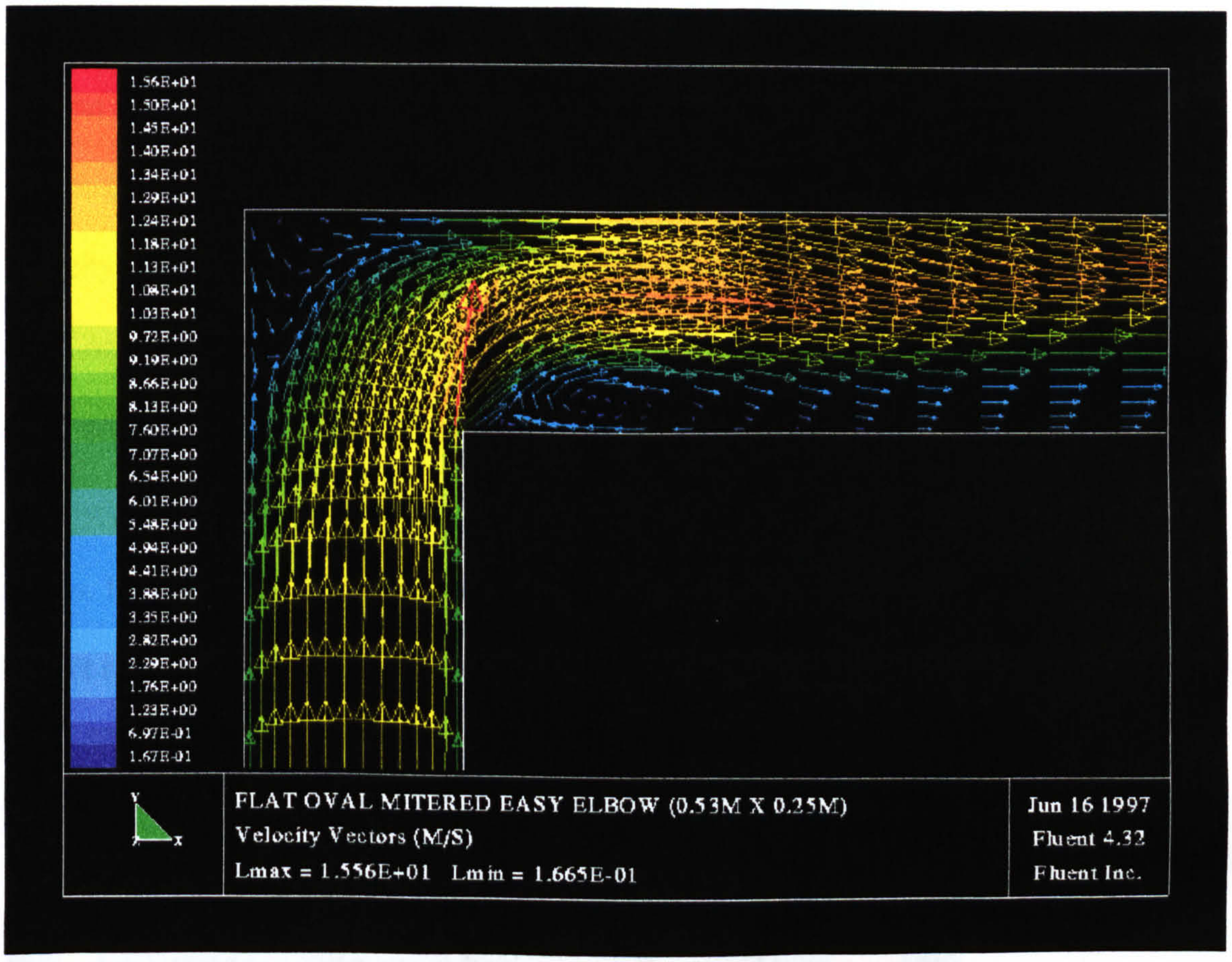


**Figure 5.4** CFD prediction showing velocity vectors through a bend.

Figure 5.4 shows an example of a CFD prediction with flow separation through a bend. The characteristic velocity profile can be seen to change as the flow moves round the bend giving rise to flow separation on the inside of the bend which can be seen in the form of comparatively sized vectors or by using the varying colour scale.

Figure 5.5 shows a comparison of velocity contours between a circular cross section and two different aspect ratios of rectangular cross section bends. Although the rectangular bend of aspect ratio 0.5 has a larger total area of low velocity flow, the amount of low energy fluid on the inner wall is less than in the bend of aspect ratio 2. Separation is therefore more likely in the outlet from the bend of aspect ratio 2. Bends with low aspect ratios have greater frictional losses due to more surface area, than circular cross section and higher aspect ratio bends. However the flow redevelopment losses are much smaller in bends of low aspect ratio hence the overall difference between them is relatively small.

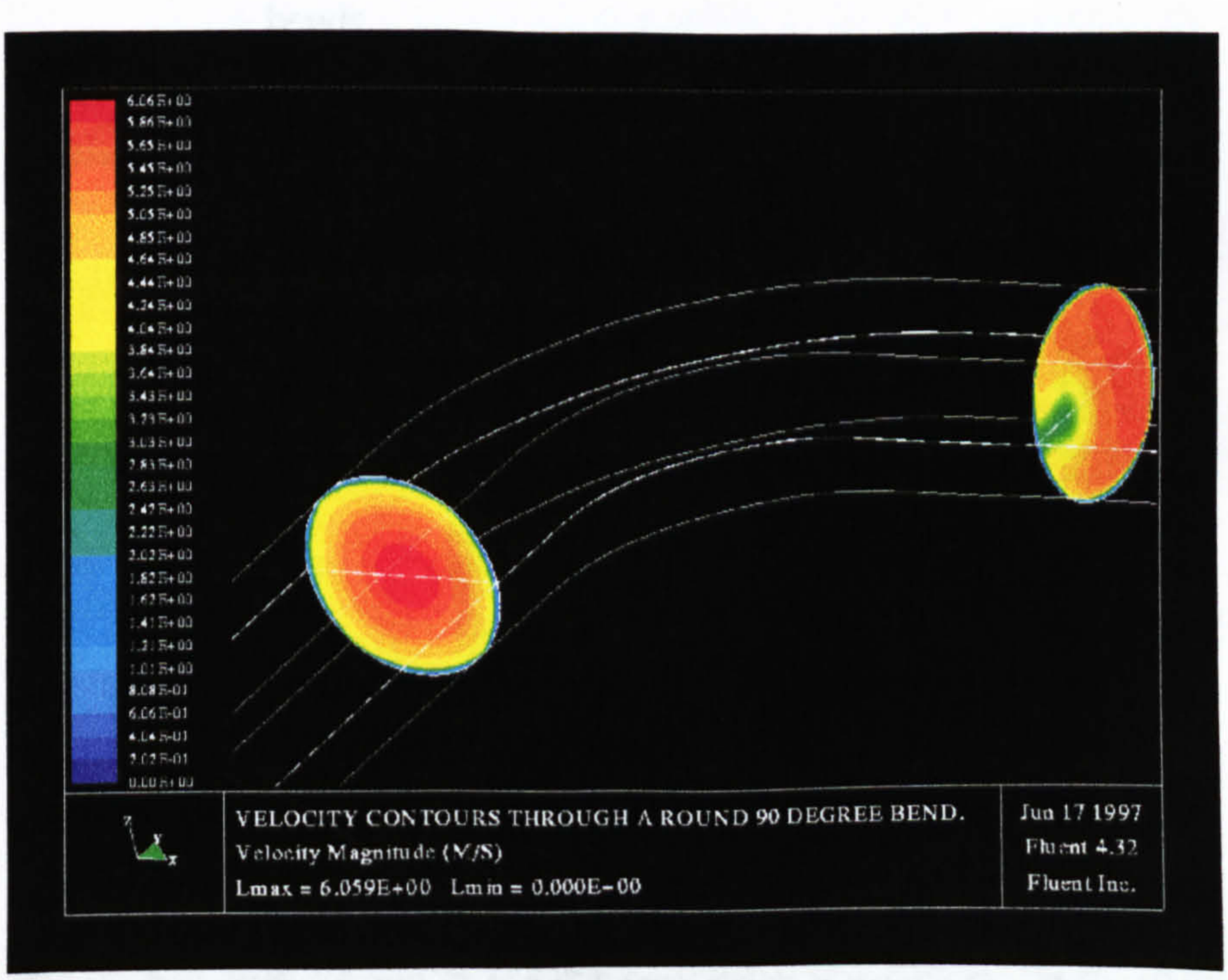


**Figure 5.5a** CFD comparison of velocity contours for different cross section bends.

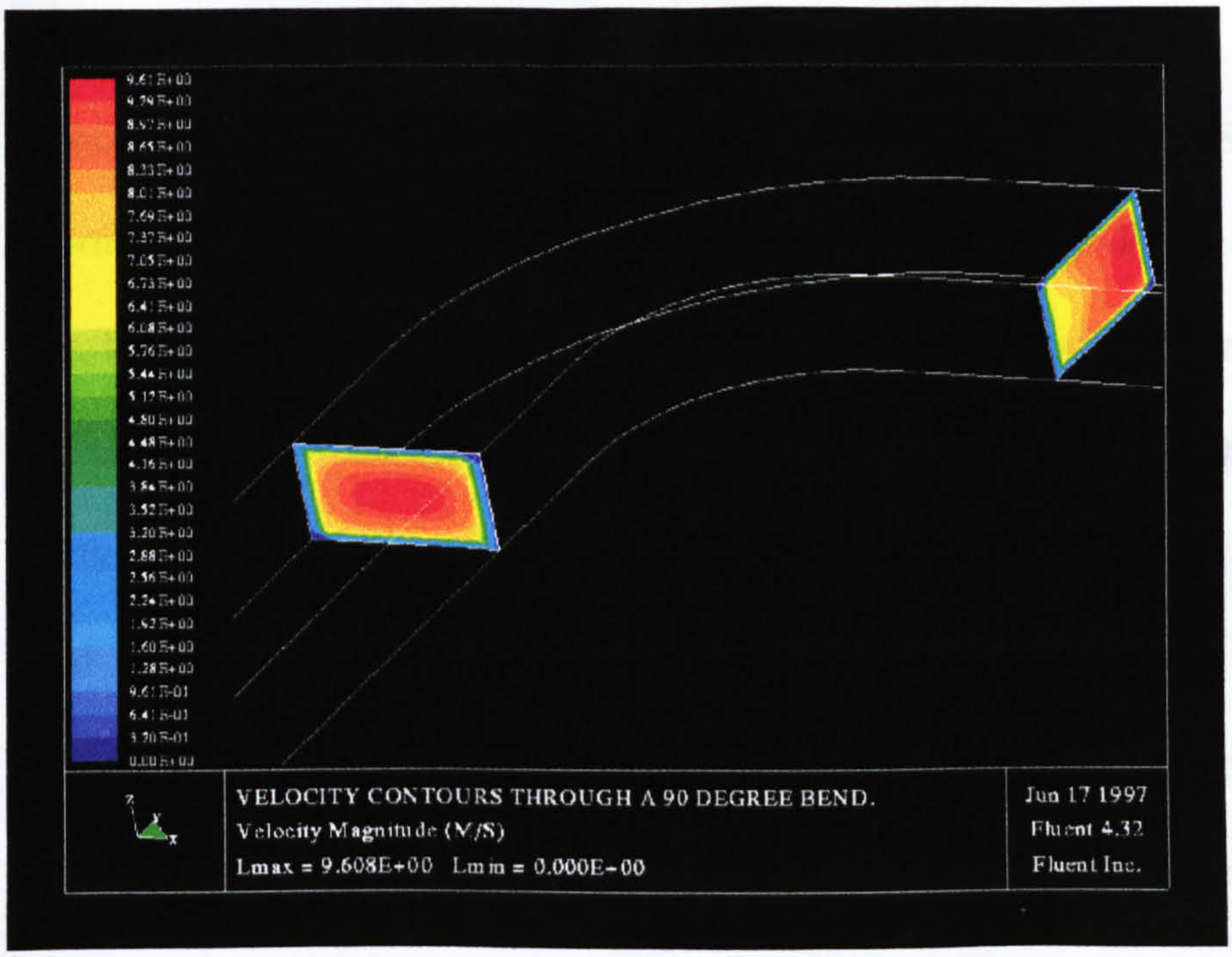


**Figure 5.5b** CFD comparison of velocity contours for different cross section bends.

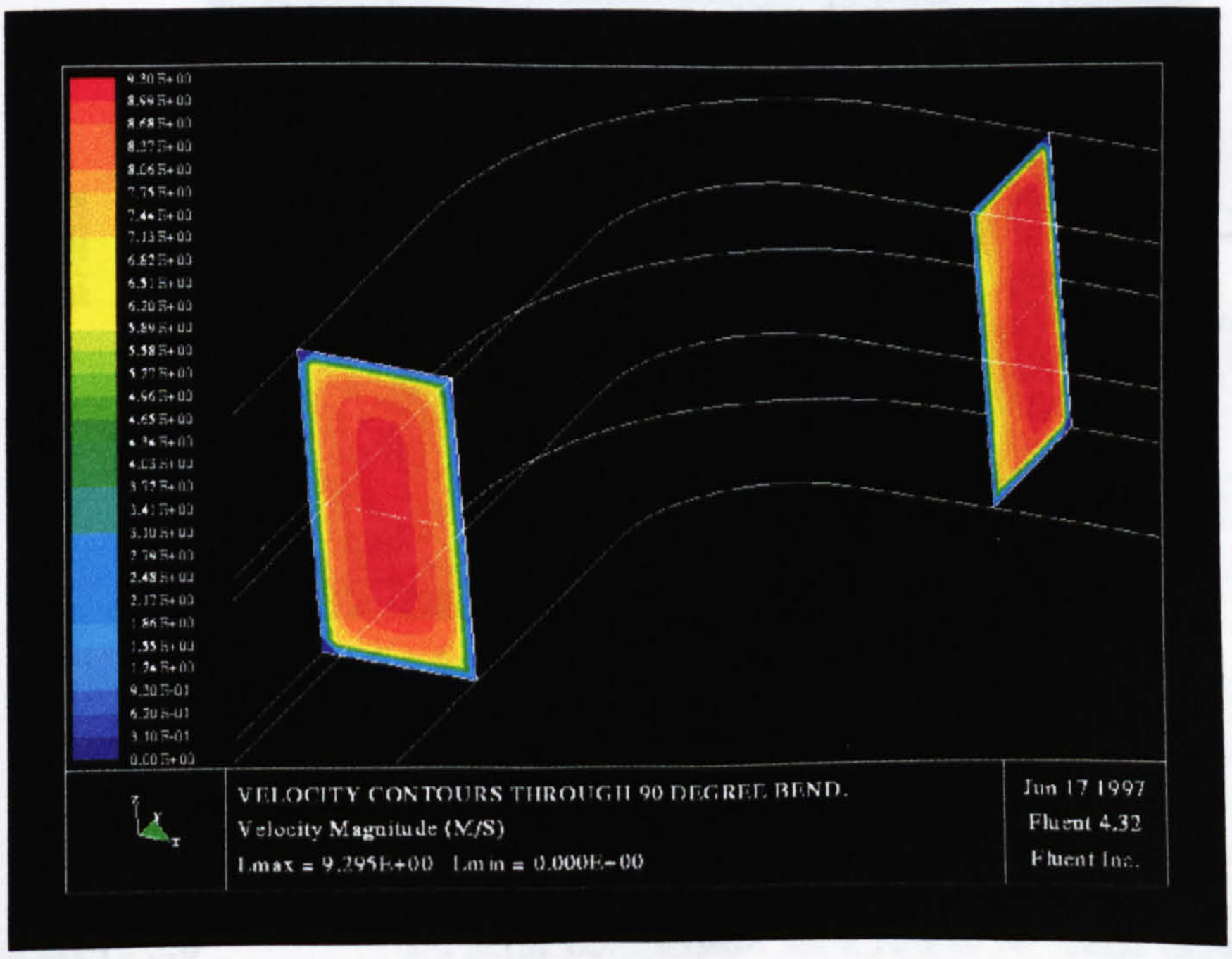


**Figure 5.5c** CFD comparison of velocity contours for different cross section bends.

Velocity pressure loss factors as given in ASHRAE and CIBSE provide information based on the variation of a few parameters only. Figure 5.6 shows that for a round 90° smooth bend with constant radius/diameter ratio and constant mean velocity, the k-factor reduces slightly according to CFD prediction, as is given in appendix 2.2.5. The k-factor values for the 90° smooth bend are also given in Table 5.1. This effect is not mentioned in CIBSE or ASHRAE. This result can also be seen in Figure 5.6 with a 5-gore 90° bend, however as the diameter increases the k-factor reduces and tends to level out at a diameter of about 0.3 m, which is given in appendix 2.3.3.

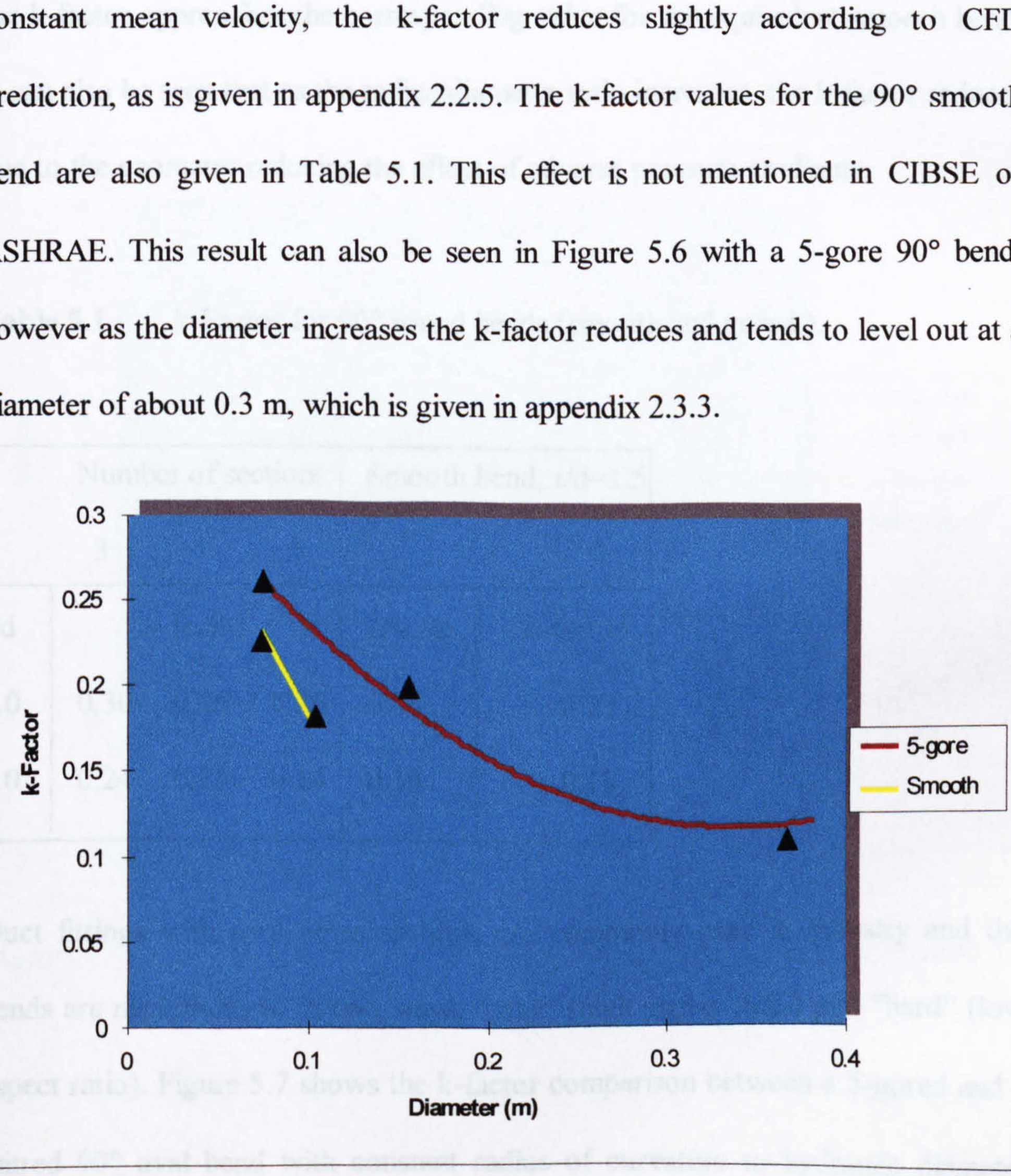


**Figure 5.6** k-Factor comparison for a round 90° bend (smooth and 5-gore), for CFD prediction.

Gored bends are used throughout industry for their cost effectiveness and it is shown here in Table 5.1 for CFD prediction, with bends of more than 4 sections the k-factor approaches the corresponding value for the equivalent smooth bend. It can also be seen that as the radius/diameter ratio increases, the k-factor reduces due to the geometry reducing the effect of adverse pressure gradients.

**Table 5.1** k-Factor for 90° round bends (smooth and gored ).

| Number of sections: | | | Smooth bend, r/d=1.5 | |
|---|---|---|---|---|
| 3 | 4 | 5 | | |
| r/d | k-factor | | Dia./m | k-factor |
| 1.0 | 0.30 | 0.26 0.26 | 0.08 | 0.23 |
| 2.0 | 0.24 | 0.15 0.14 | 0.10 | 0.18 |

Duct fittings with oval cross sections are commonly used in industry and the bends are manufactured in two ways, “easy” (high aspect ratio) and “hard” (low aspect ratio). Figure 5.7 shows the k-factor comparison between a 5-gored and a mitred 90° oval bend with constant radius of curvature to hydraulic diameter ratio. It can be seen that there is a general reduction in k-factor with increasing cross-section area. The dimensions of these duct fittings are based on the dimensions given in Figure 5.8 . It is also expected that mitred bends have a much

higher k-factor than the gored bend, however there also appears to be a characteristic increase in k-factor at about 0.12 $m^2$ cross-section area for the mitre bends. This is given in appendices 2.3.1 and 2.3.2.

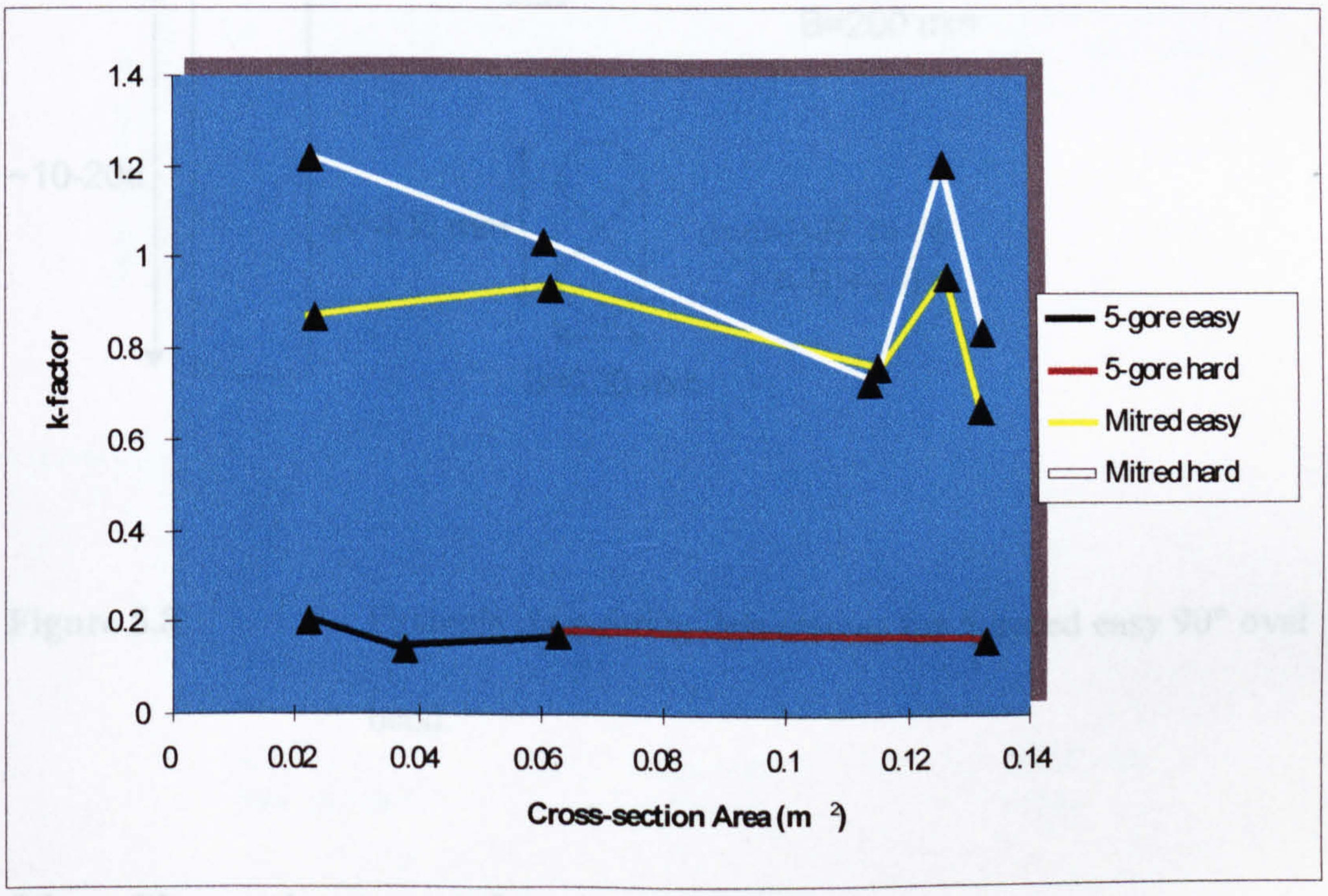


**Figure 5.7** k-factor comparison for oval bends (gored and mitred), for CFD prediction. Radius/Diameter ratio = 1.5 .

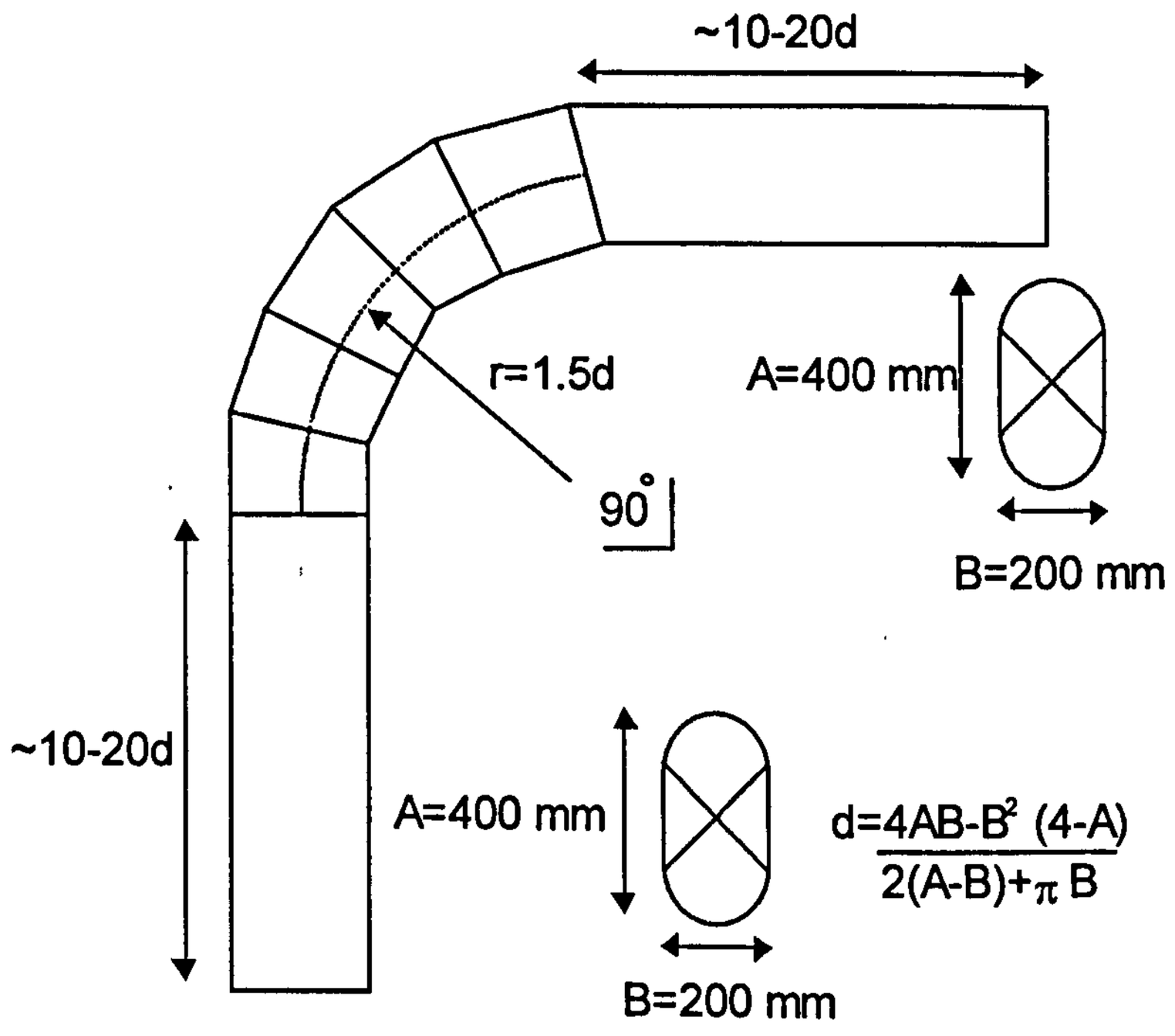


**Figure 5.8** Example duct fitting demensions for 5-gored easy 90° oval bend.

## 5.3 Changes in cross-section area

It has been discussed in the previous section that turning flow causes adverse pressure gradients leading to flow separation. Another cause resulting in adverse pressure gradients is a sudden change in cross-section area which not only produces flow separation but also large scale turbulence in the downstream flow. The effect of the turbulence is to even out the energy distribution and, aided by the flow turning back, to provide entrainment to induce flow re-attachment. After

re-attachment has occurred the large scale turbulence rapidly decays. Figure 5.9 shows the ideal situation in flow distribution throughout a sudden expansion, with also the pressure recovery.

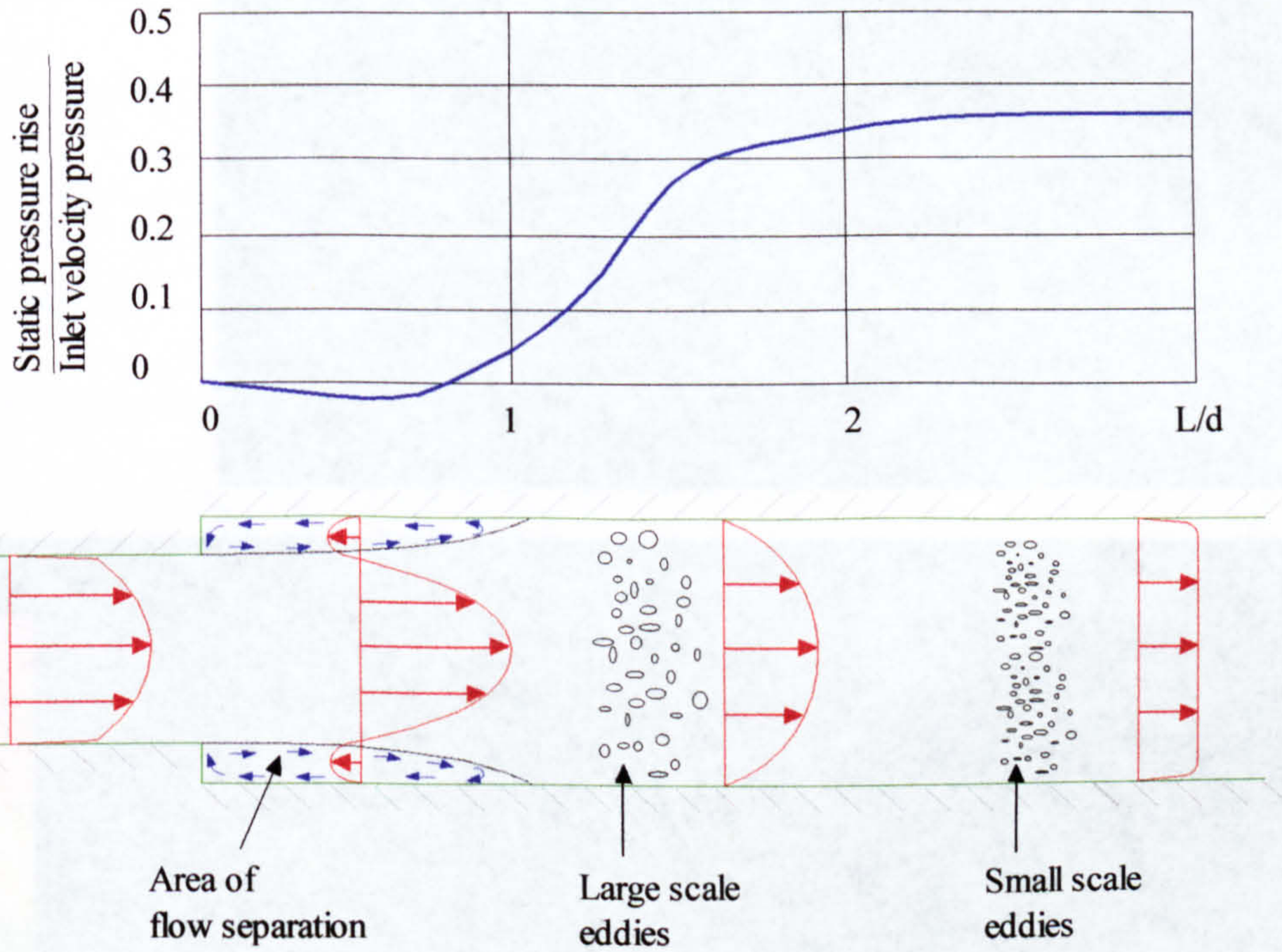


**Figure 5.9** Flow distribution and pressure recovery for a sudden expansion.

Figure 5.10 shows a CFD prediction of flow separation as found in a rectangular expansion duct. The observable grid has been reduced on the upper wall of the duct so that flow separation can be visualised more clearly. The dimensions and operating conditions for this fitting are based on those given in Figure 3.7 . The

Reynolds number is kept constant and the variations to the computer models adhere to the conditions given in section 3.2.2 .

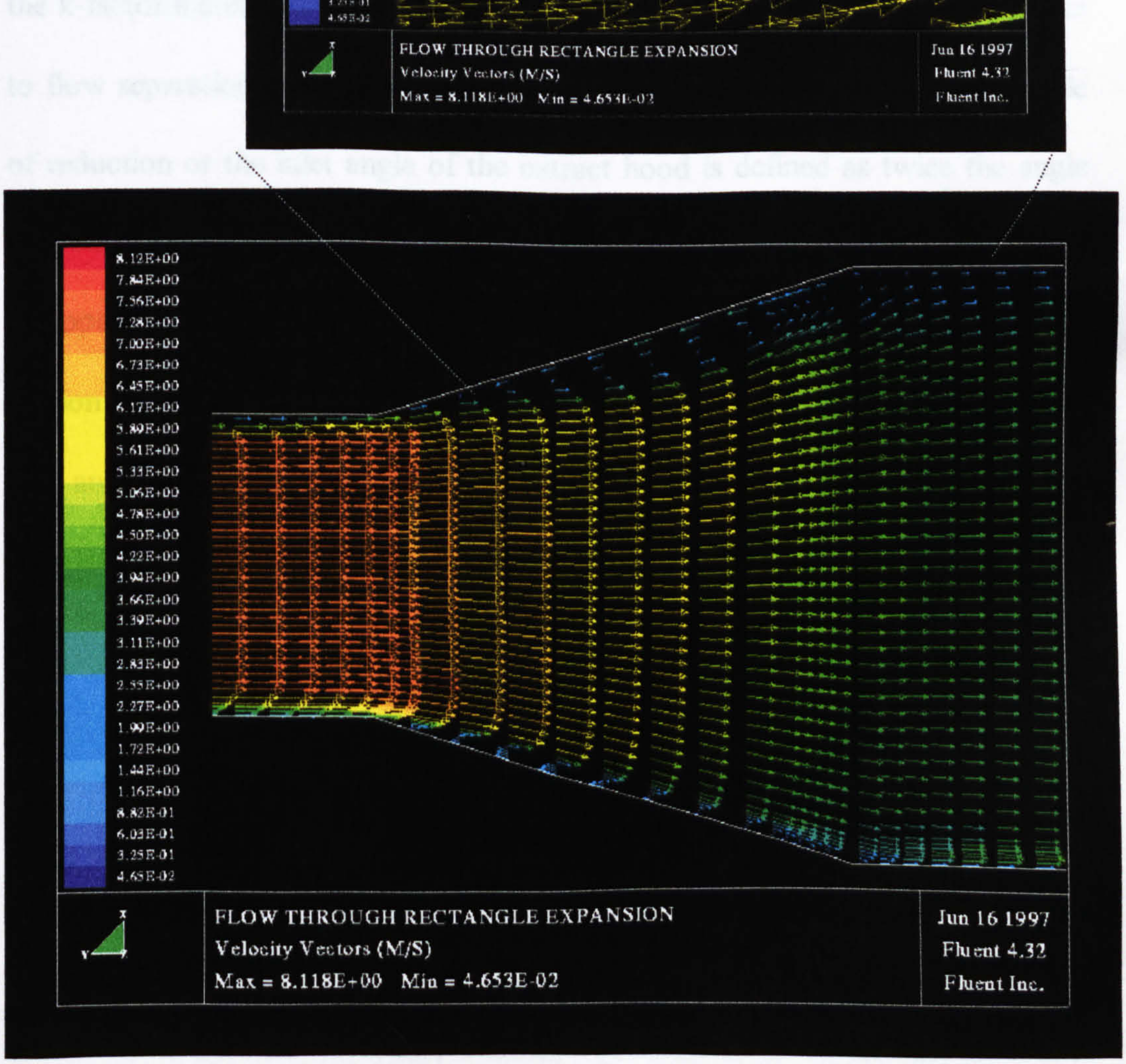


**Figure 5.10** CFD prediction, velocity vectors through a rectangular expansion.

The effect of flow separation is greatly reduced as the sudden change on cross-section area occurs an angle of reduction or expansion. Such duct fittings as used in industry are diffusers, transitions, contractions and expansions. The most significant duct fitting with a change in cross-section area is an extract hood as used in pollution and contaminant removal systems. Figure 5.11 shows the relationship between the k-factor and the angle of reduction, which shows that the k-factor increases more rapidly after an angle of about 65°. This effect is due to flow separation, which only has a significant effect at large angles. The angle of reduction or the inlet angle of the extract hood is defined as twice the angle that one wall diviates from the direction of the downstream duct, as can be seen in appendix 2.2.8. The k-factor for fittings where there is a change in cross-section area is defined in section 3.1.1.1. The dimensions of extract hood at 58° inlet angle can be seen in Figure 3.19.

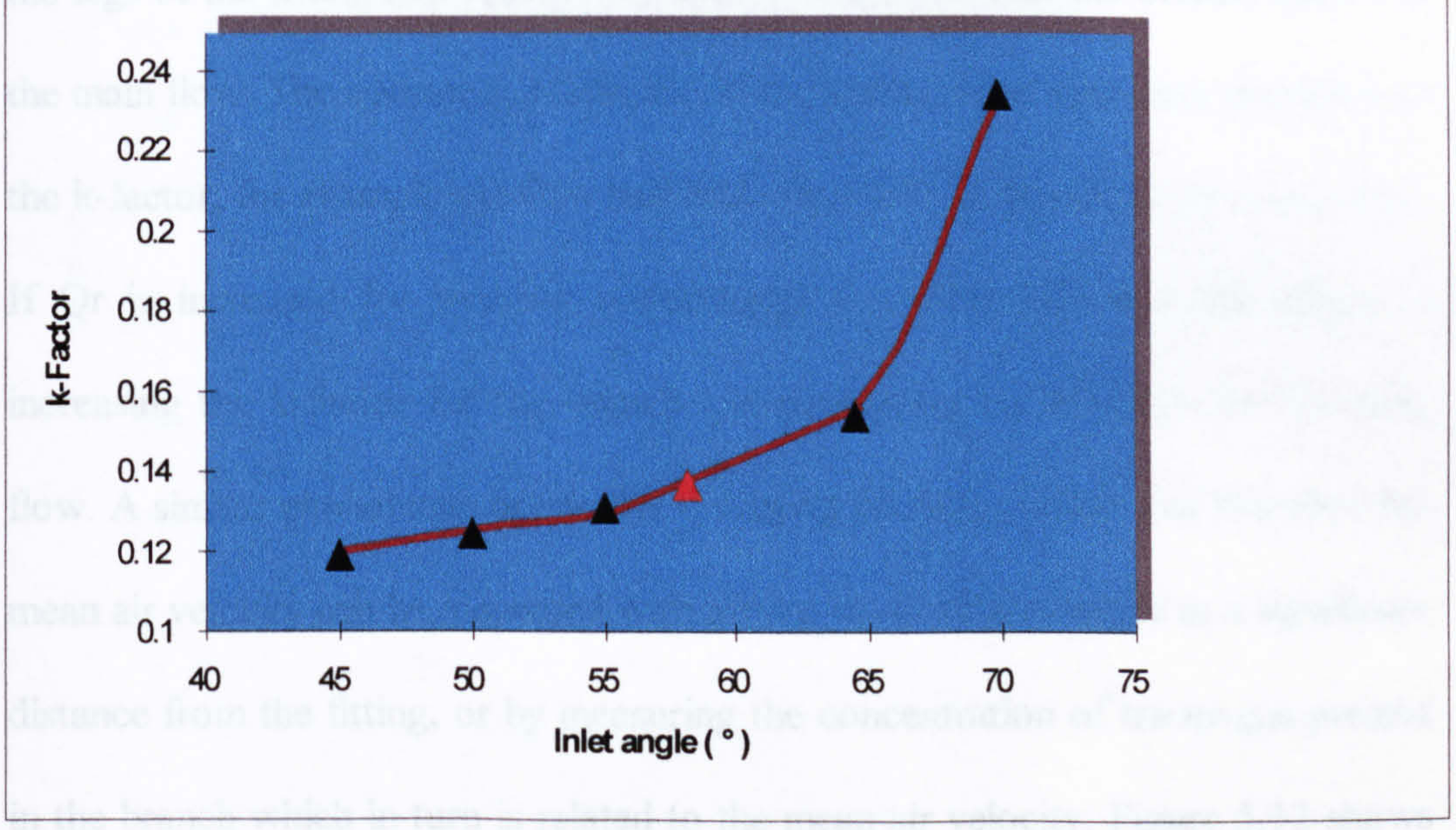


**Figure 5.11** k-Factor relationship with extract hood inlet angle. Data points in red are for experimental tracer-gas and data points in black are for CFD prediction.

## 5.4 Multi-flow fittings

Multi-flow duct fittings are mainly branches or flow dividers, the k-factor for such fittings is defined in section 3.1.1.1 . Whether they are merging or diverging flow these fittings commonly have a main flow which is usually found in a straight direction, and they also have a branch placed at an angle to the main flow. The important geometrical parameters that effect the k-factor include the area ratio before and after the fitting (if a difference in area is required), the angle between

the legs of the fitting and finally the radius of curvature that the branch makes to the main flow. The operating conditions of such fittings can also have an effect on the k-factor, for example the flow rate ratio Qr from the branch to the main flow. If Qr is increased for merging (combining) flow then this has the effect of increasing the k-factor for the branch and decreasing the k-factor for the main flow. A similar phenomena occurs for diverging (dividing) flow. For branches the mean air velocity can be measured with a Pitot-static tube traverse at a significant distance from the fitting, or by measuring the concentration of tracer-gas present in the branch which in turn is related to the mean air velocity. Figure 5.12 shows a comparison between the flow rate ratio and the k-factor for rectangular Wye-branches with dividing flows and aspect ratios between 0.5 and 2.0 . This is also given in appendix 2.1.7. The dimensions for a square cross-section branch are given in Figure 3.18 and the variations of CFD models based on this duct fitting are based on conditions given in section 3.2.2 .

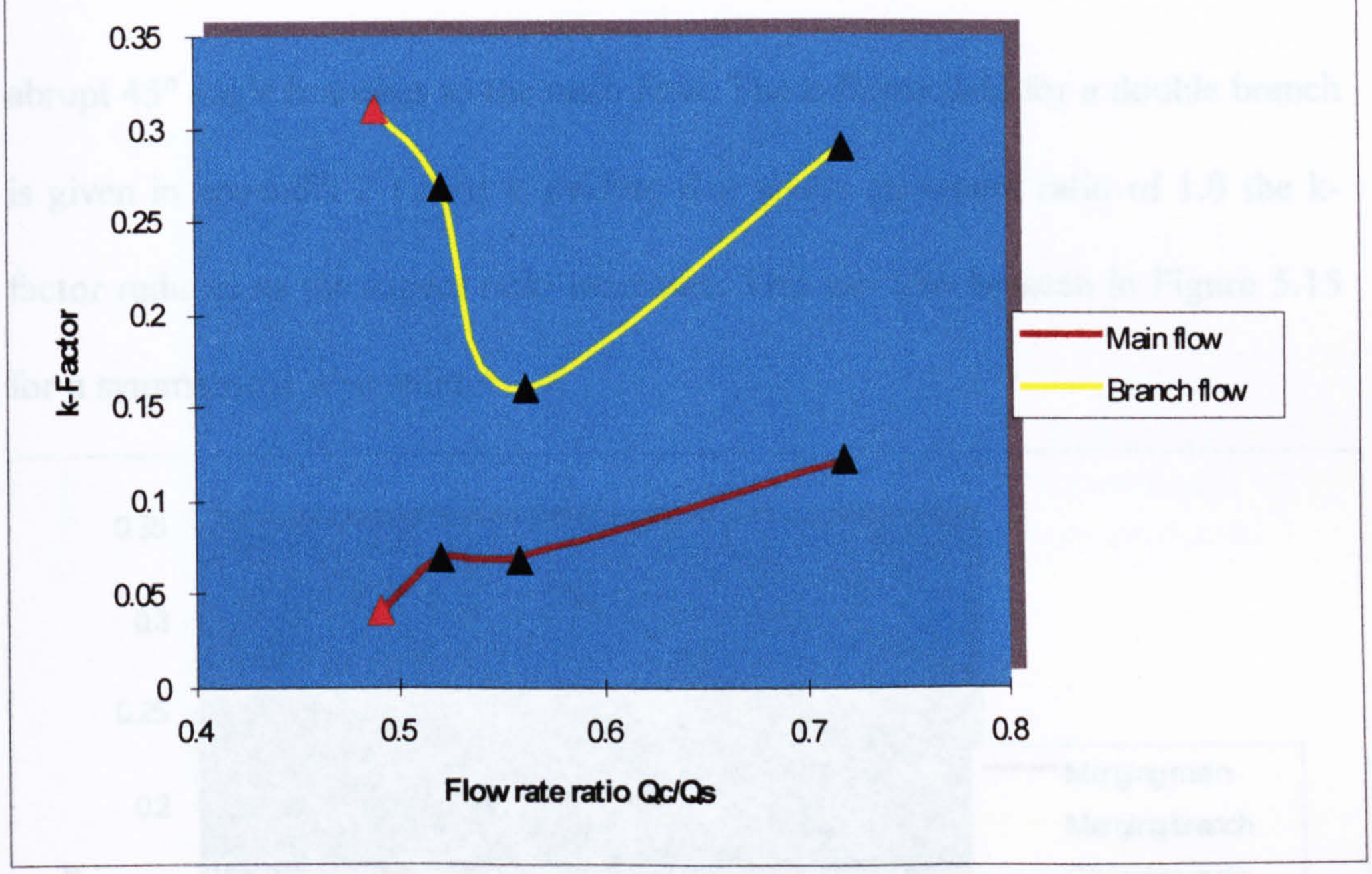


**Figure 5.12** k-Factor comparison with flow rate ratio for diverging flows in rectangular Wye-branches. Data points in red are for experimental tracer-gas and datta points in black are for CFD prediction.

It can be seen in Figure 5.12 that the flow rate relationship with k-factor for the main flow is almost linear whilst the relationship for the branch appears to have an optimum k-factor at about 0.55 for the flow rate ratio.

The shape of cross-section plays an important role in determining the k-factor for any given duct fitting. Figure 5.13 and Figure 5.14 show the relationship between k-factor and the aspect ratio for merging and diverging flow through a rectangular Wye-branch and a double branch, respectively. The double branch has

abrupt 45° angle branches to the main flow. The k-factor data for a double branch is given in appendix 2.1.8. It is evident that above an aspect ratio of 1.0 the k-factor reduces as the aspect ratio increases. This can also be seen in Figure 5.15 for a symmetrical Wye splitter.

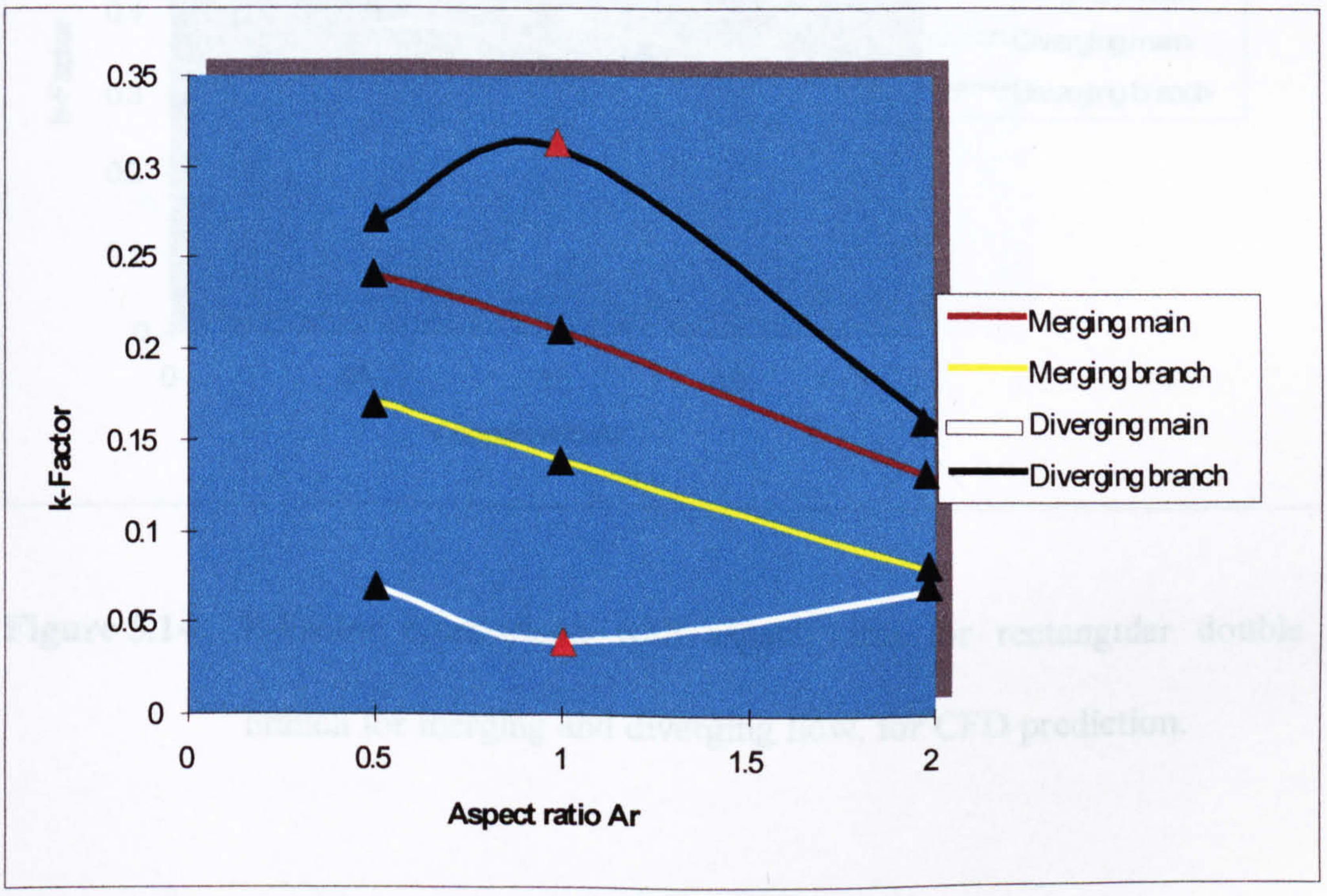


**Figure 5.13** k-Factor comparison with aspect ratio for rectangular Wye-branch for merging and diverging flow. Data points in red are for experimental tracer-gas and data points in black are for CFD prediction.

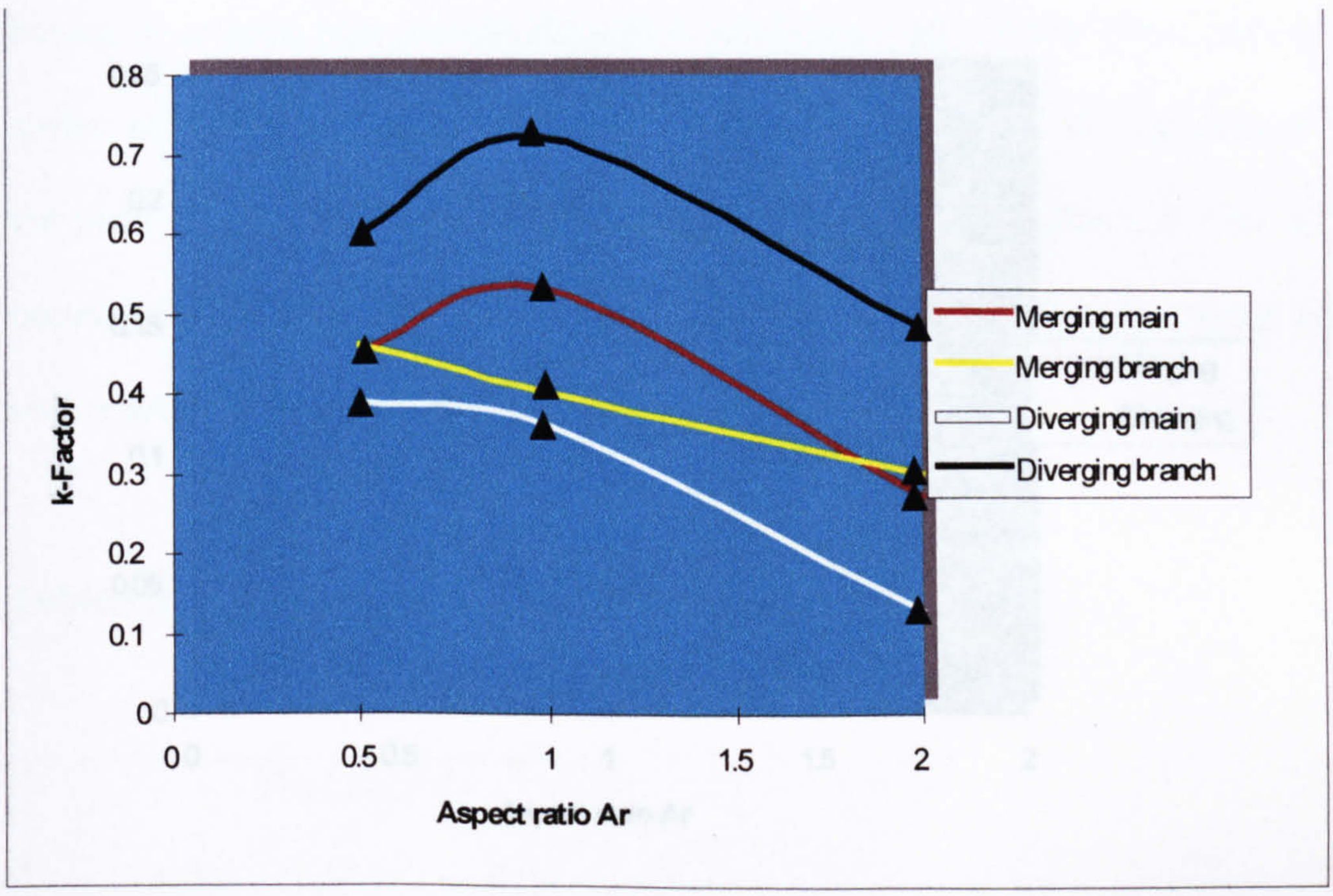


**Figure 5.14** k-Factor comparison with aspect ratio for rectangular double branch for merging and diverging flow, for CFD prediction.

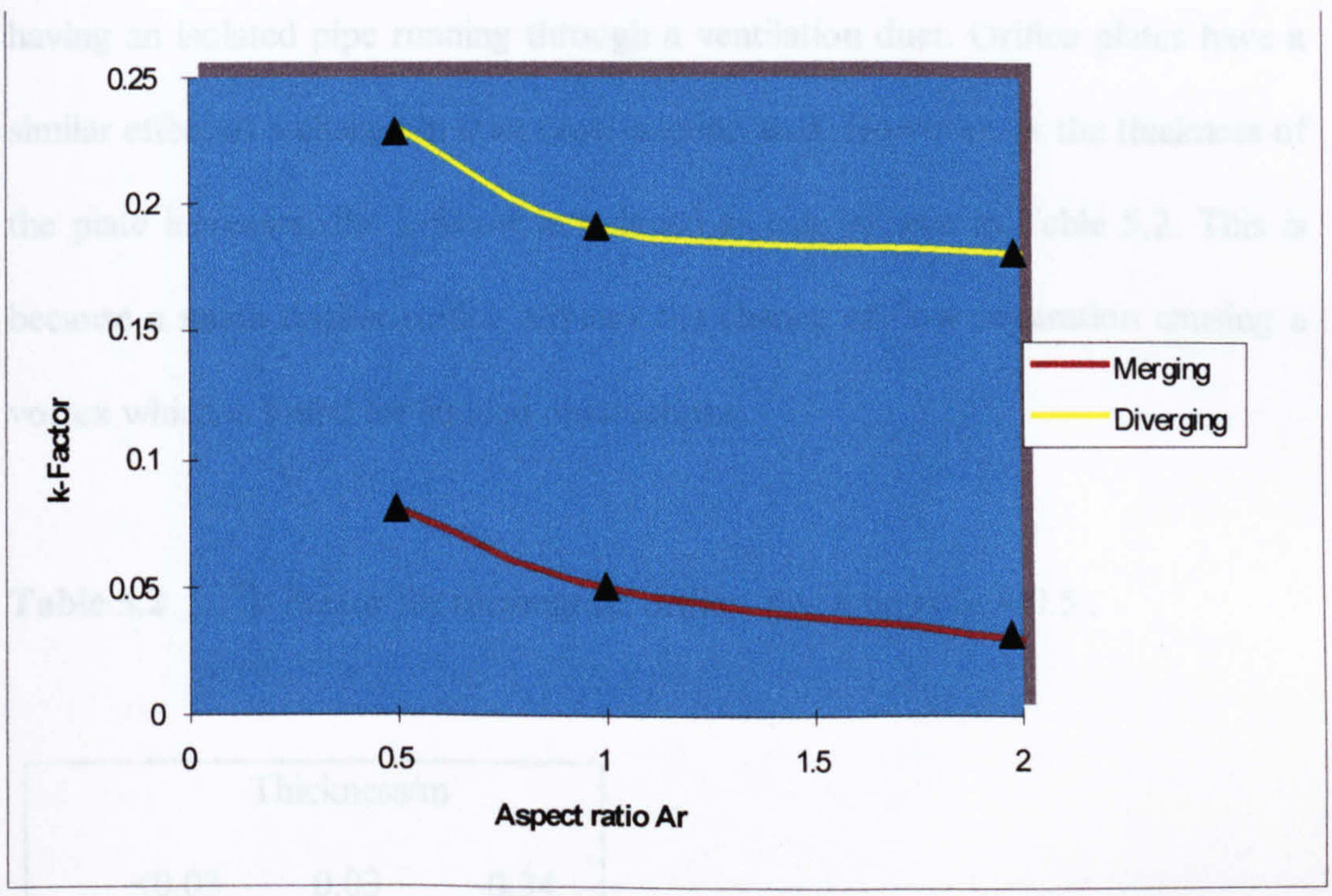


**Figure 5.15** k-Factor comparison with aspect ratio for symmetrical Wye splitter for merging and diverging flow, for CFD prediction.

## 5.5 Obstructed flow

There are many ways of restricting the flow through a duct fitting which all have purely geometrical effects on the k-factor. However, this investigation looks at the common methods of flow obstructions such as the orifice plate, wire mesh, perforated sheet, damper and lateral pipe obstruction. All but the lateral pipe obstruction have the purpose of controlling the air-flow rate and/or the flow distribution whilst lateral pipe obstructions are for example the occurrence of

having an isolated pipe running through a ventilation duct. Orifice plates have a similar effect as a change in duct cross-section area. However, as the thickness of the plate increases, the k-factor is reduced as can be seen in Table 5.2. This is because a much thicker orifice reduces the chance of flow separation causing a vortex which is found for sudden obstructions.

**Table 5.2** k-Factor for rectangular orifice, free area ratio = 0.5 .

| | Thickness/m | | |
|---|---|---|---|
| | <0.03 | 0.03 | 0.34 |
| k | 4.19 | 3.79 | 2.66 |

The critical effect the free area ratio has on the k-factor for different obstructions can be seen in Figure 5.16 . The free area ratio is the area ratio of the cross section which allows the flow to pass to the area which does not allow the flow to pass. It can be concluded from Figure 5.16 that as the free area becomes more distributed for any particular free area ratio then the k-factor reduces indicating that a wire mesh is more efficient at passing air-flow than a perforated sheet and a single orifice if they were to be used for the same application. The data for these can be seen in appendices 2.1.5, 2.1.6 and 2.1.14.

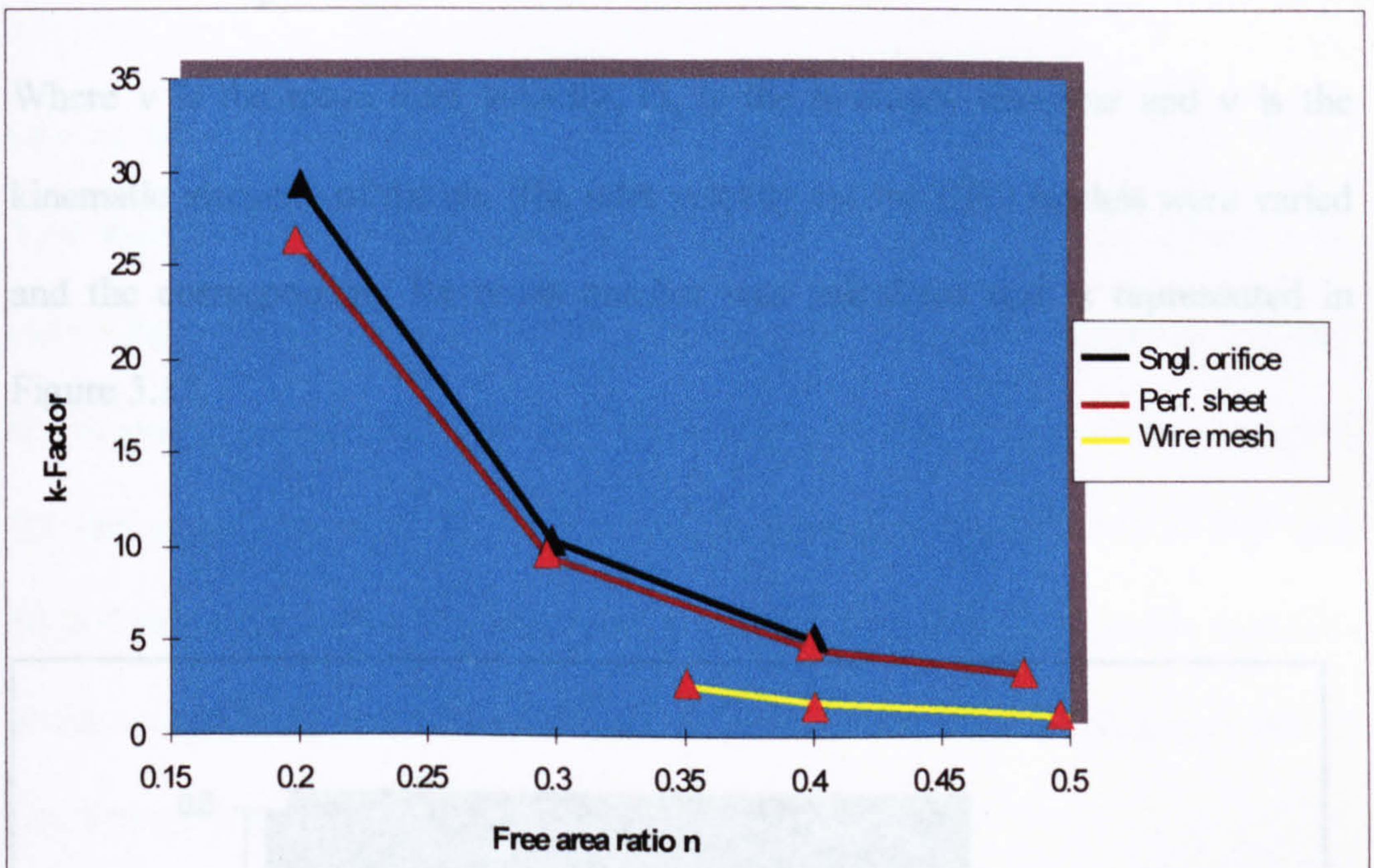


**Figure 5.16** k-Factor comparison with free area ratio for a single orifice, perforated sheet and a wire mesh for a rectangular duct.

A damper is often used to control the air-flow rate where the damper angle is the governing characteristic on the air-flow rate and therefore the k-factor. Figure 5.17 shows a comparison between k-factor and Reynolds number for single and double lateral obstructions in a rectangular duct. It shows clearly that below a certain Reynolds number the k-factor becomes very high and that air-flow operating conditions for such obstructions should be kept above this level. This is also represented in appendix 2.1.16. The Reynolds number is defined by :

$$\mathrm{Re} = \frac{vD_h}{\nu} \tag{5.1}$$

Where v is the mean duct velocity, $D_h$ is the hydraulic diameter and ν is the kinematic viscosity of the air. The inlet velocity for the CFD models were varied and the corresponding Reynolds number was calculated and is represented in Figure 5.17.

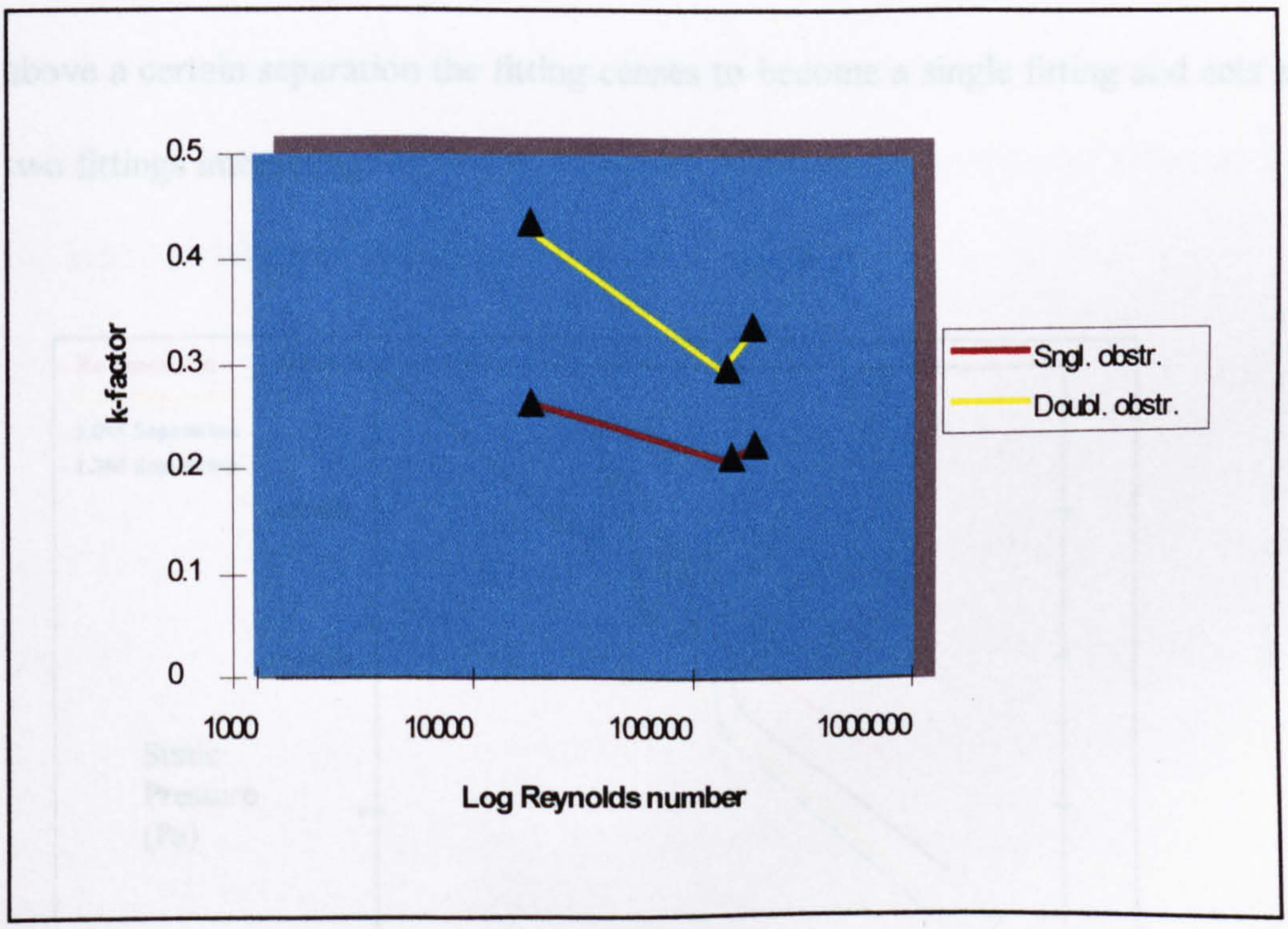


**Figure 5.17** k-Factor comparison with Reynolds number for single and double lateral obstructions in a rectangular duct, for CFD prediction.

## 5.6 Interacting duct fittings

One of the most common interaction of duct fittings is the 180° u-bend. Figure 5.18 shows a CFD prediction of pressure loss through a rectangular u-bend with increasing separation. The aspect ratio for this bend was kept constant at 1.0, and the Reynolds number was also kept constant at 165,000. The computational grid for this model was kept at a constant grid density using between 35,000 and 50,000 grid cells, with a high grid density at the near wall area. It can be seen that above a certain separation the fitting ceases to become a single fitting and acts as two fittings interacting.

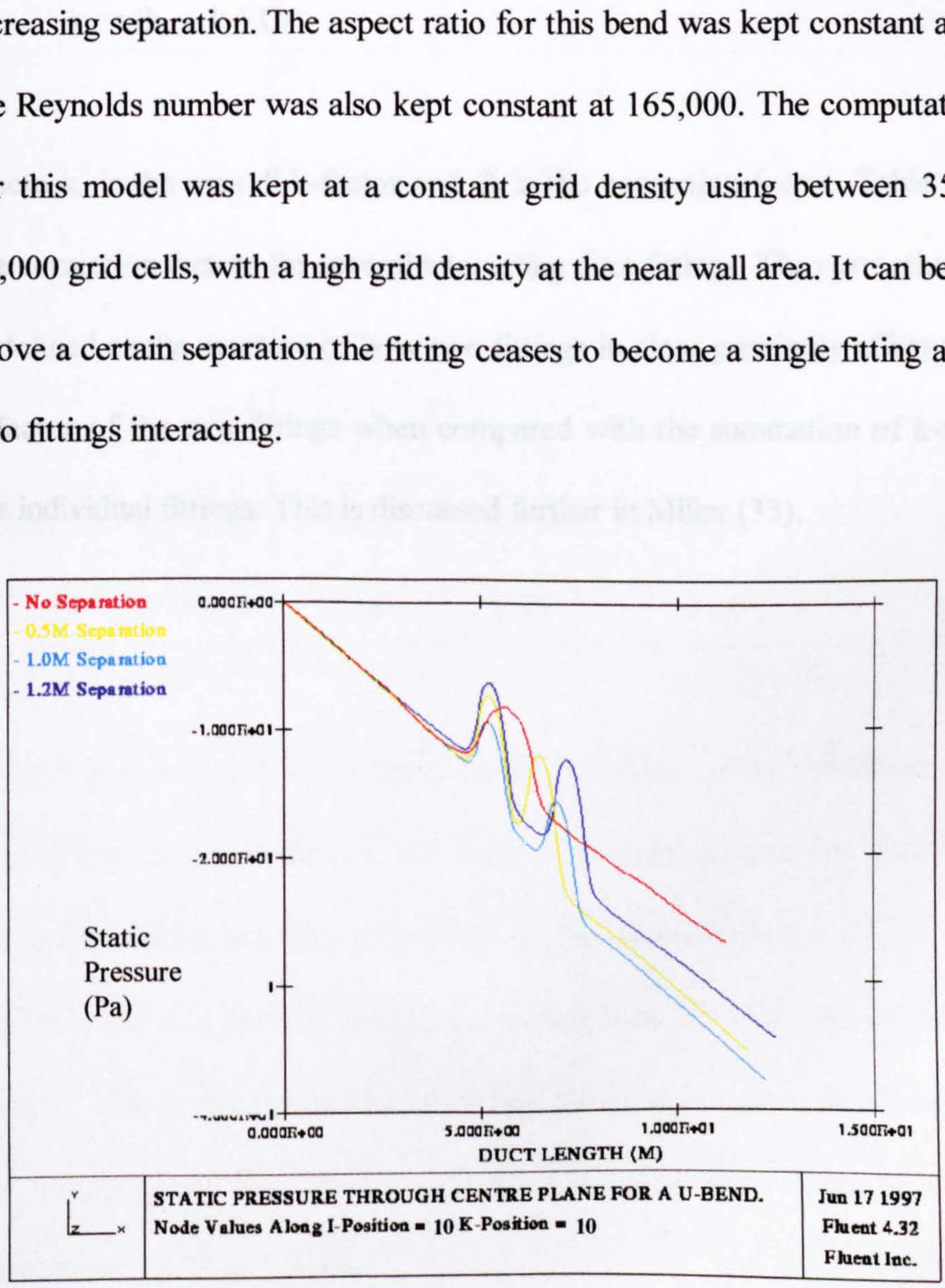


**Figure 5.18** CFD prediction of pressure loss through a rectangular u-bend.

When duct fittings interact in close proximity the overall k-factor is found by summing the k-factors of the individual duct fittings and applying a correction factor :

$$k_o = (k_1 + k_2)\, C_f \qquad (5.2)$$

where $k_o$ is the overall k-factor and $C_f$ is the correction factor. Table 5.3 shows the correction factors for several interacting duct fittings. The correction factor $C_f$ is defined as the measure of how two fittings in close proximity affect the overall k-factor of the two fittings when compared with the summation of k-factors for the individual fittings. This is discussed further in Miller (33).

**Table 5.3** Correction factors for interacting duct fittings.

| Duct fitting | k-Factor | | | |
|---|---|---|---|---|
| | 1st fitting | 2nd fitting | Interacting fittings | Correction factor |
| Circular | | | | |
| 90° bend+90° bend. | 0.17 | 0.17 | 0.22 | 0.65 |
| Rectangular: | | | | |
| 90° bend+90° bend. | 0.18 | 0.18 | 0.20 | 0.56 |
| 90° bend+contraction. | 0.18 | 0.06 | 0.18 | 1.00 |
| Expansion+90° bend. | 0.10 | 0.18 | 0.24 | 0.86 |
| 90° bend+30° damper. | 0.18 | 3.38 | 2.75 | 0.77 |

Table 5.3 shows that when the k-factor for either of the individual interacting duct fittings is very small (i.e. 90° bend + contraction) then the duct fitting with the small k-factor has very little effect on the overall k-factor. It also shows that the 90° bend can actually reduce the overall k-factor when placed before a 30° damper. This is due to the bend directing the flow in a more parallel direction to the damper plate. The k-factor data for interacting duct fittings is also given in appendices 2.1.11 to 2.1.13.

## 5.7 Experimental and prediction comparison with design data

When experimental results are compared with CFD prediction and design data published in handbooks such as CIBSE and ASHRAE, a common trend is found throughout. The currently available data for designers of HVAC systems is very limited, however, a satisfactory comparison can be made with the data given. Table 5.4 shows a comparison of k-factor data between experimental results, CFD prediction and data taken from CIBSE and ASHRAE for a selection of duct fittings. Figure 5.19 shows the relationship between damper angle and k-factor through a square duct. It shows that CFD prediction clearly relates more closely to tracer-gas results whilst Pitot-static tube results also relate very closely to data taken from ASHRAE. This characteristic shows that when the data was collated by ASHRAE for these duct fittings then conventional techniques with similar accuracy's to Pitot-static tubes were used. It can also be concluded from Figure 5.19 and Table 5.4 that CFD predictions relate very closely to more modern experimental techniques for measuring air-flow velocity such as the tracer-gas method. The difference between Pitot-static tube results and tracer-gas results, and the difference between CFD predictions and data taken from CIBSE and ASHRAE is about the same in both incidences, i.e. 26 % . This finding is coherent with the alleged k-factor over estimation found in CIBSE and ASHRAE which have been obtained using conventional techniques for measuring the mean

air velocity. It can also be seen from Table 5.4 that data for common duct fittings such as a u-bend and a Wye-branch are either not provided by CIBSE and ASHRAE or they fail to show characteristics like the change in k-factor with u-bend separation.

**Table 5.4a** Comparison of k-factor data for various duct fittings.

| Duct Fitting: | k-Factor CFD | Pitot-static tube | Tracer-gas | CIBSE | ASHRAE |
|---|---|---|---|---|---|
| U-bend (App2.1.1) | | | | | |
| separation=0 m. | 0.197 | 0.192 | 0.146 | - | 0.240 |
| separation=0.5 m. | 0.214 | 0.265 | 0.216 | - | 0.260 |
| separation=1.0 m. | 0.244 | - | - | - | 0.260 |
| separation=1.2 m. | 0.250 | 0.334 | 0.269 | - | 0.260 |
| 35° Contraction (App2.1.2) | 0.064 | 0.079 | 0.056 | 0.030 | 0.240 |
| 35° Expansion (App2.1.3) | 0.100 | 0.326 | 0.230 | 0.330 | 0.240 |
| Wye branch | | | | | |
| converging main flow (App2.1.7) | 0.209 | 0.250 | 0.170 | - | 0.275 |
| converging branch flow | 0.142 | 0.190 | 0.160 | - | 0.170 |
| diverging main flow | 0.120 | 0.150 | 0.040 | - | 0.150 |
| diverging branch flow | 0.289 | 0.330 | 0.310 | - | 0.320 |
| Damper plate (App2.1.4) | | | | | |
| angle 10° | 0.248 | 0.320 | 0.224 | - | 0.330 |
| angle 20° | 0.957 | 1.276 | 0.937 | - | 1.200 |
| angle 30° | 3.380 | - | 2.130 | - | 3.300 |
| angle 45° | 12.490 | 15.120 | 12.810 | - | 16.050 |
| angle 60° | 47.600 | 64.530 | 44.510 | - | 70.000 |
| Wire mesh (App2.1.5) | | | | | |
| free area ratio 0.5 | - | 2.138 | 1.550 | 1.700 | 1.790 |
| free area ratio 0.4 | - | 3.170 | 2.350 | 3.000 | 3.000 |
| free area ratio 0.35 | - | 4.270 | 3.420 | 5.010 | 4.390 |

**Table 5.4b** Comparison of k-factor data for various duct fittings.

| Duct Fitting: | k-Factor | | | | |
|---|---|---|---|---|---|
| | CFD | Pitot-static tube | Tracer-gas | CIBSE | ASHRAE |
| Perforated sheet (App2.1.6) | | | | | |
| free area ratio 0.2 | 34.050 | 44.710 | 30.720 | 51.000 | 50.000 |
| free area ratio 0.3 | 11.850 | 17.560 | 11.290 | 18.000 | 17.500 |
| free area ratio 0.4 | 6.050 | 7.880 | 5.644 | 8.300 | 7.900 |
| free area ratio 0.48 | - | 4.799 | 3.859 | 4.900 | 4.100 |
| Exit diffuser (App2.1.10) | - | 0.910 | 0.500 | 0.610 | 0.760 |
| 90° bend + contraction (App2.1.11) | 0.180 | 0.270 | 0.200 | - | - |
| Expansion + 90° bend (App2.1.12) | 0.240 | 0.430 | 0.330 | - | - |
| 90° bend + damper (App2.1.13) | | | | | |
| damper angle 10° | 0.310 | 0.380 | 0.260 | - | - |
| damper angle 20° | 1.140 | 1.690 | 1.060 | - | - |
| damper angle 30° | 2.750 | 3.660 | 1.980 | - | - |
| Extract hood inlet angle 58° (App2.2.8) | 0.135 | 0.216 | 0.156 | 0.230 | - |

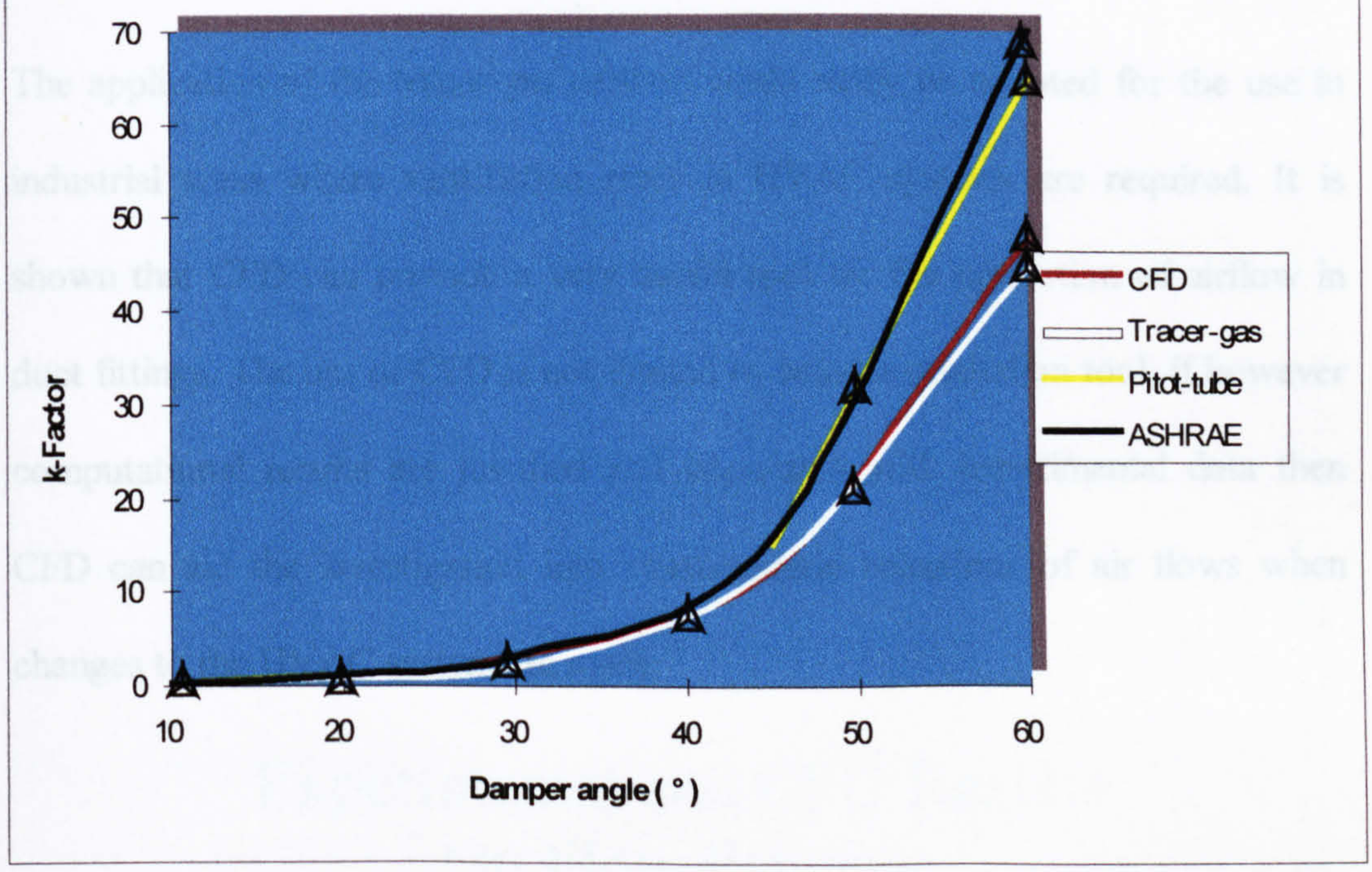


**Figure 5.19** k-Factor comparison for a damper with experimental results, CFD prediction and data taken from ASHRAE.

## 5.8 Summary

With the limited availability of recent k-factor data and the lack of k-factor characteristic with different fittings, there is a clear need for a more detailed and comprehensive database of k-factor information. This is more apparent now with reducing manufacturing costs that allow the wide spread use of more smoother and geometrically complex duct fittings. It can be seen that for laboratory purposes the application of more modern experimental tecniques for measuring the mean airflow rate in a duct can be easily made, such as the tracer-gas method.

The application of the tracer-gas method could easily be adapted for the use in industrial areas where ventillation rates in HVAC systems are required. It is shown that CFD can provide a very useful tool for the prediction of airflow in duct fittings. The use of CFD is not limited to being a prediction tool, if however computational results are justified and correlated with experimental data then CFD can aid the investigation into characteristic behaviour of air flows when changes to the HVAC system are made.

# Chapter 6

# Experimental and CFD Results On Flow Patterns

# 6.0 Experimental and CFD results on flow patterns

The use of CFD codes for the prediction of pressure losses and velocity distributions in ducted air flows is only one of the advantages that advancement in computer technology has provided. The results from a CFD model can be presented in a variety of ways as is shown in this chapter.

## 6.01 Literature search

Flow patterns of duct fittings have been investigated for many years using various visualisation techniques, however as more complex and streamlined fittings become more common place in industry, the use of CFD for flow visualisation can be easily applied. Fluid flow visualisation of turbulence using dye emitters in cylinders are described in Tritton (34). Vortex shedding, which is discussed in this chapter can also be viewed by smoke patterns in Douglas (35). The phenomena of flow separation which is also described in this chapter has been discussed and investigated by Tritton (36) and Ward-Smith (37) using flow visualisation.

## 6.1 Laminar and turbulent flow

Generally laminar flow is considered to be present in ducted flows, away from disturbances, if the dimensionless Reynolds number is less than 2000. However, laminar flow is also associated with viscous fluids, low flow velocities and small pipe dimensions. When the Reynolds number becomes very low then the viscous forces become very important and the shear and, hence, the energy dissipation becomes directly proportional to the velocity. Using the pressure loss equation 6.1, the loss coefficient for any given duct fitting can be obtained :

$$\Delta P = \frac{k\rho v^2}{2} \tag{6.1}$$

and that the k-factor (k) is inversely proportional to the Reynolds number :

$$k = \frac{\text{Constant}}{\text{Reynolds number}} \tag{6.2}$$

It is important to remember that in fluid flow that is considered to be laminar, there may by areas of temporary high velocity such as changes in cross section area resulting in small pockets of turbulence . Once turbulence has been induced, then the loss coefficient (k-factor) is no longer inversely proportional to the Reynolds number. Flow patterns can give a very crude visualisation whether the flow is laminar or turbulent for any given application. This is because at very low Reynolds numbers (i.e. about 10), in areas of abrupt change in area the flow will creep around the change in area without producing any flow separation. As the Reynolds number increases but still lower than 2000, it is possible due to inertia forces beginning to take over, to achieve temporary laminar separation and flow re-attachment. Increasing the Reynolds number further still and the flow around the change in area becomes separated and turbulence is induced. Figure 6.1 shows the basic difference between the velocity profile of laminar and turbulent flow in terms of energy coefficient.

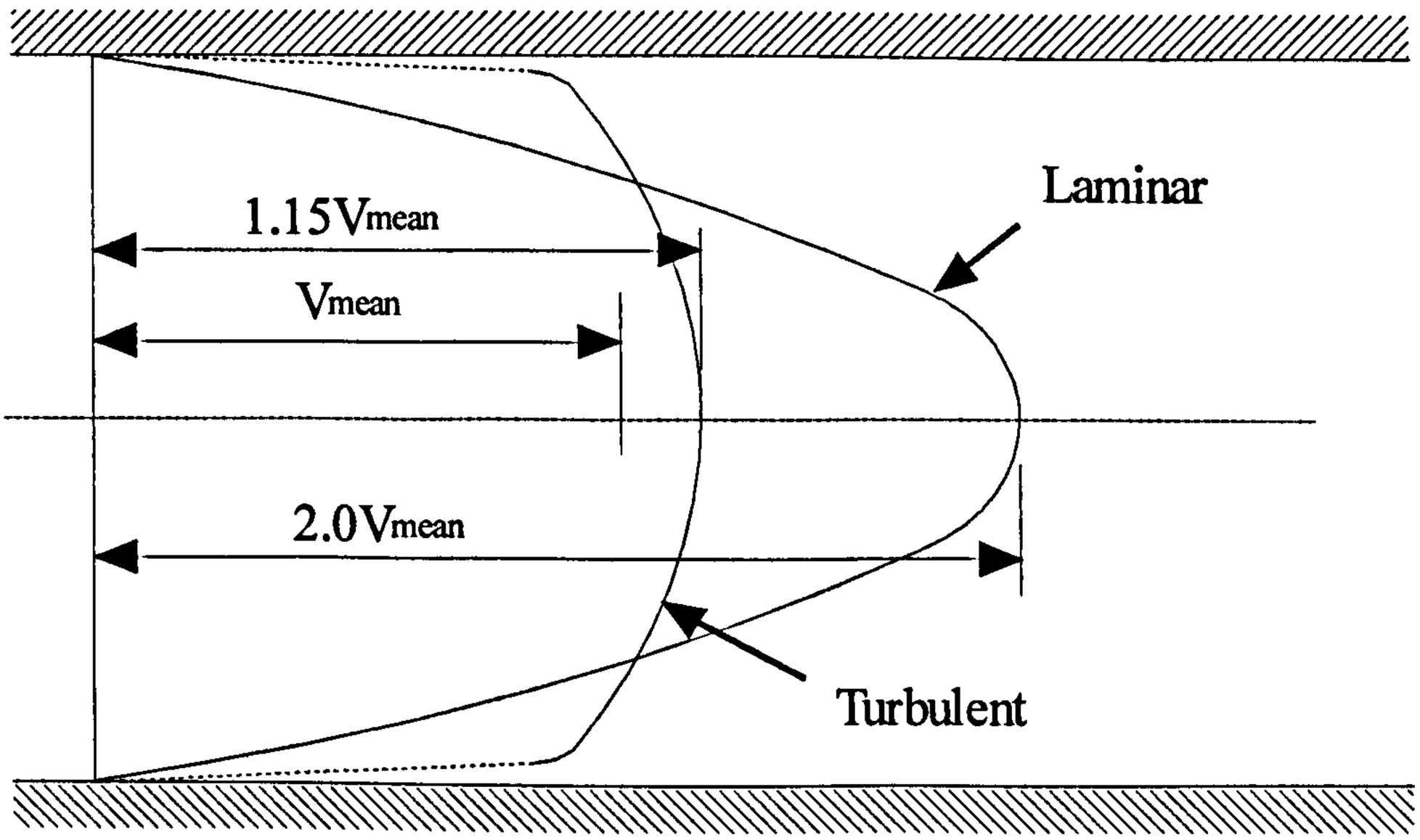


**Figure 6.1** Laminar and turbulent velocity profiles

Developed laminar flow has a kinetic energy coefficient and a peak to mean velocity ratio of 2, whilst the developed turbulent flow has a kinetic energy coefficient of about 1 and a peak to mean velocity ratio of about 1.2 . The developed velocity profiles for laminar and turbulent flow can be seen in Figure 6.1. The velocity profile for laminar flow appears conical in shape and remains fairly unifor for all values of Reynolds number in the laminar region. The turbulent velocity profile is fairly flat in appearance, however, changes shape dependant on the Reynolds number varying within the turbulent region. The transition stage between laminar and turbulent flow is generally taken as the most unpredictable type of flow, which is why CFD codes can not predict flow in this

region and use equations based on either laminar or turbulent flow. It is also generally accepted that most airflows in HVAC systems are turbulent.

## 6.2 Flow visualisation

A unique but fairly crude technique for comparison between CFD prediction and ducted air flows is flow visualisation. Many methods of obtaining visual results of flow patterns prove to be difficult to implement due to strict test conditions and also the method of capturing the flow pattern on photographic film. Good flow visualisation is dependent on the control over experimental procedures. Tight laboratory methods must be employed to create the desired pattern and also being in a position to visualise the flow whilst keeping the test true to real applications. The method applied in these investigations is smoke visualisation with the discission of other techniques of viewing flow patterns.

### 6.2.1 Particle tracers/streamers

This method involves releasing small lightweight but visible particles into the flow and their motion can be captured on photographic or video film. Particles can be made from polystyrene or similar materials. However particle tracers are not

useful for displaying continuous flow required to show distint flow patterns, and a photographic plate used for flow visualisation made up of individual particles is difficult to observe. Releasing streamers such as paper into the flow can also provide flow visualisation to a certain degree. However, the representation of flow patterns using streamers particularly in ducted air flows is very limited.

### 6.2.2 Smoke visualisation

This technique involves releasing smoke from a smoke generator into the entrance of a ducted air flow. The resultant smoke patterns can then be photographed through clear perspex windows on the side of the duct just after a particular duct fitting. Plate 6.1 shows the experimental set-up of a smoke visualisation test. The smoke generator burns oil to produce the smoke and uses carbon dioxide to inject the smoke into the duct.

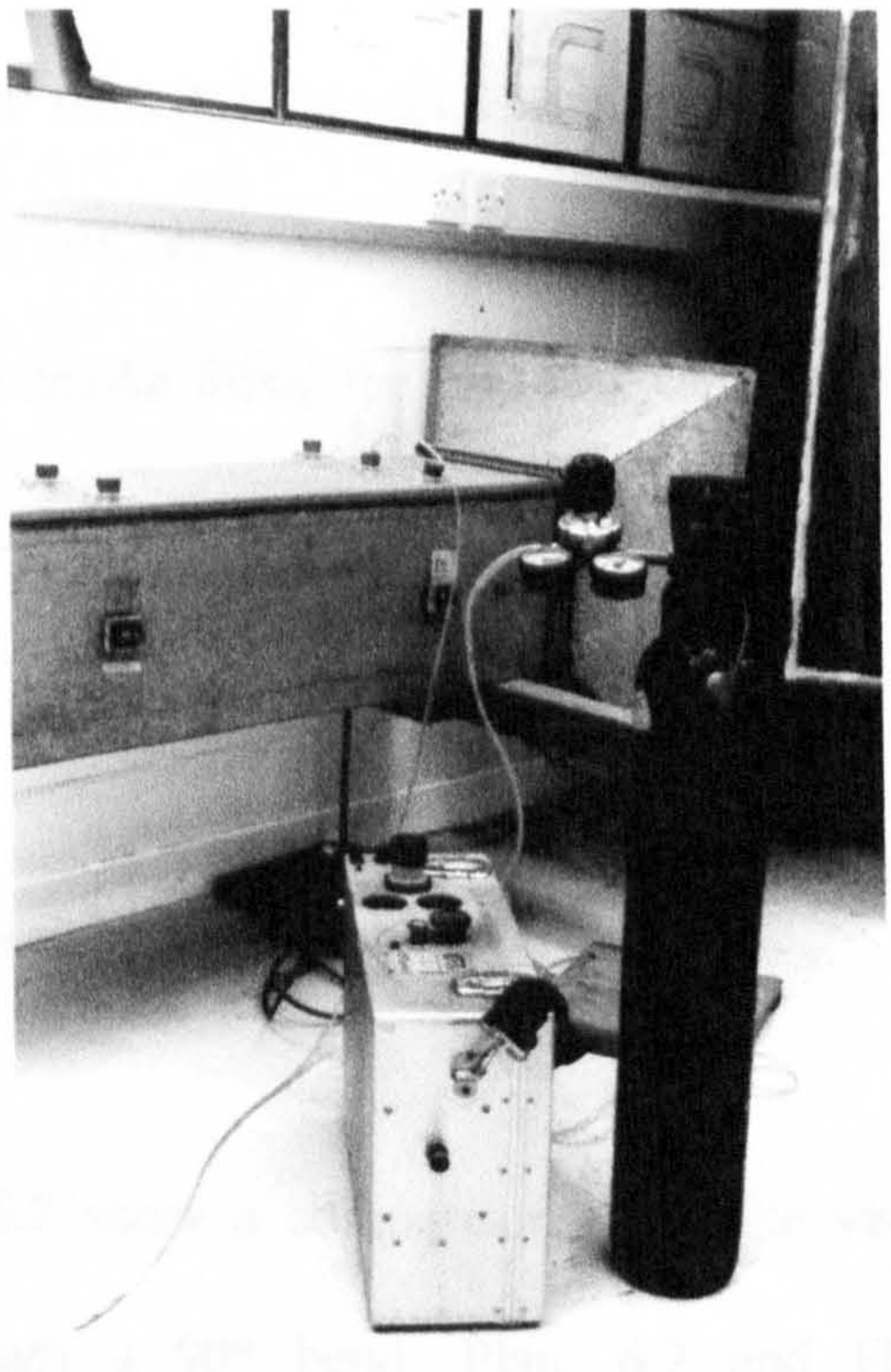

**Plate 6.1** Smoke visualisation test.

In order to observe the smoke within the duct, the walls were painted black so that the smoke appears as white in colour on the photographic plates. The air flow velocity plays an important role for smoke and other visualisation techniques. If the mean flow velocity is too high then the smoke is taken out of the duct before a clear picture of the flow characteristics can be obtained. If the

flow velocity is too low then due to a difference in pressure between the duct interior and the ambient air, back flow can cause several problems to the test. These problems include smoke filling the laboratory area making it impossible to continue the test.

### 6.2.3 Smoke visualisation and CFD comparison

Plate 6.2 and Figure 6.2 show a comparison of smoke visualisation and CFD velocity vectors through a 90° bend. Plate 6.2 and Figure 6.2 show an experimental comparison with CFD prediction for flow patterns for an identical 90° rectangular bend. The dimensions of this bend can be seen in Figure 3.5 . Similarities of flow pattern and streaklines can be observed. Although flow separation is not evident the disstortion in velocity flow profile is evident on the inside wall just after the bend. However, in reality flow separation will be present in the form of very small eddies, due to the bend being smooth without sufficient geometric change to create a high enough adverse pressure gradient. The disstortion in velocity flow profile does, however, show the presence of an adverse pressure gradient.

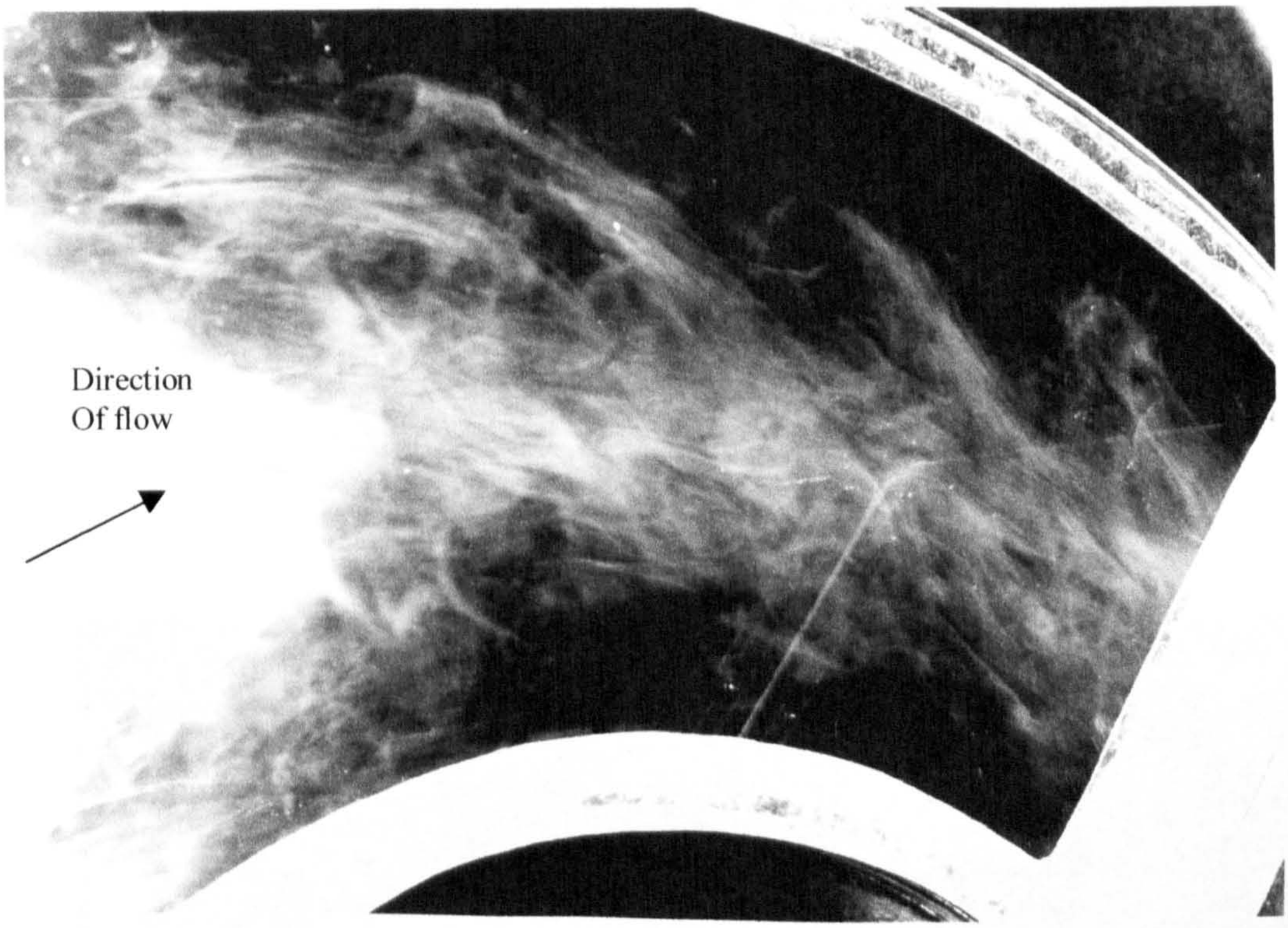


**Plate 6.2** Smoke pattern for 90° bend.

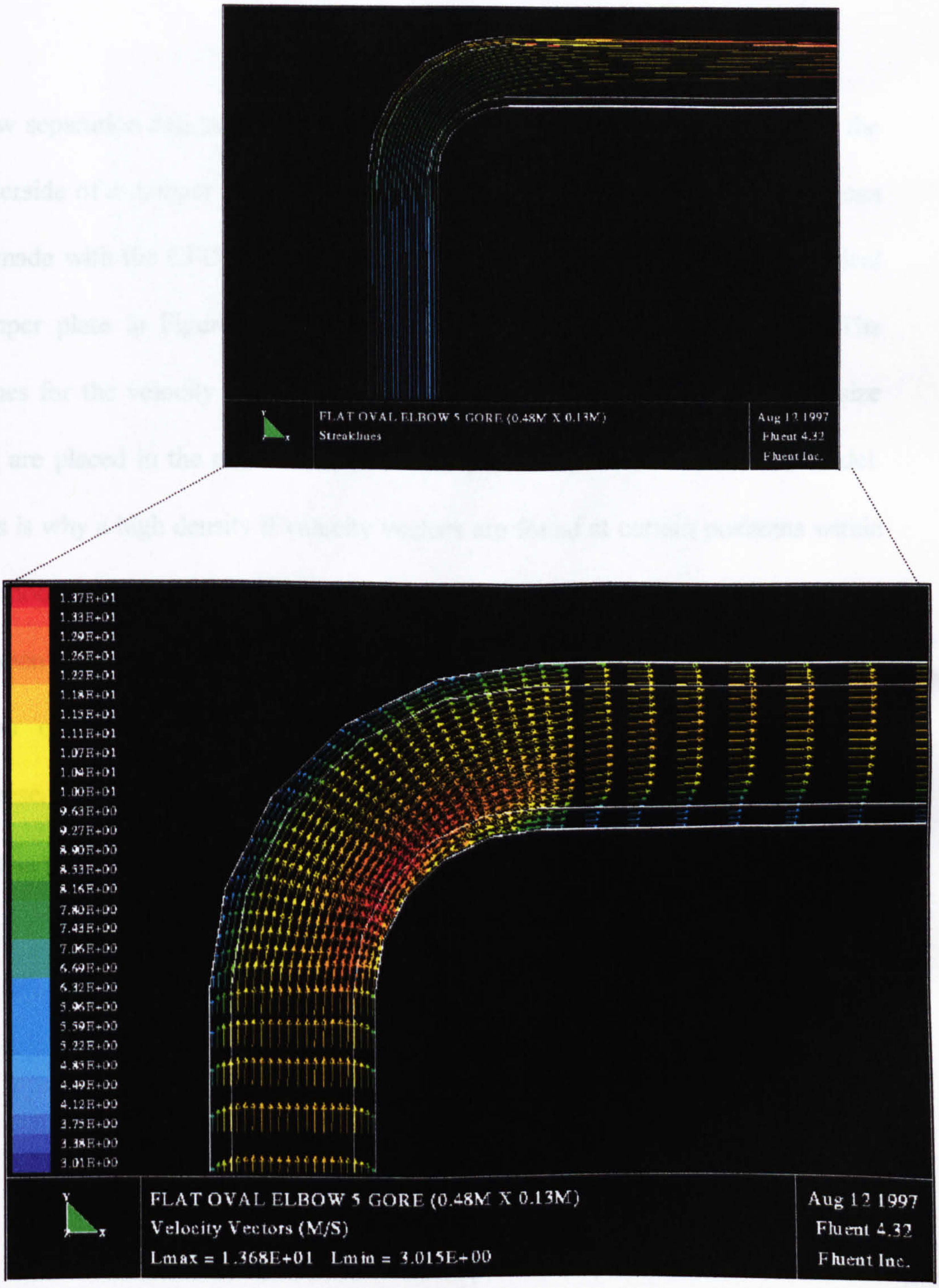


**Figure 6.2** CFD velocity vectors and streaklines through a 90° bend.

Flow separation can be seen in Plate 6.3 with the formation of a vortex on the underside of a damper plate as portrayed by a smoke pattern. A comparison can be made with the CFD prediction and similarities can be made with an identical damper plate in Figure 6.3 which shows the predicted velocity vectors. The values for the velocity vectors in Figure 6.3 are represented by colour and size and are placed in the model relative to the grid cell positions within the model. This is why a high density if velocity vectors are found at certain positoins within the model, relative to required high grid densities. The path of streaklines can also be seen in Figure 6.3 showing the outline of the flow. The streaklines appear to cross over, however they are only changing position in the z-direction represented in the direction in to the figure. This 3-dimensional effect cannot be seen in two dimensions.

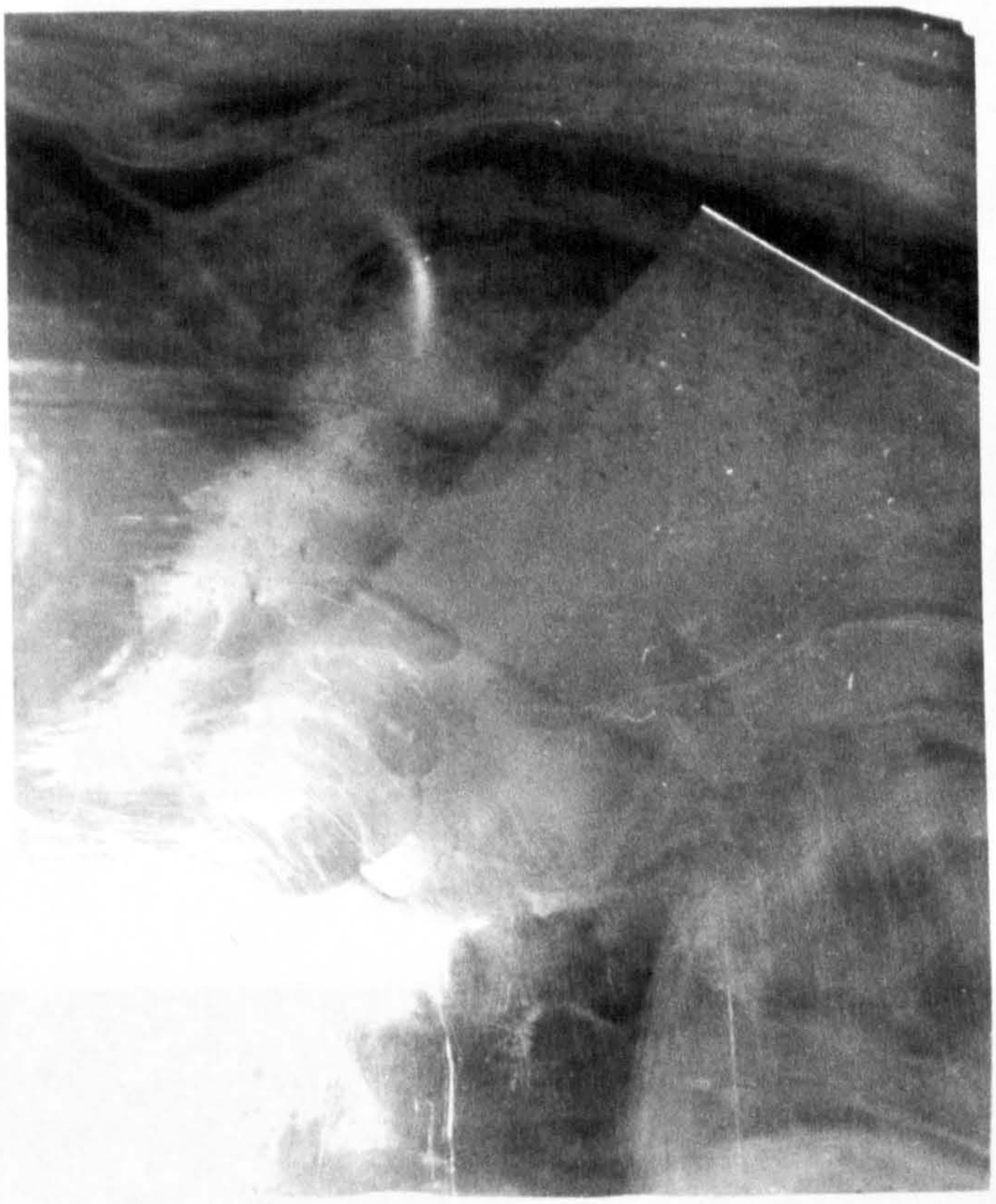

**Plate 6.3** Smoke pattern for a damper plate.

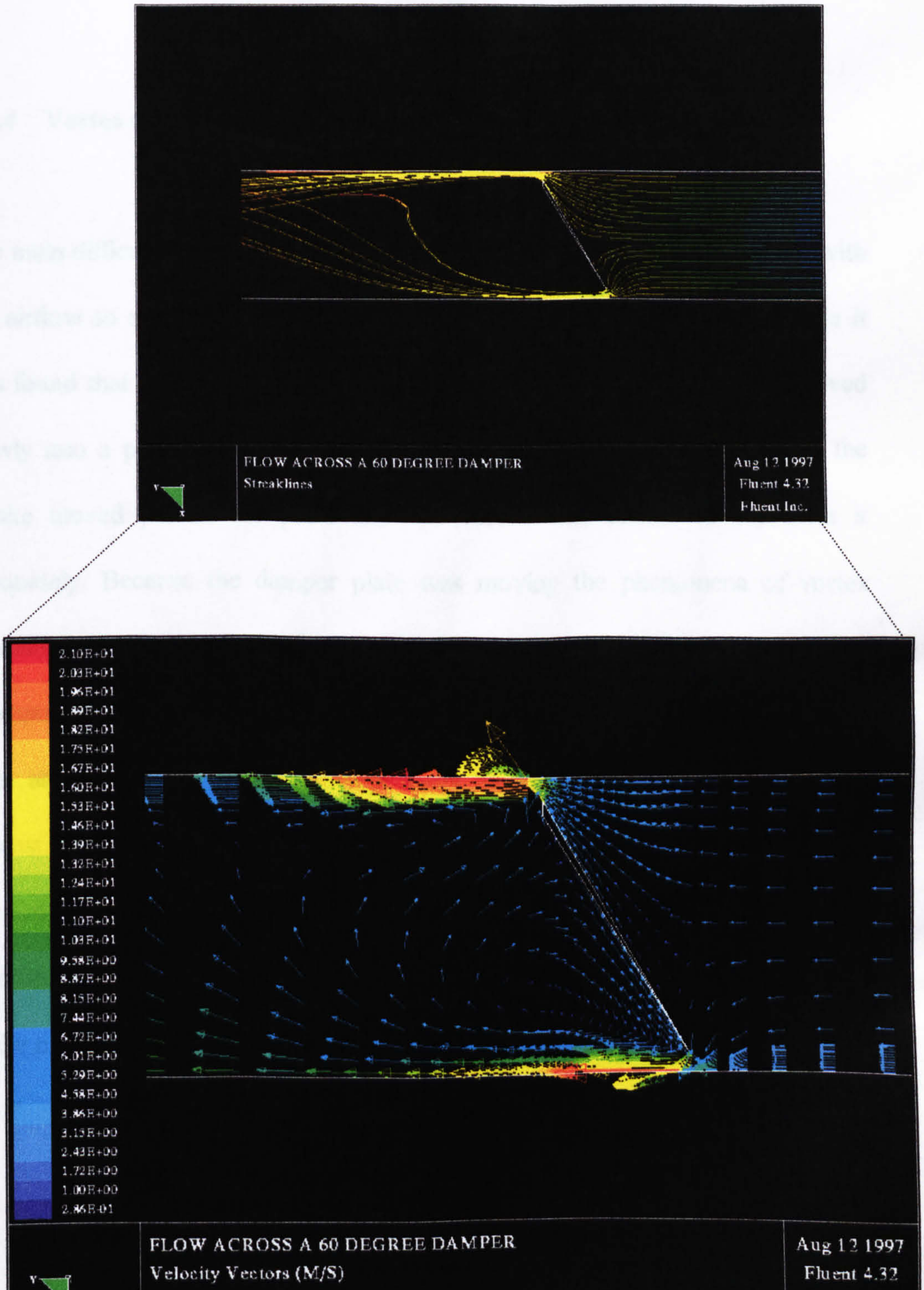


**Figure 6.3** CFD velocity vectors and streaklines over a damper plate.

### 6.2.4 Vortex shedding

The main difficulty of smoke visualisation studies is making the smoke react with the airflow so as a satisfactory result can be obtained. With the damper plate it was found that the best smoke pattern was obtained when the plate was moved slowly into a position where a vortex could be viewed. In other positions the smoke moved passed the plate and the vortex was unable to represent it adequately. Because the damper plate was moving the phenomena of vortex shedding was observed. It can be seen in Plate 6 that a small vortex is seen just downstream from the top edge of the plate. This vortex is shed by the damper plate at a certain angle and is swept away by the flow and dissipated further downstream. Below a certain plate angle the adverse pressure gradient acting on the plate is not high enough to create flow separation. Above this plate angle the pressure gradient does create flow separation and the main flow on the other side of the plate "catches" the vortex and sweeps it along.

## 6.3 CFD flow visualisation

The graphical representation of data obtained by CFD prediction can be given in various forms. These include velocity vectors, streaklines, filled and unfilled contours and X-Y plots.

### 6.3.1 Flow Profile

A useful observation can be performed with a CFD prediction, which is the notification of a developing flow by ensuring a characteristic profile develops as is described in section 5.1 . CFD provides a very useful tool for examining the characteristics and shape of such developed profiles through various obstructions such as damper plates and orifice plates. Figure 6.4 shows the CFD prediction of the flow through a 90° bend and a 30° damper plate. It can be seen that the flow develops into the correct shape profile and that the bend and the damper plate cause severe profile distortions with the flow redeveloping some distance from the duct fitting. Using the colour distribution for the velocity vectors and the velocity contours the changes in flow velocity can also be observed.

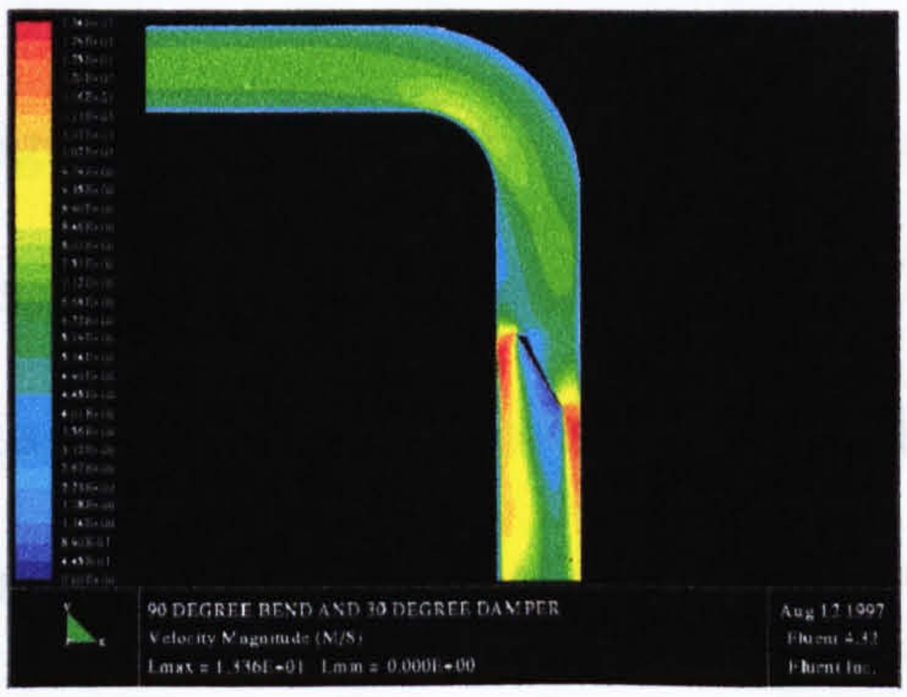


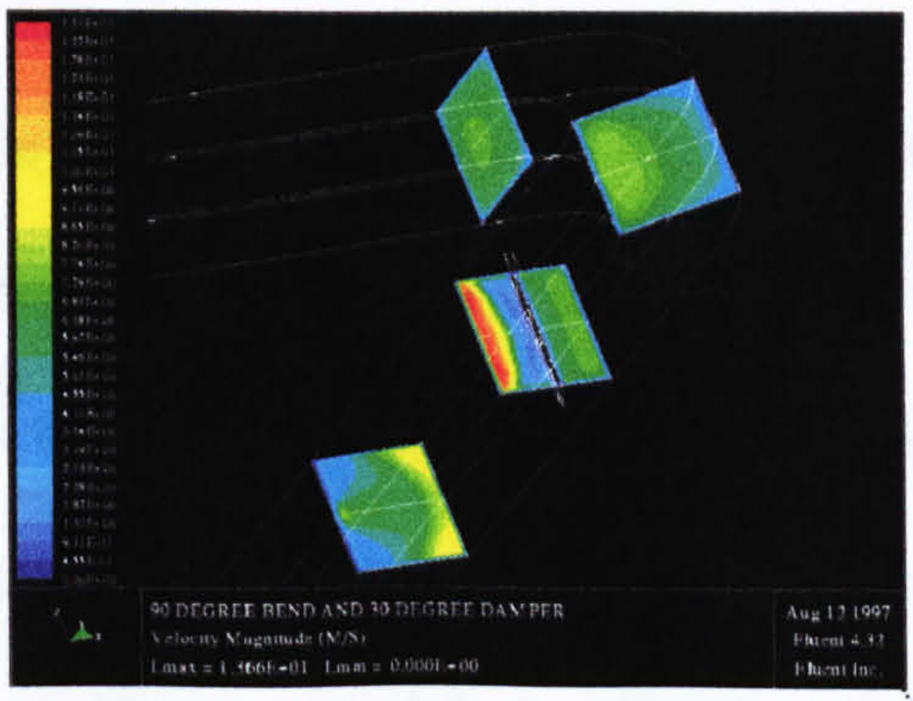


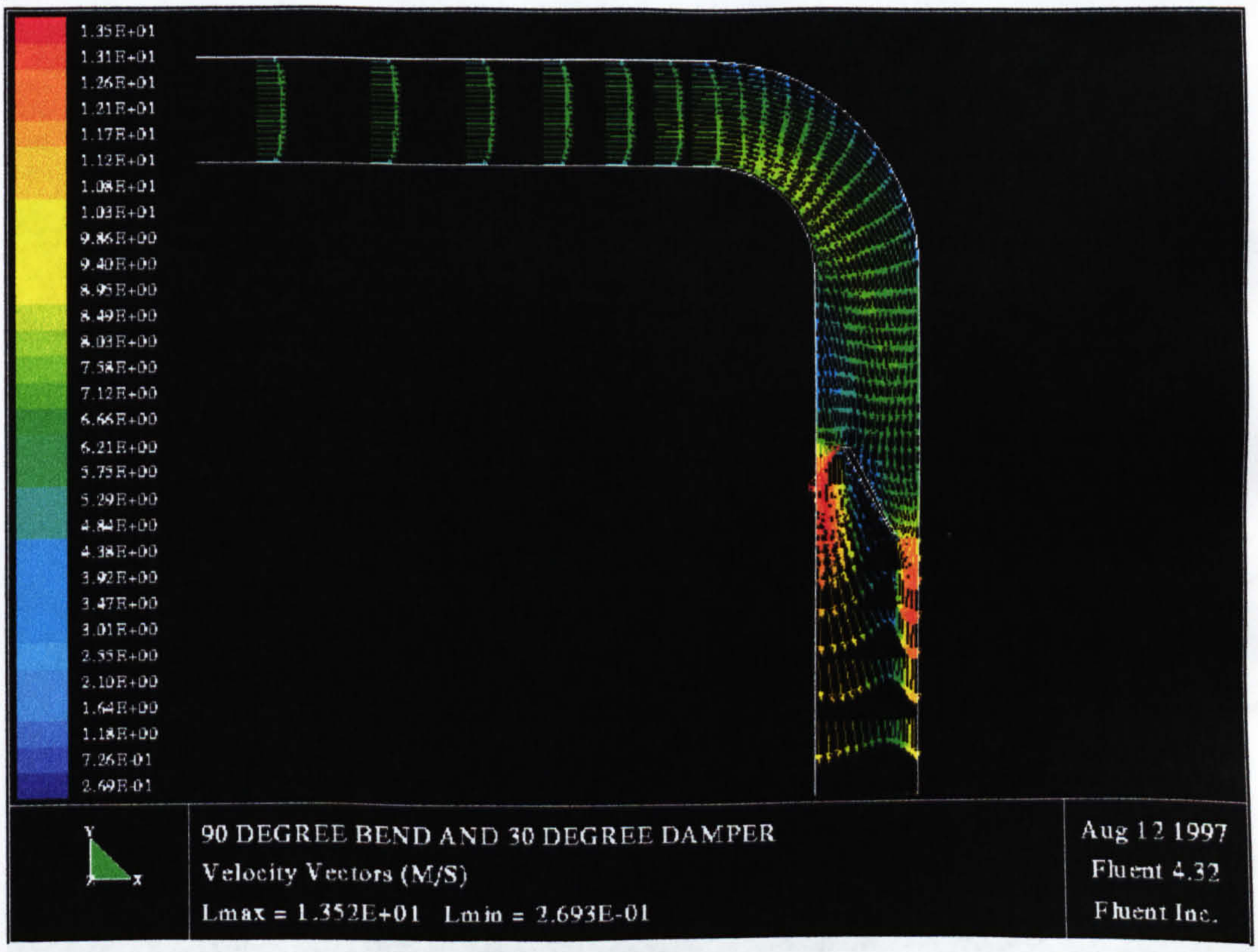


**Figure 6.4** CFD prediction of flow through a 90° bend and a 30° damper plate.

Figure 6.5 shows the flow through the same fitting where streaklines are represented. Streaklines map out the outline of the main flow and can in some cases indicate to areas of interest such as the outline of the large vortex formed on the reverse side of the damper plate. FLUENT has the ability to draw streaklines in slow motion from any point within the model allowing the user to observe the animated drawing.

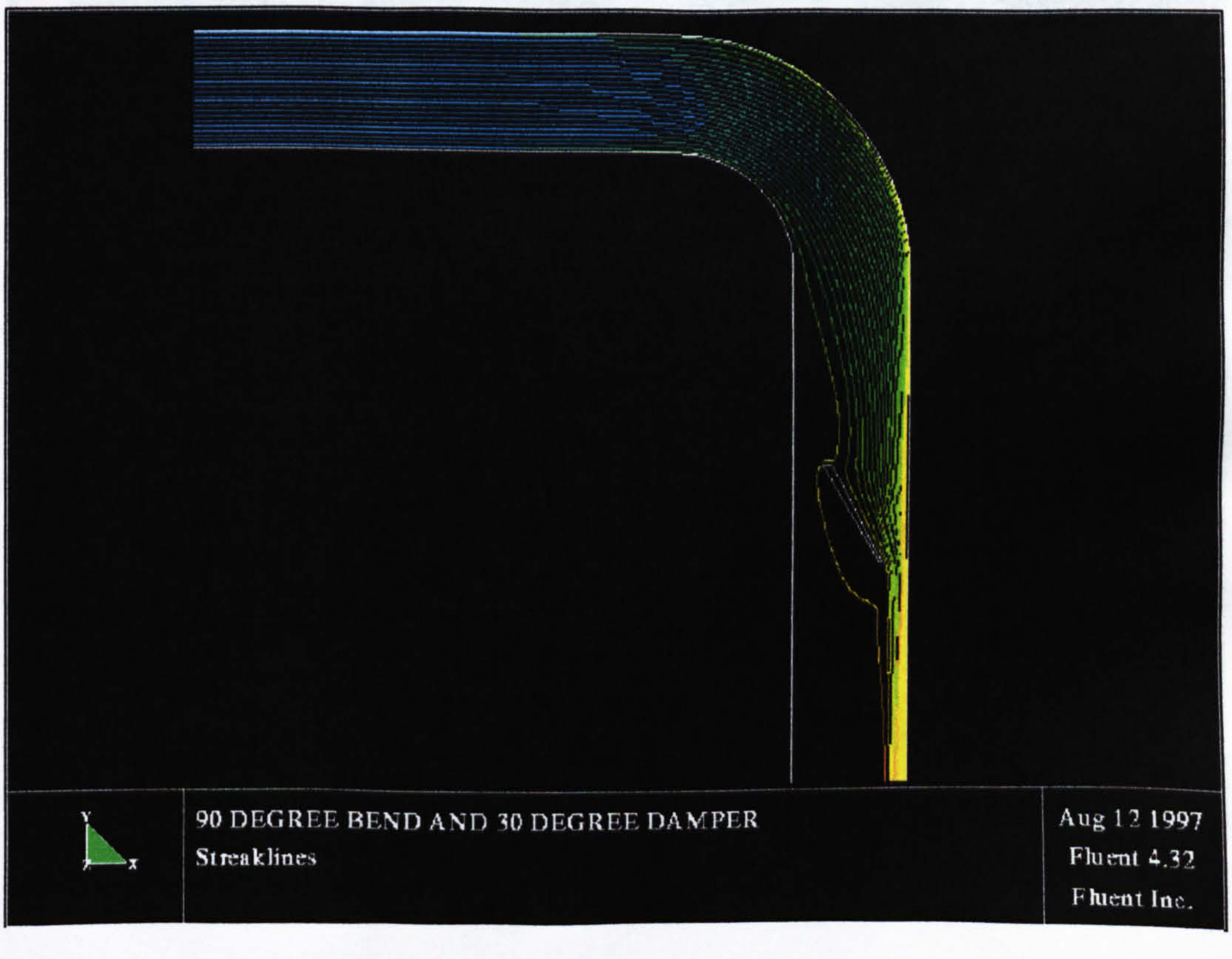


**Figure 6.5** CFD prediction of streaklines through a 90° bend and a 30° damper plate.

Other examples of flow development and redevelopment are shown in Figures 6.6 and 6.7, representing the CFD simulation of flow through an orifice plate and a diverging branch respectively.

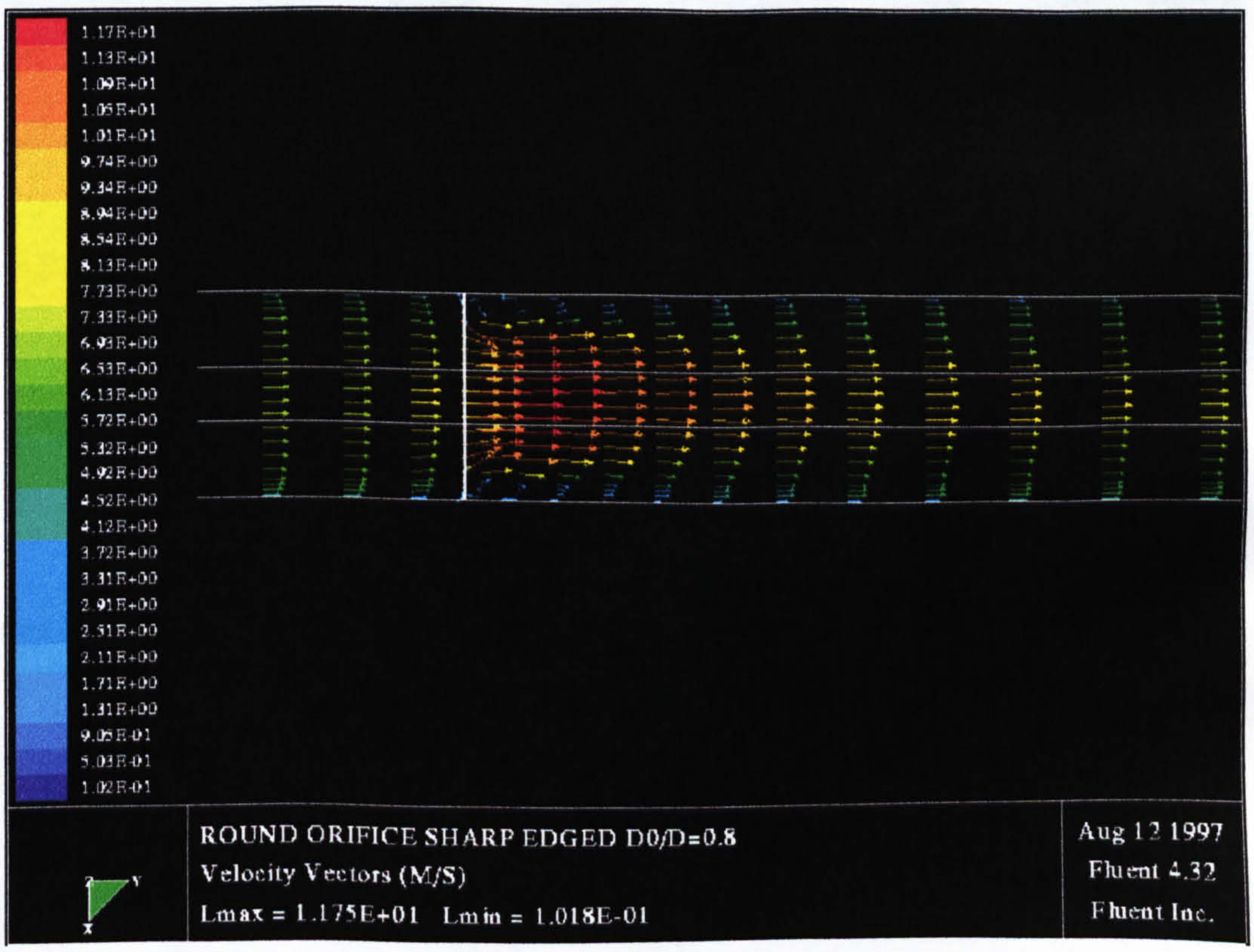


**Figure 6.6** Flow development and redevelopment through an orifice plate as predicted by CFD.

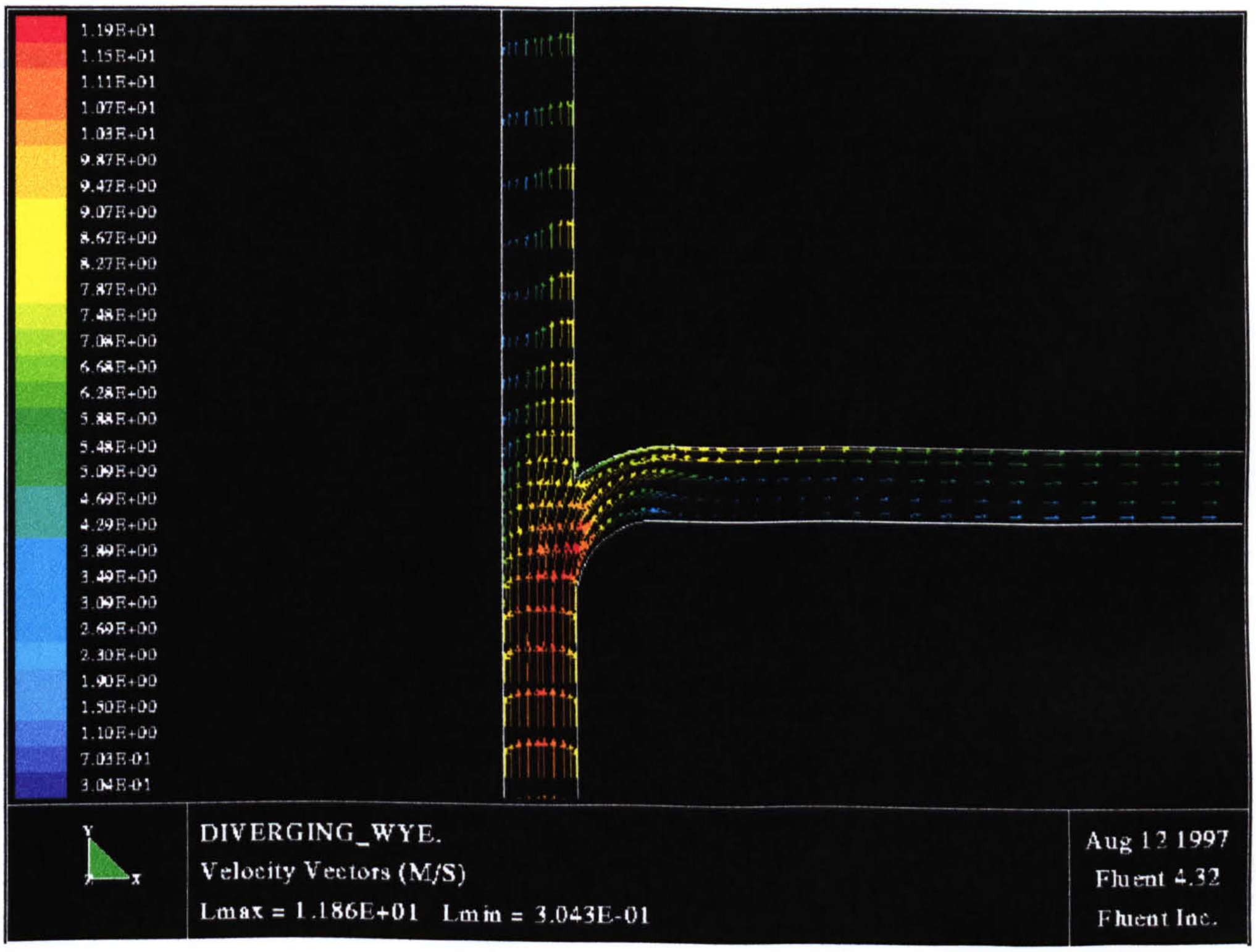


**Figure 6.7** Flow development and redevelopment through a diverging branch as predicted by CFD.

### 6.3.2 Flow separation

One of the most common characteristics of ducted air flows, and one of the most important for flow visualisation is flow separation. As weak flow due to abrupt changes in duct geometry is forced away from a duct wall with adverse pressure

gradients, a vortex can often form. Figures 6.8 to 6.12 show examples of flow separation and vortex formation as predicted by CFD in a variety of duct fittings.

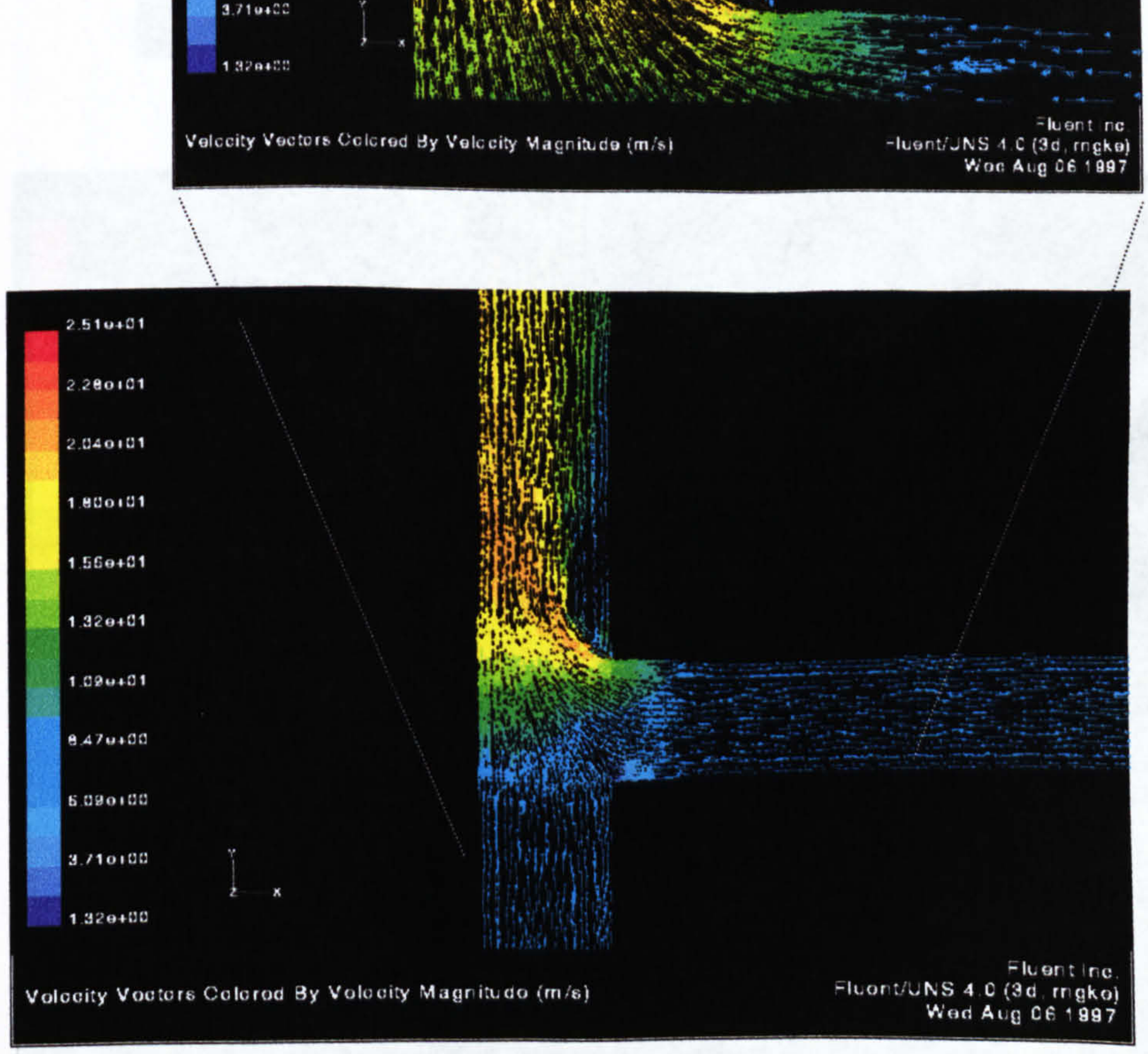


**Figure 6.8** Converging flow showing flow separation as predicted by CFD through a circular cross section T-branch.

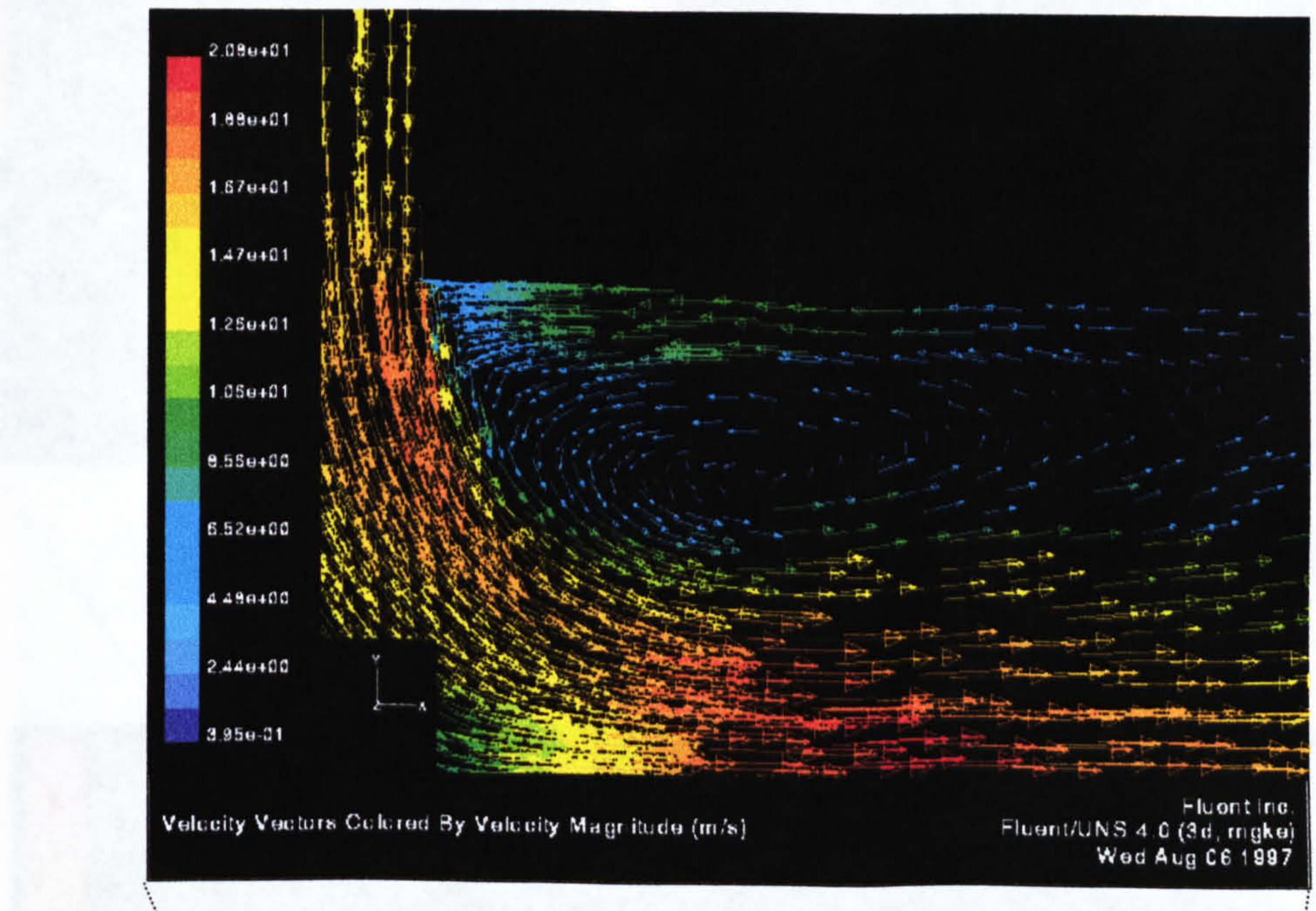


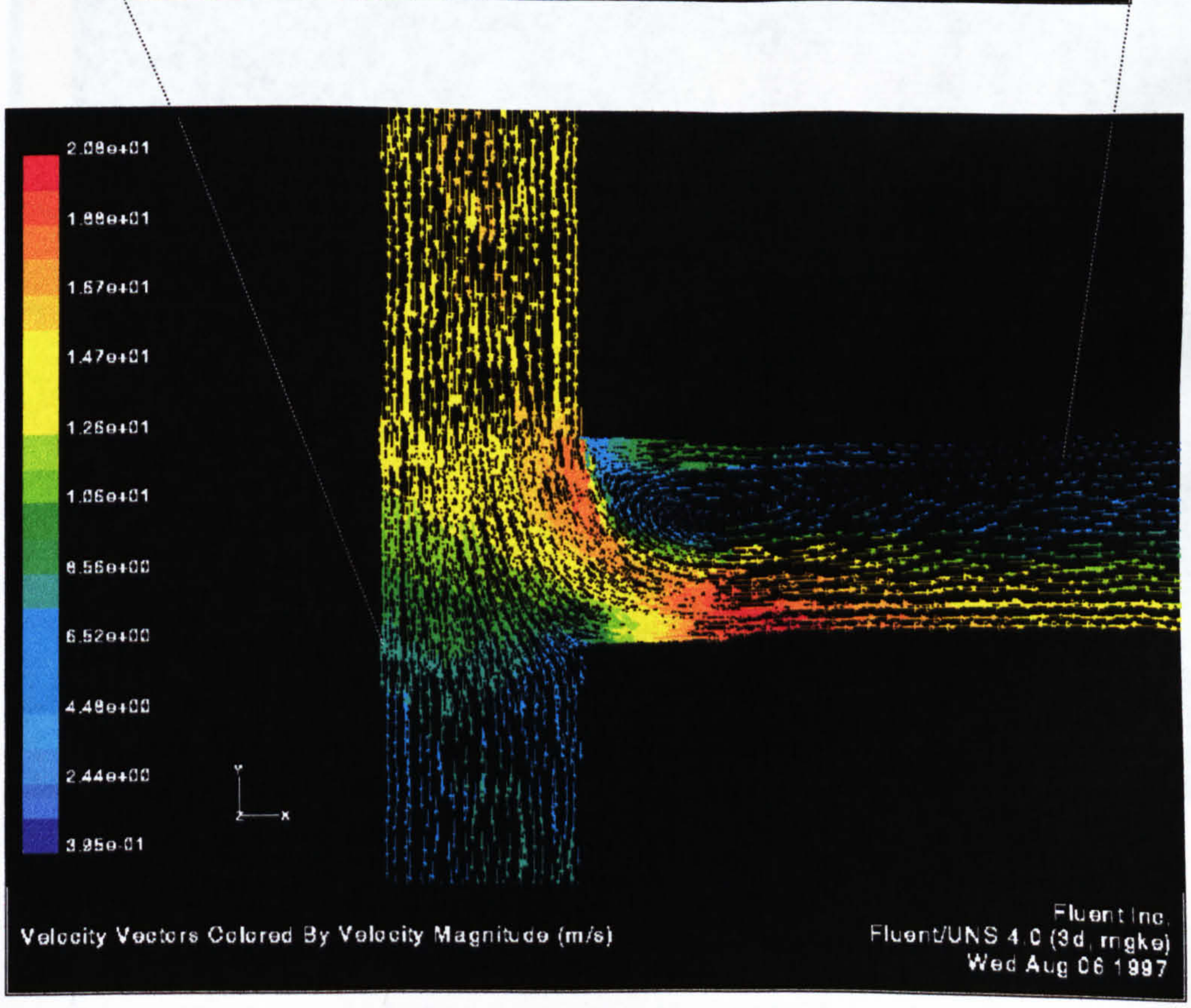


**Figure 6.9** Diverging flow showing flow separation as predicted by CFD through a circular cross section T-branch.

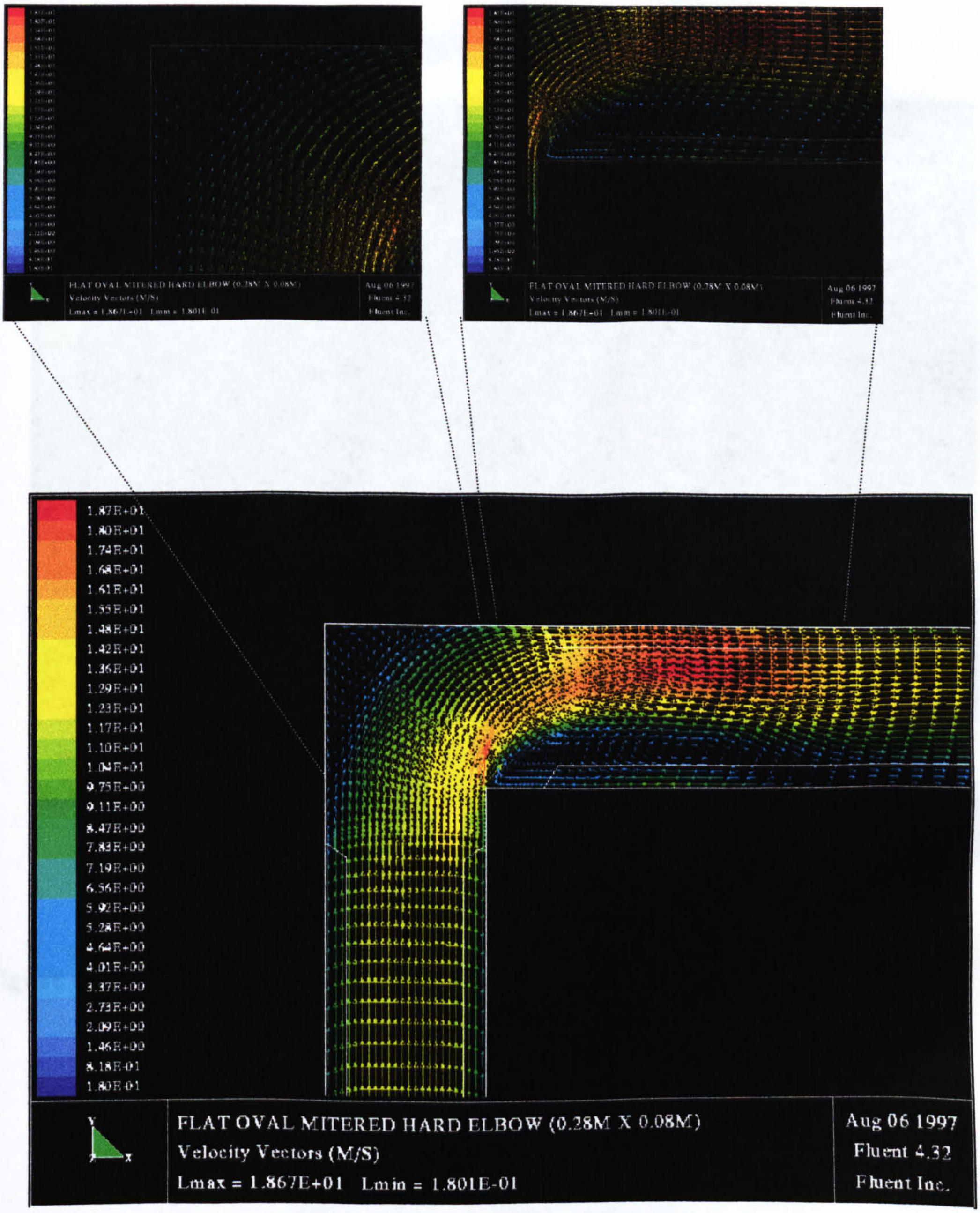


**Figure 6.10** Air flow separation as predicted by CFD through a 90° oval cross section mitre bend.

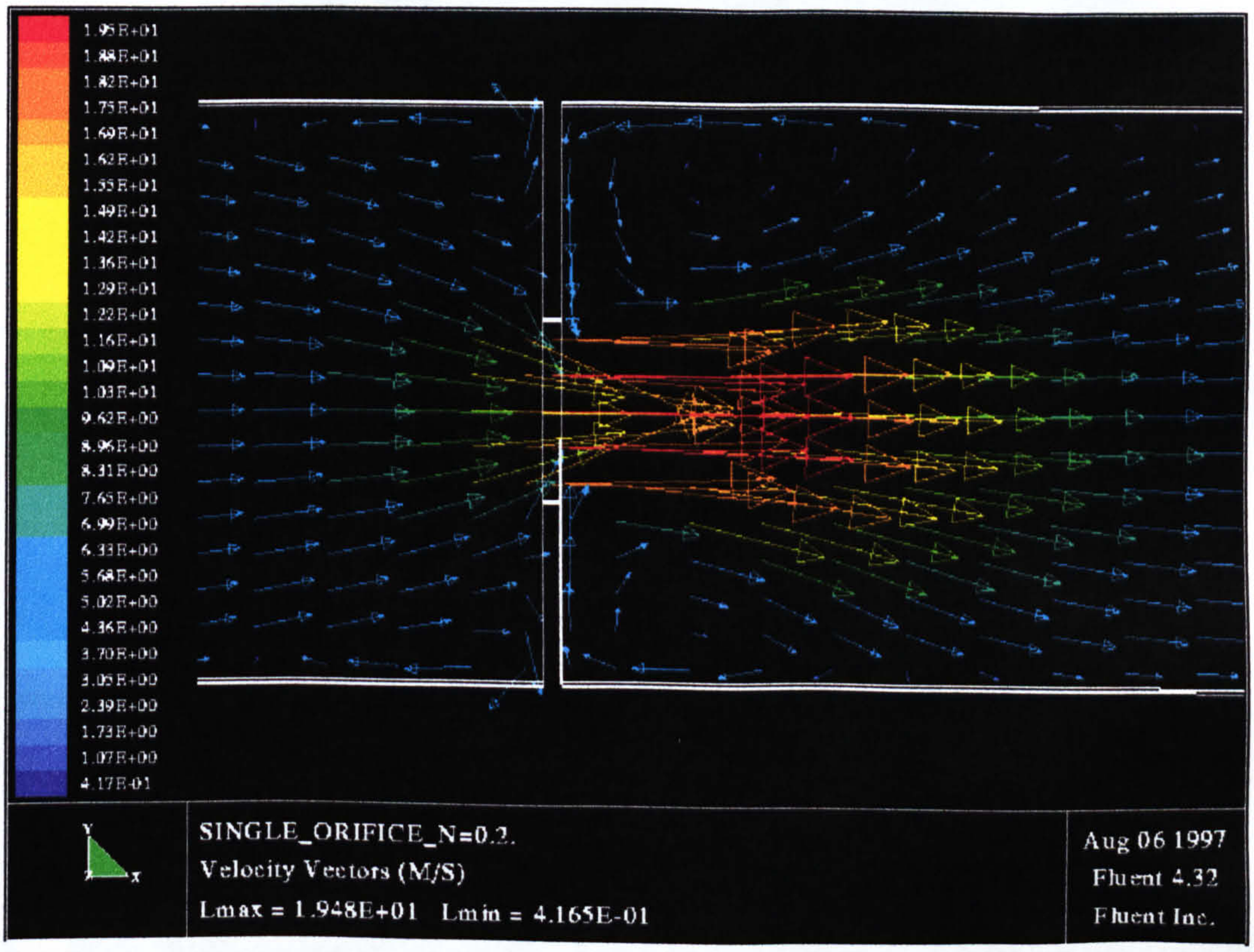


**Figure 6.11** Air flow separation as predicted by CFD through a square cross section single orifice. Free area ratio is 0.2 .

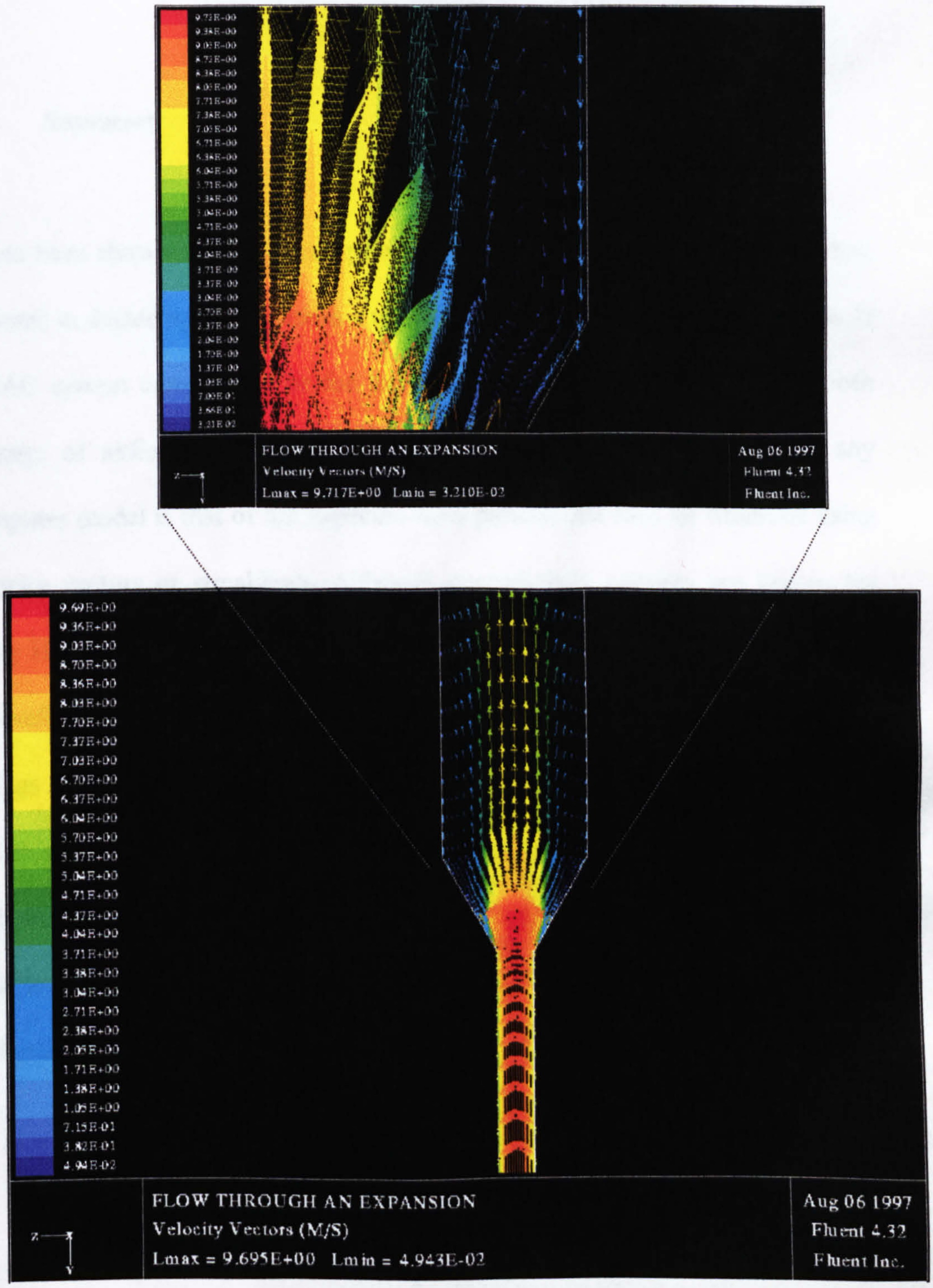


**Figure 6.12** Air flow separation as predicted by CFD through a square cross section expansion. Transition ratio is 4 and expansion angle is 60°.

## 6.4 Summary

It has been shown that CFD can provide a tool for the visualisation of airflow patterns in ducted systems. This is a useful aspect when considering the design of HVAC system components or for the fault finding diagnosis where a smooth passage of airflow is required. It is noted that the first recognition in any computer model is that of the expected flow pattern that may be observed using velocity vectors or streaklines. Although general flow patterns are known for many HVAC duct fittings, the detailed effect flow separation has on flow profile redevelopment is not known. CFD can therefore be applied to more complex duct fittings and in partucular duct fittings in close proximity and there velocity profile can be observed. Although the minimum size of eddy that CFD is able to predict is limited to the smallest size of grid cell, it has been shown that CFD can predict flow separation very well. The future application for flow visualisation using CFD will make a significant reduction in experimental tests.

# Chapter 7

# Conclusions and Discussion

# 7.0 Conclusions and discussion

This chapter presents the findings concluded from this investigation.

## 7.1 Conclusions of tracer-gas application

The implementation of tracer-gas for the use of measuring mean air-flow velocity in HVAC ducted systems has yielded the following conclusions :

i ). Various tracer-gas methods exist, however it has been shown that the most simplest to apply to experimental tests is the constant injection method. Provided that adequate tracer-gas mixing exists and proper duct joint sealing is employed, then results obtained from experimental tests of a wide range of duct fittings have been shown to give accurate results. Other tracer-gas methods such as pulse injection and concentration decay are more difficult to control and evidently introduce errors into the calculation that are not found in constant concentration.

ii ). The correct and precise application of constant injection tracer-gas has been shown to reduce errors in calculations to a minimum and k-factors

obtained using this experimental technique have been found to be on average 20 % lower than k-factors given in reference manuals such as ASHRAE and CIBSE. This difference is attributed to the overestimation of velocity pressure losses found in the pre-mentioned reference manuals leading to overestimation of HVAC system pressure loss and therefore an increase in system energy wastage.

iii ). It has been shown that tracer-gas methods for measuring duct mean air-velocity can be applied easily to a range of experimental tests and the results used to justify predictions obtained using modern computational techniques. Although the constant use of tracer-gas methods in a wide scale investigation without the use of prediction methods in conjunction, can be expensive, there are many advantages of using injection techniques rather than more conventional methods of measuring air-flow velocity such as the Pitot-static tube, vane anemometers and hot wire methods. These advantages include the air flow not being restricted or obstructed by the measuring device. With adequate tracer-gas and air mixing the calculation is taken over the entire duct in the experiment and not just at a single point. The tracer-gas method may actually prove not to be as expensive as using devices such as venturi meters and the laser-Doppler technique because these methods are not as flexible when using them on different duct cross-sections and aspect ratios.

iv ). Experimental studies have shown that adequate tracer-gas / air mixing can be achieved with a suitable injection array and that duct lengths can be kept to a minimum provided that sufficient duct lengths are used to allow for air flow development and redevelopment. This was achieved with duct lengths between 10 and 20 duct diameters.

v ). Tests on circular cross section ducts and various aspect ratio rectangular ducts have shown that there is on average a 20 % drop in k-factor when a comparison is made between the Pitot-static tube method and the tracer-gas technique. Results taken using the tracer-gas technique compare very well with computational fluid dynamics whilst experimental results obtained using the Pitot-static tube compare very well with k-factors given in reference manuals such as CIBSE and ASHRAE.

vi ). Sulphur-hexafluoride has been used as a tracer-gas in obtaining the mean air flow velocity in ducts and the pressure loss across various HVAC duct fittings such as branches, bends, obstructions, transitions, inlets and outlets. Sf6 has proven to be a very suitable tracer allowing non-toxic injection and sampling without posing a threat to equipment or the environment.

vii ). Sulphur-hexafluoride has also been used as an adequate tracer to determine the air-tightness of duct system joints. However proper sealing ensured that the errors due to leakage were negligible.

## 7.2 Conclusions of CFD application

The application of computational fluid dynamics for the prediction of pressure loss in HVAC duct fittings produced the following conclusions :

i ). It has been shown that CFD can be applied successfully to the prediction of pressure loss through various HVAC duct fittings. In comparison with identical duct fittings tested for pressure loss in the laboratory, CFD prediction is shown to be on average 94 % in agreement with results obtained using the tracer-gas method.

ii ). CFD provides a useful tool for the design of duct fittings and once correlation with experimental results has been achieved, CFD can easily be used to refine ductwork design and predict the effects of design alterations with good accuracy.The many different computational models, discretisation schemes and

solution controls available in CFD software such as FLUENT provides the scope for a wide range of HVAC system components to be modelled.

iii ). Computational fluid dynamics has been shown to provide various ways of presenting pressure loss and flow visualisation in ducted flows. Velocity vectors predicted using CFD show to be in agreement with experimental visualisation techniques such as smoke visualisation. Important flow characteristics such as vortex formation and flow separation have been predicted successfully with CFD.

iv ). Other air flow characteristics such as air flow rate ratio and extraction efficiency for ducted inlets for extraction hoods, have also been predicted using CFD. It has been shown that when compared to experimental results the CFD simulations are in 80 % agreement.

## 7.3 Other conclusions

When CFD is applied to other areas important to ventilation such as refrigeration then the following conclusions are made :

i ). The pressure loss through evaporator and condenser coils plays an important role in the performance of heat pump systems used in refrigeration. It has been shown that CFD can be a useful tool when predicting compressible two-phase and single-phase flow through different types of coil using various refrigerants. The simulations show that there is a much higher pressure loss when using more modern environmentally friendly refrigerant blends such as R407B as opposed from the older less environmentally friendly refrigerants such as R717 (Ammonia). R407B is a blend of Difluoromethane, Pentafluoroethane and Tetrafluoroethane. When these predictions are compared with theoretical analysis it is found that CFD is 16 % more accurate at predicting flow through an S-shaped coil than predicting flow through a spiral coil. It is also shown that CFD is 25 % more efficient at predicting single phase flow than predicting two-phase flow through coils.

ii ). The coefficient of performance (COP) of ejectors in heat pump systems such as the combined ejector absorption cycle are crucial to the efficiency of the refrigeration process. CFD can be used to predict the flow of refrigerant through the ejector and an analysis of the coefficient of performance can be made. It is shown that CFD can predict the flow under a wide range of ejector operating conditions, whether the ejector is generally working at a high pressure ( e.g. 18 bar generator pressure ) or working at low pressure ( e.g. 0.5

bar generator pressure ). CFD simulations show that ejectors with a high COP produce a strong positive entrainment through the evaporator whilst ejectors with a low COP may have back pressure in the ejector diffuser causing a weak negative entrainment through the evaporator.

iii ). CFD prediction has been compared with the experimental analysis of low pressure ejectors and have been shown to be in 87 % agreement and simulations show that low pressure ejectors are much more unstable and geometry dependant than high pressure ejectors. It has been shown that CFD can be used to optimise the ejector operating conditions with respect to COP. CFD has also been used to observe the flow through high pressure ejectors with different refrigerants, and nozzle designs and orientations. The COP has been found to reduce by up to 40 % when the nozzle is moved further inside the ejector chamber.

## 7.4 Further work

This investigation has shown the wide scope for which CFD prediction can be applied to different areas of ventilation and refrigeration. In order to justify further the findings reported in this investigation more research is needed in the following areas :

- The relationship between predicted pressure loss and experimentally derived pressure loss may be made more clearer with a comparison of a wider range of duct fittings individually and in interaction. A more detailed investigation of variations in geometric shape and perhaps material type of duct fittings should also be undertaken.

- With the main focus of this investigation including the area of ventilation, perhaps a more experimentally orientated study of the extraction performance of ventilation hoods can be made involving the extraction of steam, chemical pollutants and dust, as this is often important to industry.

- Some interesting results have been discovered when a comparison between CFD prediction and some areas of refrigeration has been made. However it is necessary to understand the limits to which CFD can be applied to this type of prediction. A much more detailed investigation is required with a wider comparison with experimental results.

- The flexibility of the FLUENT CFD software will allow a greater variability in simulations with the effect of changing the computational model and using different discretisation schemes. It is also possible to incorporate the use of

different grid topologies and hybrid schemes for the same geometry giving a better view of the optimum grid structure to use.

- With the advancement of computer technology and the importance of CFD prediction becoming more widely applicable, a detailed comparison of similar geometric models using more than one type of CFD software code could be made. CFD software codes that are available today include FLOW3D, PHEONIX and FLOWVENT. Computational simulations may be improved with the introduction of other pre-processors such as AutoCAD.

The importance of this work is such that the investigation of pressure losses in HVAC system components is ongoing and being carried out by the author with the recently awarded contract by ASHRAE. This work is being undertaken at the School of the Built Environment headed by Professor S. B. Riffat at the University of Nottingham.

# Appendix 1

## Experimental results and graphical analysis of k-factor data

# Appendix 1 Experimental results and graphical analysis of k-factor data

This section includes experimental data for tested duct fittings. The graphs show data obtained using the Pitot-static tube method and the tracer-gas method for measuring duct mean velocity. The results are regressed to obtain the best fit value for the loss coefficient.

## 1.1 Rectangle 90° smooth bend

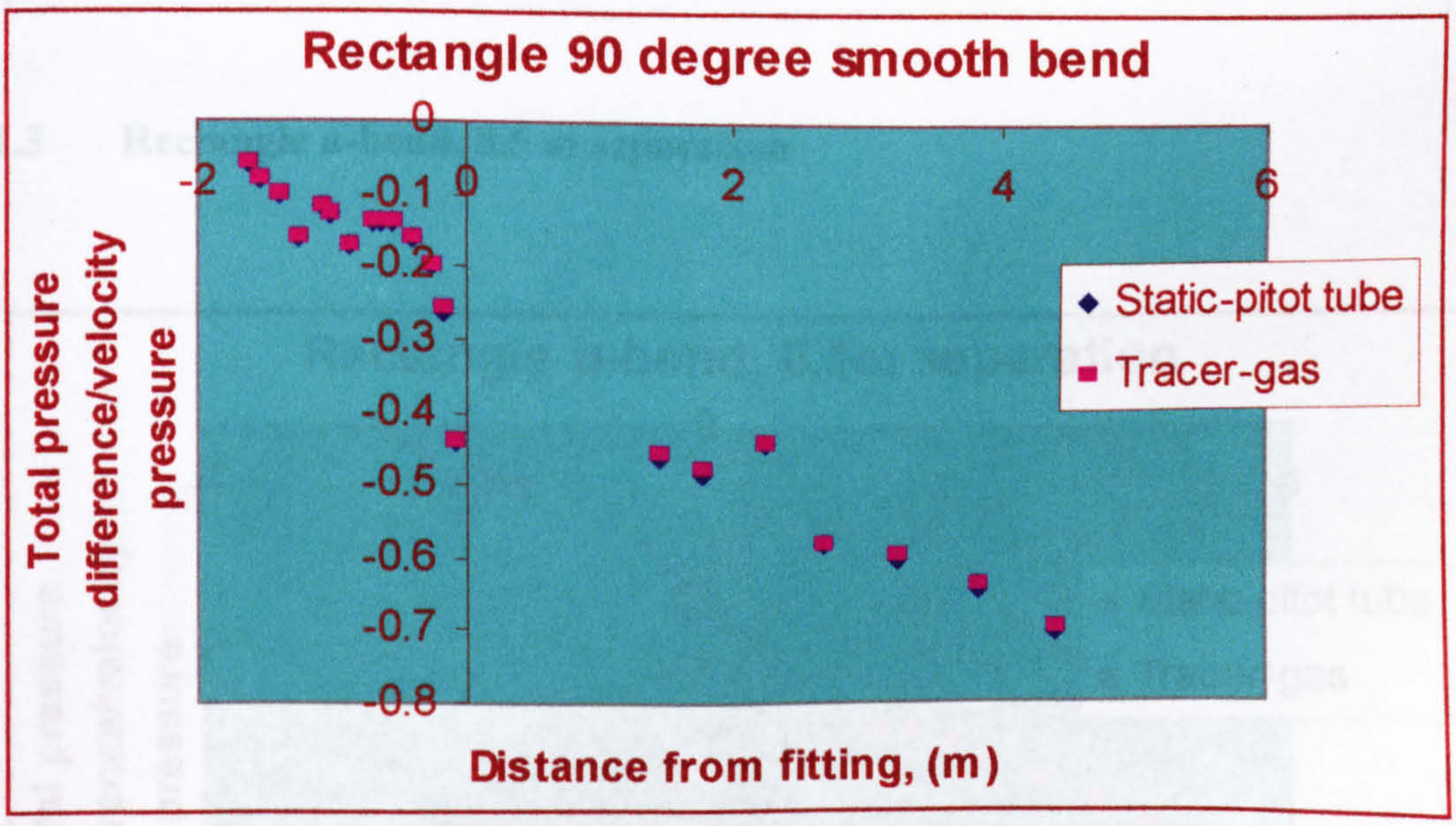

## 1.2 Rectangle u-bend, no separation

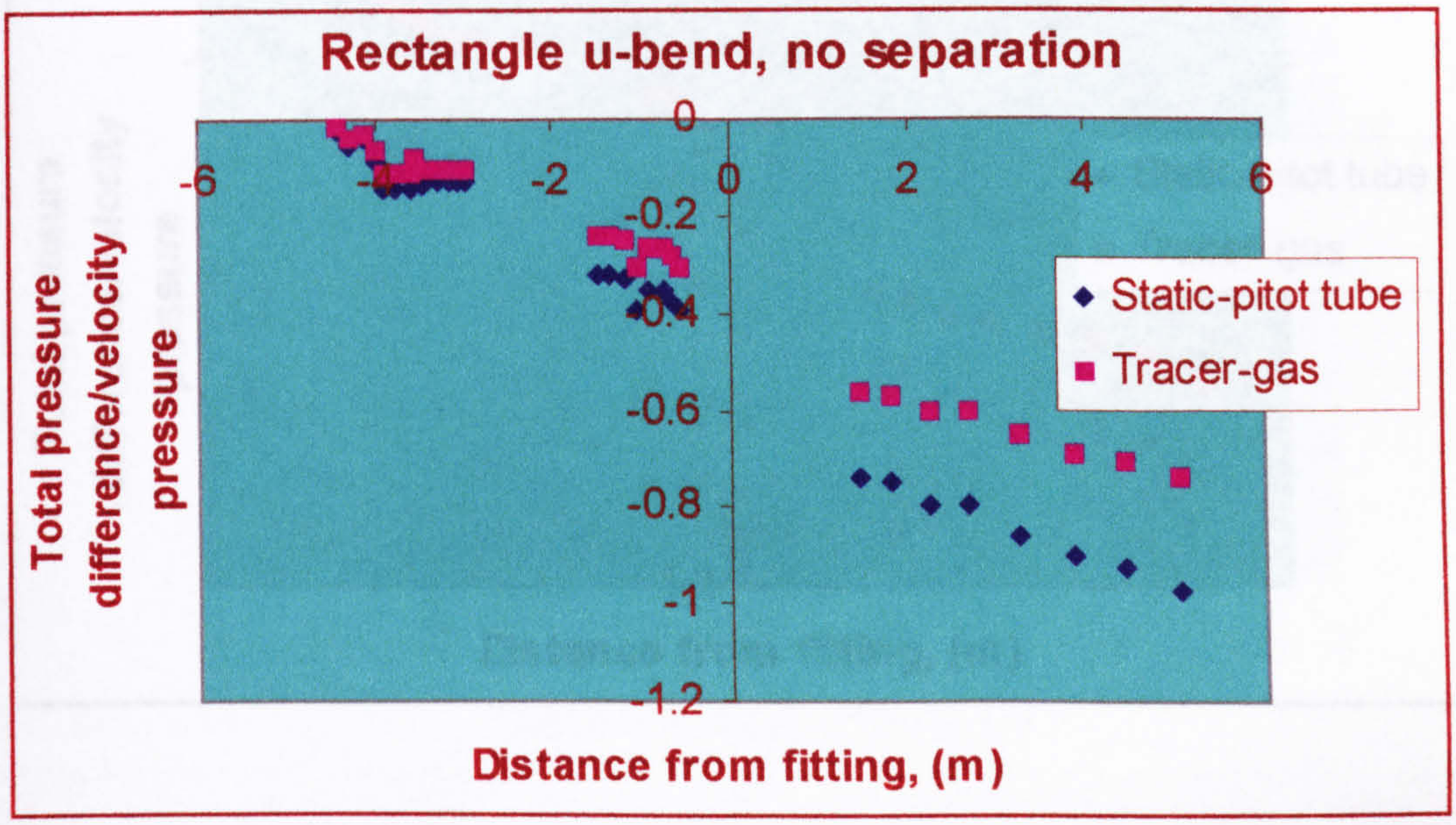


## 1.3 Rectangle u-bend, 0.5 m separation

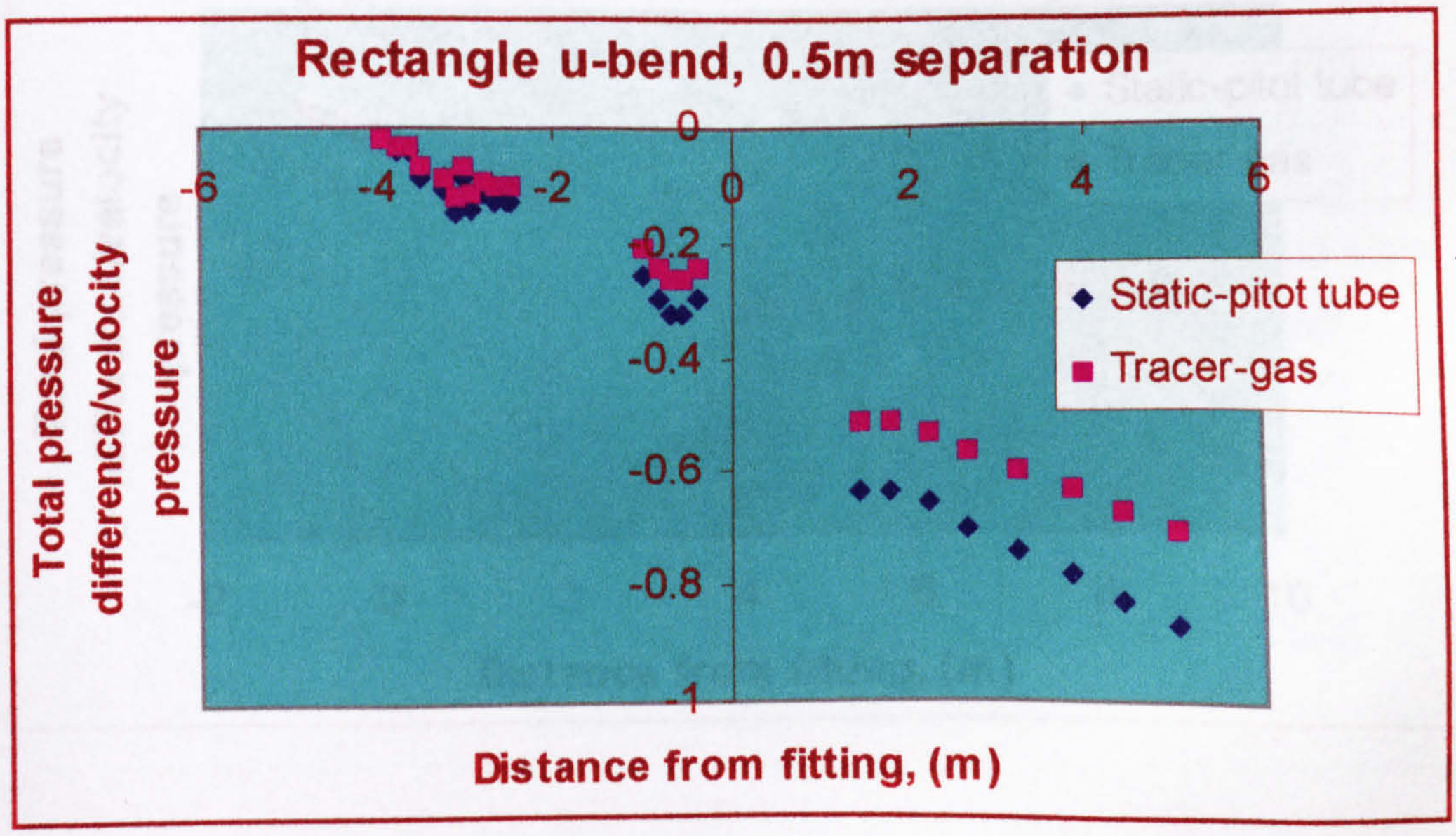

## 1.4 Rectangle u-bend, 1.2 m separation

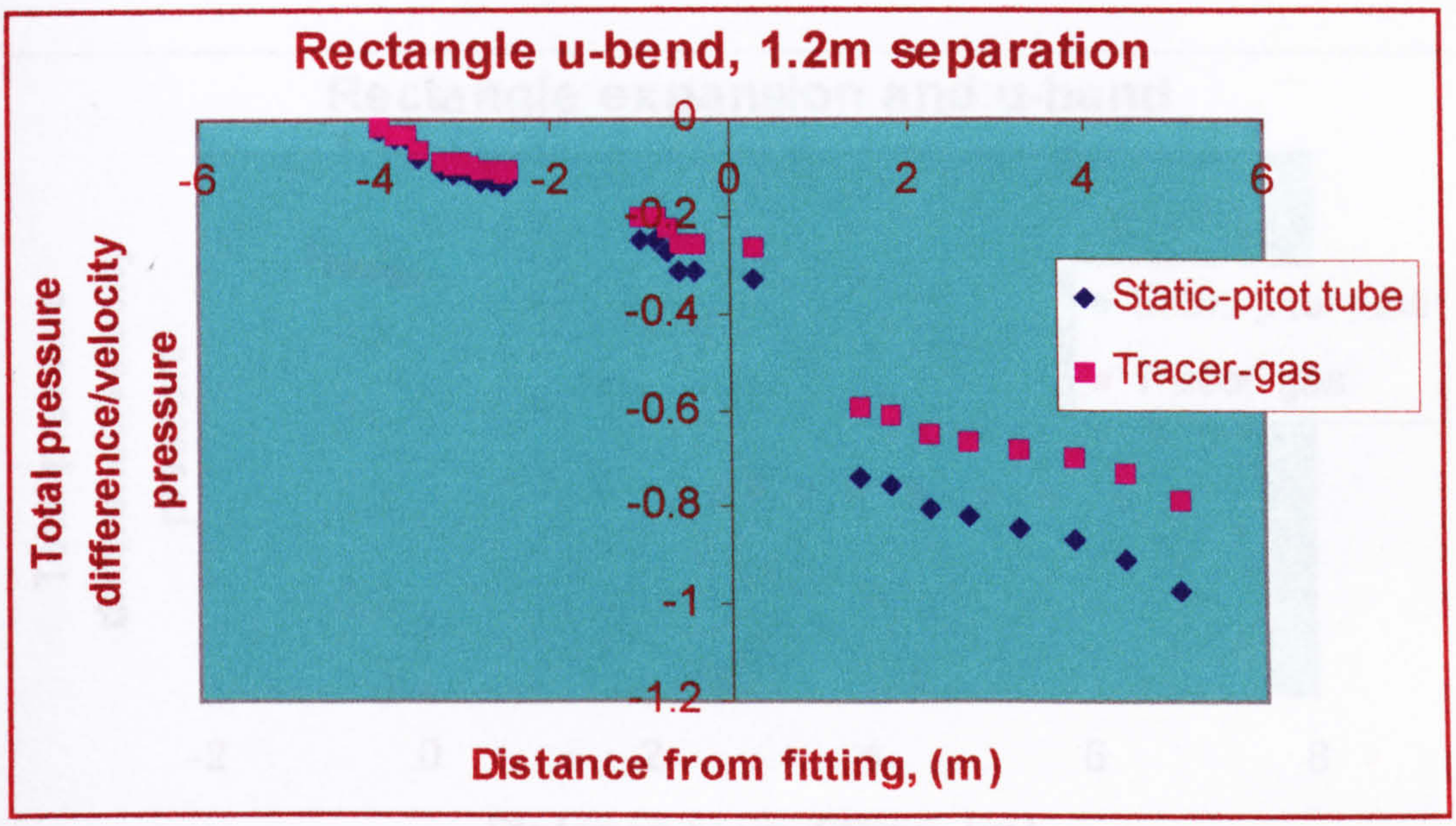


## 1.5 Rectangle expansion

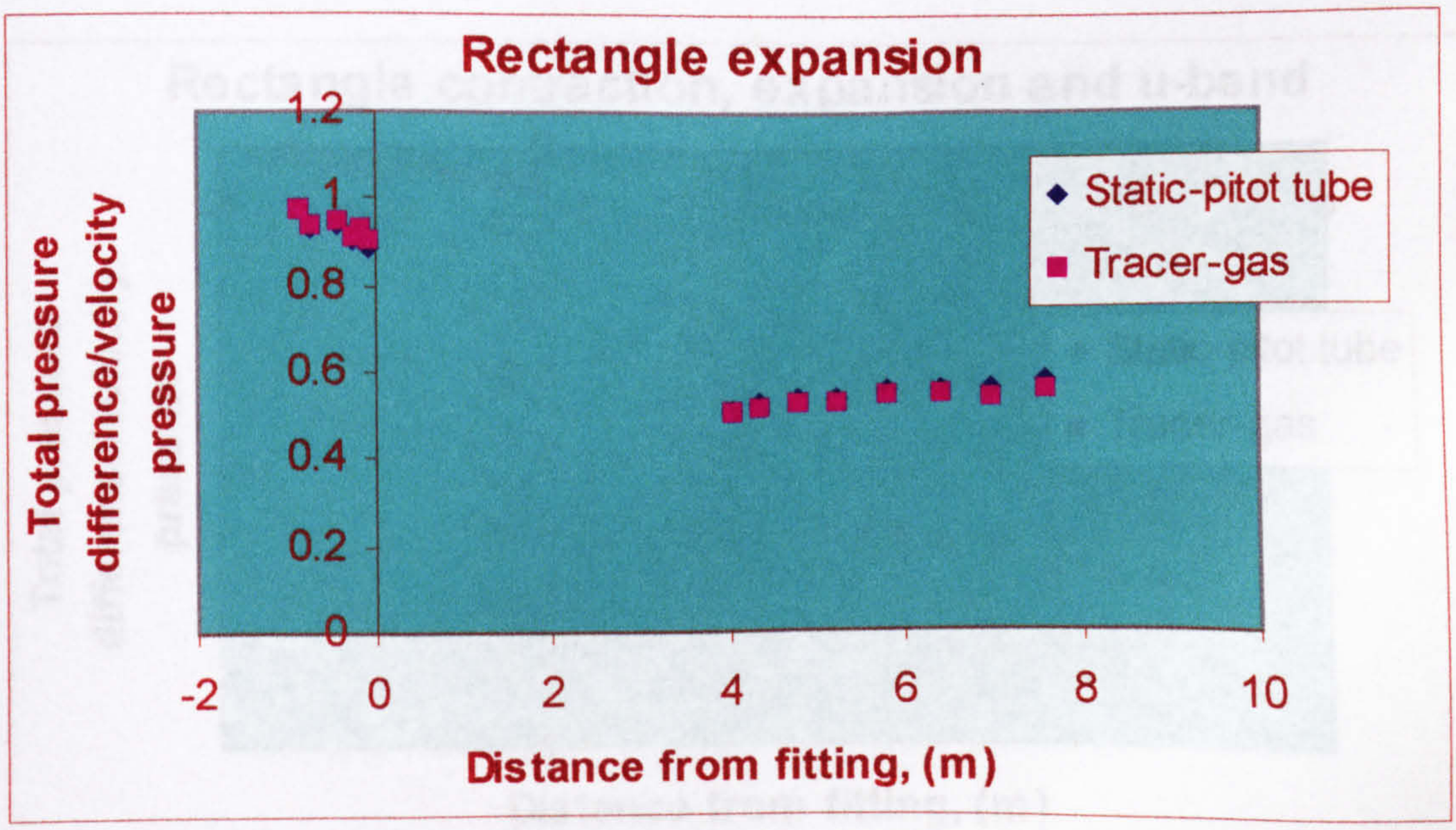

## 1.6 Rectangle expansion and u-bend

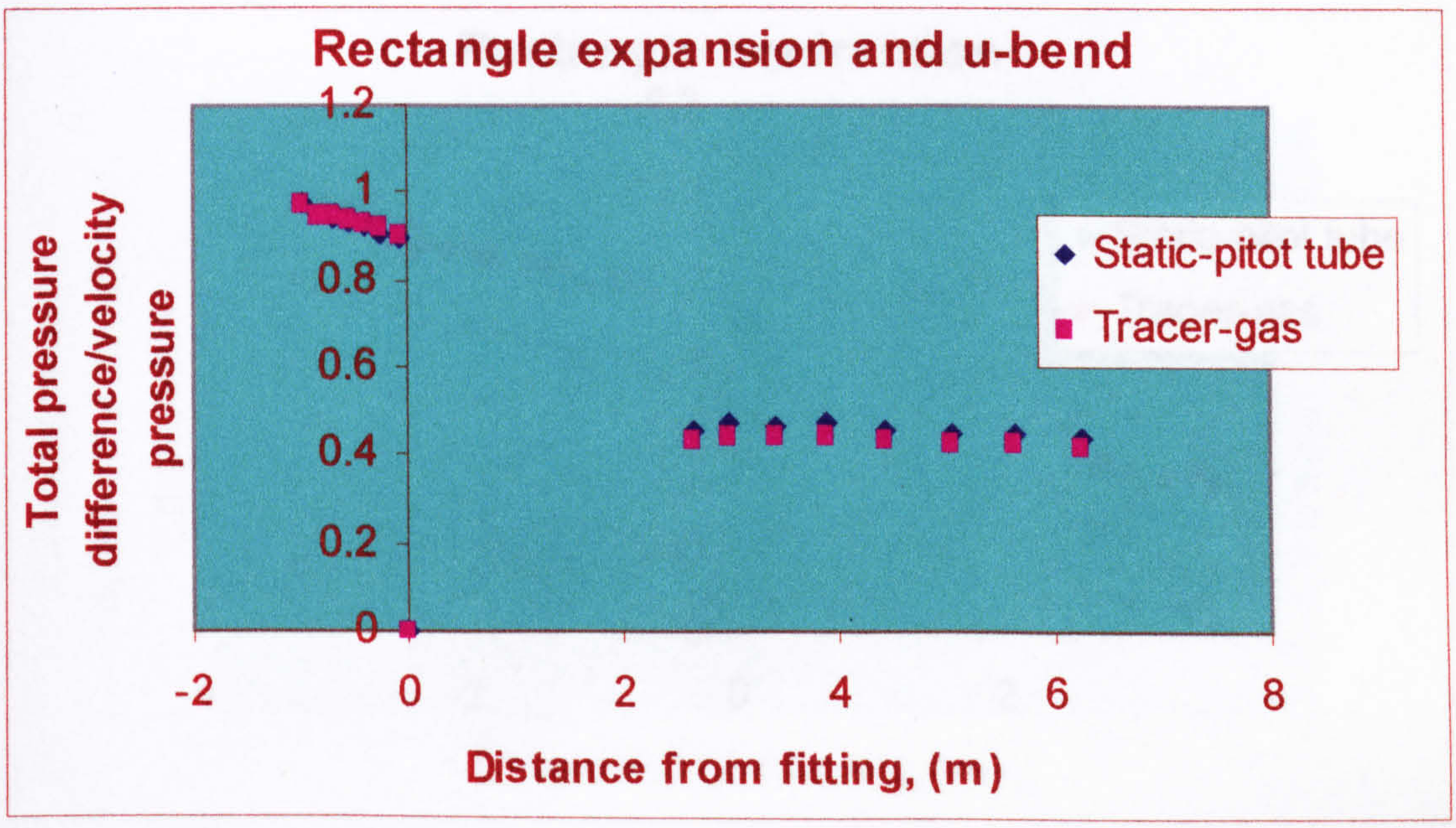


## 1.7 Rectangle contraction, expansion and u-bend

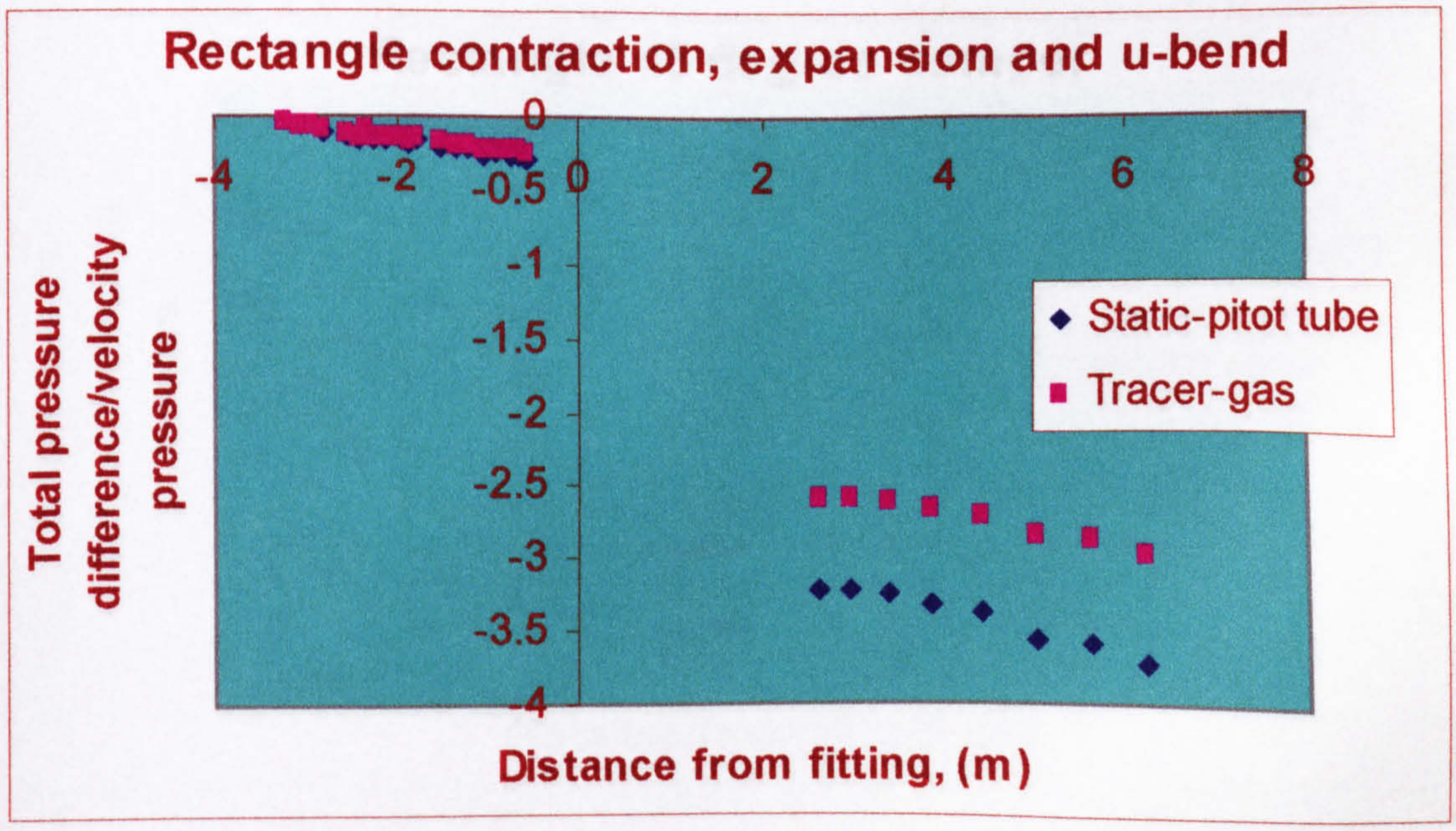

## 1.8 Rectangle contraction

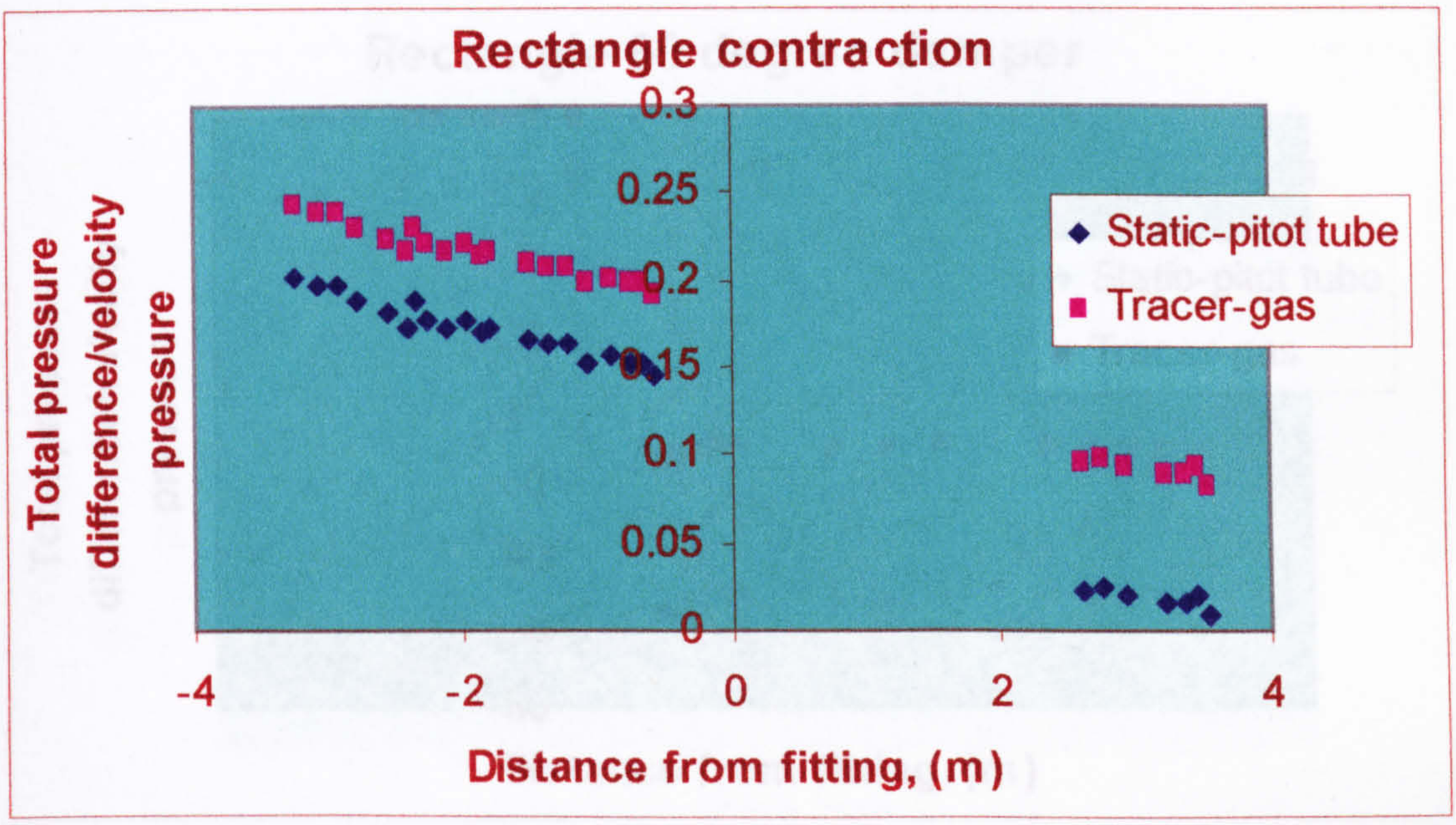


## 1.9 Rectangle 45° damper

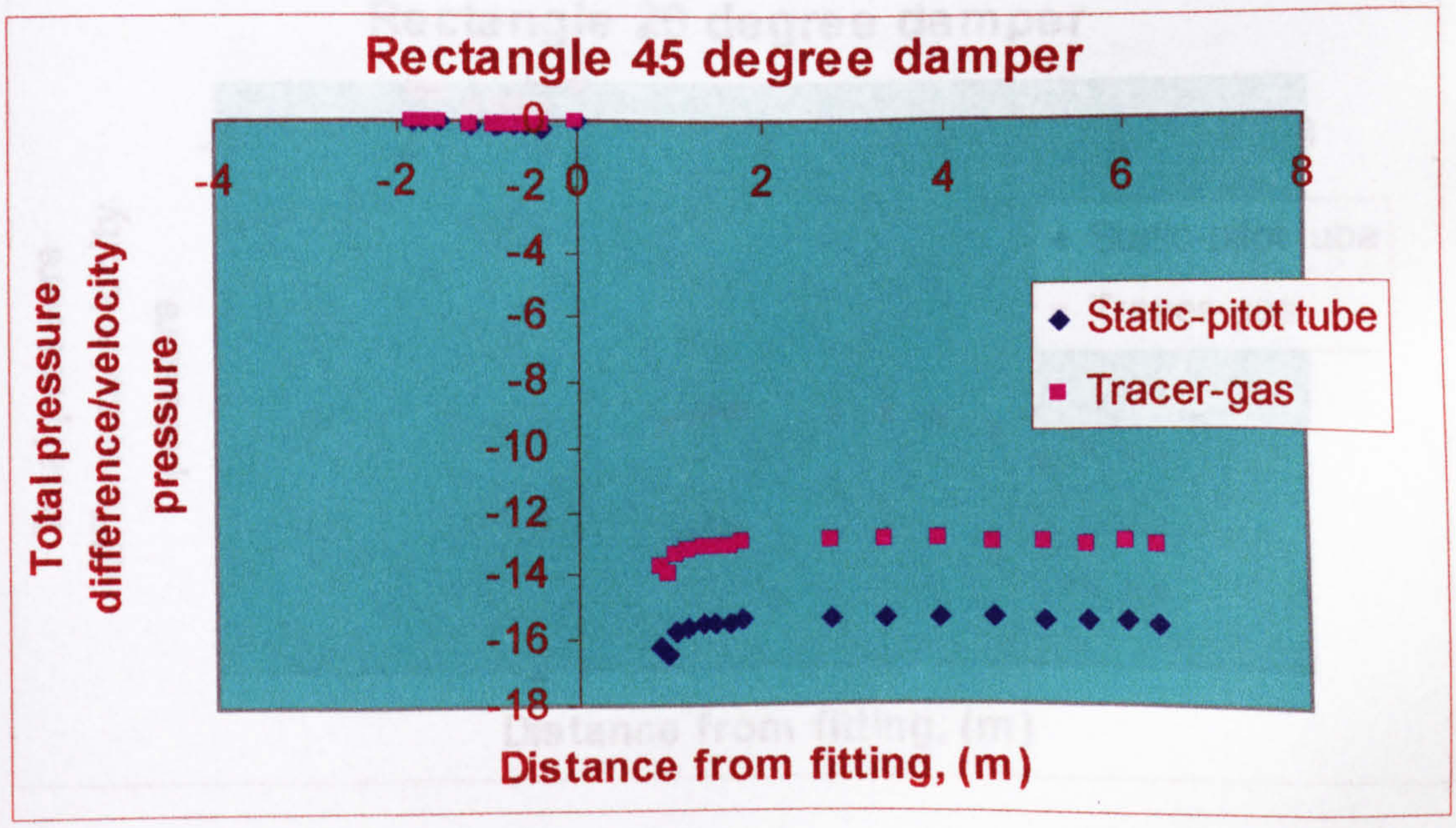

## 1.10 Rectangle 60° damper

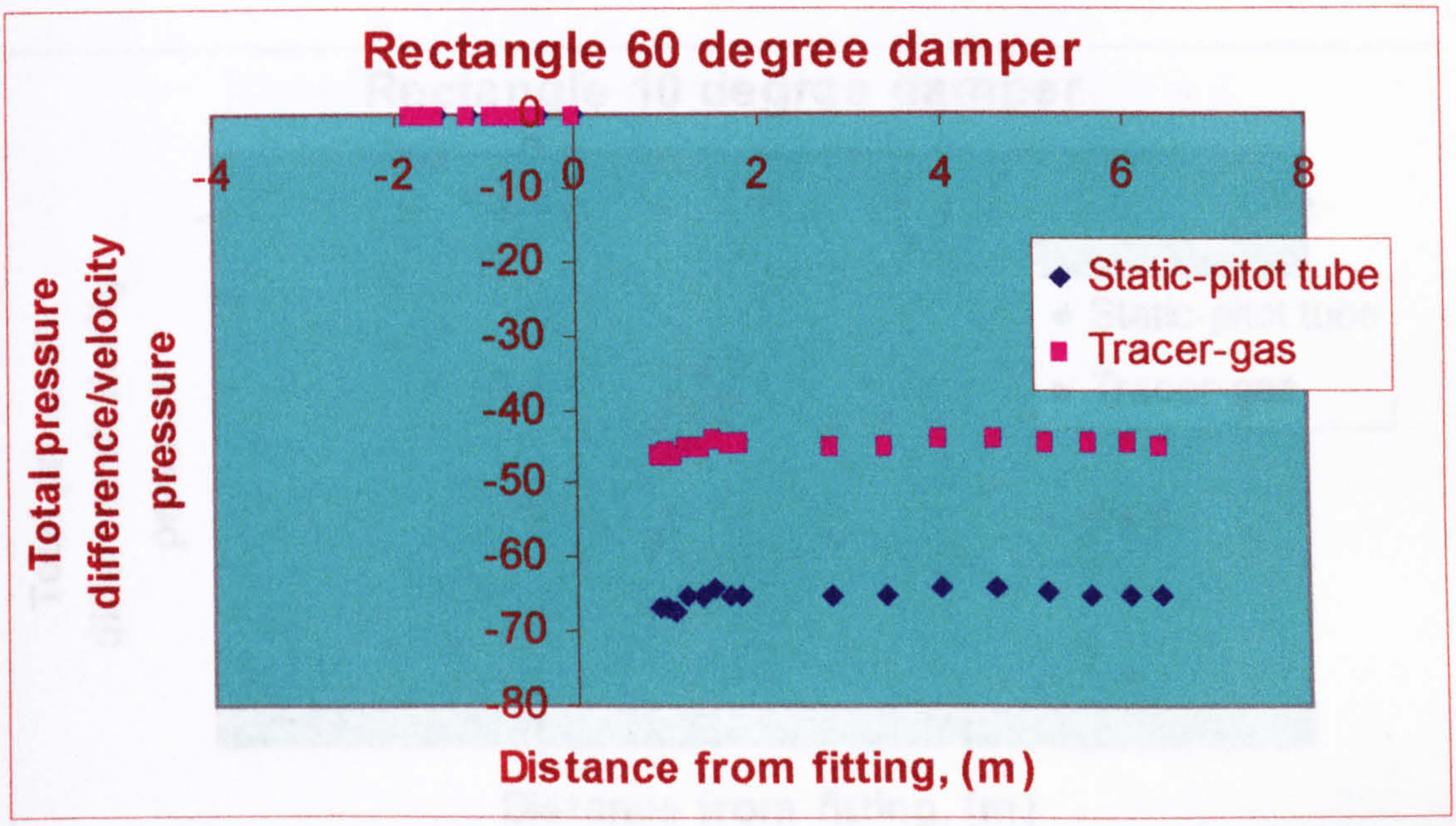


## 1.11 Rectangle 20° damper

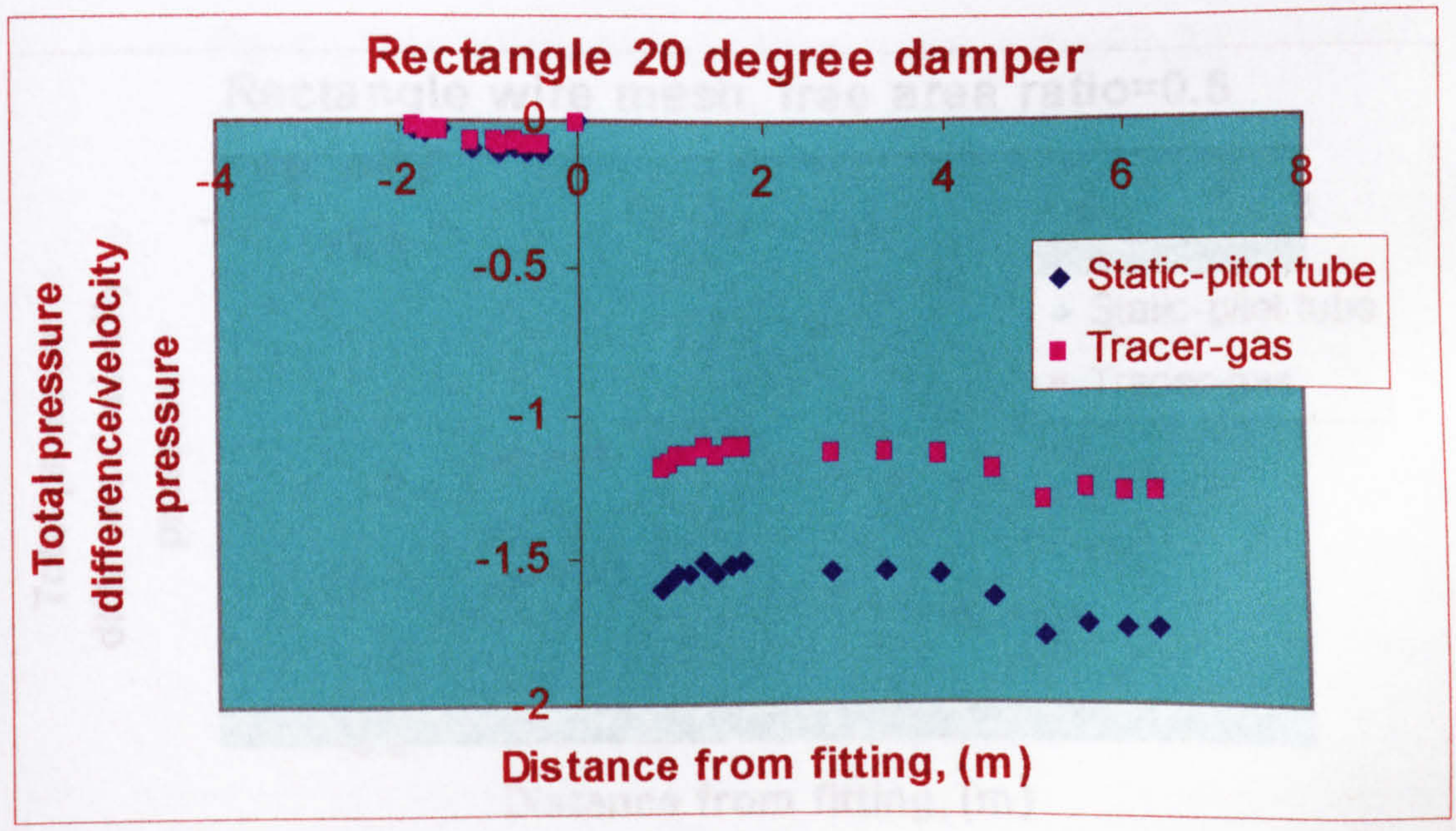

## 1.12 Rectangle 10° damper

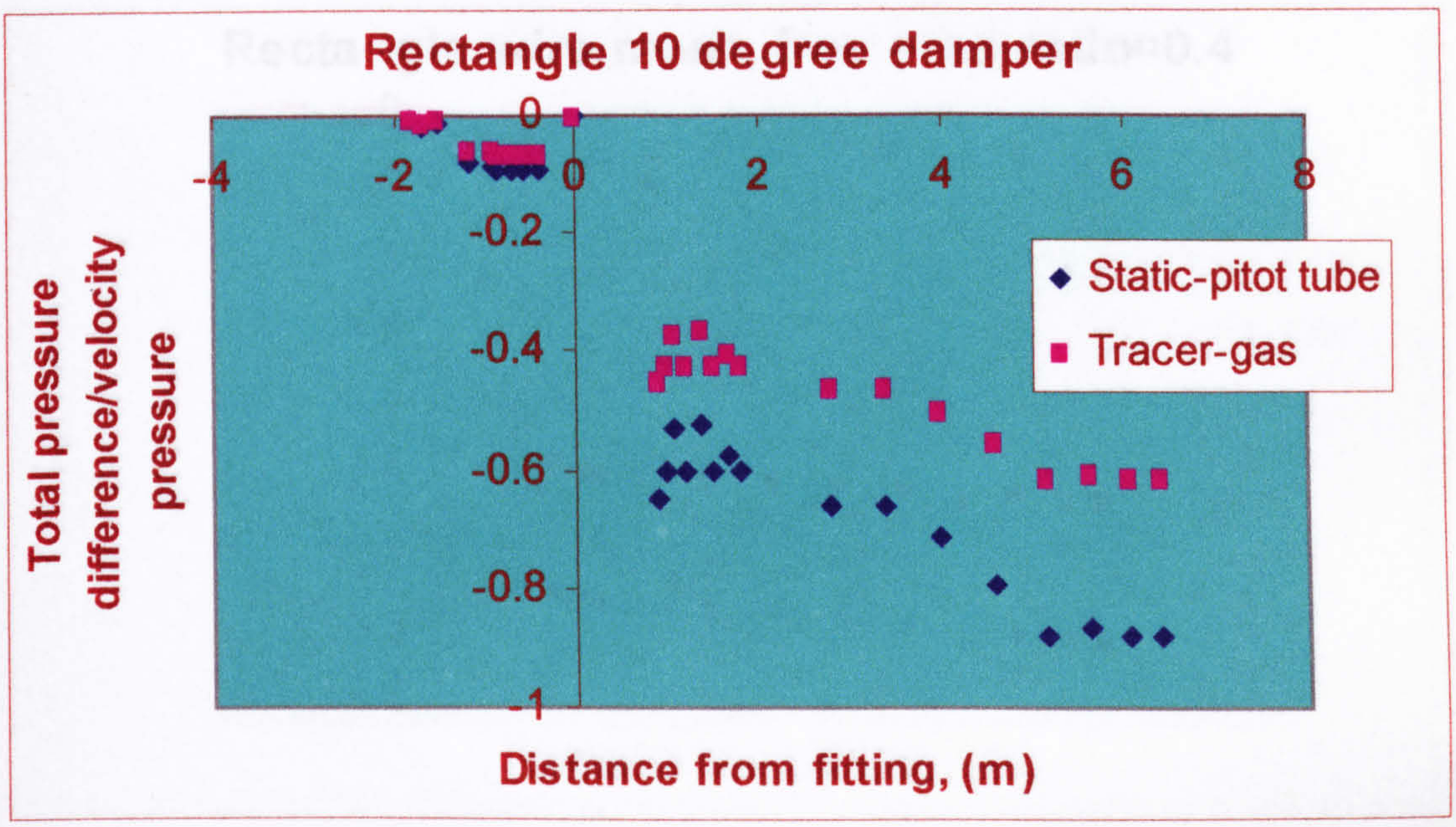


## 1.13 Rectangle wire mesh, free area ratio = 0.5

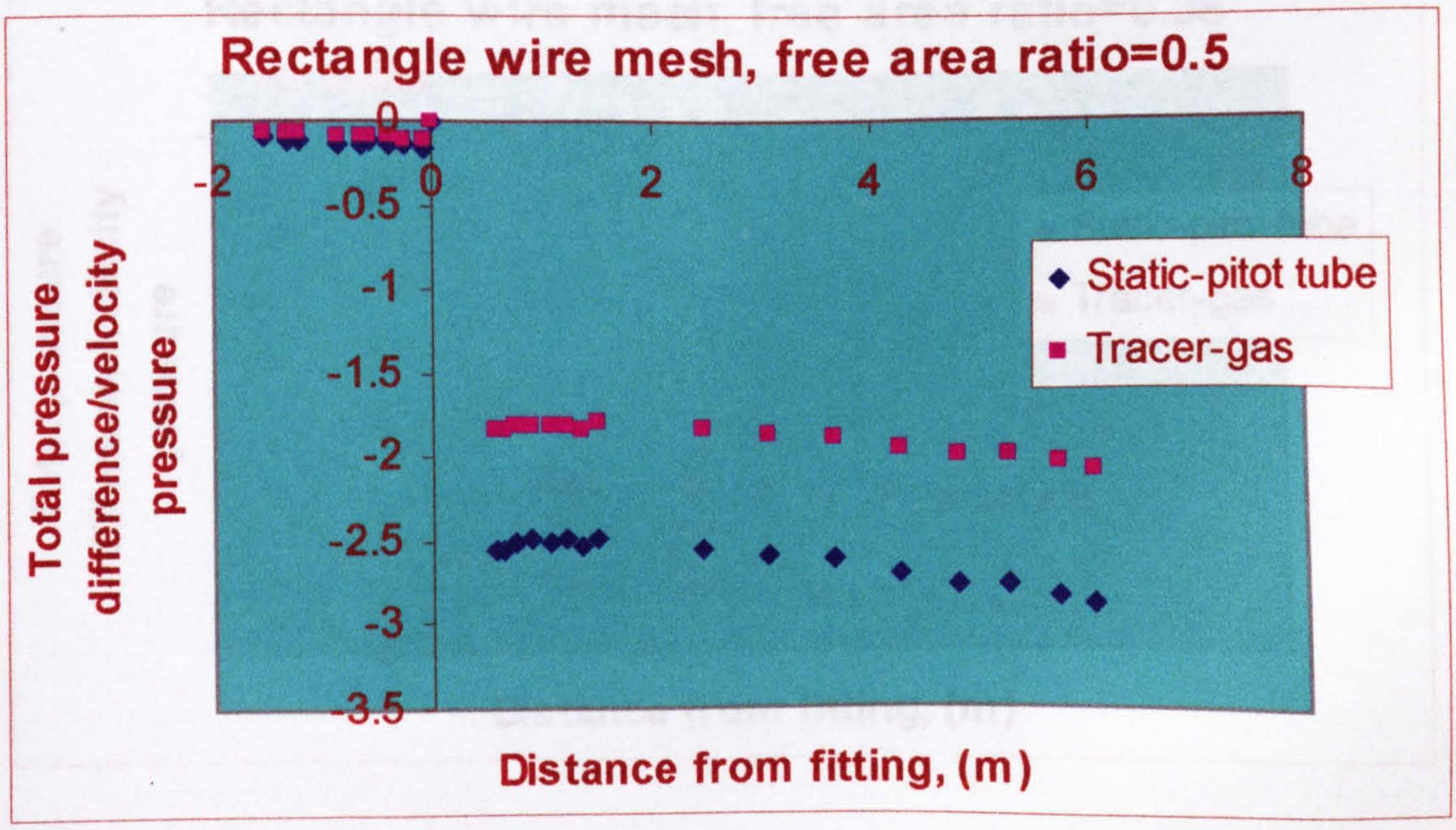

## 1.14 Rectangle wire mesh, free area ratio = 0.4

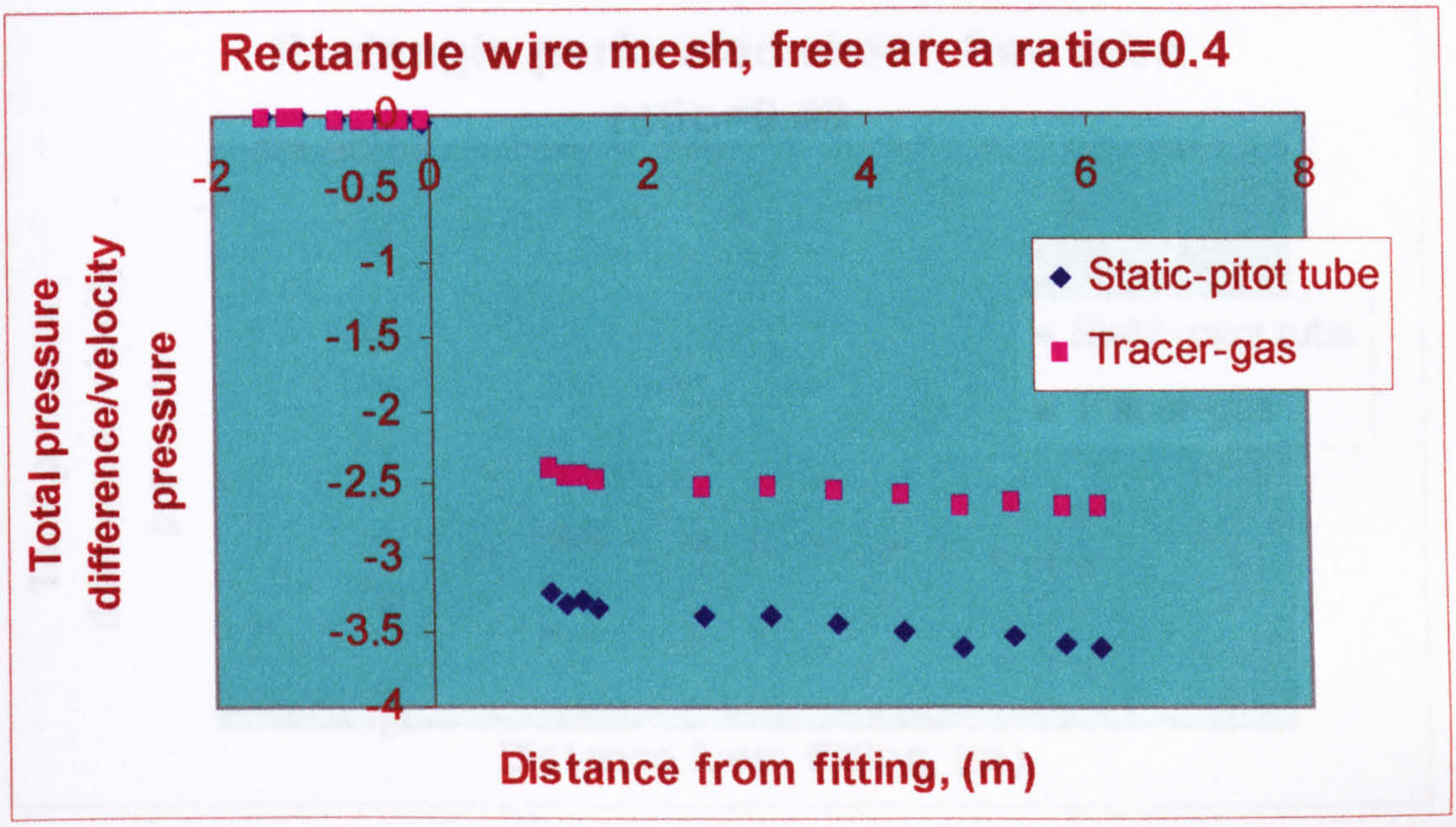


## 1.15 Rectangle wire mesh, free area ratio = 0.35

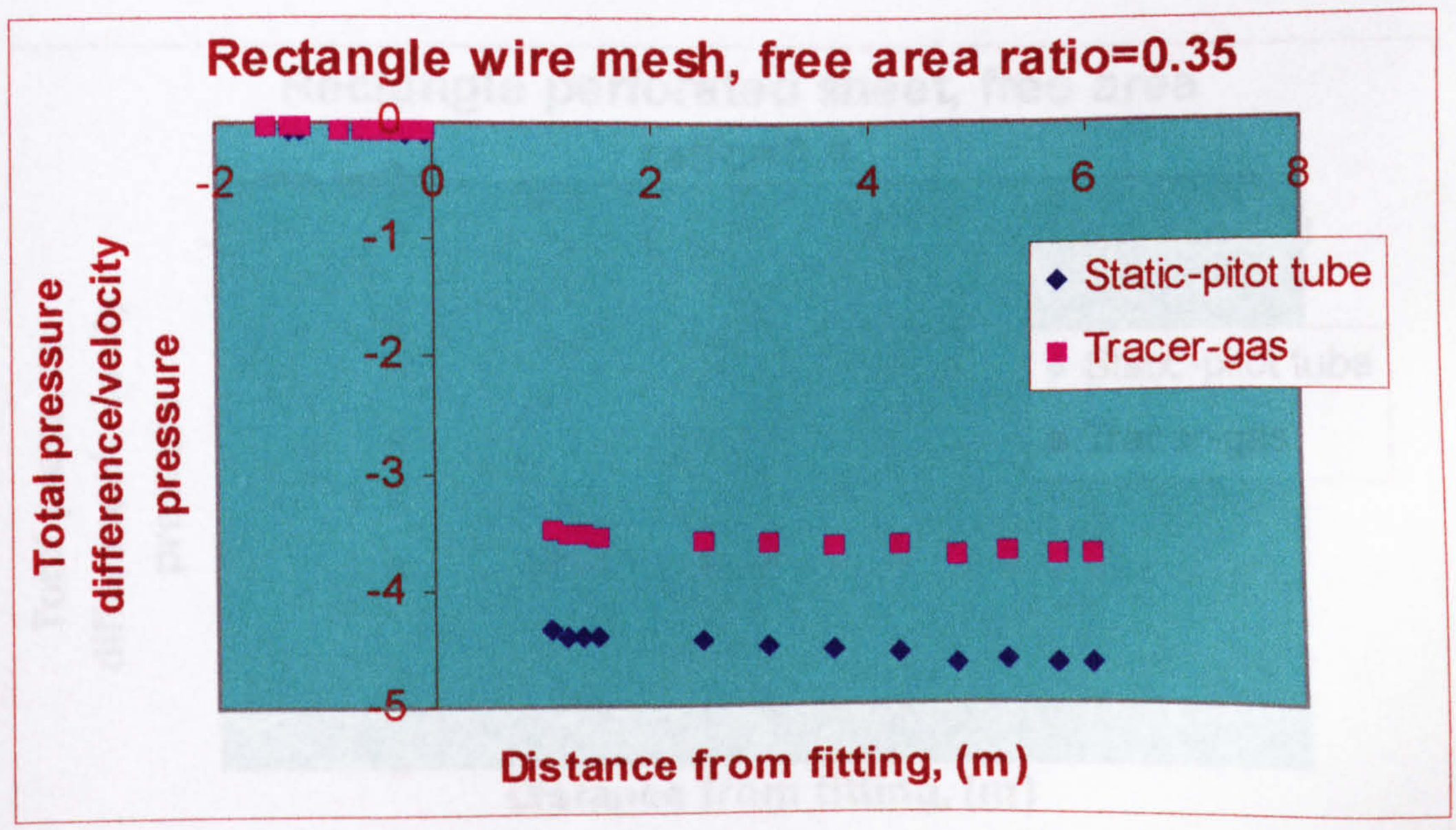

## 1.16 Rectangle perforated sheet, free area ratio = 0.48

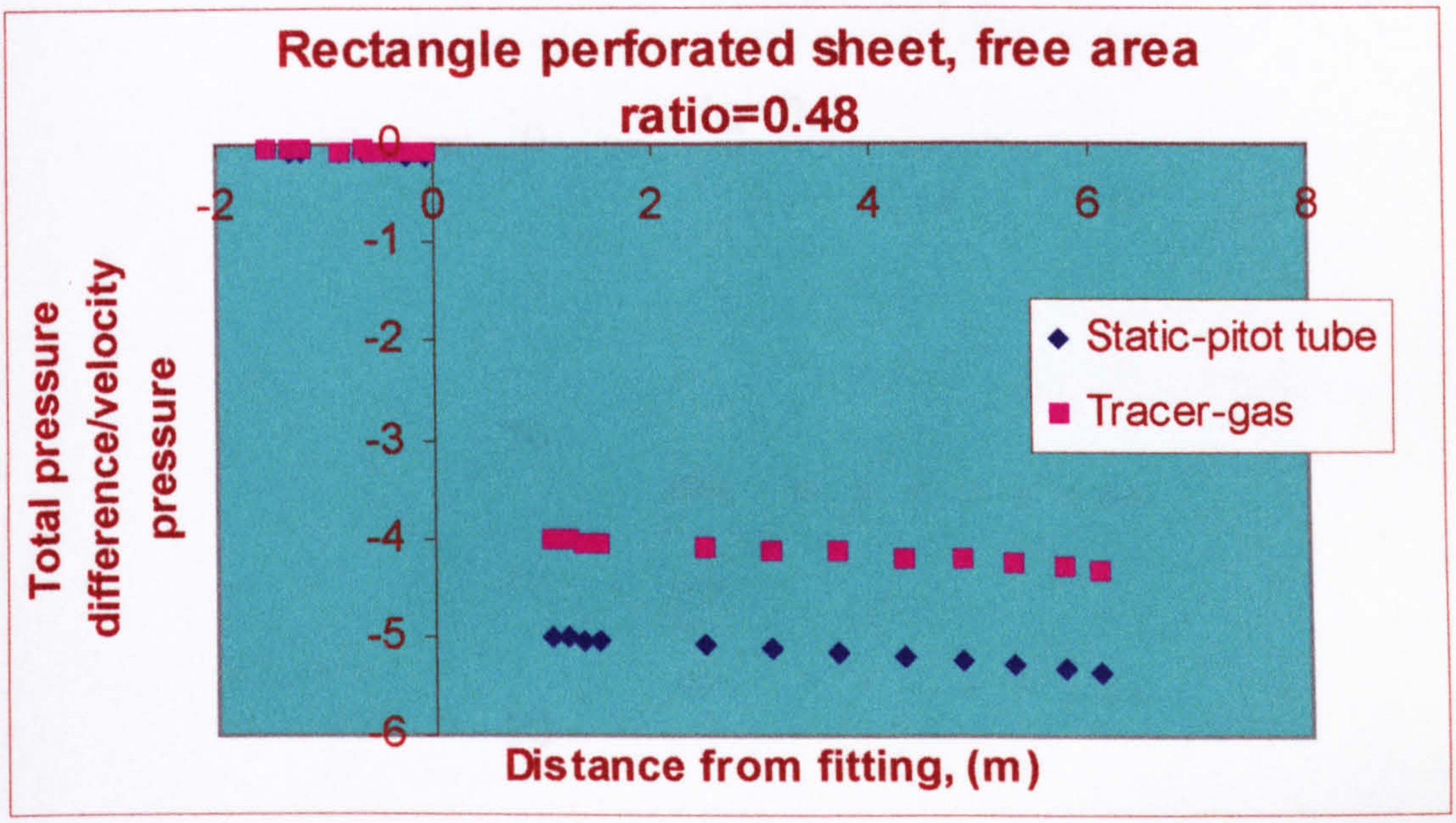


## 1.17 Rectangle perforated sheet, free area ratio = 0.4

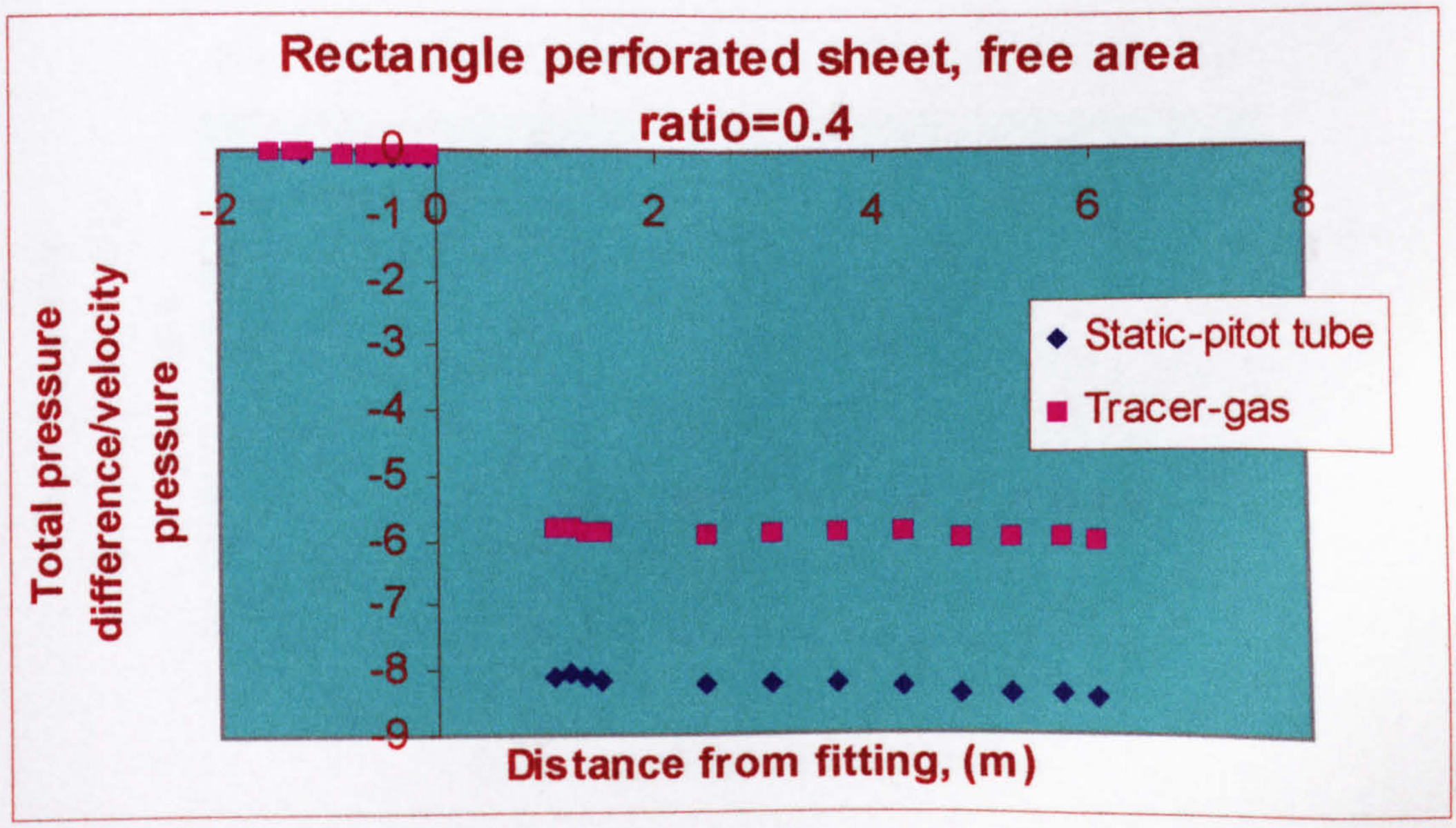

## 1.18 Rectangle perforated sheet, free area ratio = 0.3

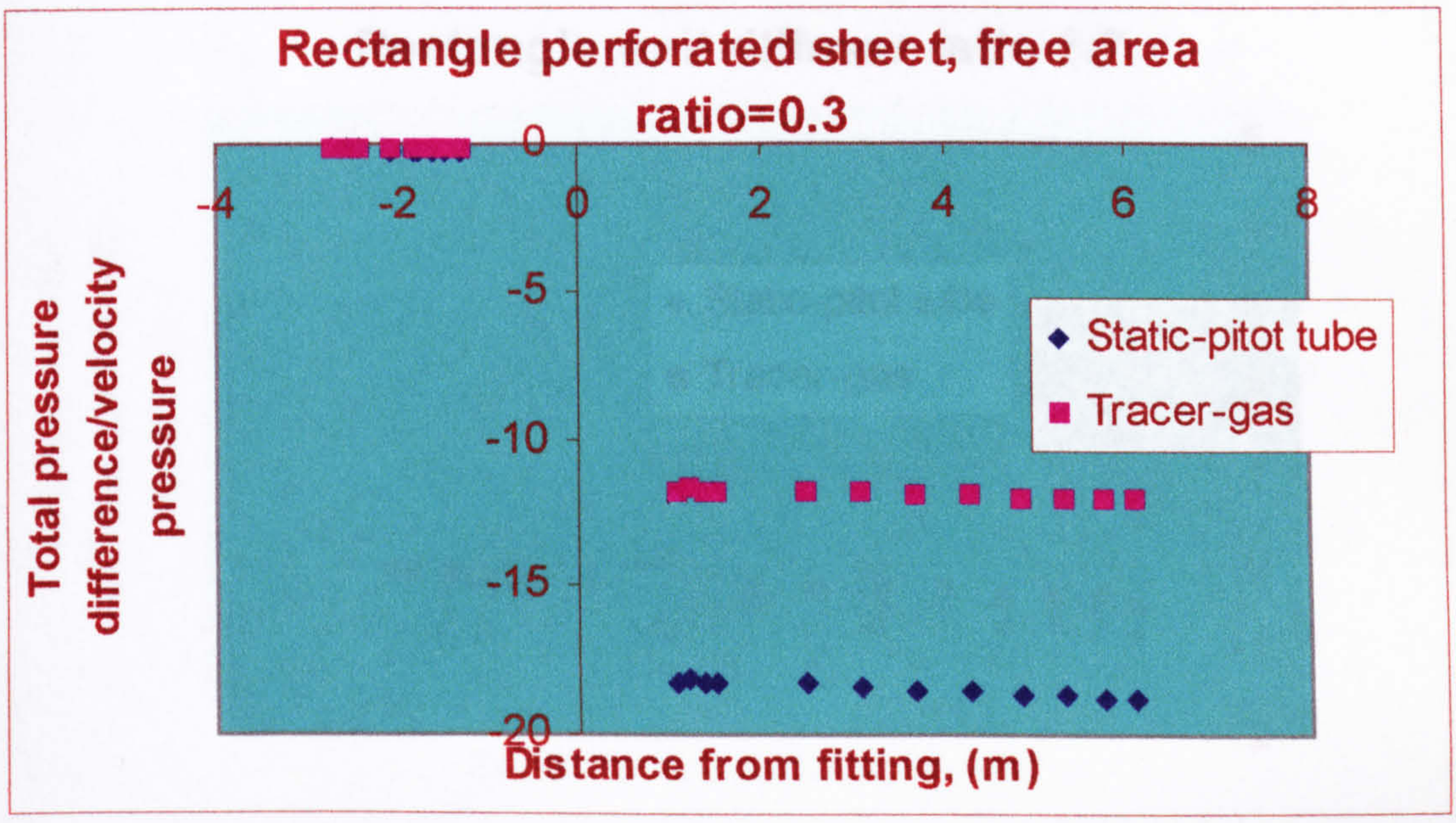


## 1.19 Rectangle perforated sheet, free area ratio = 0.2

## 1.20 Rectangle exit diffuser, transition area ratio 1:7

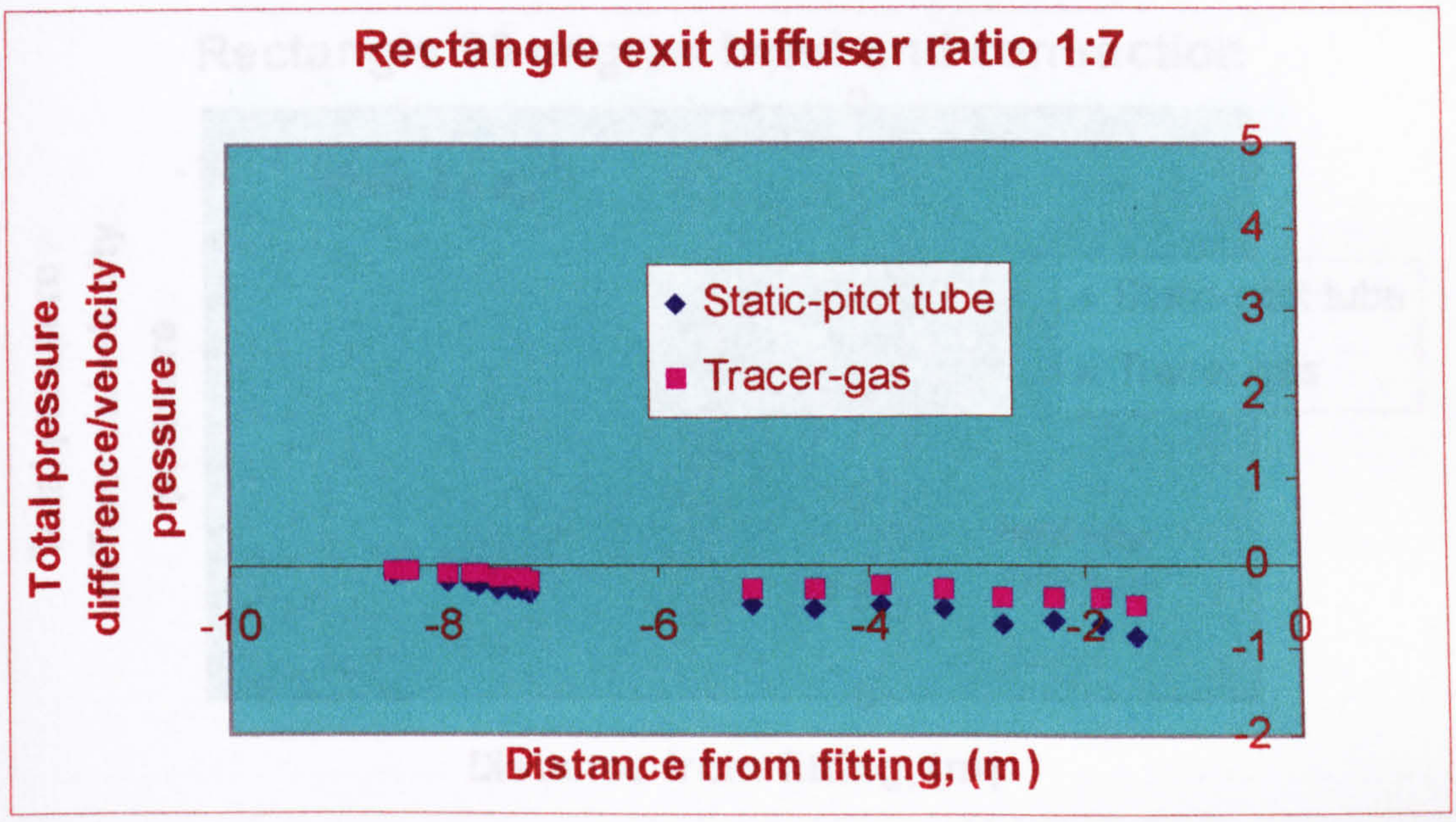


## 1.21 Rectangle expansion and 90° bend

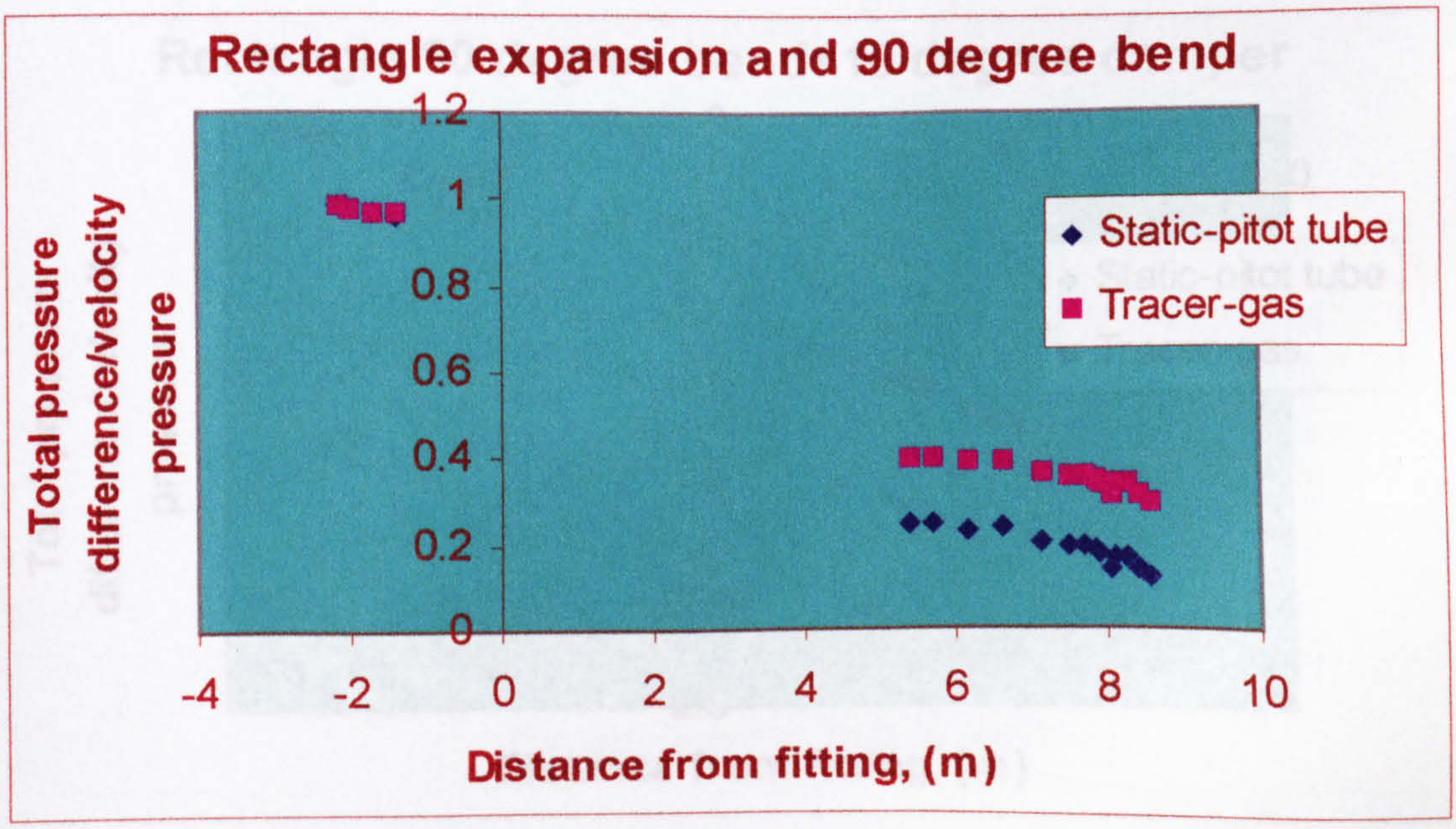

## 1.22 Rectangle 90° bend and contraction

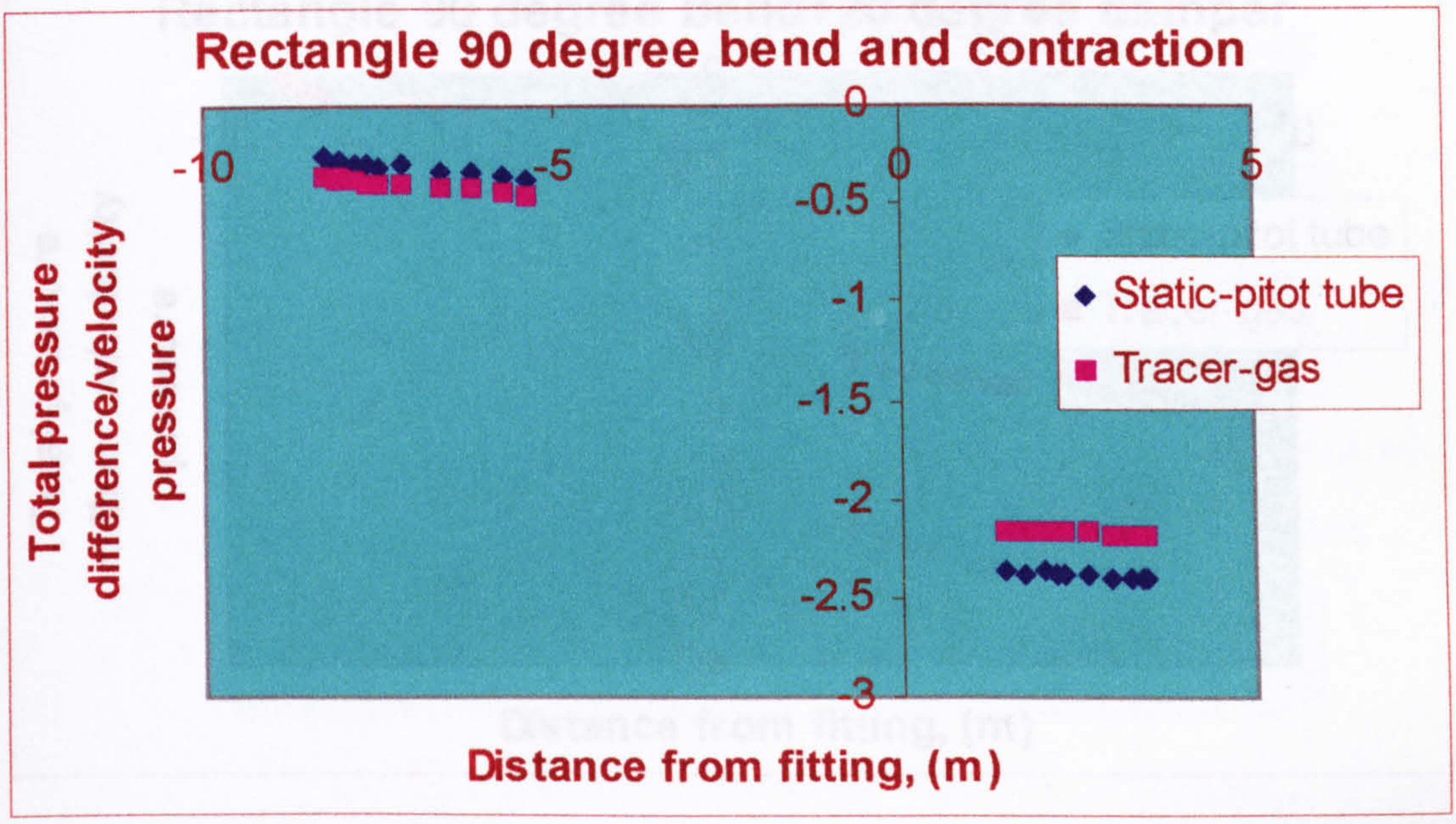


## 1.23 Rectangle 90° bend + 10° damper

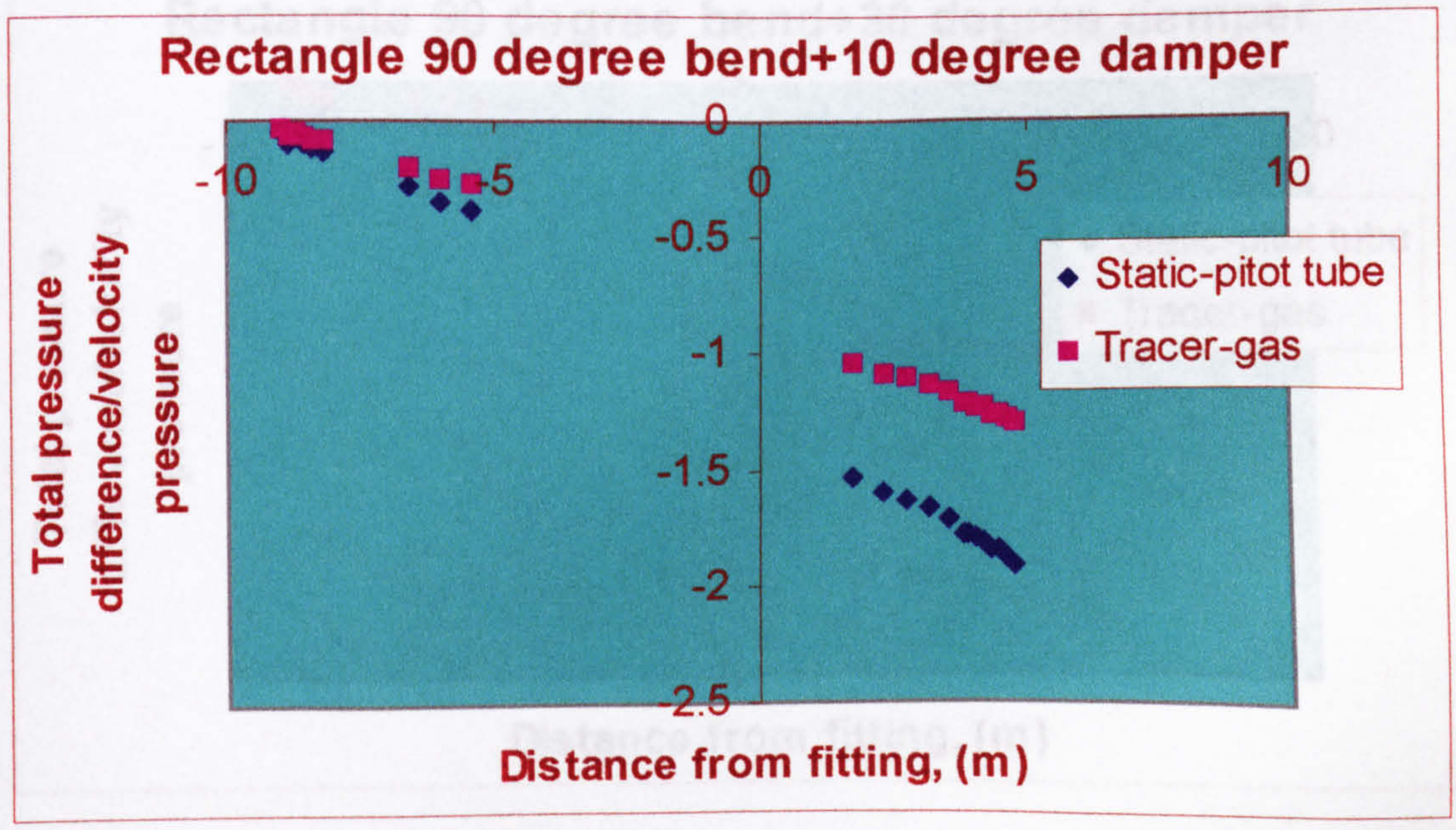

## 1.24 Rectangle 90° bend + 20° damper

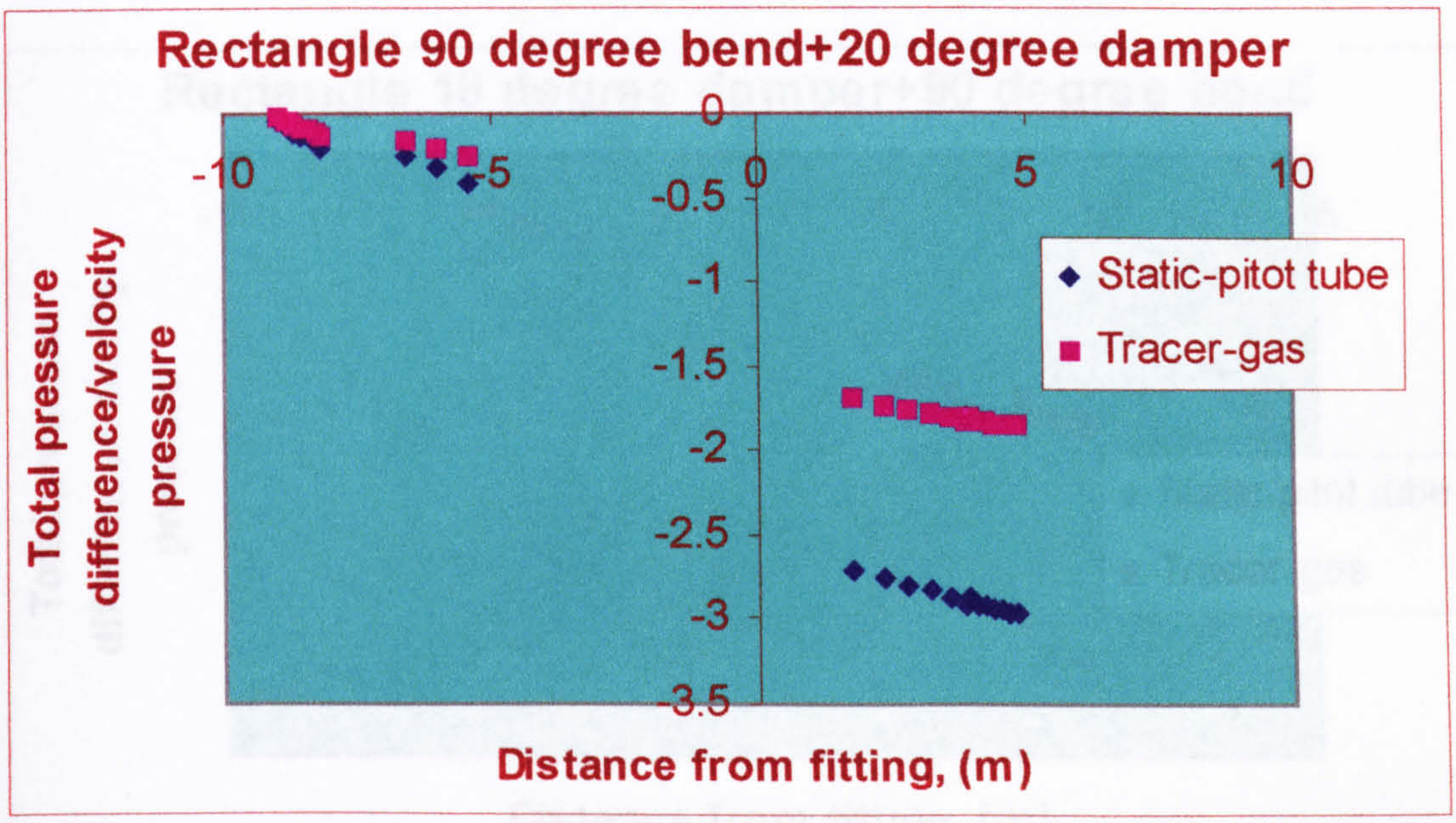


## 1.25 Rectangle 90° bend + 30° damper

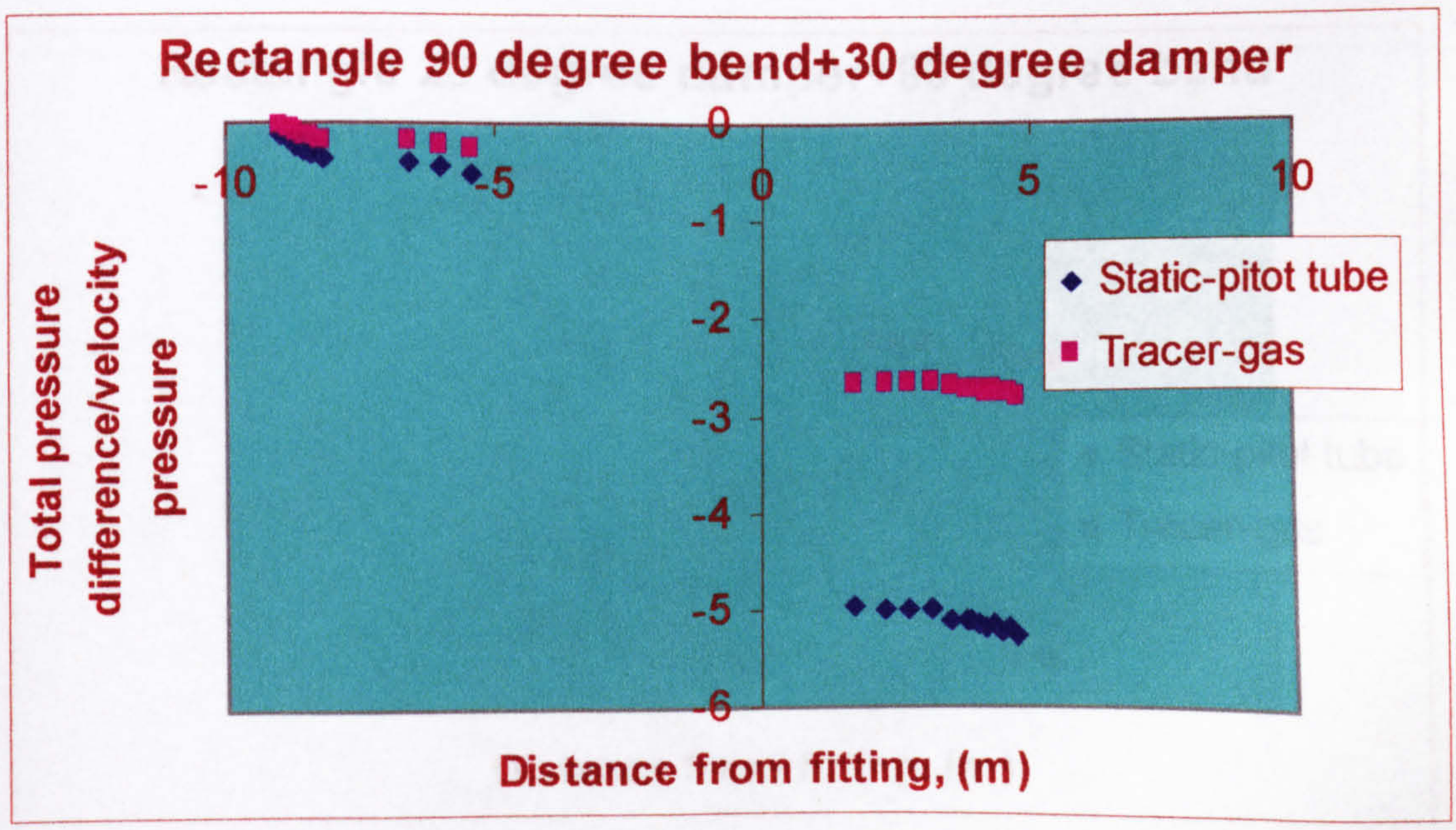

## 1.26 Rectangle 10° damper + 90° bend

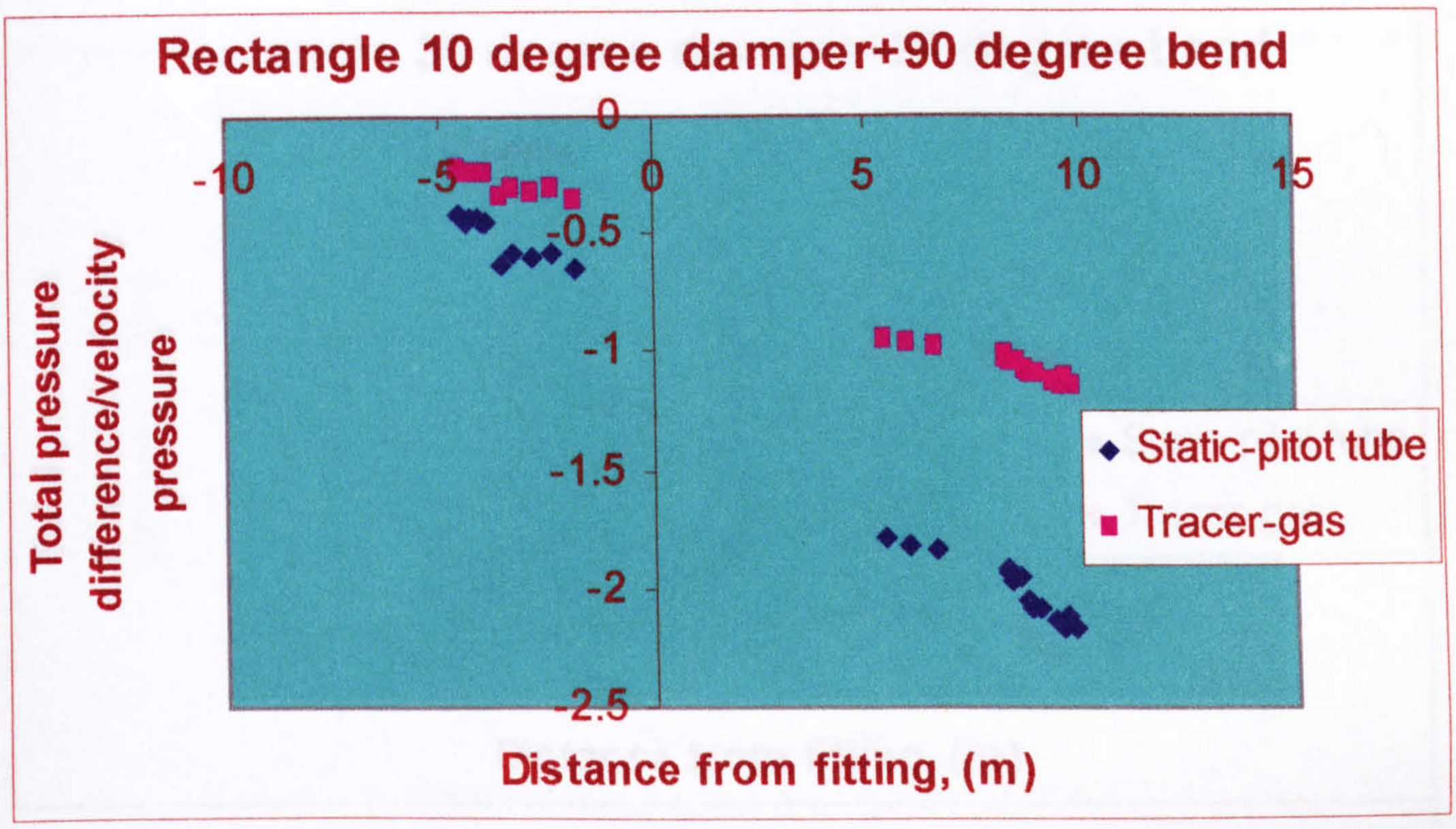


## 1.27 Rectangle 20° damper + 90° bend

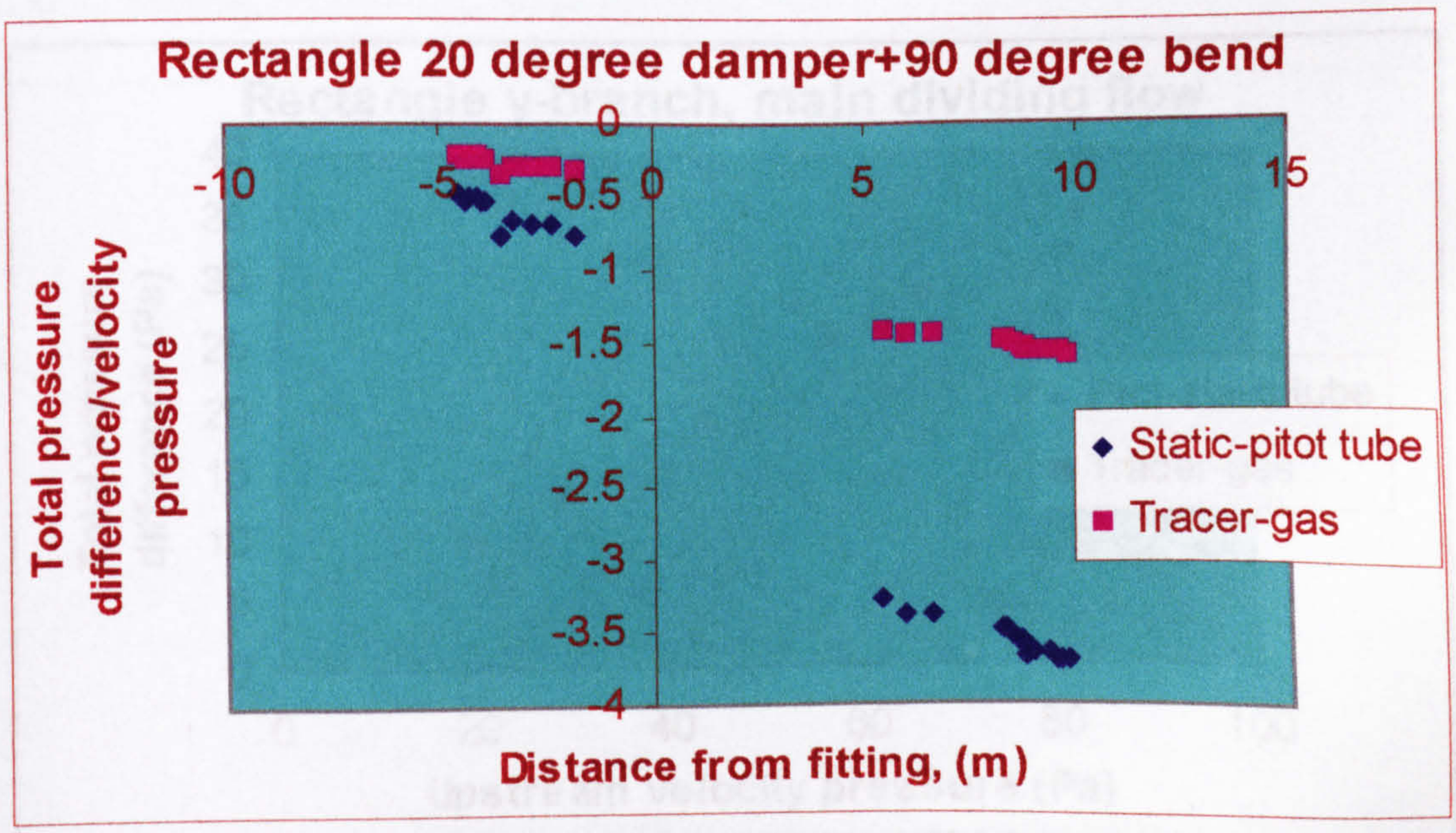

## 1.28 Rectangle 30° damper + 90° bend

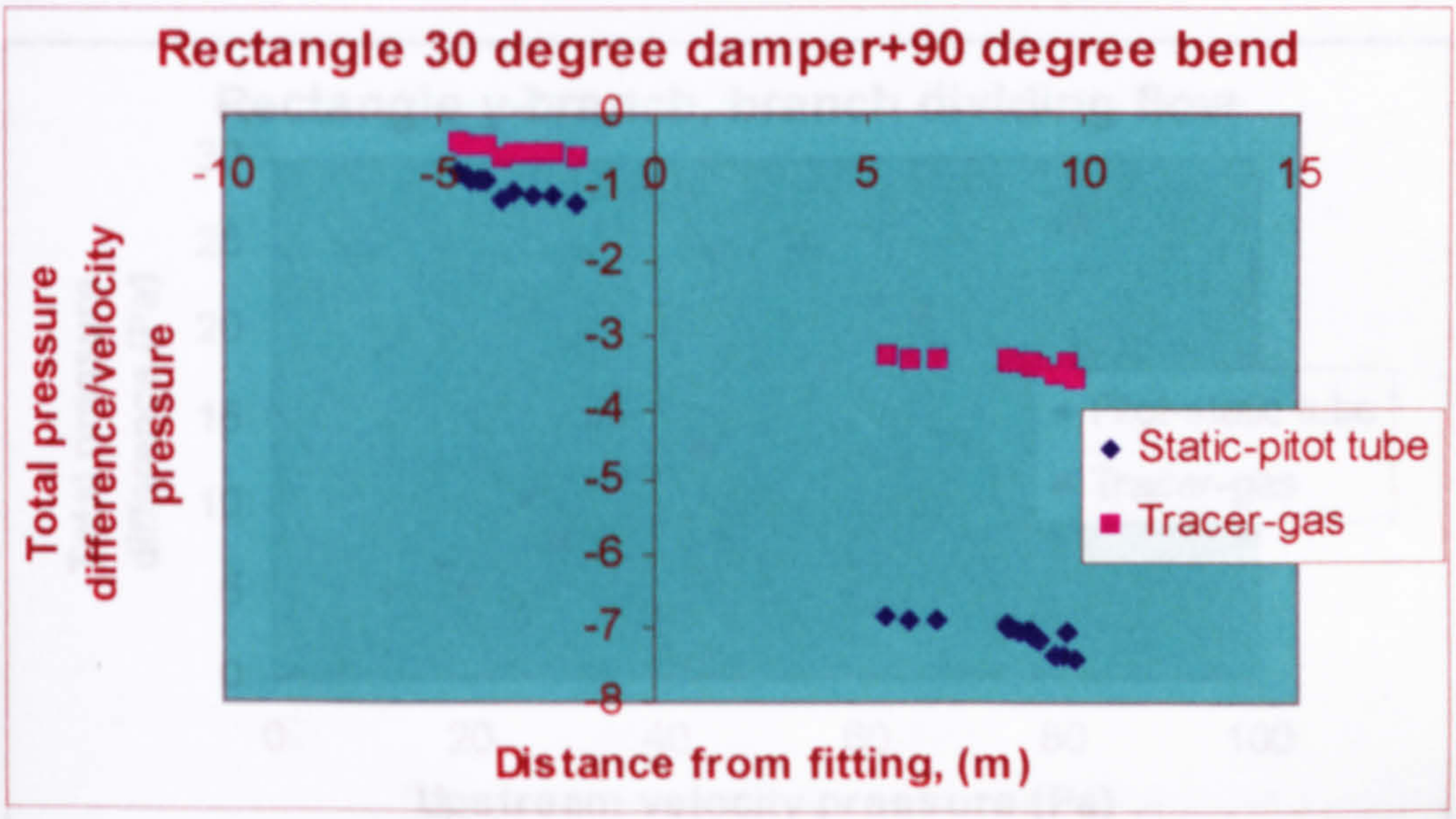


## 1.29 Rectangle y-branch, main dividing flow

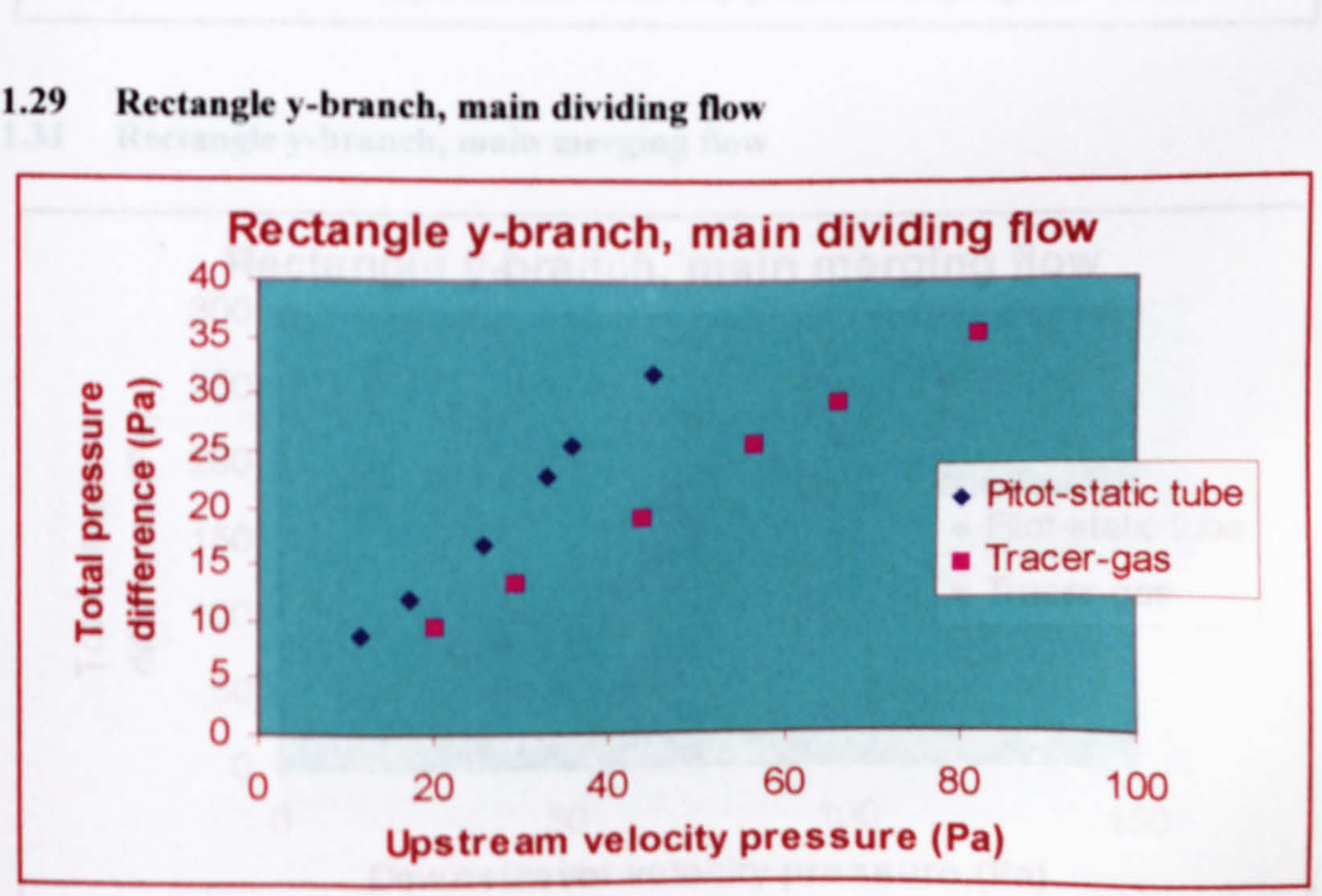

## 1.30 Rectangle y-branch, branch dividing flow

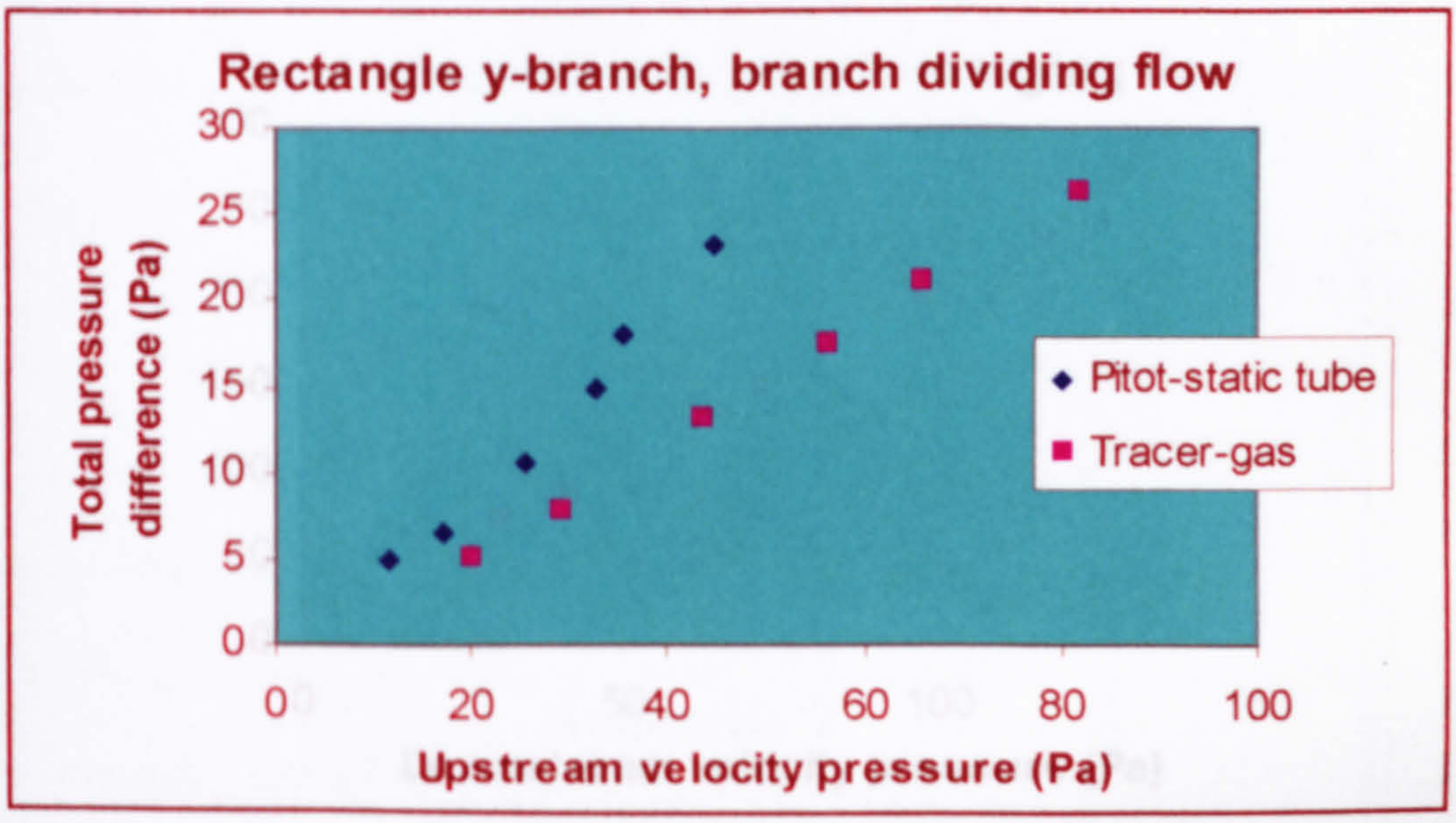


## 1.31 Rectangle y-branch, main merging flow

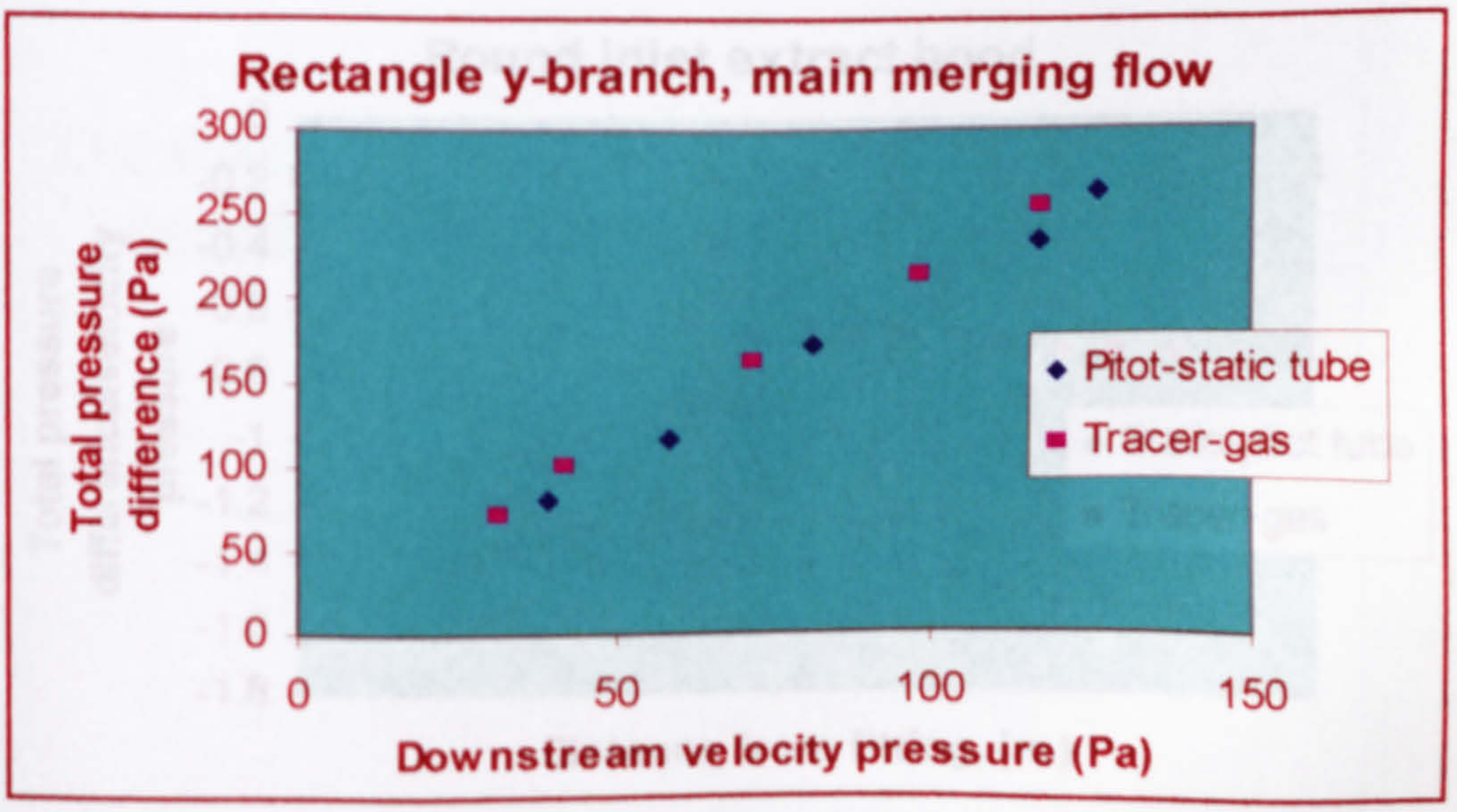

## 1.32 Rectangle y-branch, branch merging flow

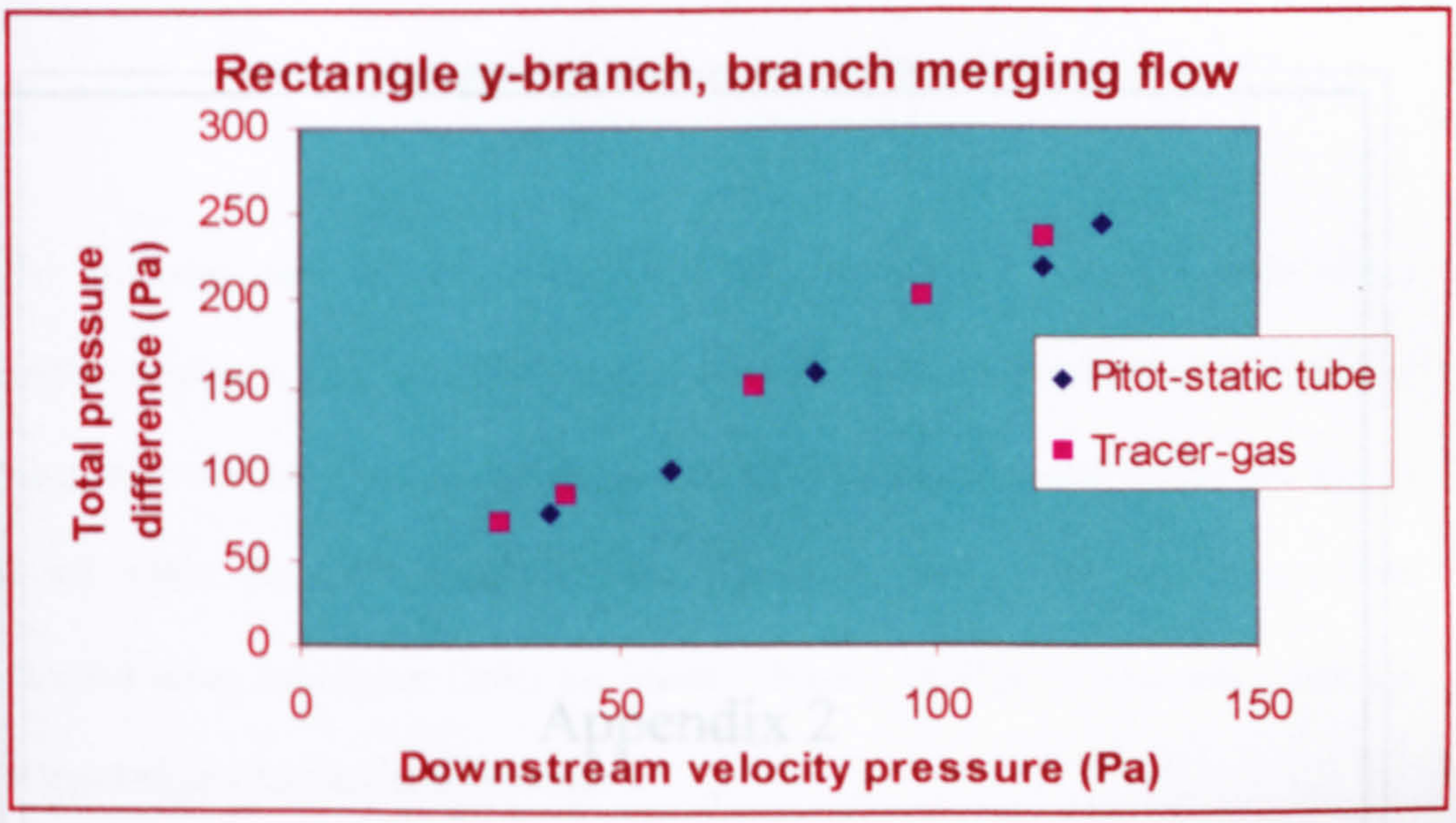


## 1.33 Round inlet extractor hood

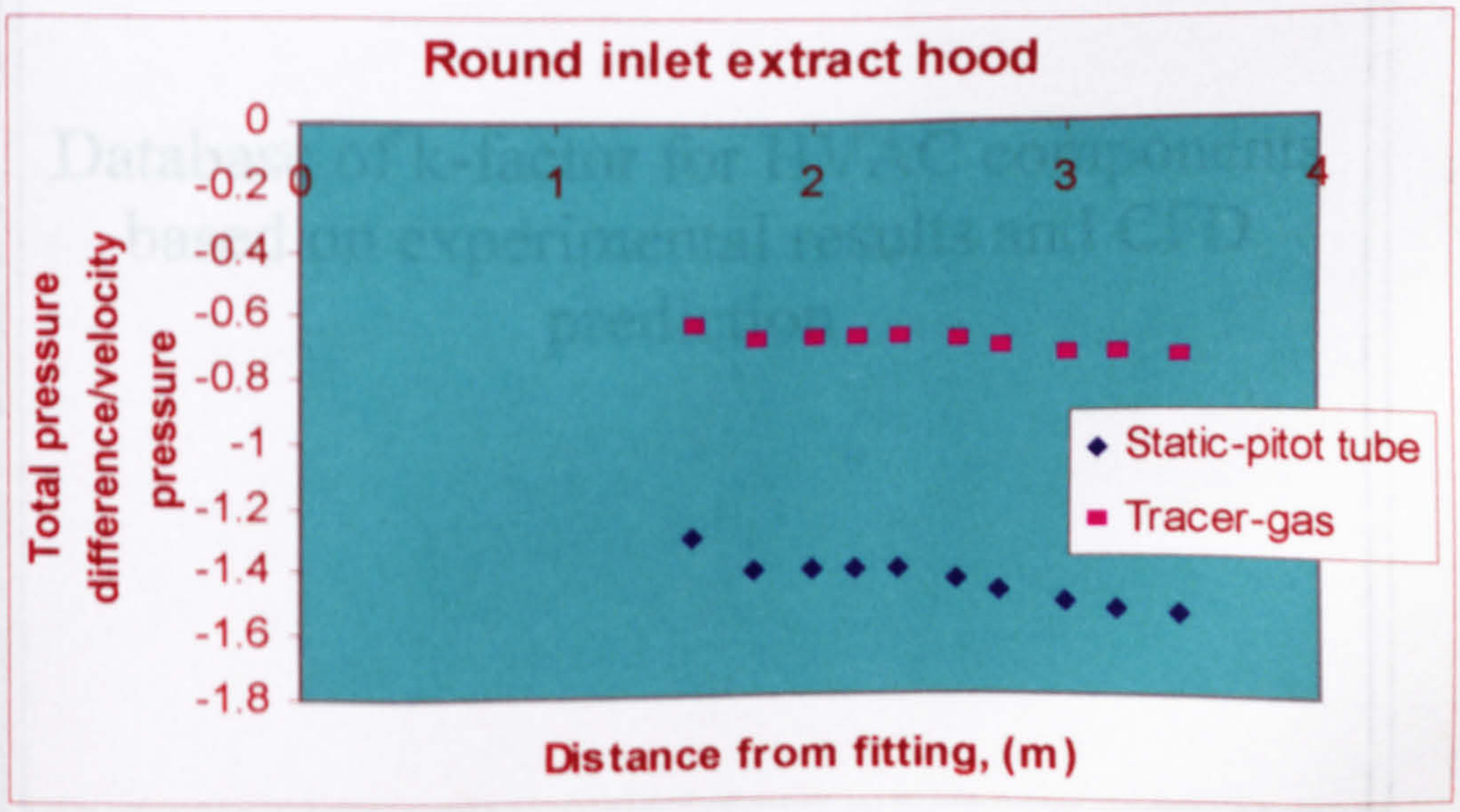

# Appendix 2

Database of k-factor for HVAC components based on experimental results and CFD prediction

# Appendix 2 Database of k-factor for HVAC components based on experimental results and CFD prediction

The following sets of velocity pressure loss factors ( k-factors ) were either predicted using a CFD commercial package FLUENT, or obtained experimentally using the constant-injection tracer-gas method. The experimental results are shown in red whilst the CFD predictions are shown in black. The predictions were obtained using the Higher Order k-ε model with the QUICK ( Quadratic Upstream Interpolation ) discretisation scheme.

## 2.1 Square cross-section :

### 2.1.1 U-bend.

Ar = h / w, x = separation, duct cross-section Fs = const.

$\alpha = 90°$ , r / w = 1.0

| x | 0 | 0.5 | 1.0 | 1.2 |
|---|---|---|---|---|
| Ar | k-factor | | | |
| 0.5 | 0.24 | 0.26 | 0.31 | 0.33 |
| 1.0 | 0.20 | 0.21 | 0.24 | 0.25 |
| 2.0 | 0.13 | 0.19 | 0.20 | 0.21 |

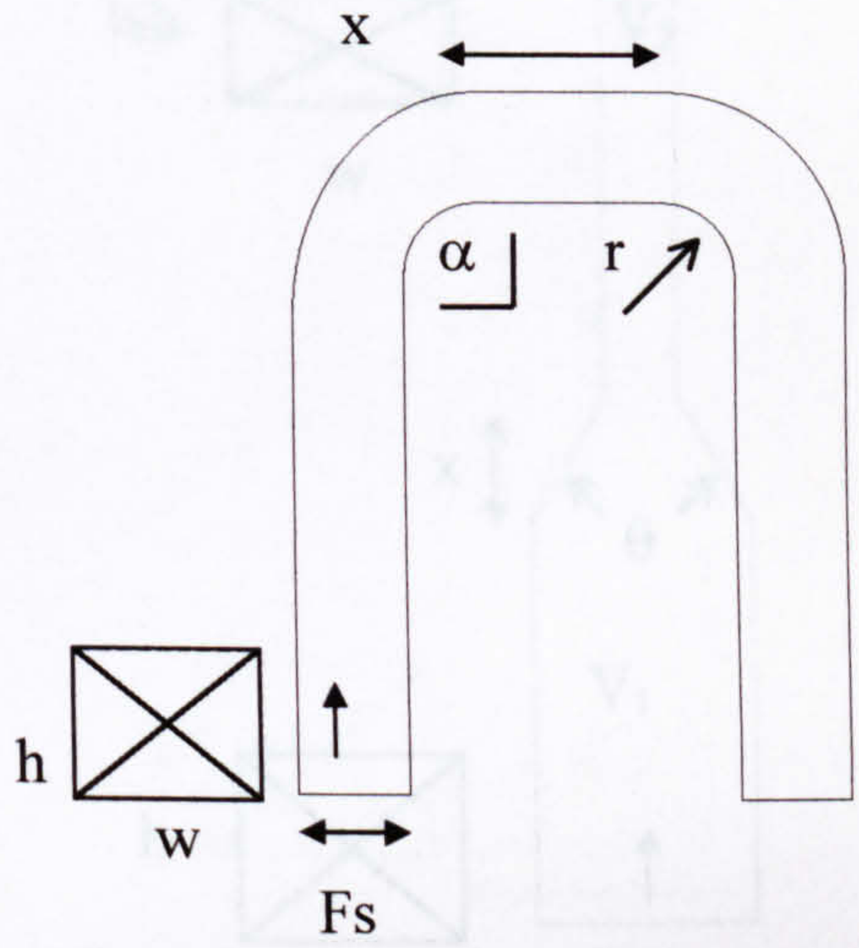


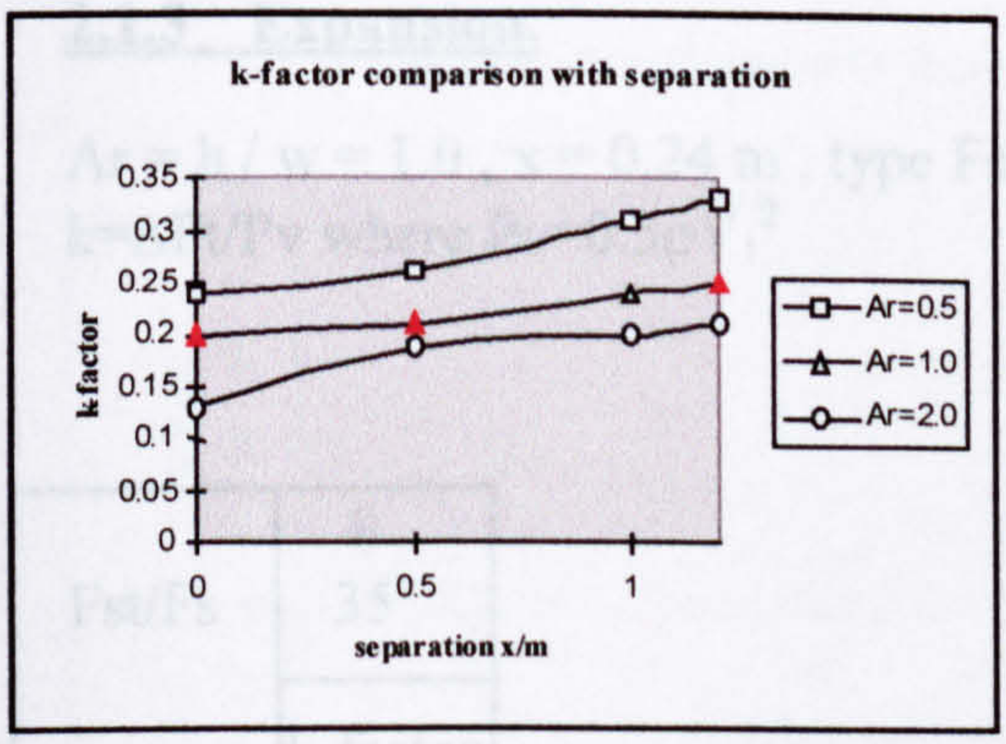


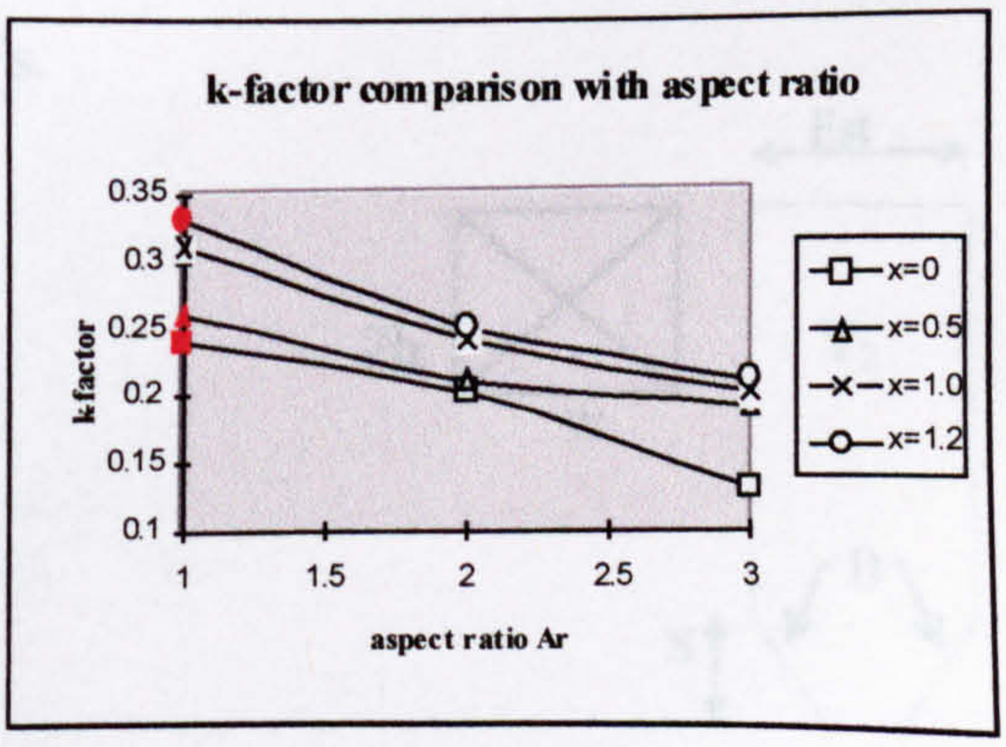

## 2.1.2 Contraction.

Ar = h / w = 1.0 , x = 0.24 m , type Fst = ½ Fs.
k=ΔPt/Pv where $Pv=0.5\rho V_2^2$

| Fs/Fst | θ 35 |
|---|---|
| 2.0 | k-factor 0.06 |

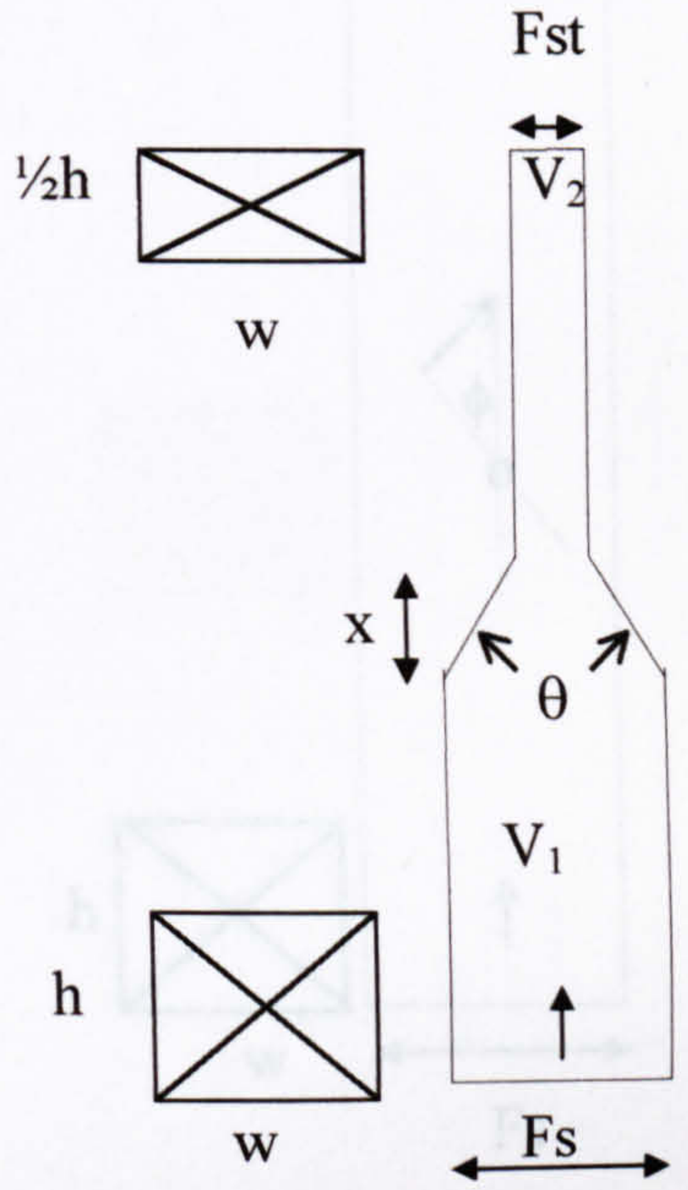


## 2.1.3 Expansion.

Ar = h / w = 1.0 , x = 0.24 m , type Fst = 2Fs.
k=ΔPt/Pv where $Pv=0.5\rho V_1^2$

| Fst/Fs | θ 35 |
|---|---|
| 2.0 | k-factor 0.10 |

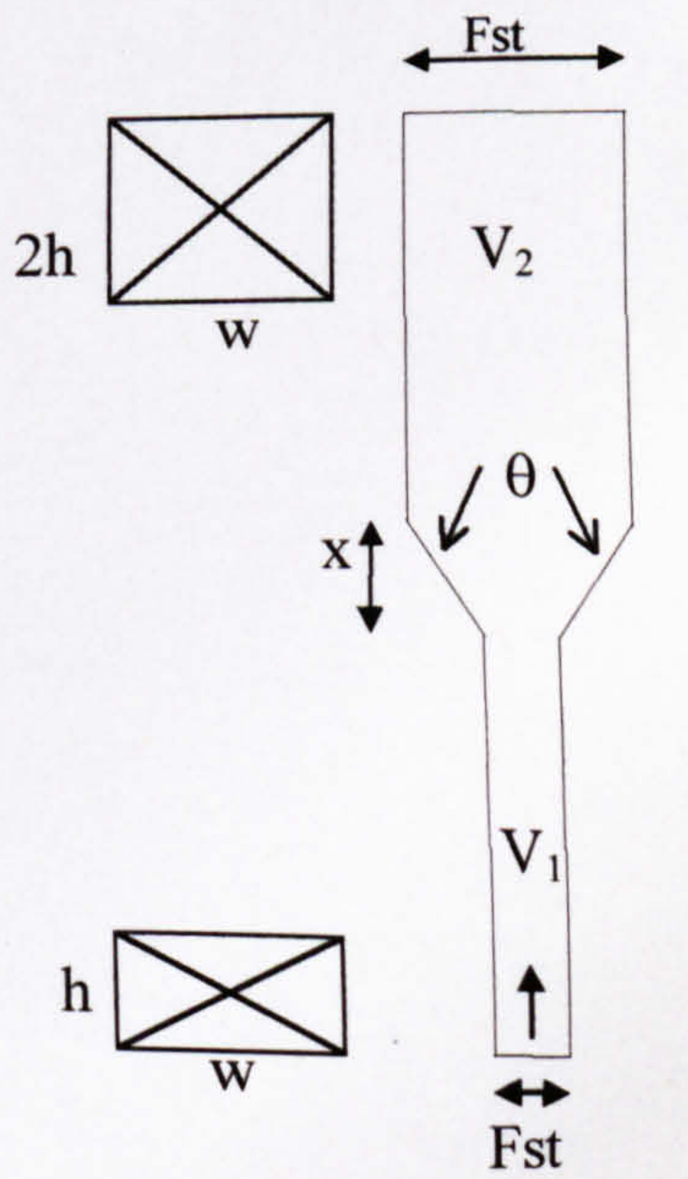

## 2.1.4 Damper.

$\phi$ = damper angle, degrees, Ar = h / w , Fs = const.

| $\phi$ | 10 | 20 | 30 | 45 | 60 |
|---|---|---|---|---|---|
| k | 0.22 | 0.94 | 2.13 | 12.81 | 44.51 |

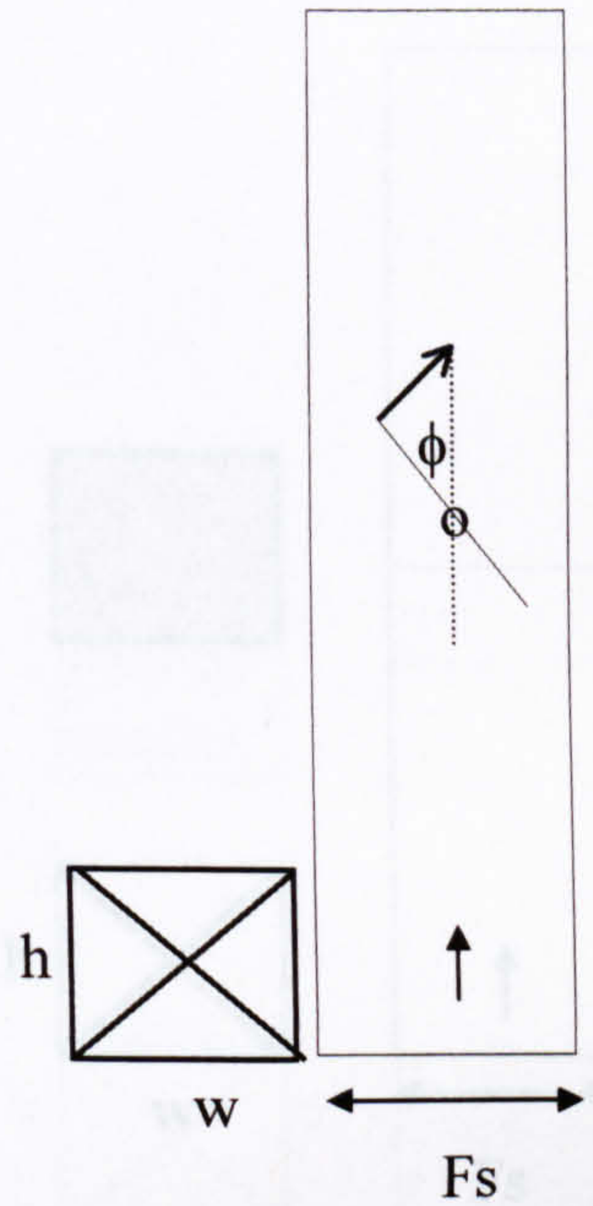


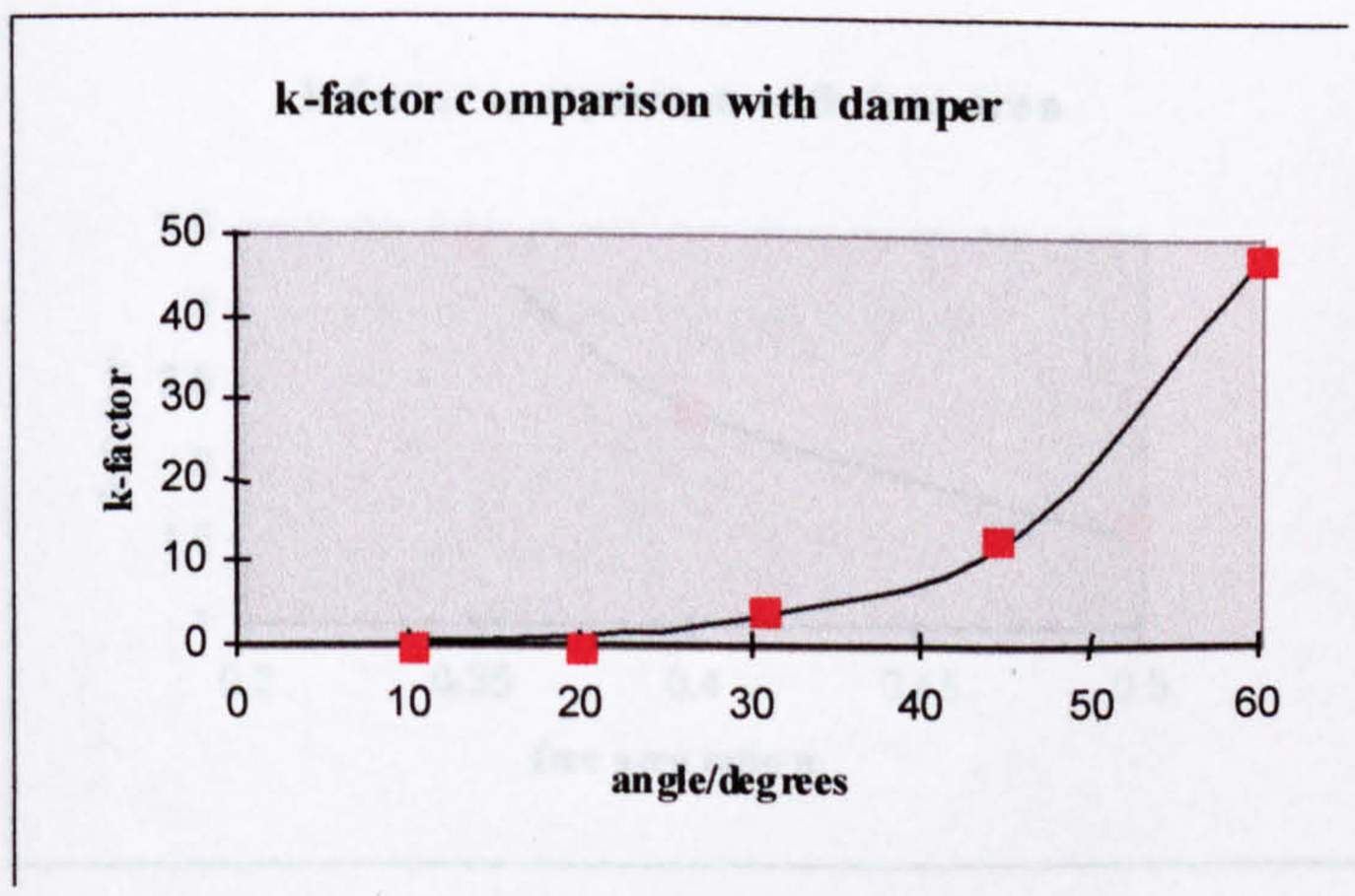

## 2.1.5 Wire mesh.

n = free area ratio, Ar = h / w = 1.0 , Fs = const.

| n | 0.35 | 0.4 | 0.5 |
|---|---|---|---|
| k | 3.42 | 2.35 | 1.55 |

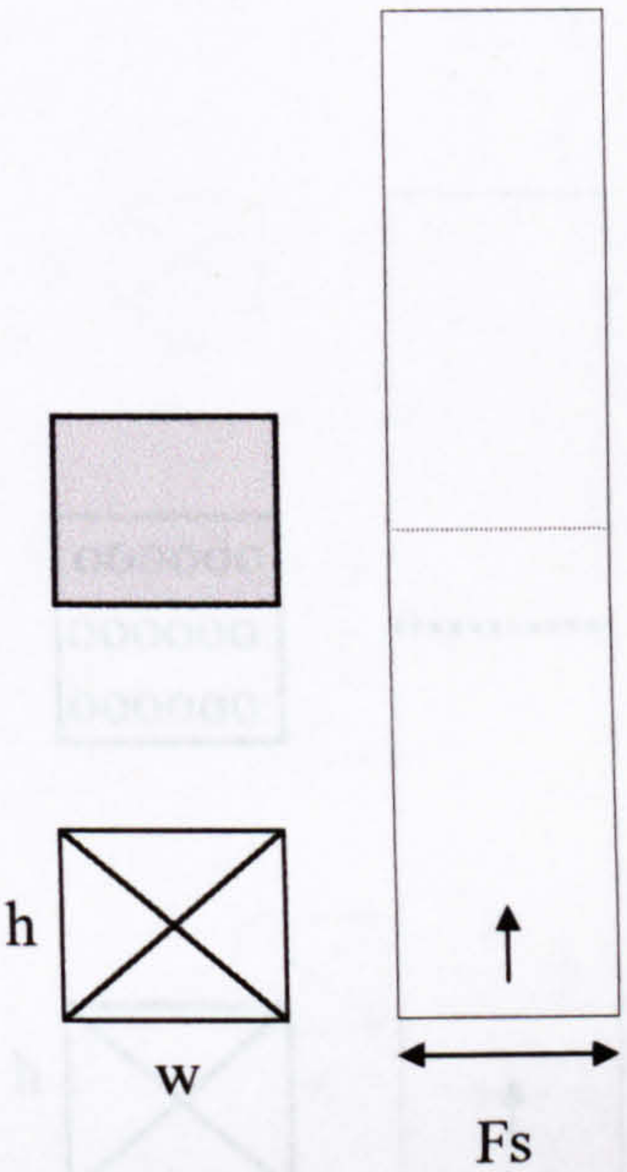


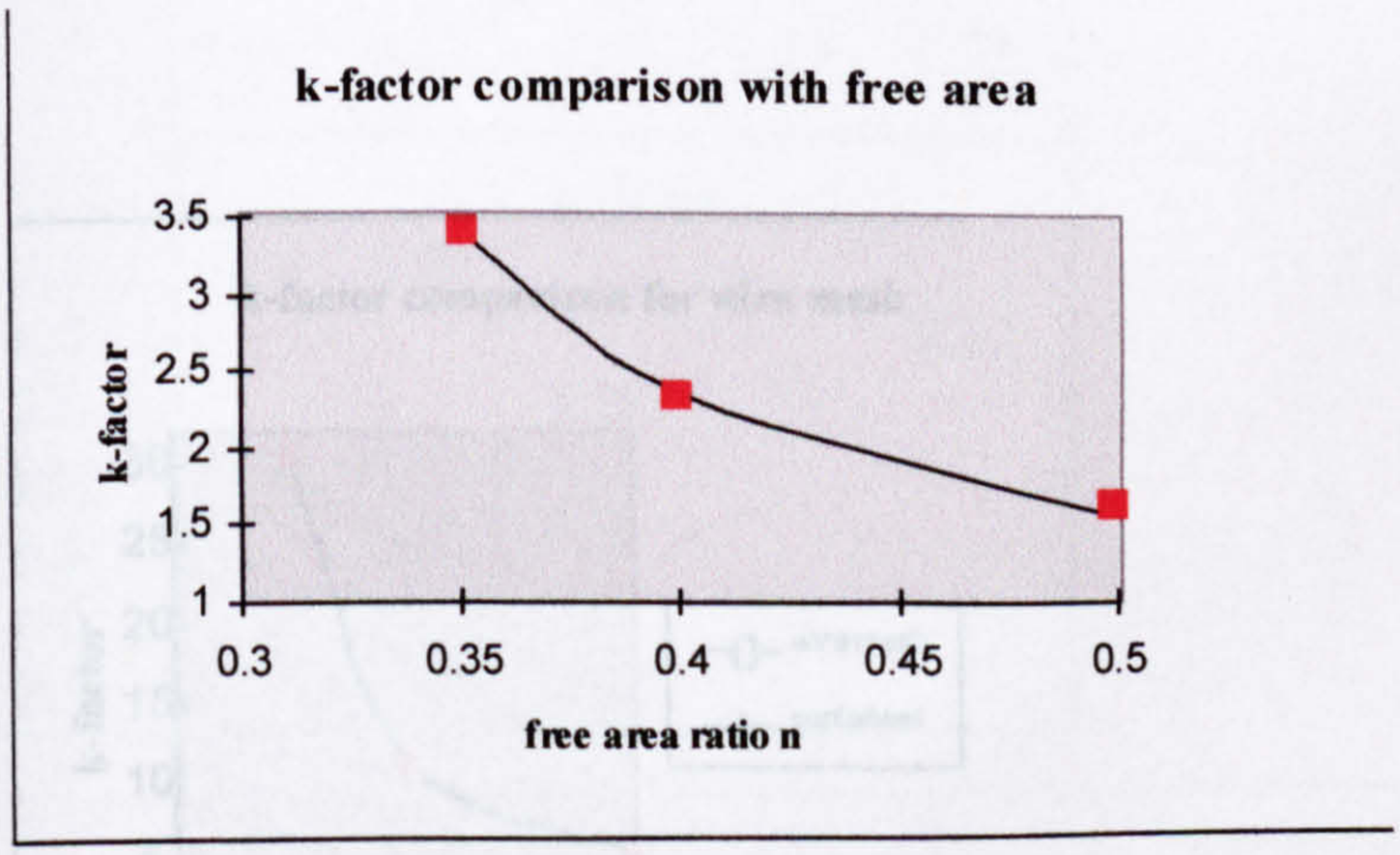

## 2.1.6 Perforated sheet.

n = free area ratio, Ar = h / w = 1.0 , Fs = const.

| n | 0.2 | 0.3 | 0.4 | 0.48 |
|---|---|---|---|---|
| k | 30.72 | 11.29 | 5.64 | 3.86 |

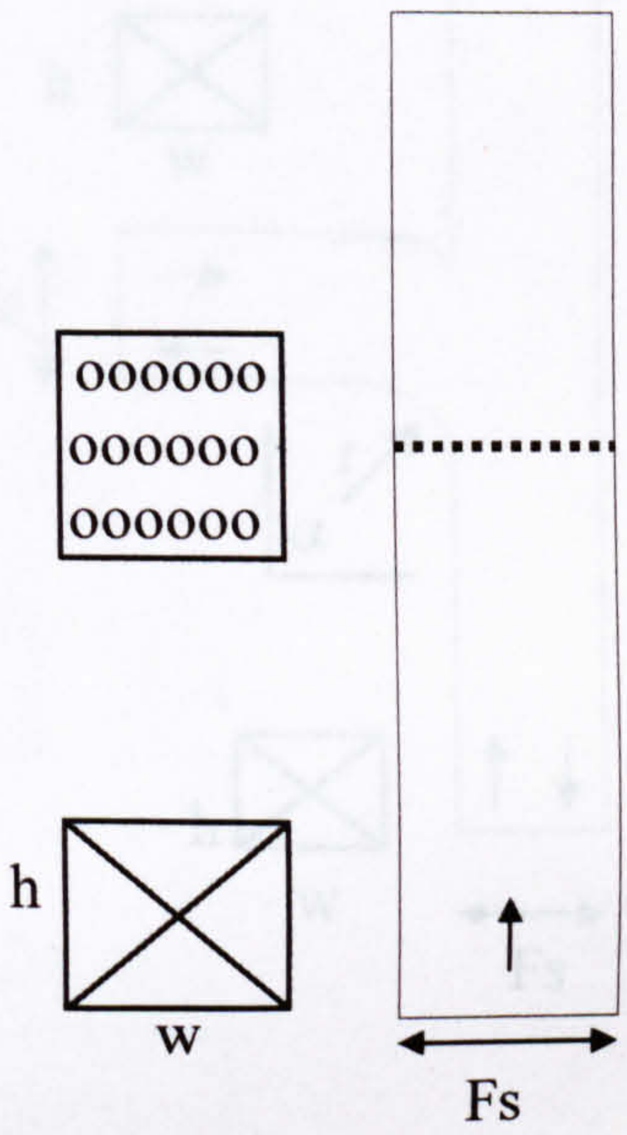


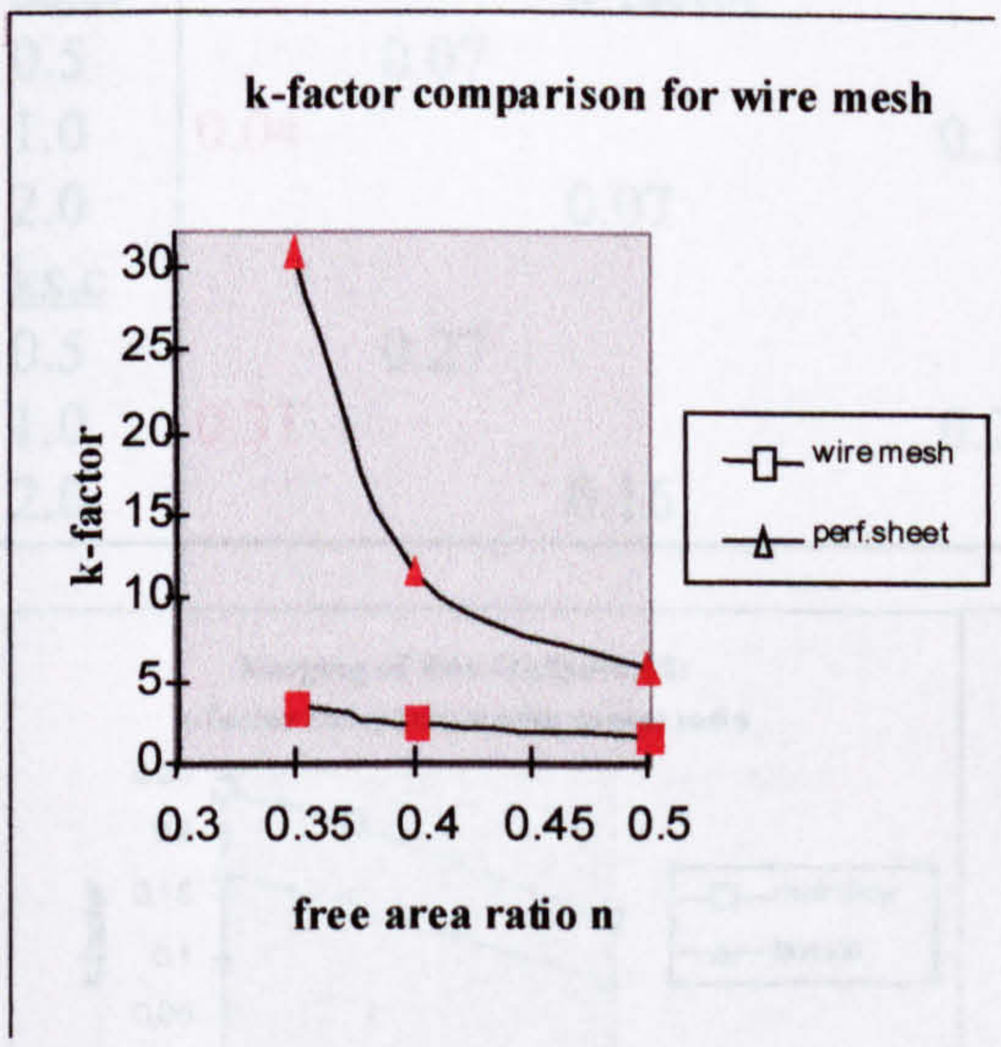

## 2.1.7 Wye branch.

Ar = h / w , r / w = 1.0 , $\alpha = 90°$ , type Fs + Fst > Fc.
Qc / Qs = flow rate ratios from branch to main.

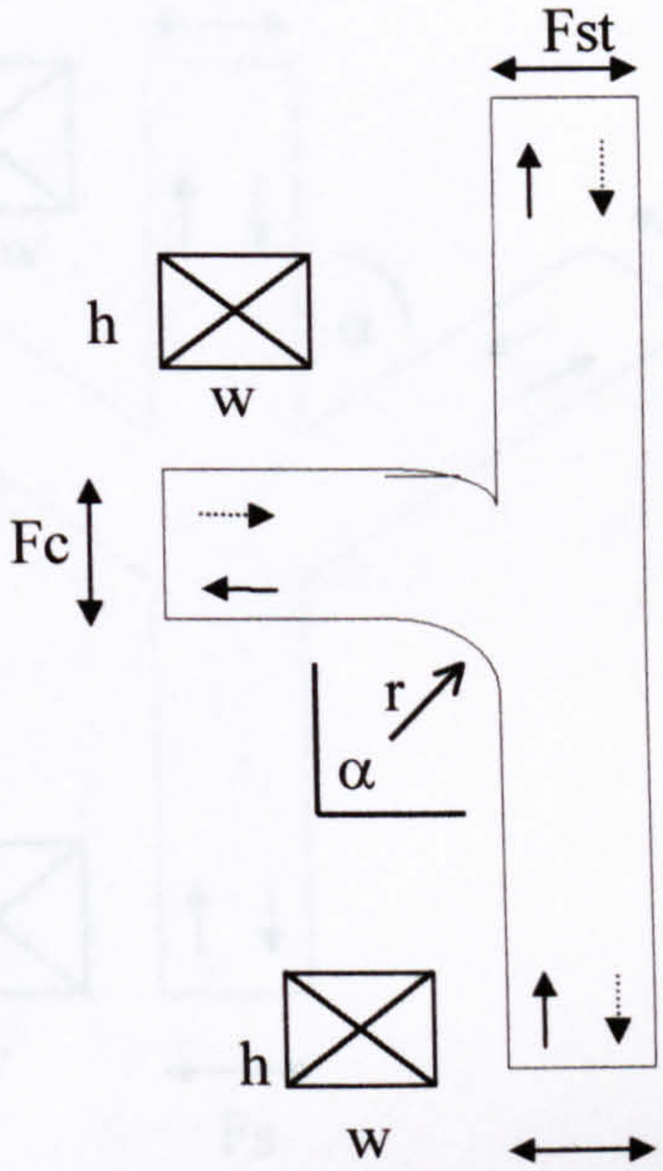


merging of flow

| Ar | Qc/Qs | | | | |
|---|---|---|---|---|---|
| | 0.49 | 0.52 | 0.56 | 0.59 | 0.72 |
| kst,s | k-factor | | | | |
| 0.5 | | 0.24 | | | |
| 1.0 | | 0.21 | | 0.17 | |
| 2.0 | | 0.13 | | | |
| kst,c | | | | | |
| 0.5 | | 0.17 | | | |
| 1.0 | | 0.14 | | 0.16 | |
| 2.0 | | 0.08 | | | |

separation of flow

| Ar | Qc/Qs | | | | |
|---|---|---|---|---|---|
| | 0.49 | 0.52 | 0.56 | 0.59 | 0.72 |
| ks,st | k-factor | | | | |
| 0.5 | | 0.07 | | | |
| 1.0 | 0.04 | | | | 0.12 |
| 2.0 | | | 0.07 | | |
| ks,c | | | | | |
| 0.5 | | 0.27 | | | |
| 1.0 | 0.31 | | | | 0.29 |
| 2.0 | | | 0.16 | | |

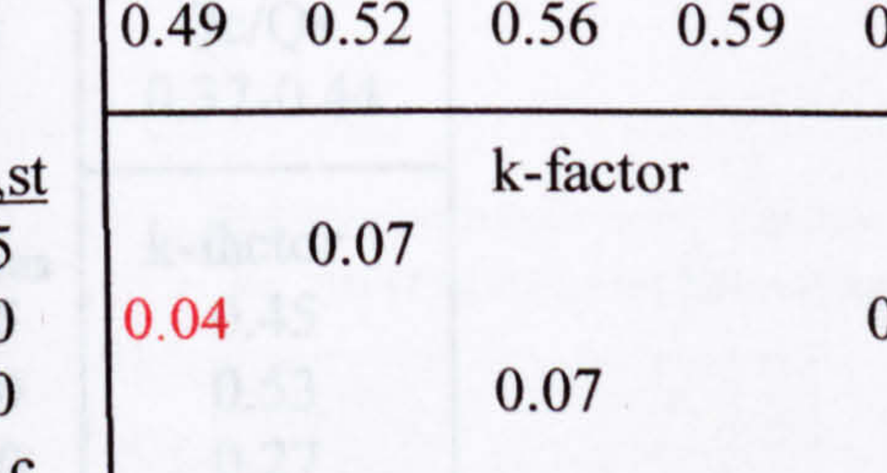


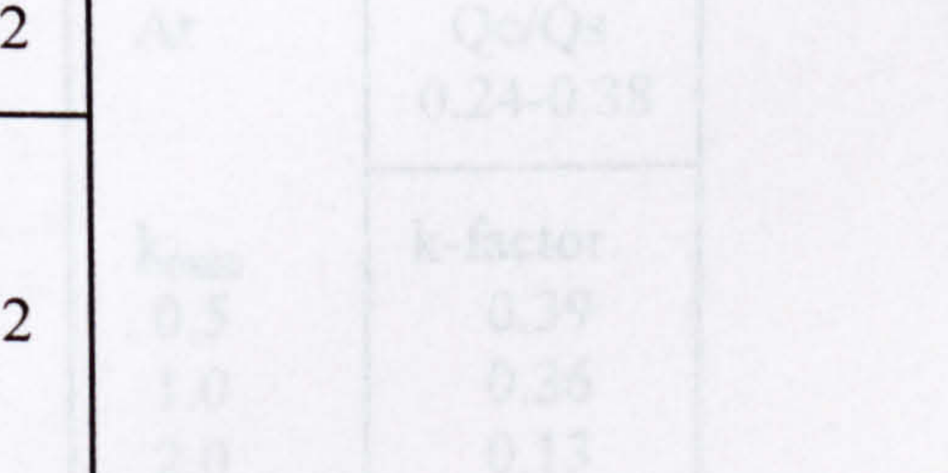

## 2.1.8 Multi-branch.

Ar = h / w , $\alpha = 45°$
type Fs = Fst = Fc.
Qs / Qc = flow rate ratios from branch to main.

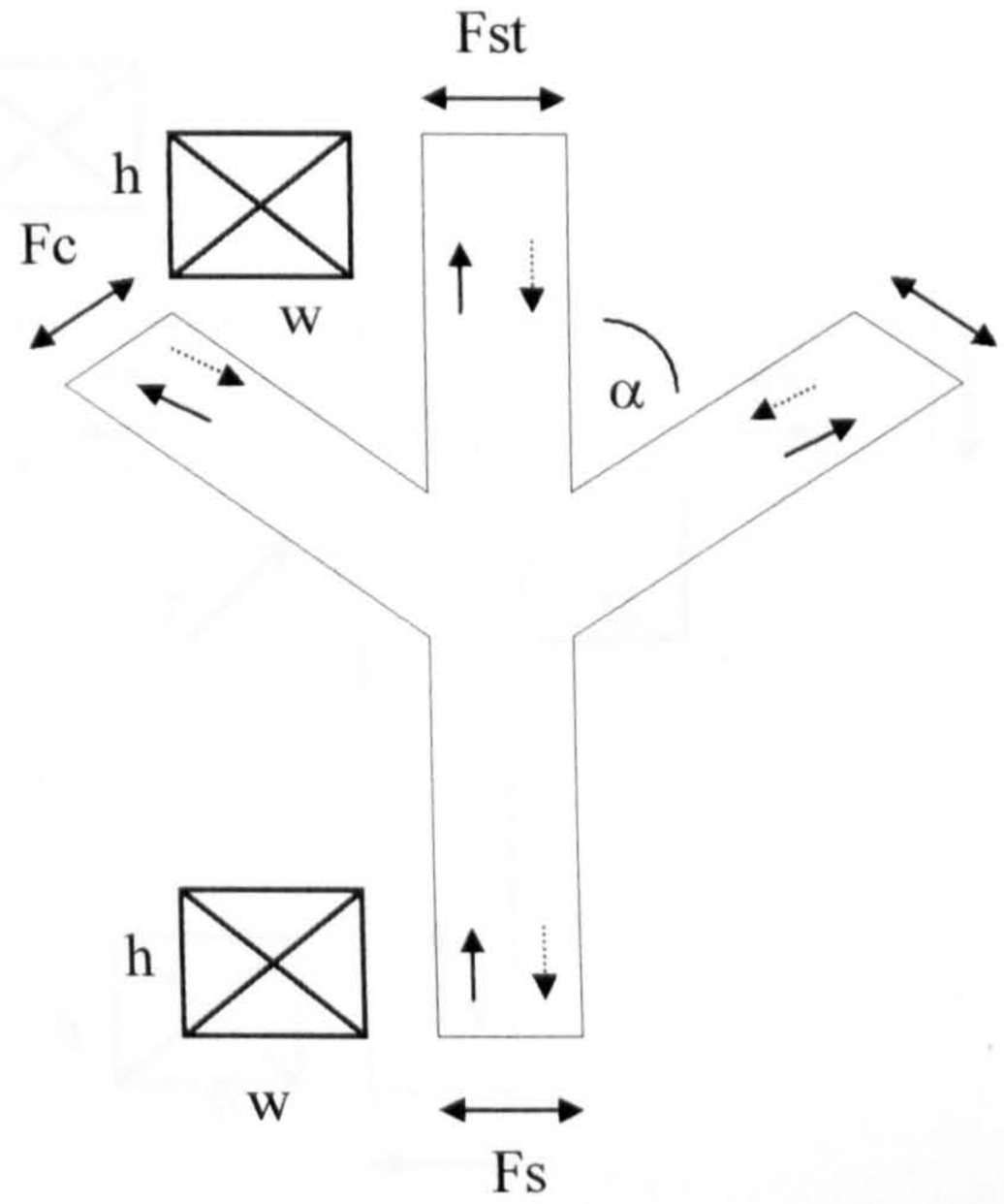


merging of flow

| Ar | Qc/Qs 0.37-0.44 |
|---|---|
| $k_{main}$ | k-factor |
| 0.5 | 0.45 |
| 1.0 | 0.53 |
| 2.0 | 0.27 |
| $k_{branch}$ | |
| 0.5 | 0.46 |
| 1.0 | 0.40 |
| 2.0 | 0.30 |

separation of flow

| Ar | Qc/Qs 0.24-0.38 |
|---|---|
| $k_{main}$ | k-factor |
| 0.5 | 0.39 |
| 1.0 | 0.36 |
| 2.0 | 0.13 |
| $k_{branch}$ | |
| 0.5 | 0.60 |
| 1.0 | 0.72 |
| 2.0 | 0.48 |

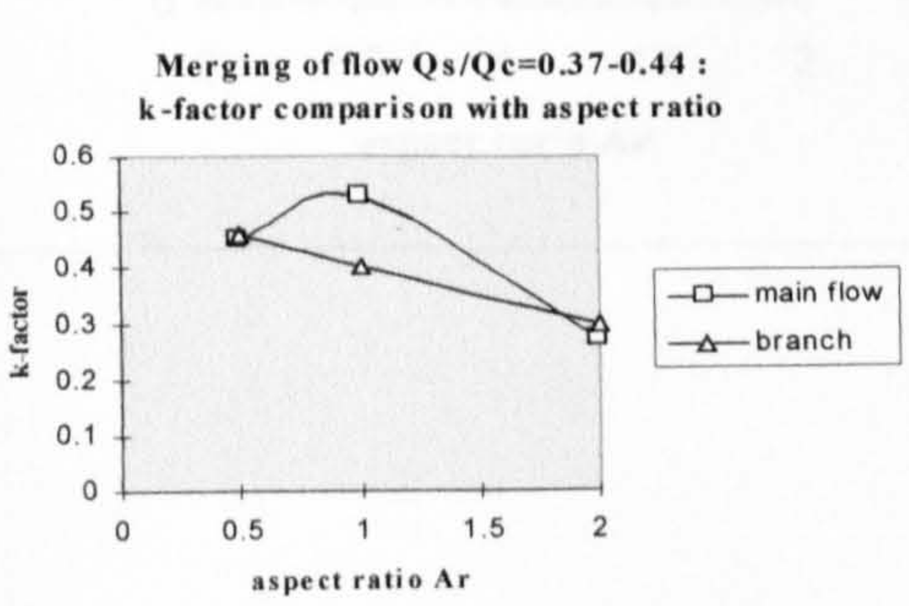


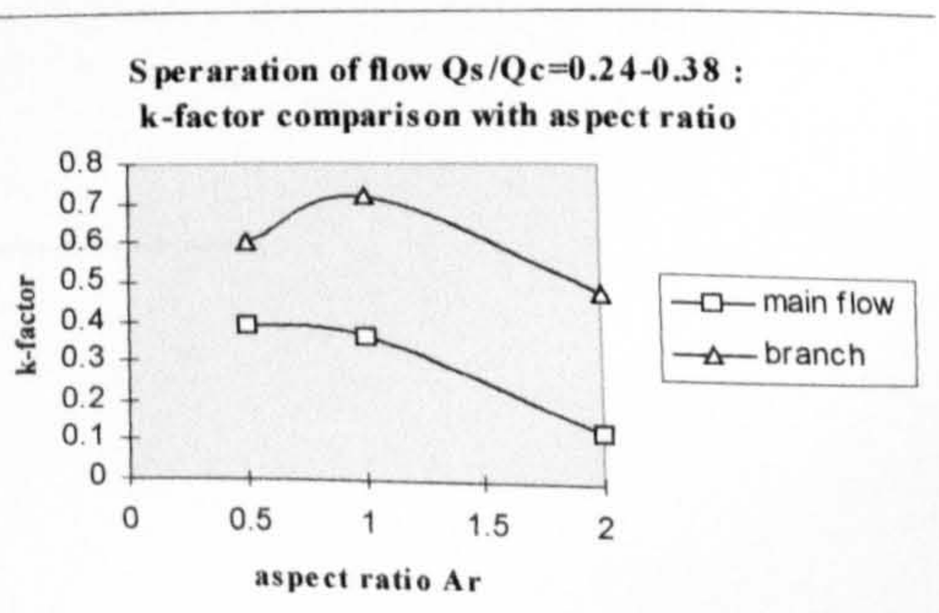

## 2.1.9 Symmetrical wye.

Ar = h / w , $\alpha = 90°$.
r /w = 1.50 , type Fs = Fc.

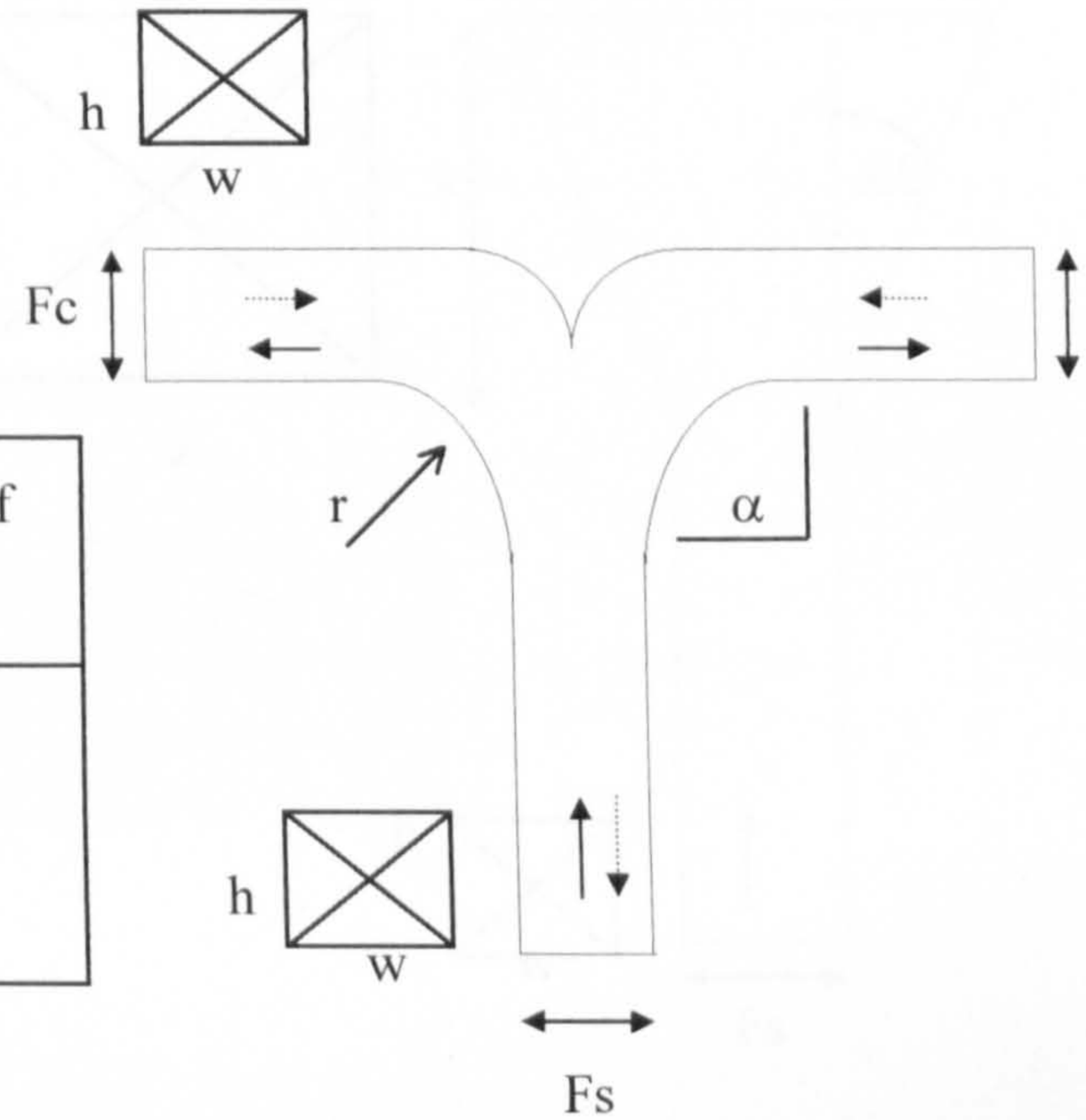


| Ar | merging of flow k | separation of flow k |
|---|---|---|
| 0.5 | 0.08 | 0.23 |
| 1.0 | 0.05 | 0.19 |
| 2.0 | 0.03 | 0.18 |

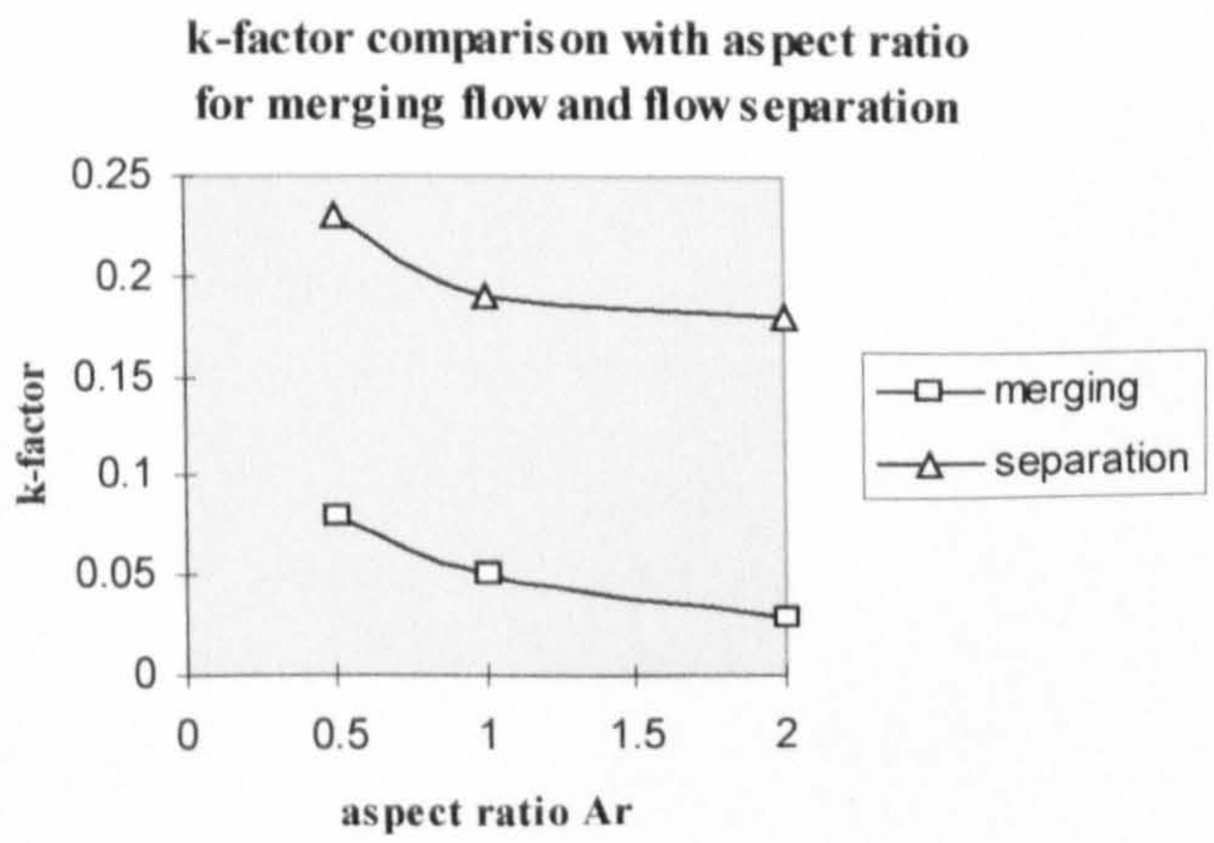

## 2.1.10 Exit diffuser.

Ar = h / w = 1.0
x = 0.68 m .

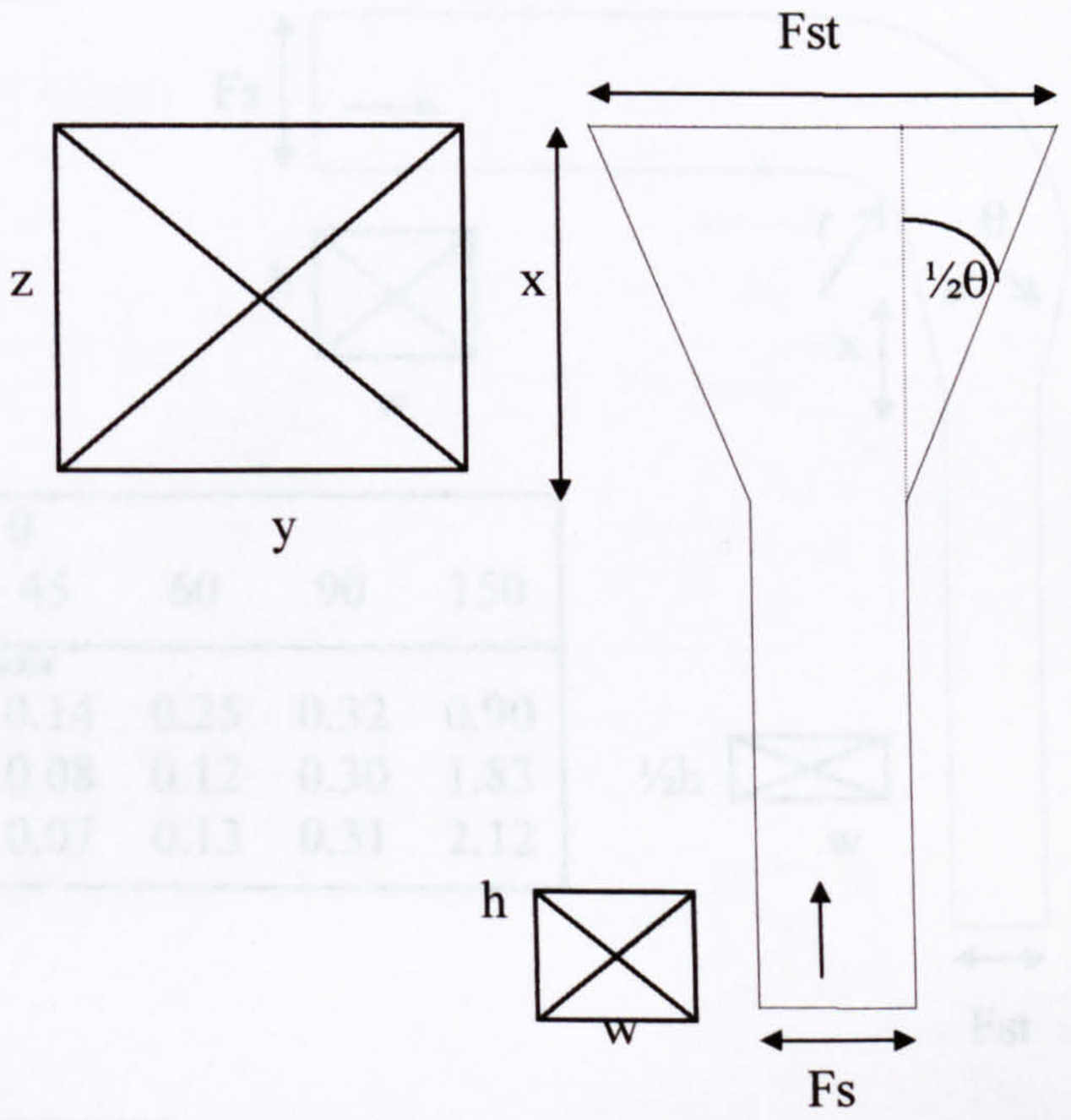


| Fst/Fs | θ<br>20 |
|---|---|
| 7.0 | k-factor<br>0.50 |

## 2.1.11 90° bend plus contraction.

Ar = h / w = 1.0 , r / w = 1.0
x = ( 0.24 m – 0.48 m )
type Fs > Fst.

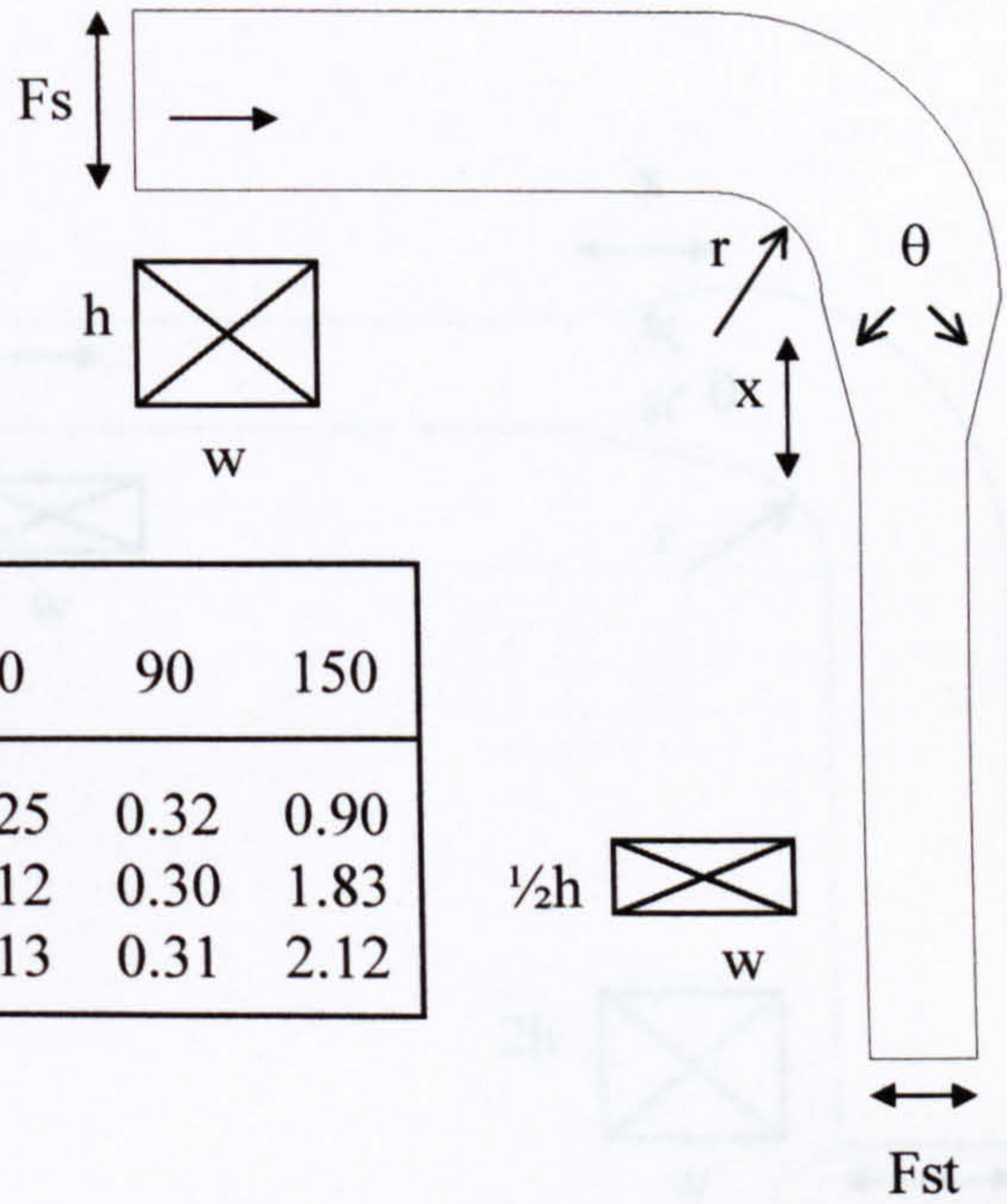


| Fs/Fst | θ | | | | | | |
|---|---|---|---|---|---|---|---|
| | 10 | 20 | 35 | 45 | 60 | 90 | 150 |
| | k-factor | | | | | | |
| 2.0 | 0.09 | 0.11 | 0.20 | 0.14 | 0.25 | 0.32 | 0.90 |
| 4.0 | 0.08 | 0.09 | 0.08 | 0.08 | 0.12 | 0.30 | 1.83 |
| 6.0 | 0.07 | 0.07 | 0.09 | 0.07 | 0.13 | 0.31 | 2.12 |

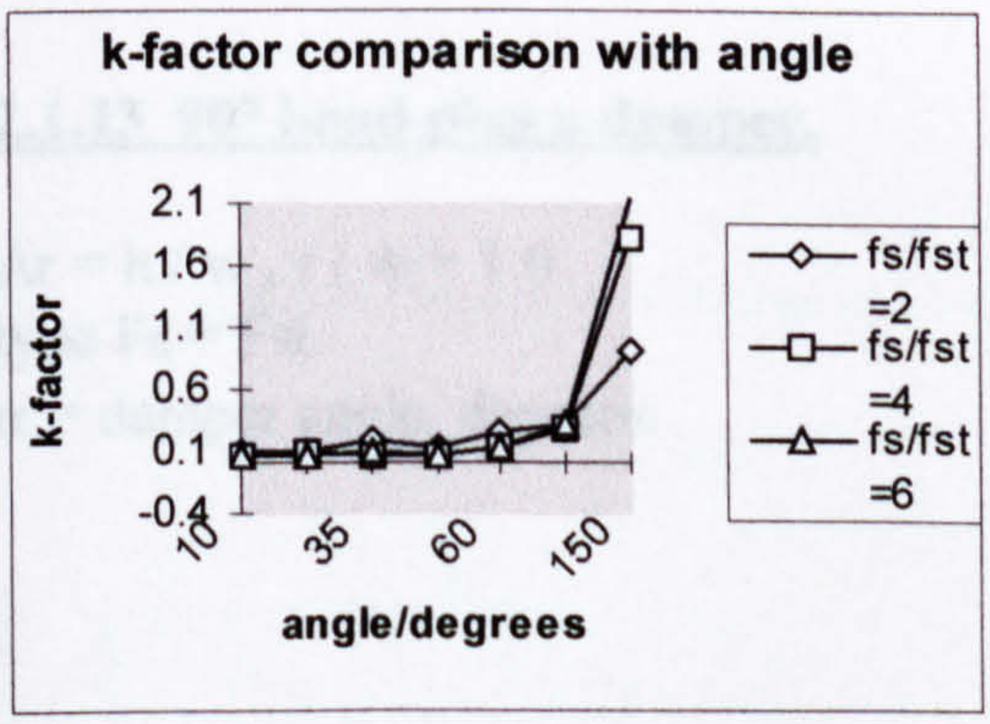


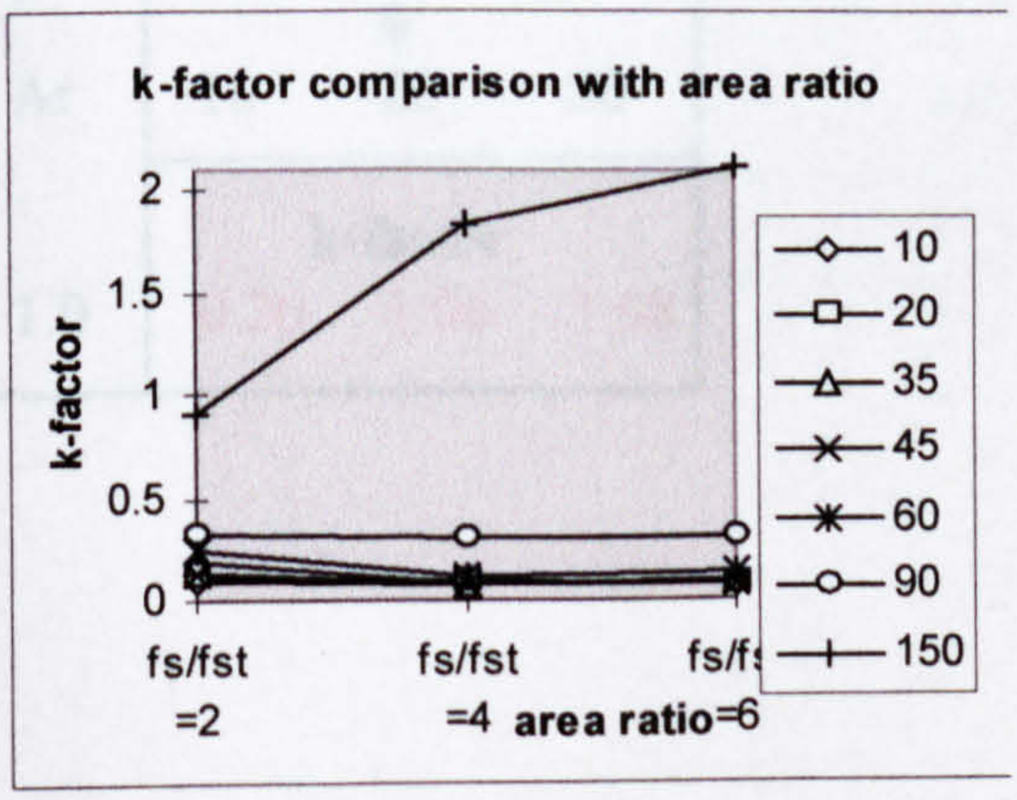

## 2.1.12 Expansion plus 90° bend.

Ar = h / w = 0.5 , x = ( 0.24 m –0.48 m )
r / w = 1.0 , type Fs < Fst.

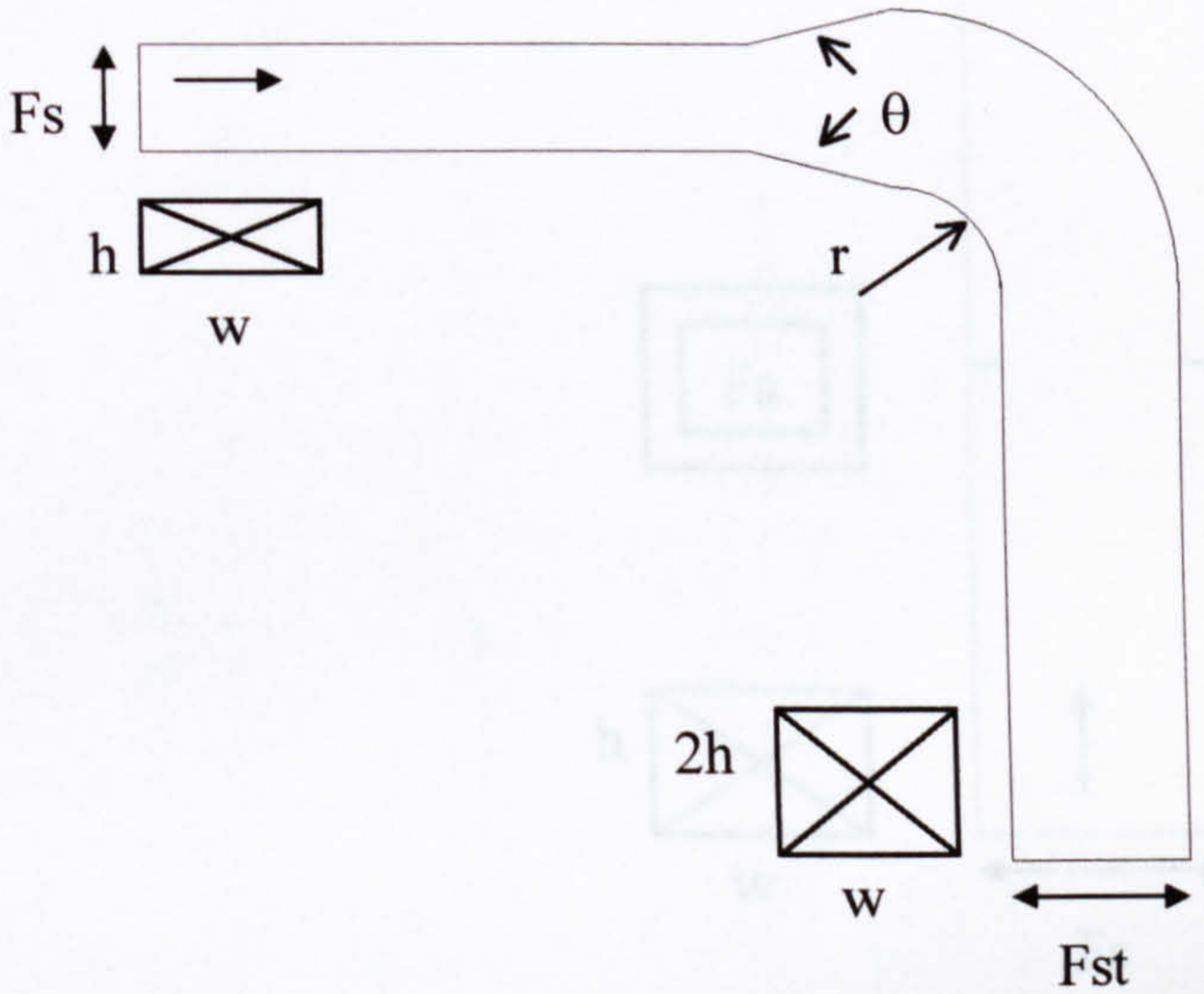


| Fst/Fs | θ 35 |
|---|---|
| 2.0 | k-factor 0.33 |

## 2.1.13 90° bend plus a damper.

Ar = h / w , r / w = 1.0
type Fs = Fst.
α = damper angle, degrees.

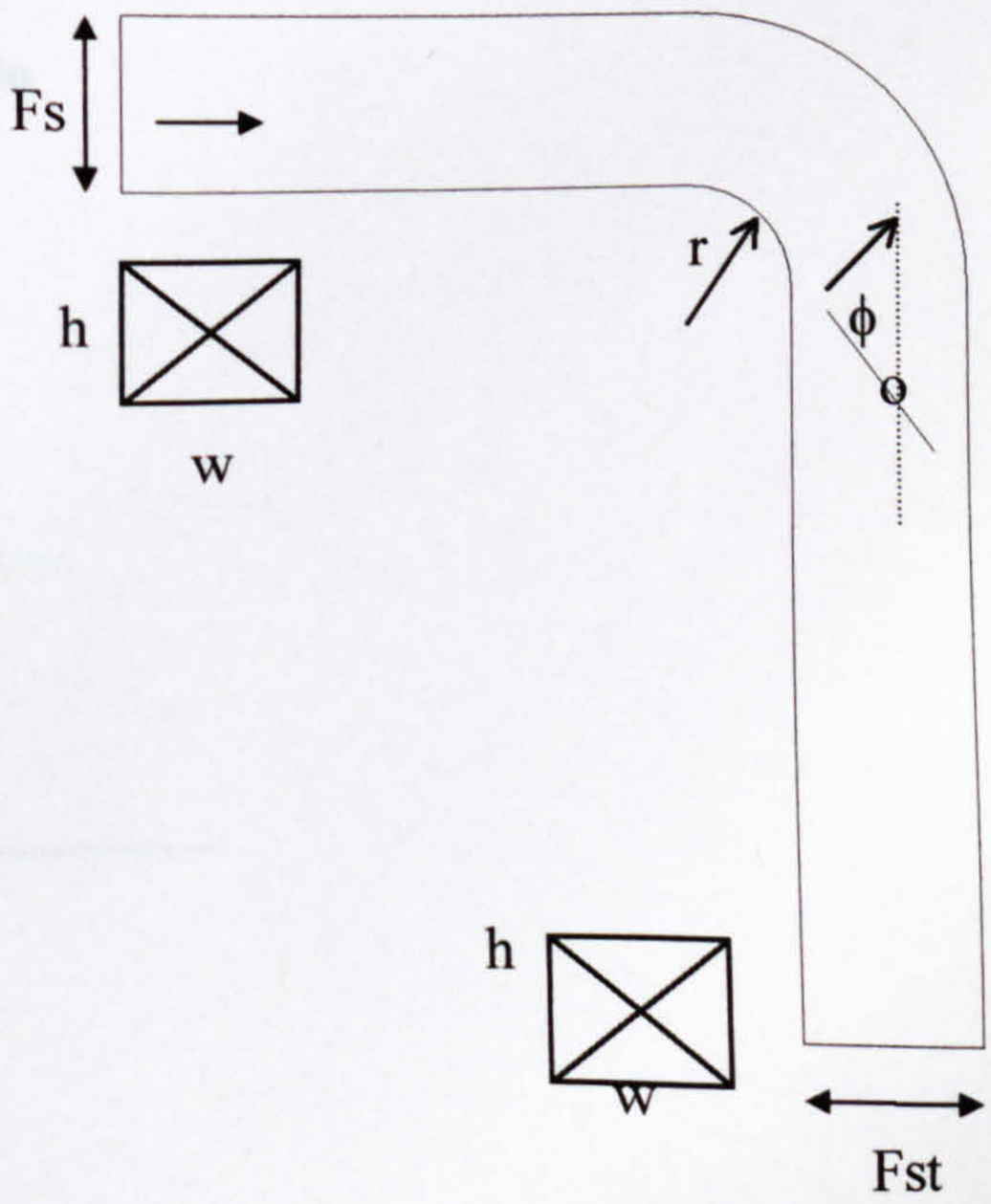


| Ar | ϕ 10 | 20 | 30 |
|---|---|---|---|
| 1.0 | k-factor 0.26 | 1.06 | 1.98 |

## 2.1.14 Rectangular single orifice.

Square centrally placed.
n = free surface area ratio = Fa / Fs.
Ar = h / w = 1.0, Fs = const.

| n | 0.2 | 0.3 | 0.4 |
|---|---|---|---|
| k | 34.05 | 11.85 | 6.05 |

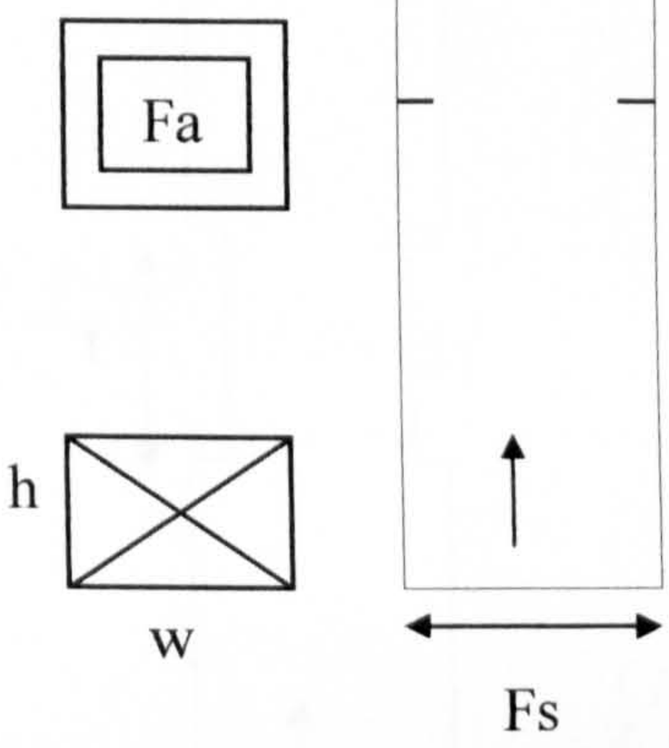


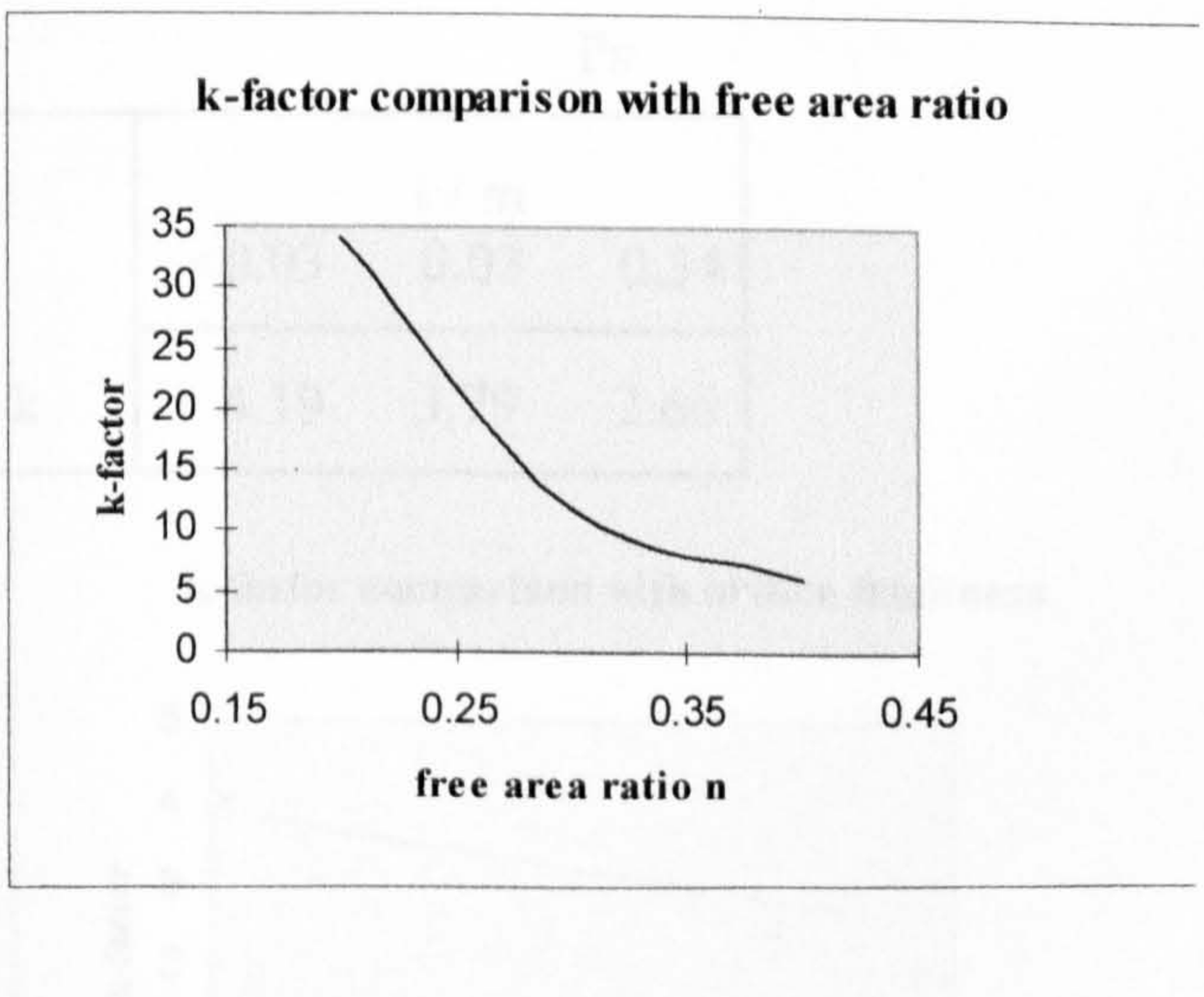

## 2.1.15 Circular single orifice.

Circular centrally placed.
n = free surface area ratio = Fa / Fs = 0.5
Ar = h / w = 1.0, t = plate and step thickness .

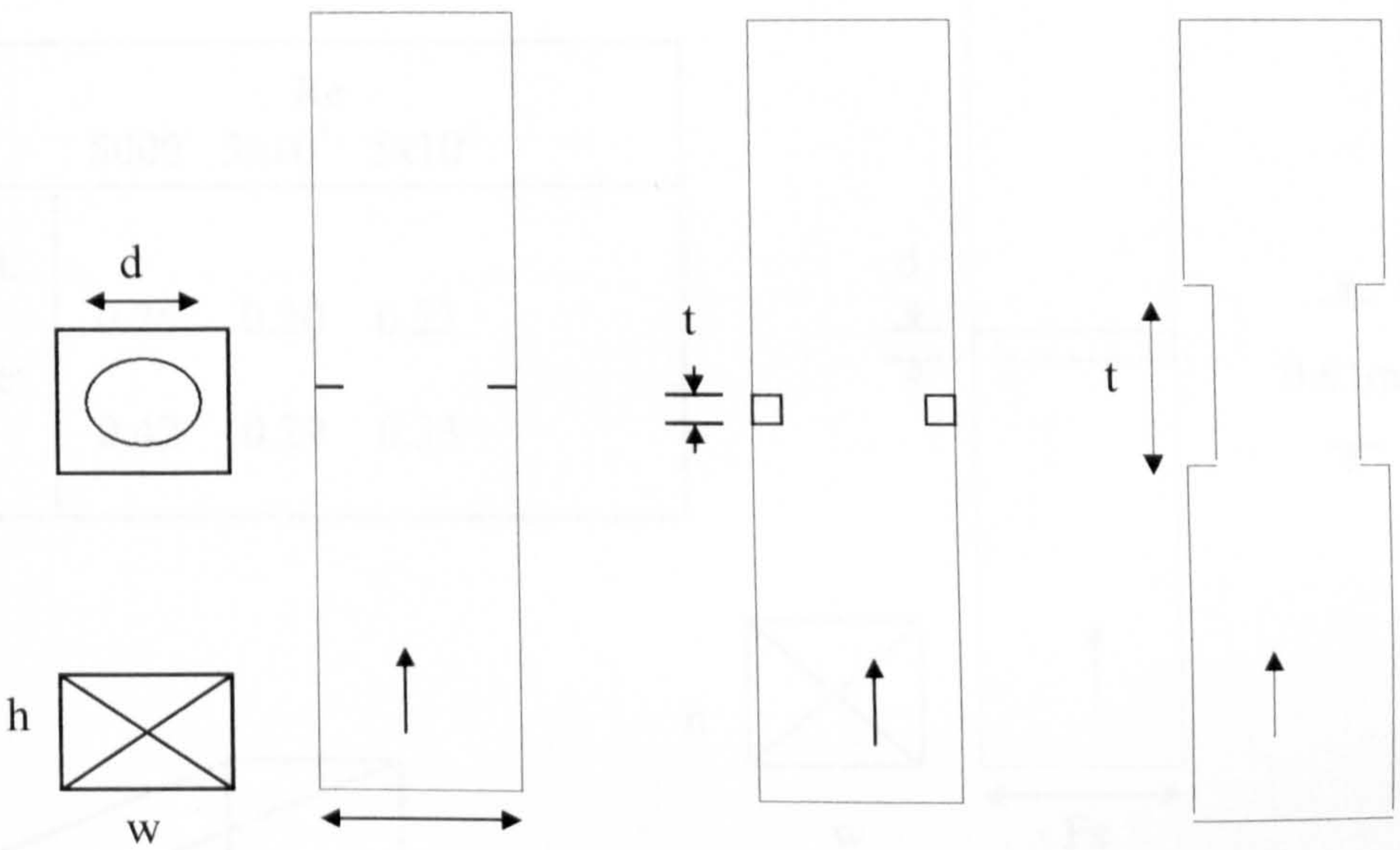


| | t / m | | |
|---|---|---|---|
| | <0.03 | 0.03 | 0.34 |
| k | 4.19 | 3.79 | 2.66 |

**k-factor comparison with orifice thickness**

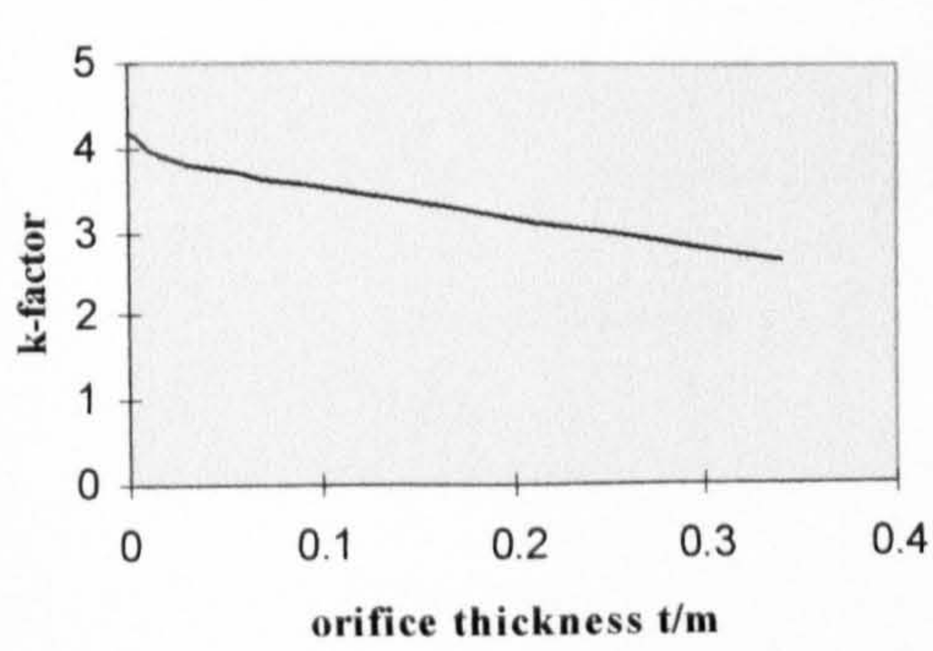

## 2.1.16 Circular obstruction.

Cylindrical obstruction centrally placed perpendicular to flow.
d = 0.075 m, Ar = h / w = 1.0
Double obstruction separation = 0.061 m
Re = Reynolds number.

| | Re | | |
|---|---|---|---|
| | 5000 | $3x10^5$ | $5x10^5$ |
| Sngl: k | 0.25 | 0.20 | 0.22 |
| Dble: k | 0.42 | 0.29 | 0.33 |

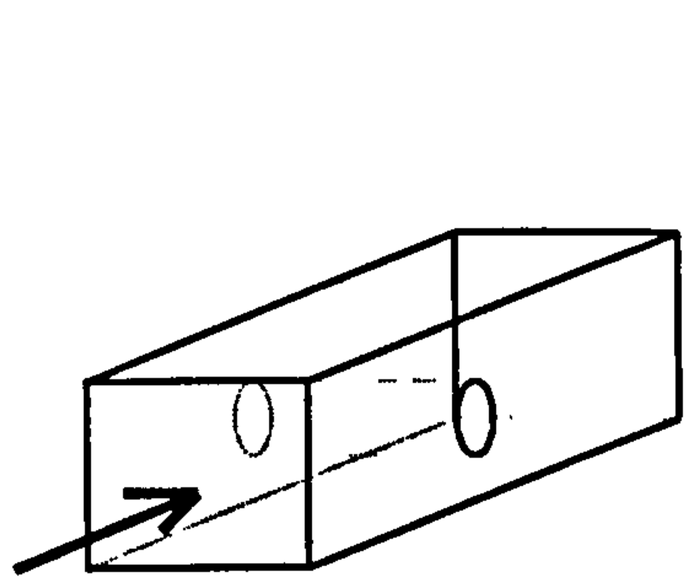

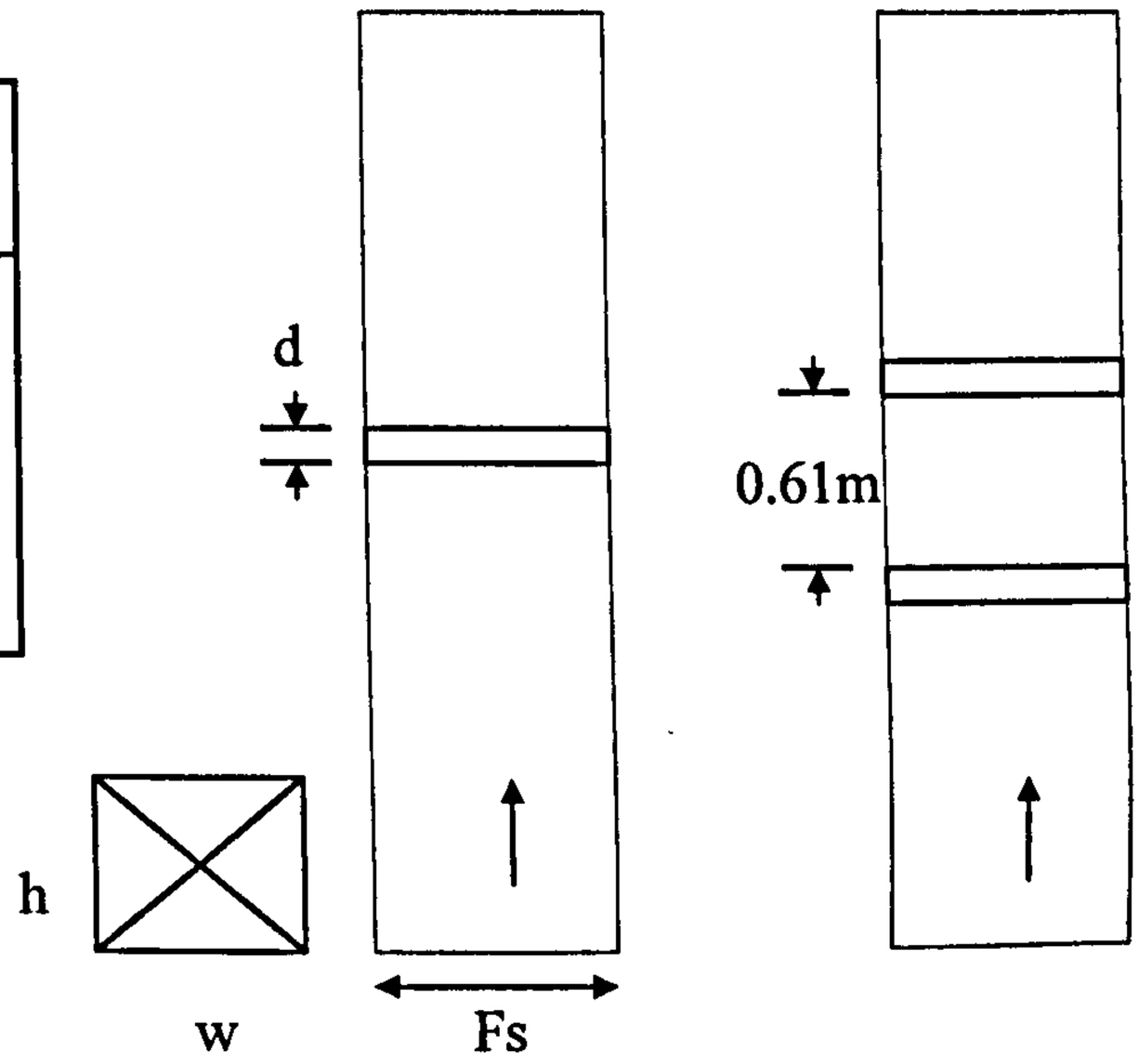

## 2.2 Circular cross-section :

### 2.2.1 U-bend.

d = diameter, duct cross-section Fs = const. x

$\alpha = 90°$, r / d = 1.0

| x | 0 | 0.5 | 1.0 | 1.2 |
|---|---|---|---|---|
| k | 0.22 | 0.22 | 0.31 | 0.27 |

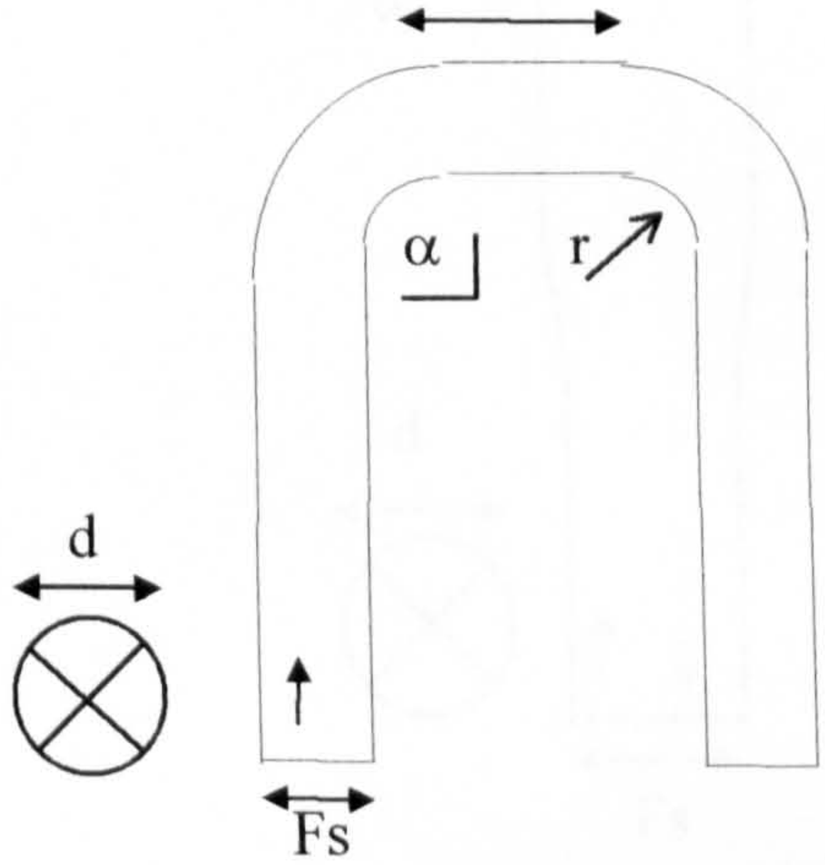


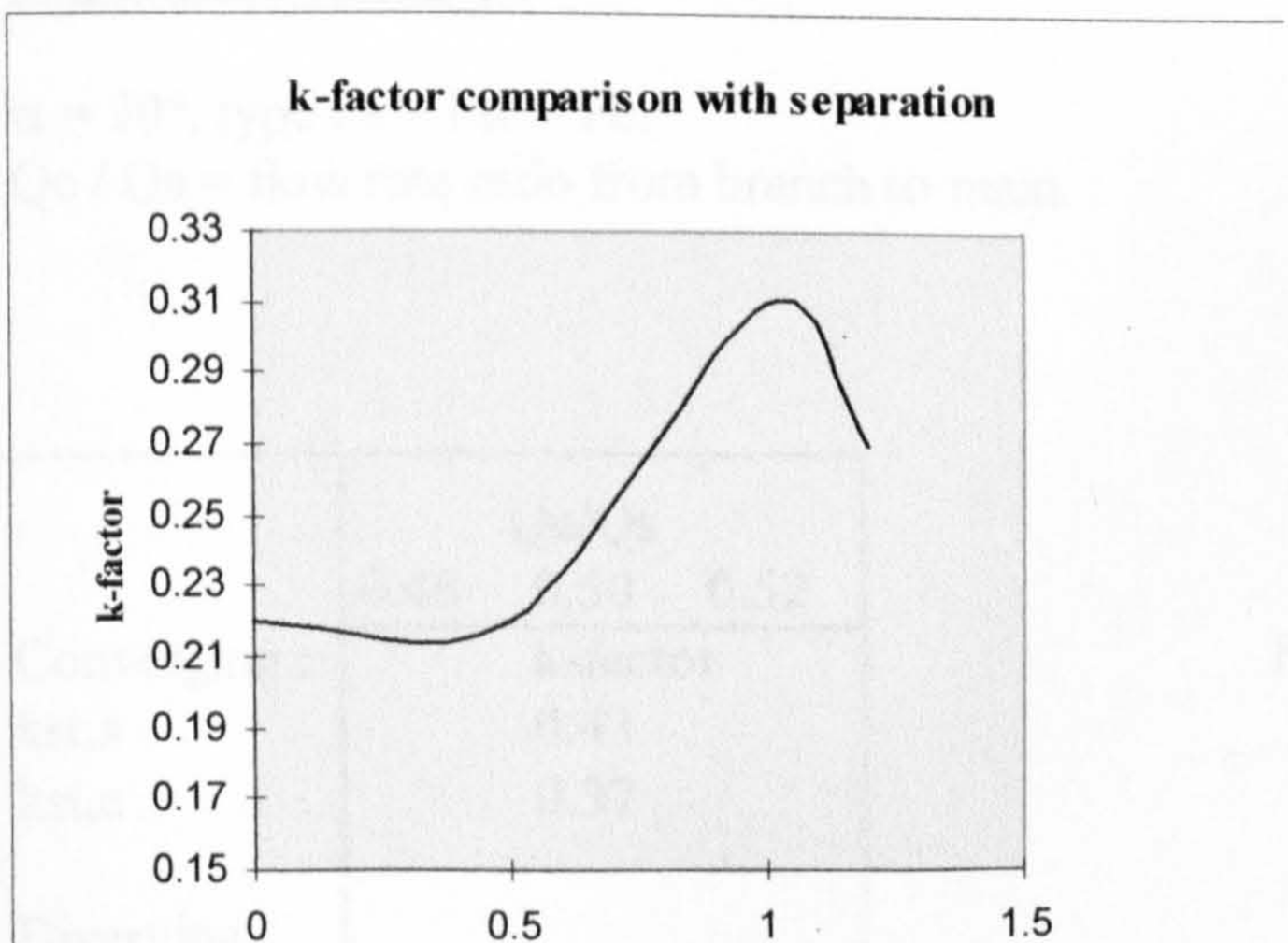

## 2.2.2 Circular / Square transition.

Ar = h / w = 1.0, type d = w.
Fs / Fst = 0.25.

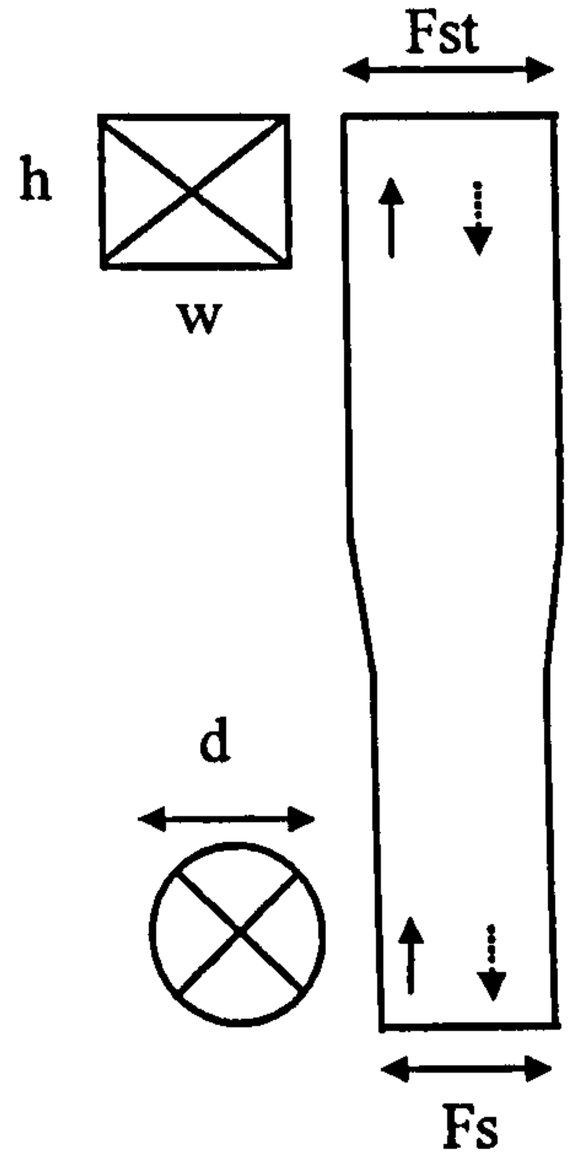


| Direction | k |
|---|---|
| ○ → □ | 0.47 |
| □ → ○ | 0.02 |

## 2.2.3 90° T-Branch.

α = 90°, type Fs + Fst > Fc.
Qc / Qs = flow rate ratio from branch to main.

| | Qc/Qs | | |
|---|---|---|---|
| | 0.48 | 0.50 | 0.52 |
| Converging : | | k-factor | |
| kst,s | | 0.43 | |
| kst,c | | 0.37 | |
| Diverging : | | | |
| ks,st | -0.02 | | |
| ks,c | | | 0.85 |

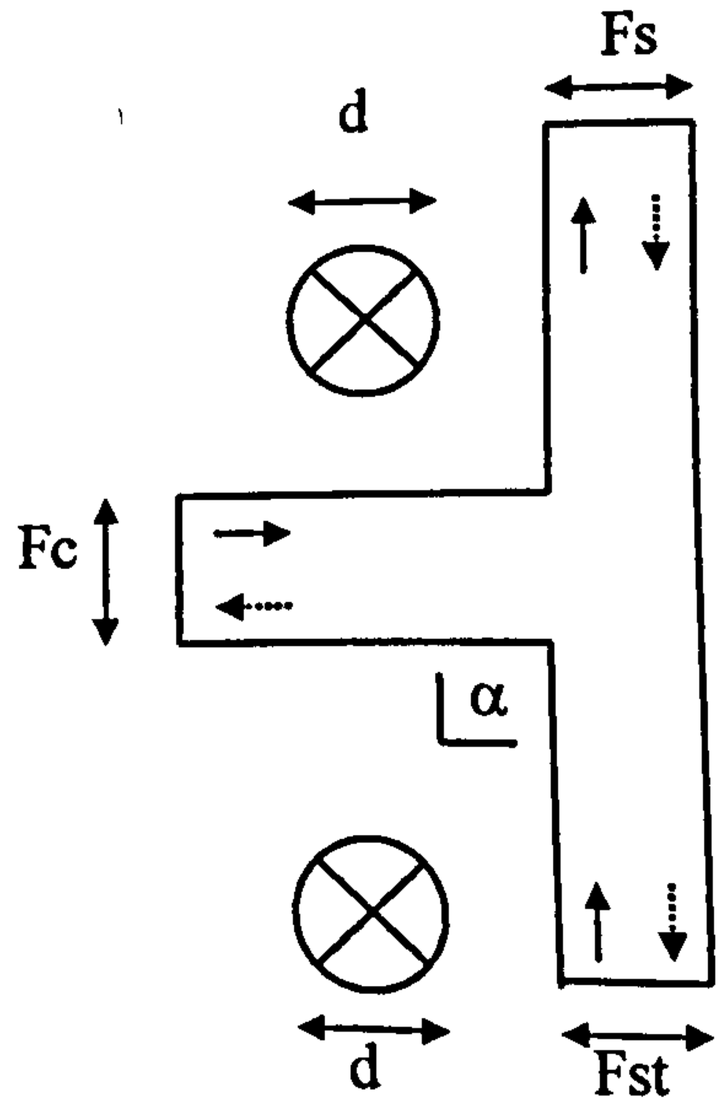

## 2.2.4 45° T-Branch.

$\alpha = 45°$, type Fs + Fst > Fc.
Qc / Qs = flow rate ratio from branch to main.

| | Qc/Qs | | | |
|---|---|---|---|---|
| | 0.34 | 0.42 | 0.49 | 0.66 |
| Converging : | | k-factor | | |
| Main kst,s | | | 0.08 | |
| Branch kst,c | | 0.03 | | |
| Diverging : | | | | |
| Main ks,st | | | | 0.004 |
| Branch ks,c | 0.52 | | | |

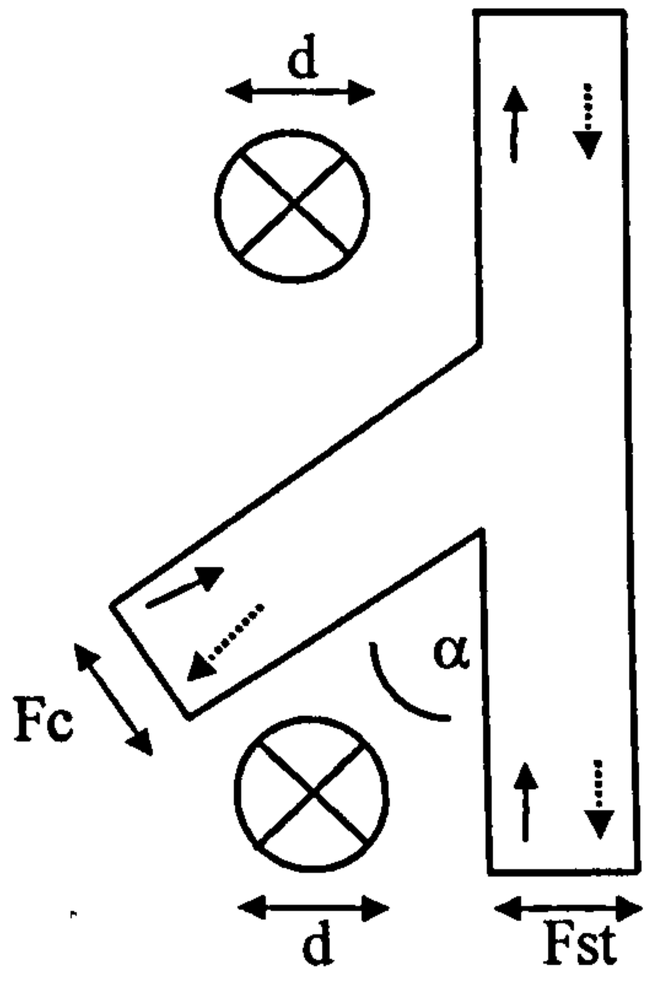


## 2.2.5 90° Round smooth bend:

Type Fs=Fst, r/d=1.5

| Dia/d | k-factor |
|---|---|
| 0.0762 | 0.23 |
| 0.1016 | 0.18 |

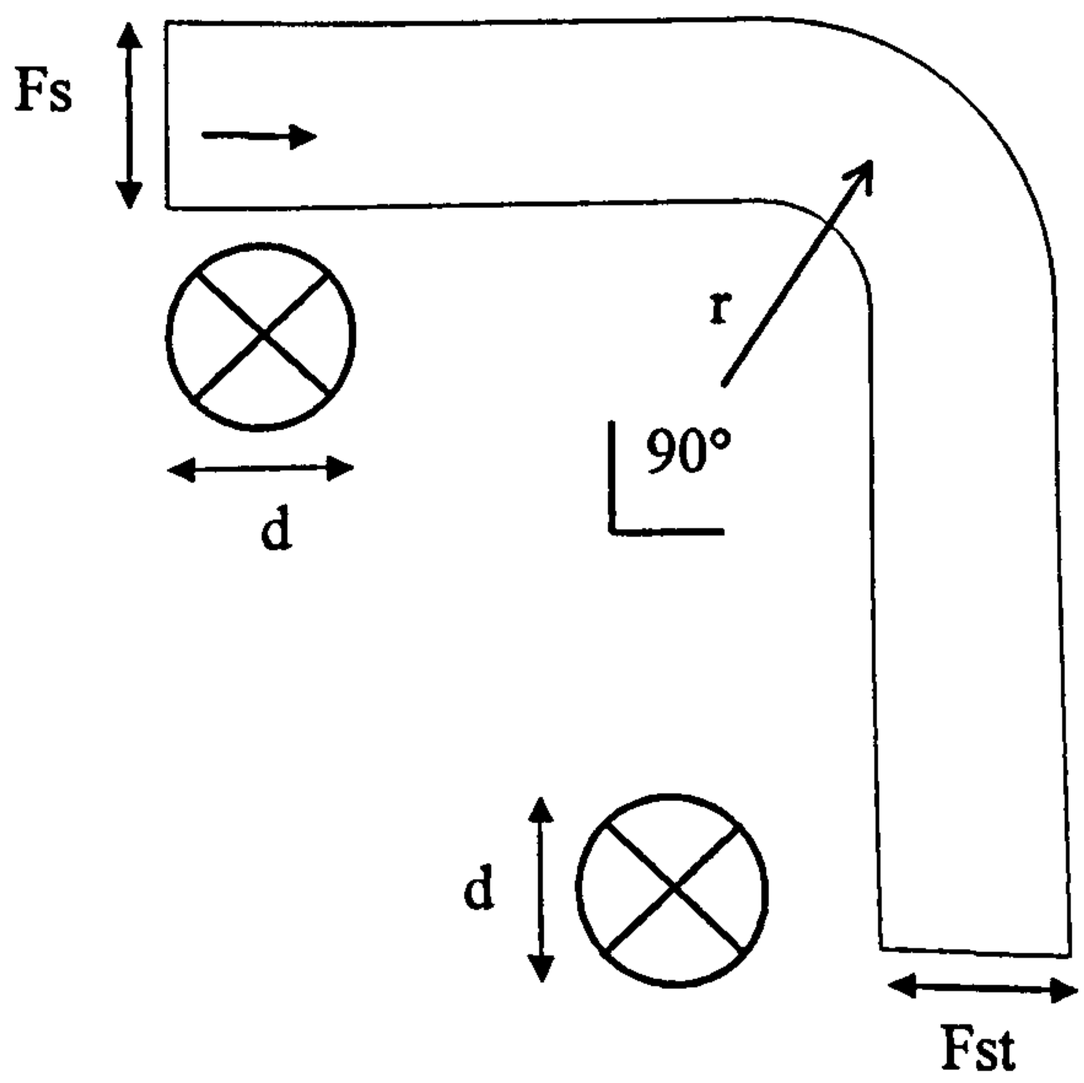

## 2.2.6 90° Bend ( sectioned ).

Type Fs = Fst, r / d = radius to diameter ratio.

| number of sections : 3 4 5 | | | |
|---|---|---|---|
| r/d | k-factor | | |
| 1 | 0.30 | 0.26 | 0.26 |
| 2 | 0.24 | 0.15 | 0.14 |

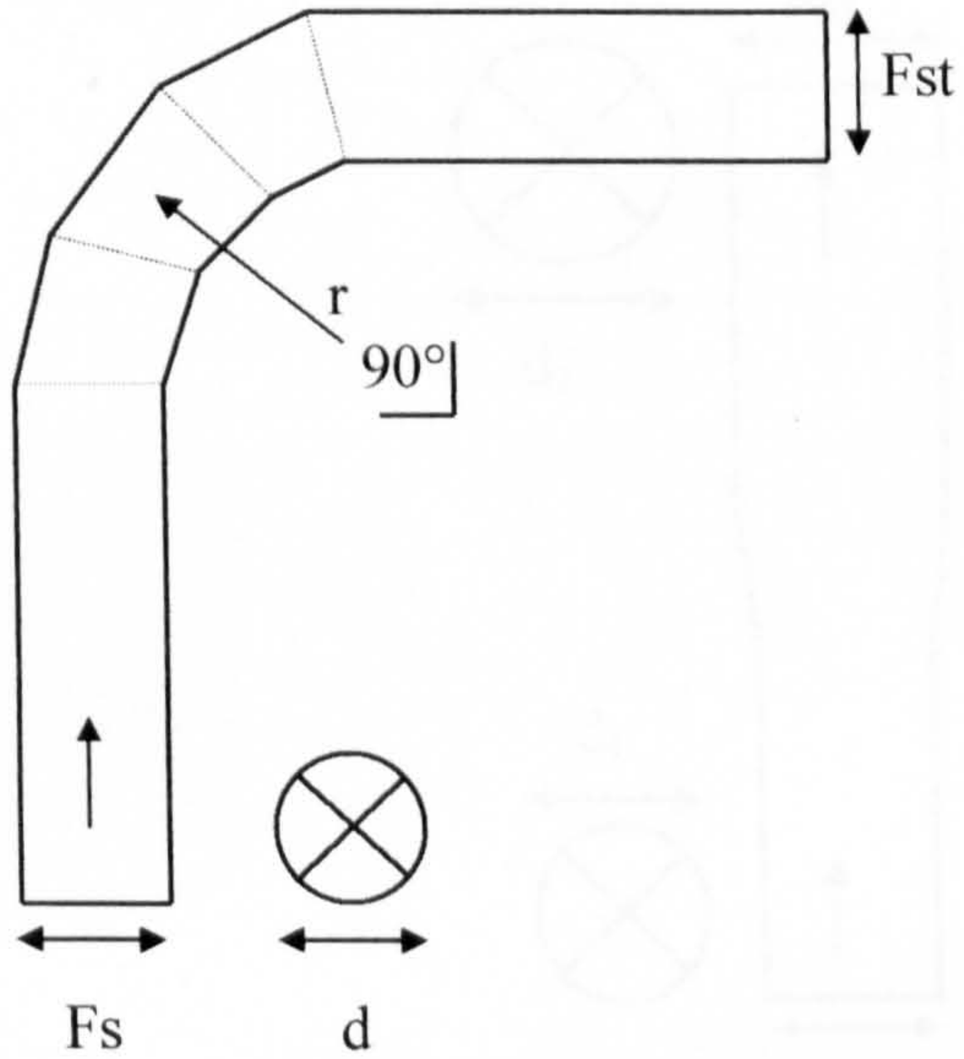


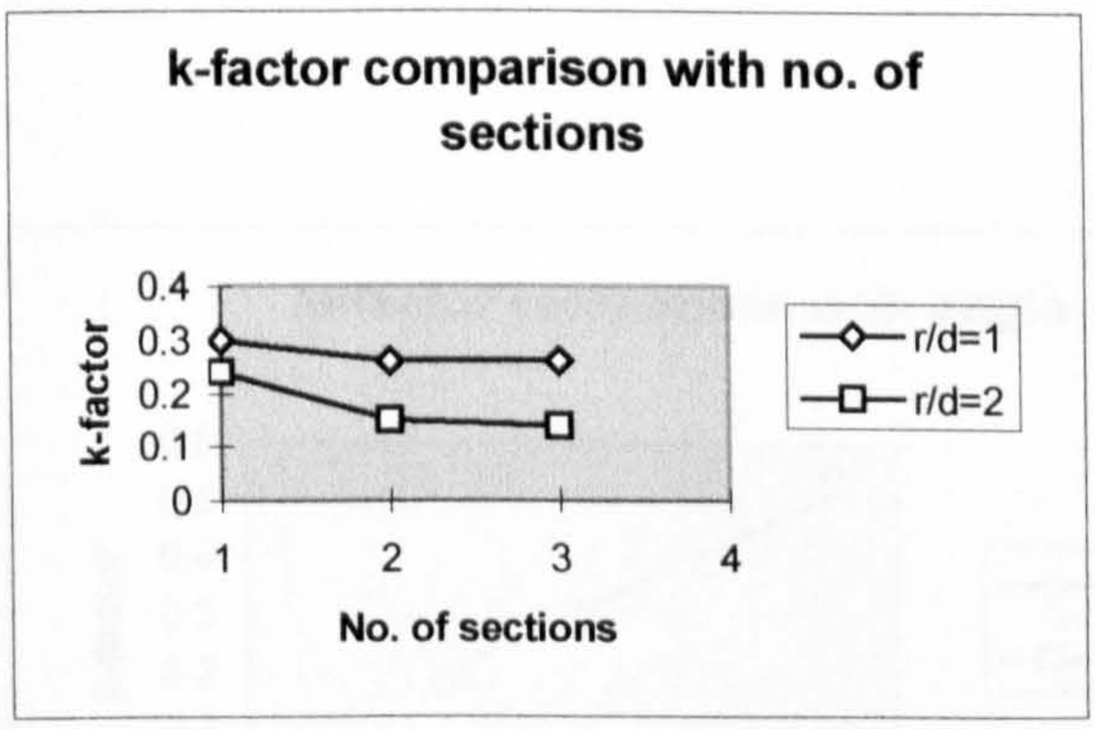

## 2.2.7 Round Transition:

Type Fs/Fst=area transition ratio

| | Fs/Fst=0.1 | Fs/Fst=2 |
|---|---|---|
| Angle | k-factor | |
| 30 | 0.19 | |
| 60 | | 0.08 |
| 90 | 0.55 | 0.06 |

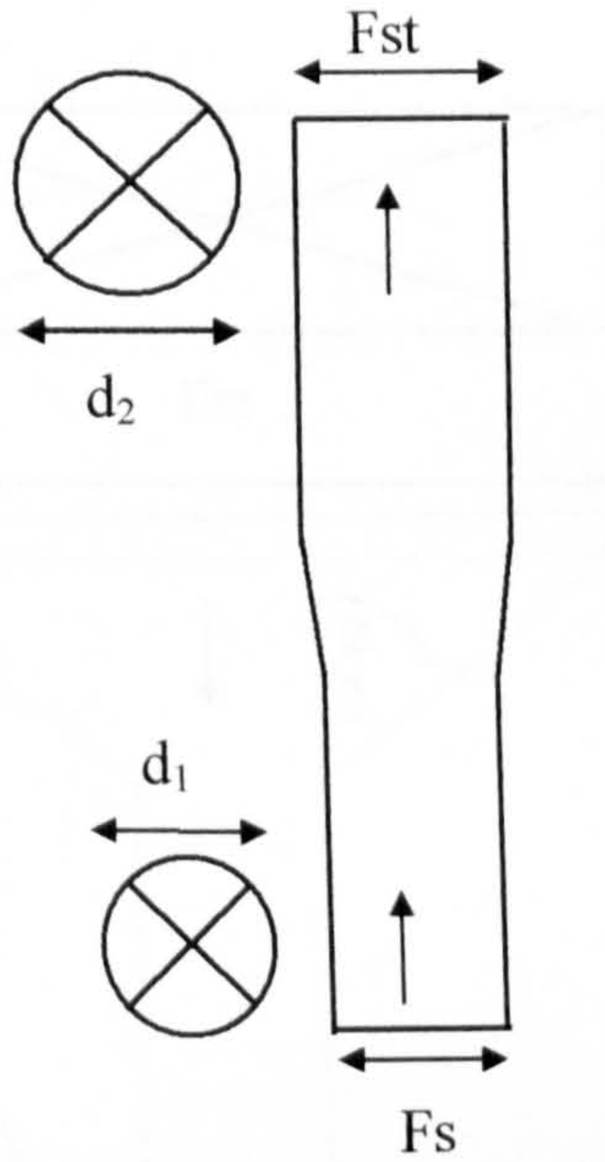


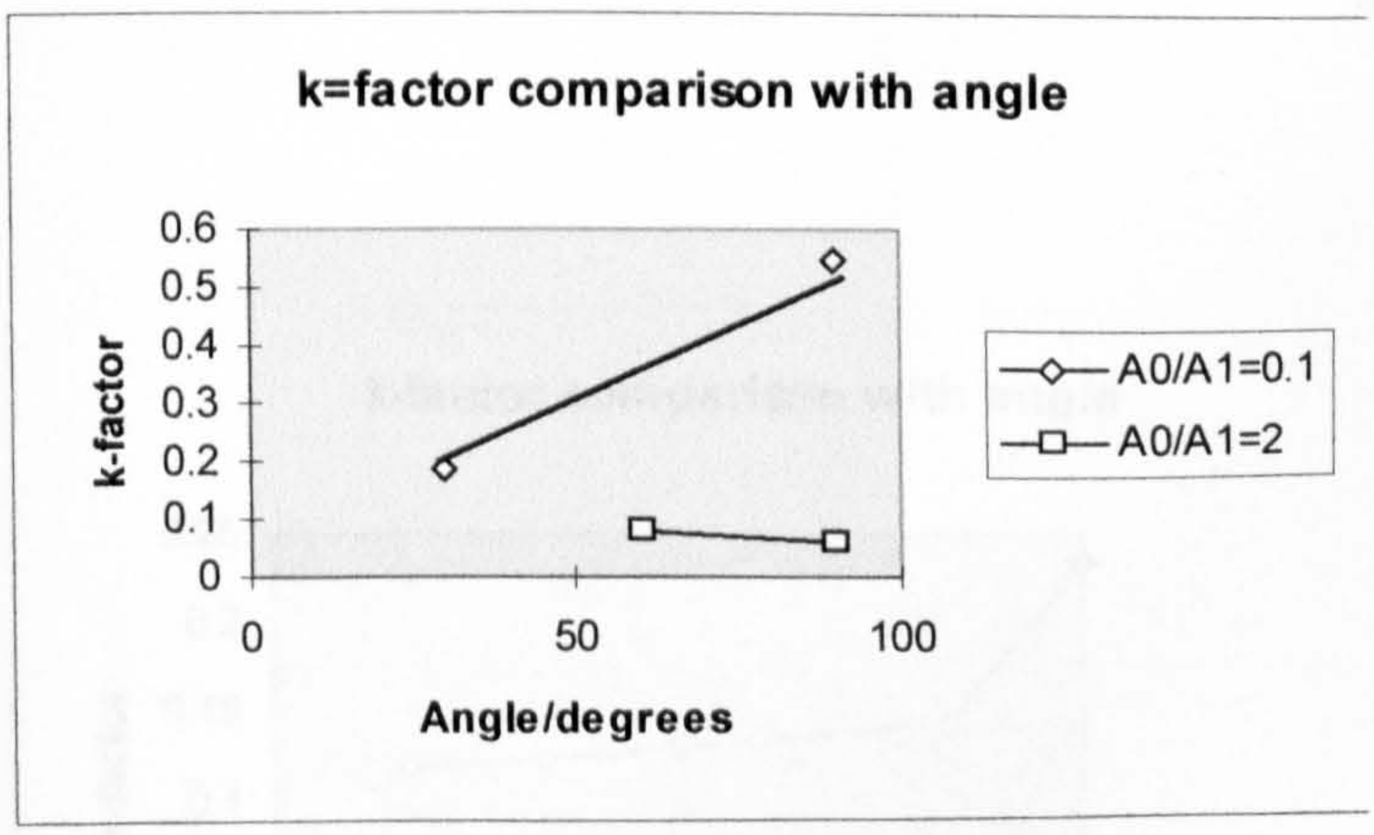

## 2.2.8 Rectangle extract hood:

Type Fst/Fs=22.6, t=0.01 m, x=0.14 m, d=0.14 m

| Angle α/ ° | k-factor |
|---|---|
| 45 | 0.120 |
| 50 | 0.125 |
| 55 | 0.130 |
| 58 | 0.135 |
| 65 | 0.144 |
| 70 | 0.234 |
| 58 (unstructured grid ) | 0.160 |
| Belmouth | 0.120 |

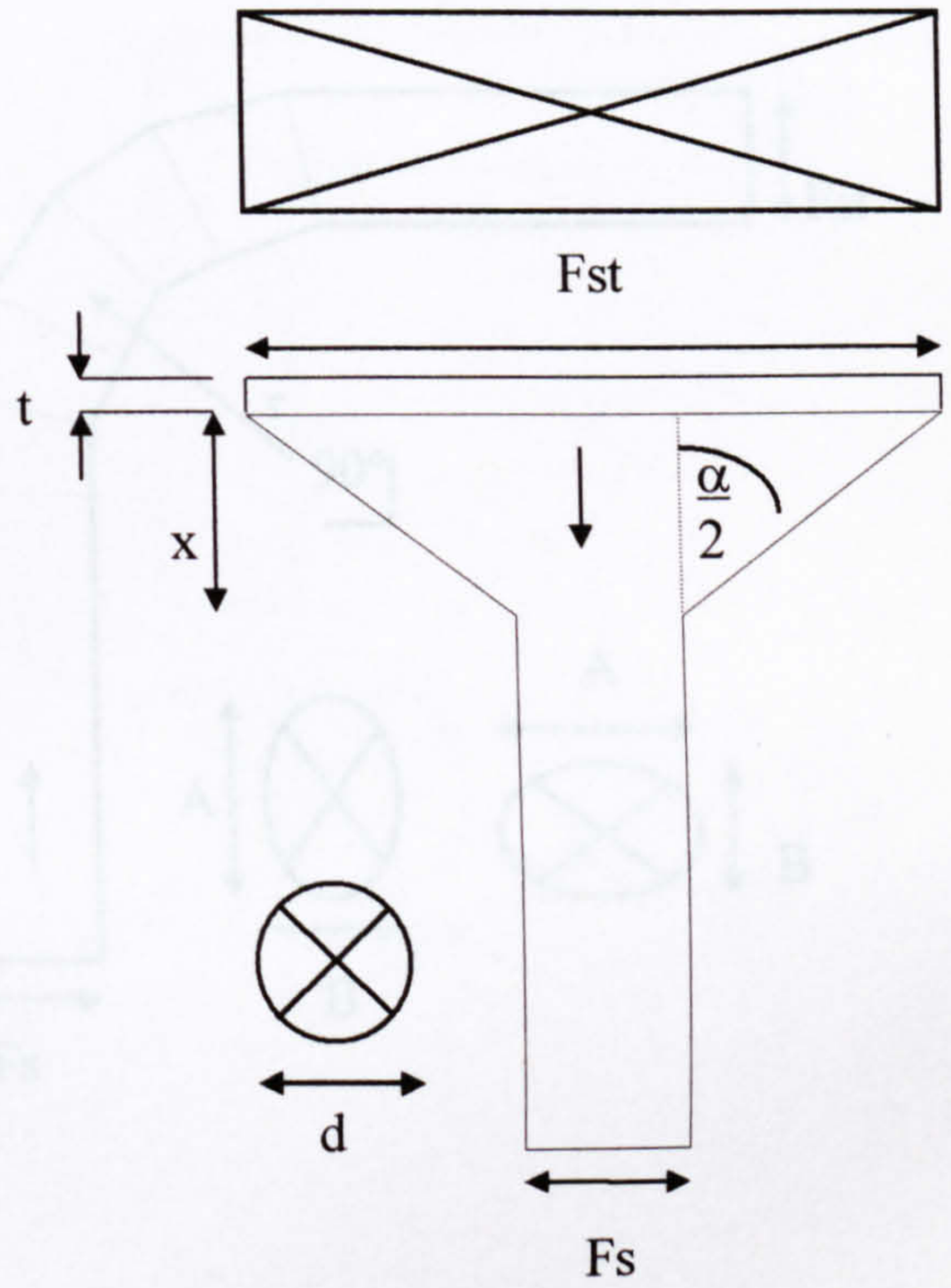


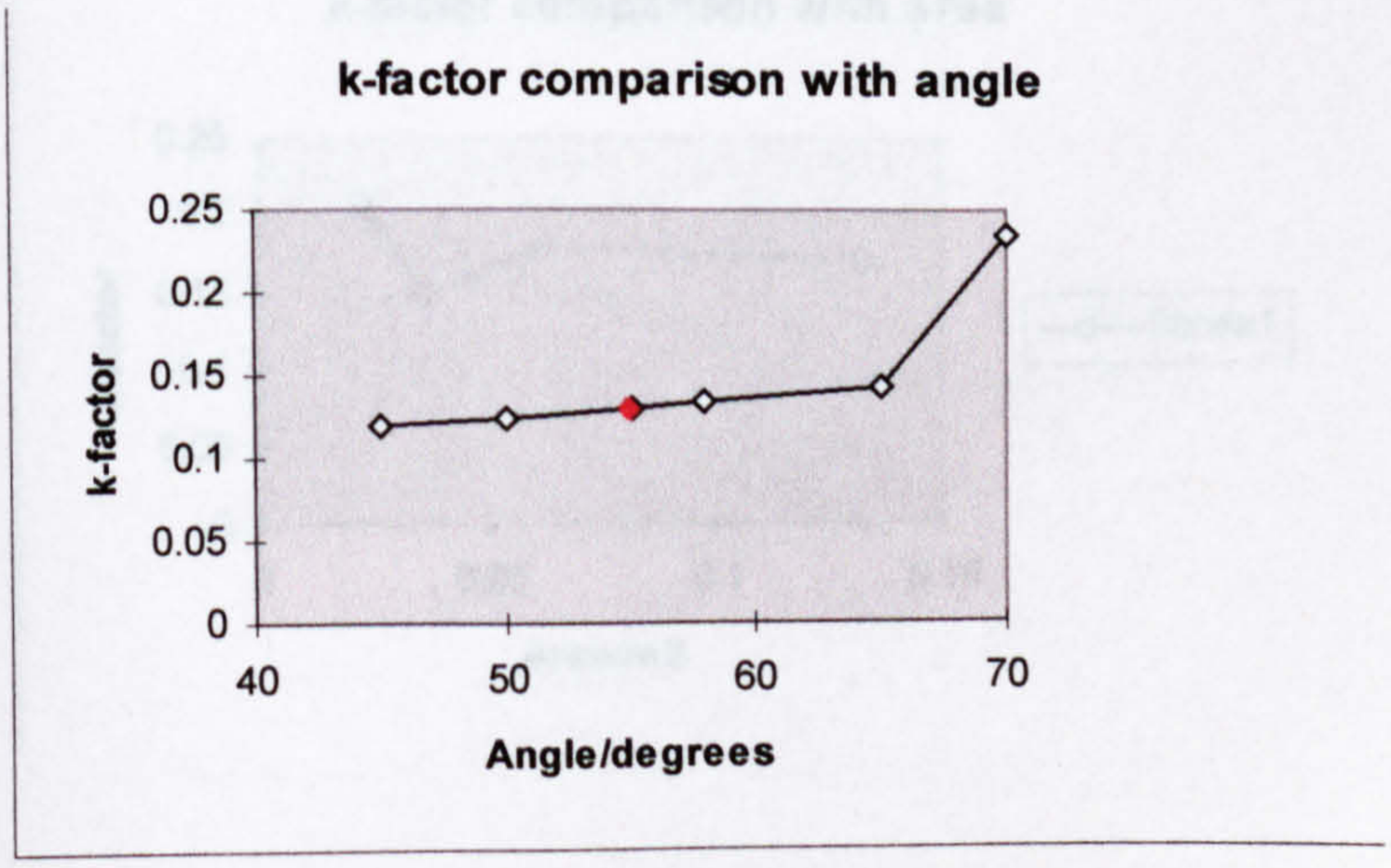

## 2.3 Oval cross-section :

### 2.3.1 90 °Flat oval bend (5-gore):

Type Fs = Fst, r/A = 1.5

| Type: | Easy | Hard |
|---|---|---|
| | k-factor | |
| AxB | | |
| 0.0624 | 0.18 | 0.18 |
| 0.0224 | 0.21 | |
| 0.0364 | 0.15 | |
| 0.1325 | | 0.17 |

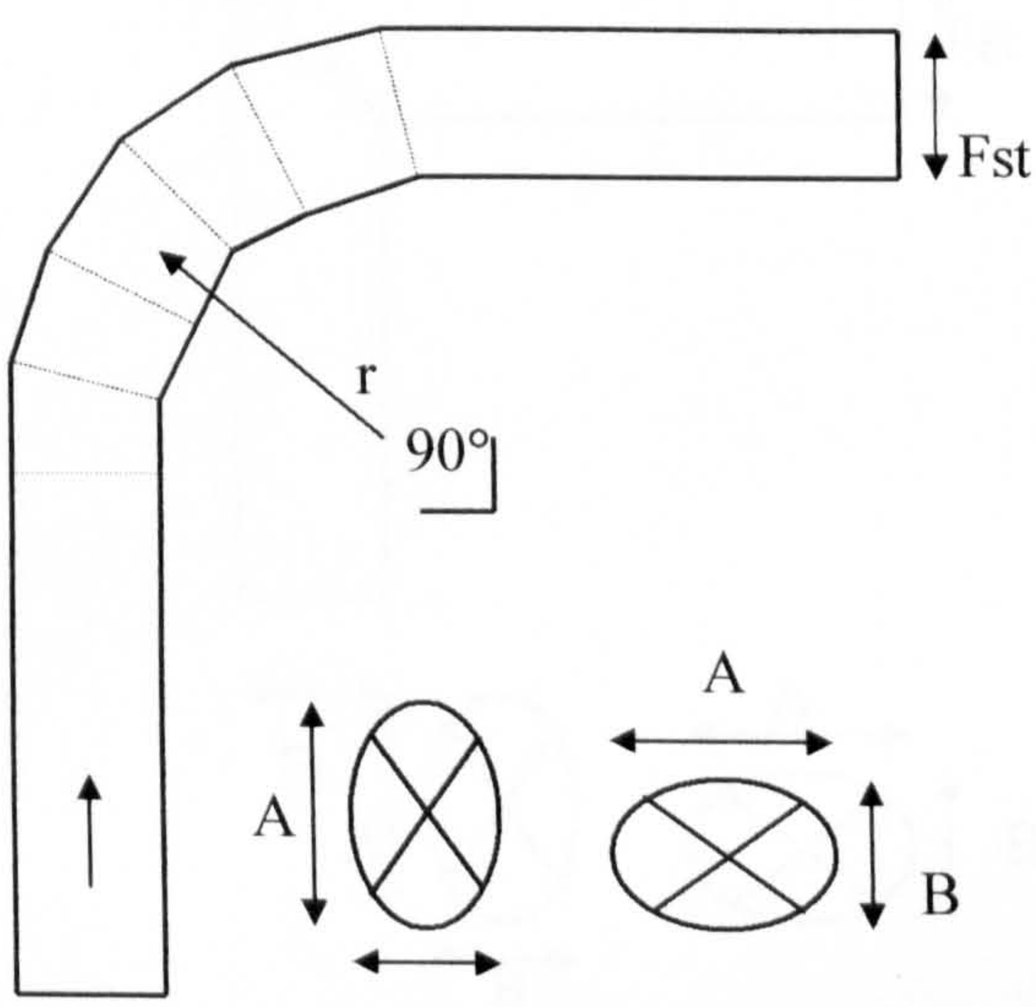


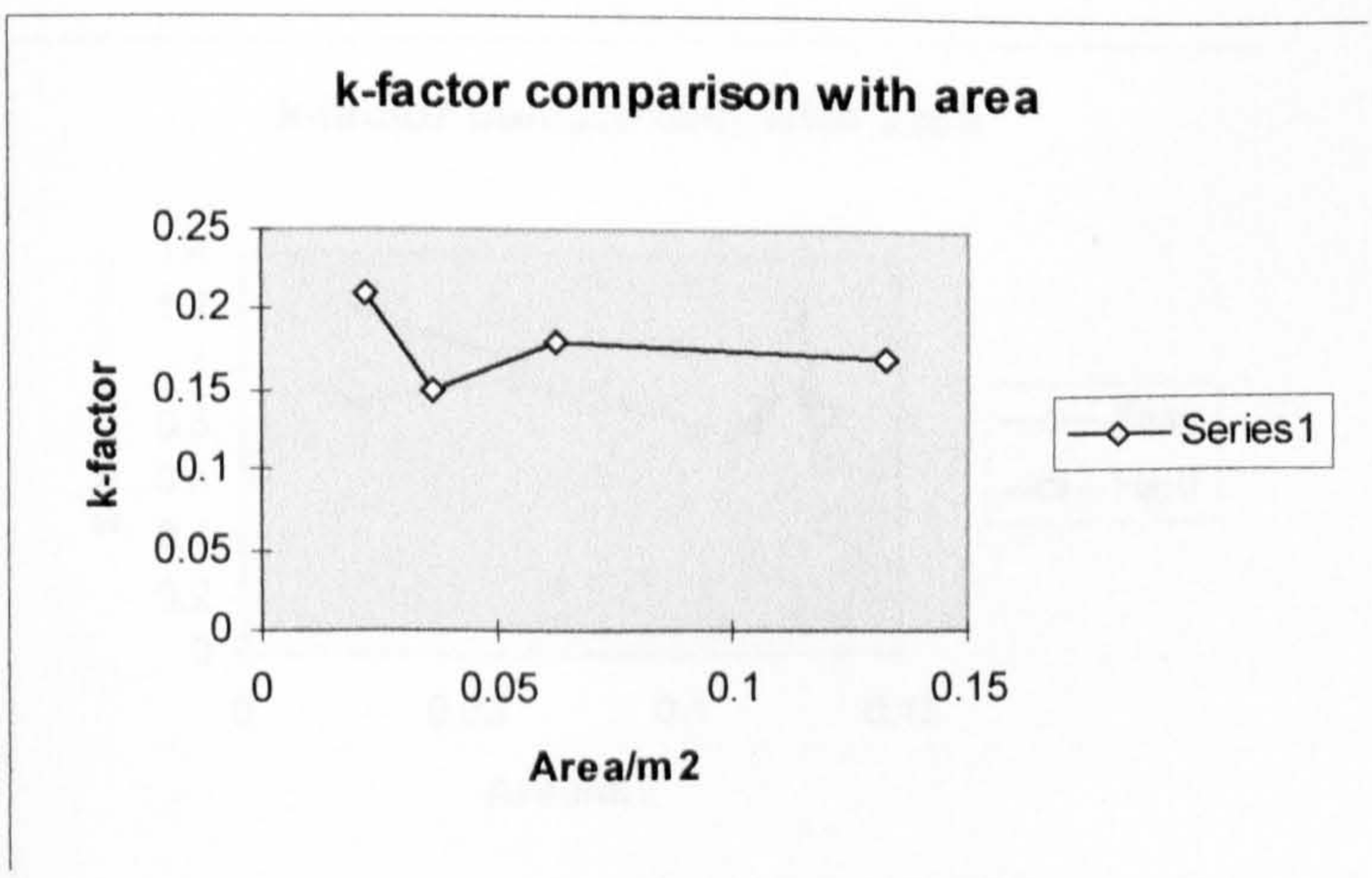

## 2.3.2 90° mitred oval bend:

Type Fs = Fst

| Type: | Easy | Hard |
|---|---|---|
| AxB | k-factor | |
| 0.1148 | 0.77 | 0.74 |
| 0.1325 | 0.67 | 0.84 |
| 0.0224 | 0.88 | 1.22 |
| 0.0624 | 0.95 | 1.03 |
| 0.126 | 0.98 | 1.21 |

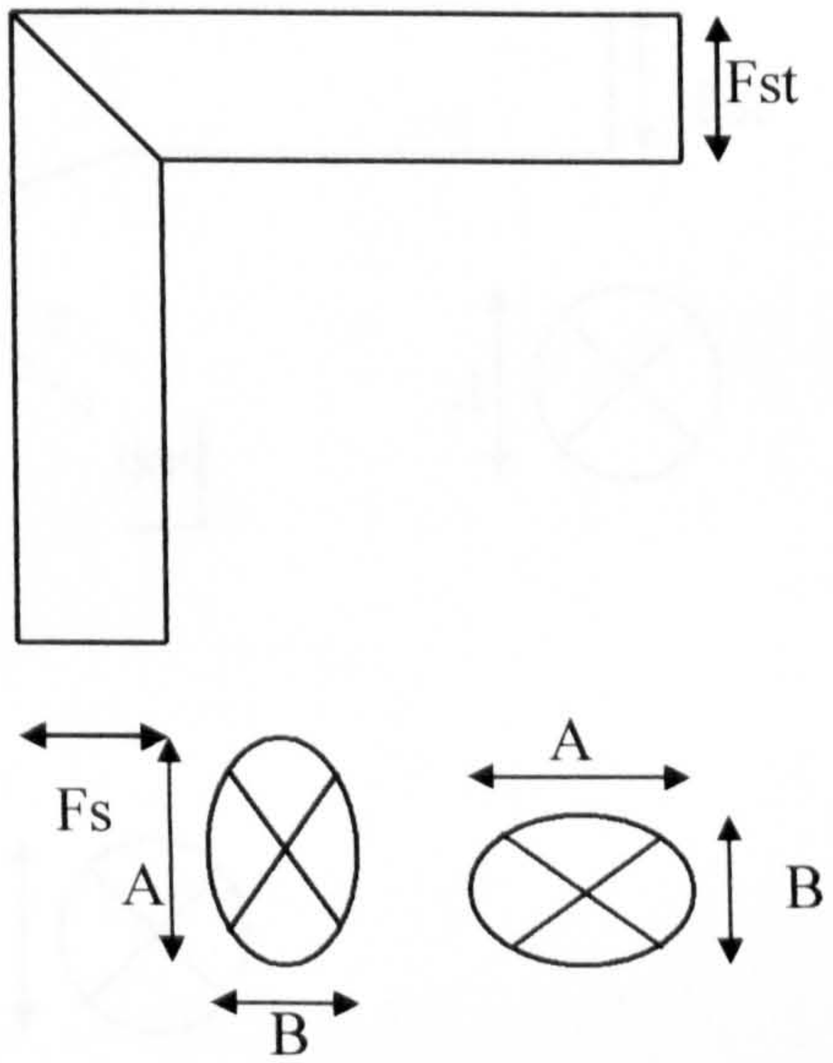


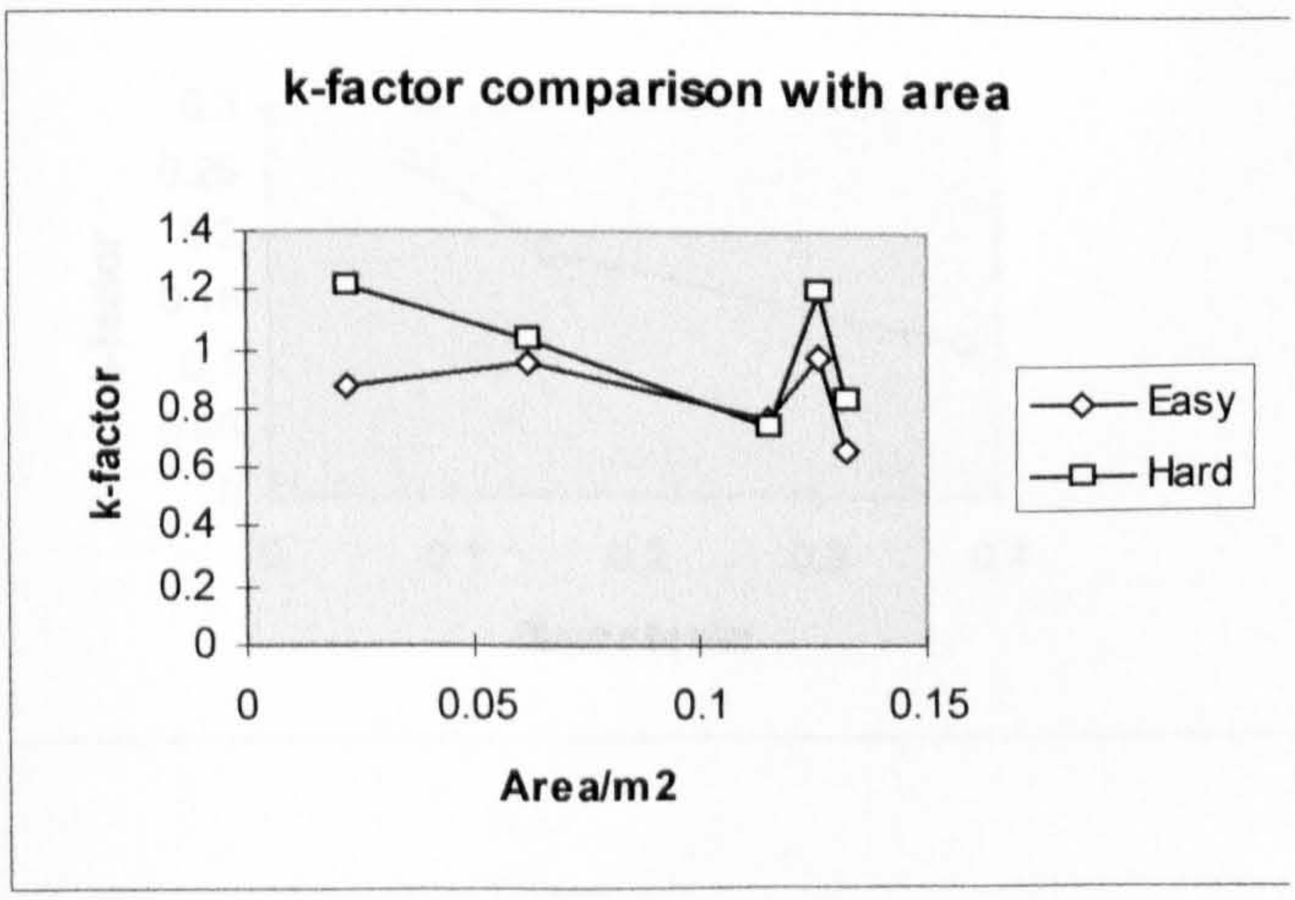

## 2.3.3 5-Gore 90° round bend:

Type Fs=Fst, r/d=1.5

| Dia | k-factor |
|---|---|
| 0.0762 | 0.26 |
| 0.1524 | 0.19 |
| 0.381 | 0.12 |

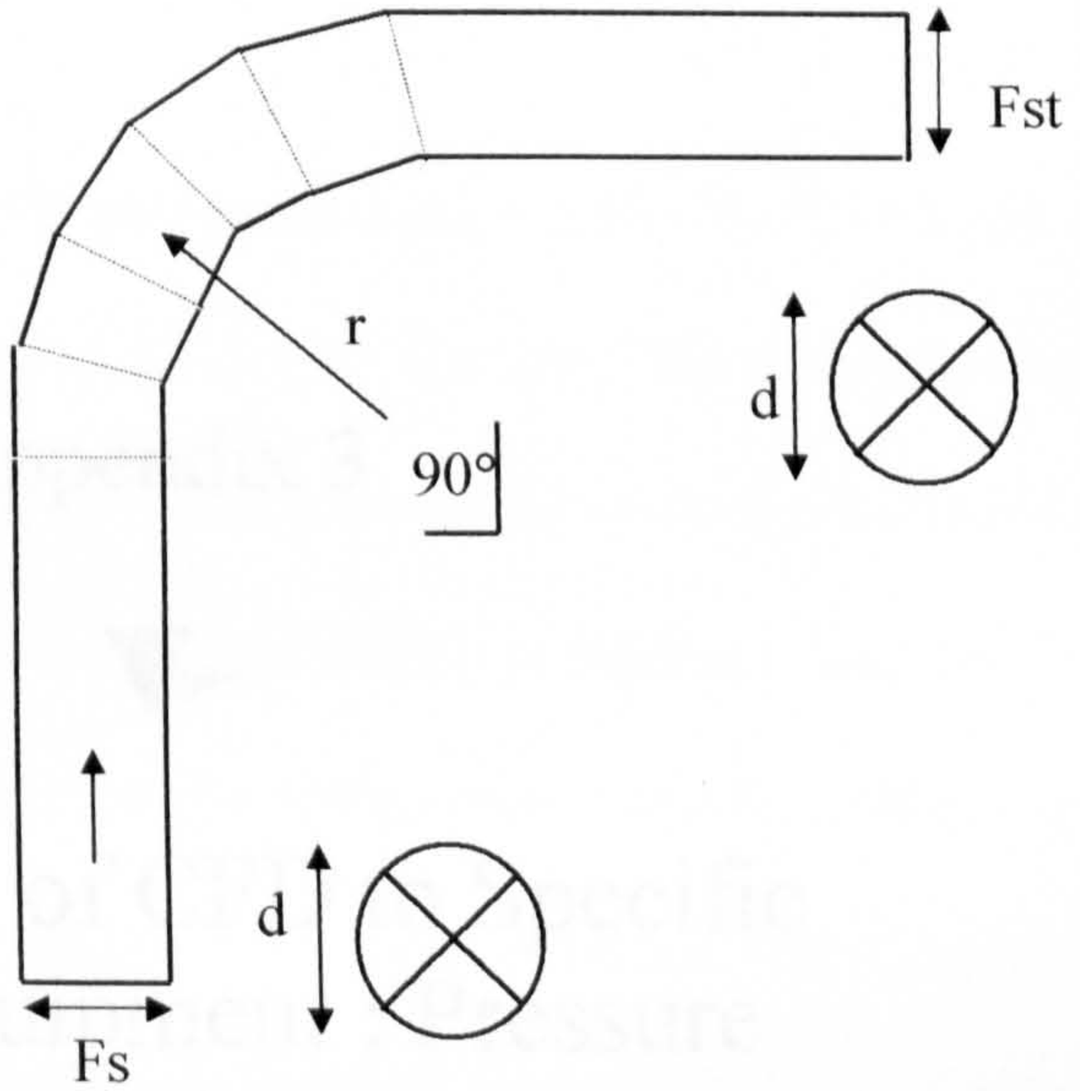


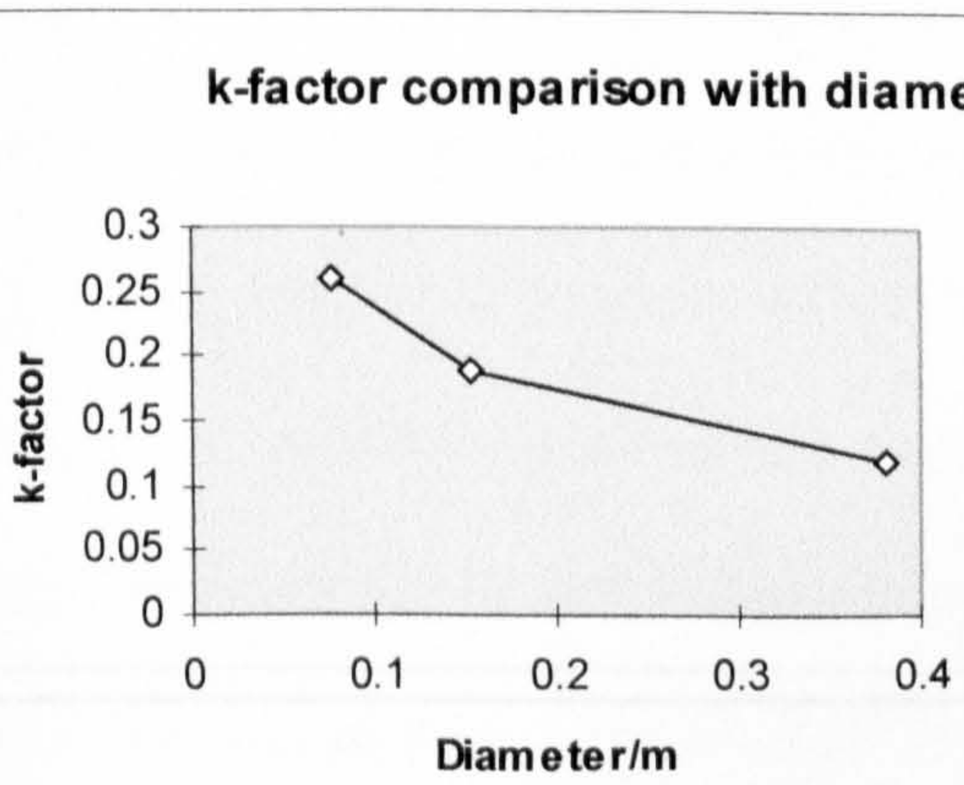

# Appendix 3

# Application of CFD to Specific HVAC Equipment : Pressure Loss in Heat Pump Coils

# Appendix 3 Application of CFD to specific HVAC equipment : pressure loss in heat pump coils

The applications to the scope of CFD prediction using the FLUENT code are not restricted to air-flow applications such as HVAC systems. This chapter presents the pressure drop inside evaporator and condenser coils of refrigeration and air conditioning systems using hydrofluorocarbon (HFC) refrigerants and blends. A refrigerant blend is a mixture of compatible refrigerants that either increase the performance or alter the characteristics of a refrigerant to suit a particular application. In this chapter CFD is used to simulate two-phase flow of different refrigerants through two types of coils common to evaporator and condenser components found in a typical vapour-compression system. The flow conditions were kept constant with a flow velocity of 10 m/s to ensure that a fair comparison of pressure loss could be made with different refrigerants. The refrigerant inlet temperature in each model was also kept constant at about 20 °C which was a typical temperature of the refrigerant entering an evaporator coil. The CFD prediction was one of fully turbulent flow and the typical values for Reynolds number in single phase flow are given in Table 3.1 . A specific Reynolds number for any given refrigerant for two phase flow can not be stated because it varies throughout the model depending on the changing viscosity which in turn is dependant on the changing temperature. The coil dimensions were taken as

typical values where the pressure loss for CFD prediction were measured across the actual coil and not over the upstream and downstream pipe lengths required for fully developed flow.

**Table 3.1** Reynolds number used for different refrigerants in single phase flow.

| Refrigerant : | Reynolds number : | |
|---|---|---|
| | Vapour : | Liquid : |
| R12 | 390,625 | 931,677 |
| R717 | 90,909 | 638,298 |
| R134a | 3,006 | 8,242 |
| R32 | 4,950 | 12,097 |

Chlorofluorocarbons (CFC's) have been widely used in refrigeration and air conditioning systems. It has been decided by the Montreal Protocol that these refrigerants should be phased out and replaced by more "ozone-friendly" refrigerants. Hydrofluorocarbon (HFC) refrigerants such as R134a and zeotropic refrigerant blends such as R407c have been introduced to replace R12 and R22, respectively.

### 3.0.1 Literature search

Little work is being carried in the specific field of the pressure loss in evaporator and condenser coils using HFC refrigerants. Experimental work on heat flow and pressure drop characteristics of HFC refrigerant blends inside horizontal enhanced surface tubing has been carried out by Sami and Song (38). Other work includes the comparison of thermal performance and pressure loss in evaporators and condensers of vehicle air conditioning systems when the refrigerant R134a is used instead of R12, by Jones (39).

### 3.0.2 Scope for CFD modelling

The optimum performance of refrigeration systems requires an accurate design technique for the prediction of refrigerant pressure drop and flow patterns through evaporator, condenser and other components of refrigeration and air conditioning systems. CFD can be used as a design tool to estimate or enhance our understanding of pressure loss in coils prior to construction. The CFD prediction would allow different types of working fluids and coils of various geometries to be examined. The coils investigated in this chapter include an S-shape coil and a spiral coil as used in radiators and in heat exchanger. Both coils

are used as evaporator and condenser components in refrigeration systems. The refrigerants used are :

- R12 = Dichlorodifluoromethane ($CH_2Cl_2F_2$)
- R717 = Ammonia ($NH_3$)
- R32 = Difluoromethane ($CH_2F_2$)
- R134a = Tetrafluoroethane ($CH_2FCF_3$)
- R125 = Pentafluoroethane ($CHF_2CF_3$)

and refrigerant blends as :

- R407A = $R32_{20\%} + R125_{40\%} + R134a_{40\%}$
- R407B = $R32_{10\%} + R125_{70\%} + R134a_{20\%}$
- R407C = $R32_{23\%} + R125_{25\%} + R134a_{52\%}$

### 3.0.3 CFD modelling approach

The FLUENT CFD code is used for the prediction of pressure loss through evaporator and condenser coils. The governing CFD equations are described in section 4.3.5 . The Power Law discretisation scheme was also used which provided a more stable solution when predicting the flow through coils. The Power Law discretisation scheme is described in section 4.3.5.2 . Because

FLUENT cannot predict the actual phase change from liquid to gas and visa-versa, the opproach of using two-phase modelling had to be used. Within a coil where phase change takes place due to heat exchange, at any significant stage the operating fluid is devided between a fraction of gas and a fraction of liquid. This fluid quality fraction changes depending on the temperature throughout the coil. It is possible to enter two sets of physical parameters in to the FLUENT code, i.e. one for the gas state of the refrigerant and one set of properties for the liquid state of the refrigerant. When the multi-phase modelling option is requested by the user in the FLUENT code, the code continuously calculates the physical properties throughout the computational domain in terms of a percentage of gas and a percentage of liquid. These calculations and the fluid quality fraction is based on the predicted temperature throughout the computational domain, which in turn is calculated from the user defined boundary conditions. For the single phase prediction, the refrigerant physical properties, i.e. density, viscosity, specific heat capacity etc. are entered as polynomial functions with respect to temperature. These physical properties were taken from refrigerant reference manuals such as ASHRAE (40) refrigerant guide and ICI (41) refrigerant technical information. For the two-phase prediction the same sources of information were used to enter the physical properties again in the form of polynomial functions for the corresponding refrigerant physical states, i.e. gas and liquid states. The same souces of reference were used to enter the coil inlet

temperature and was kept at the boiling point of the particular refrigerant which varied from refrigerant to refrigerant. This was done so that some continuety could allow a comparison to be made between the different predictions. The thermal equations included in the heat transfer model are described in section 4.3.5.1 .

Figures 3.1 and 3.2 show the grid structures for the S-shaped coil and the spiral coil created using the PREBFC pre-processor as described in section 4.3.1 . Due to the relatively long upstream and downstream coil lengths to the diameters, a high number of computational cells (~ 50,000) were used to ensure a cell aspect ratio of about one. This had the effect of increasing solution stability.

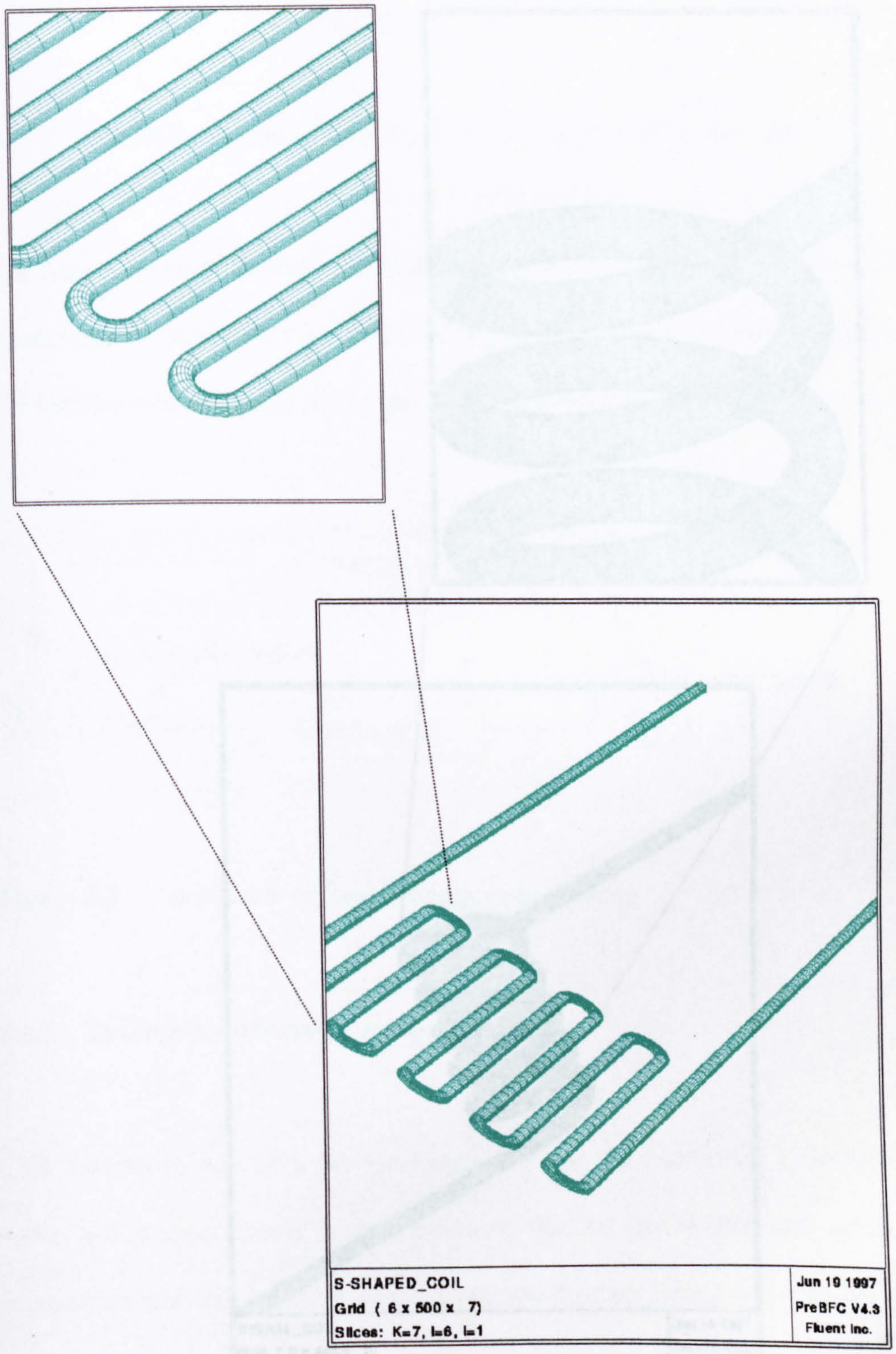


**Figure 3.1** S-shaped coil CFD surface grid created using PREBFC.

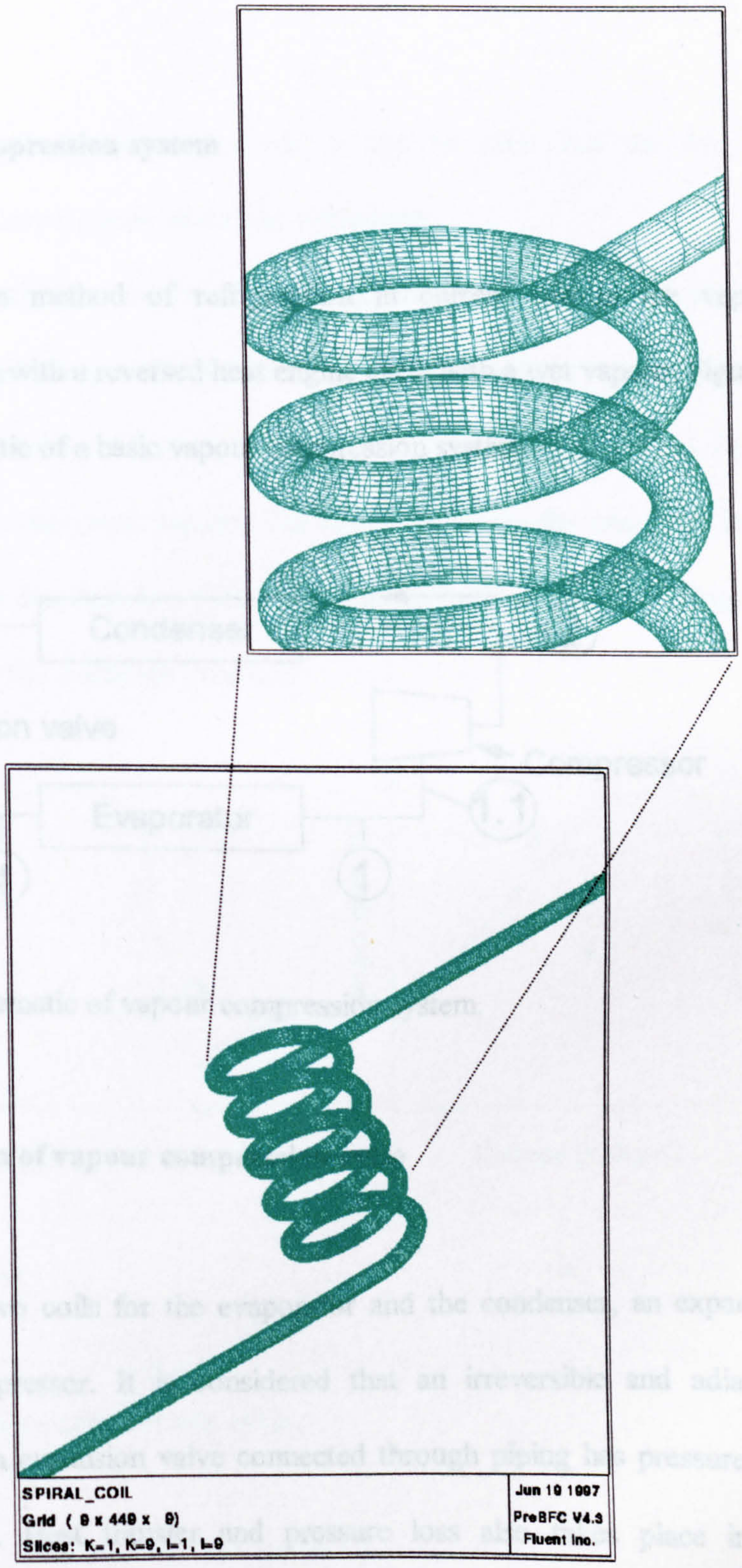


**Figure 3.2** Spiral coil CFD surface grid created using PREBFC.

## 3.1 Vapour compression system

The most common method of refrigeration in current use is the vapour compression system with a reversed heat engine cycle with a wet vapour. Figure 3.3 shows a schematic of a basic vapour compression system.

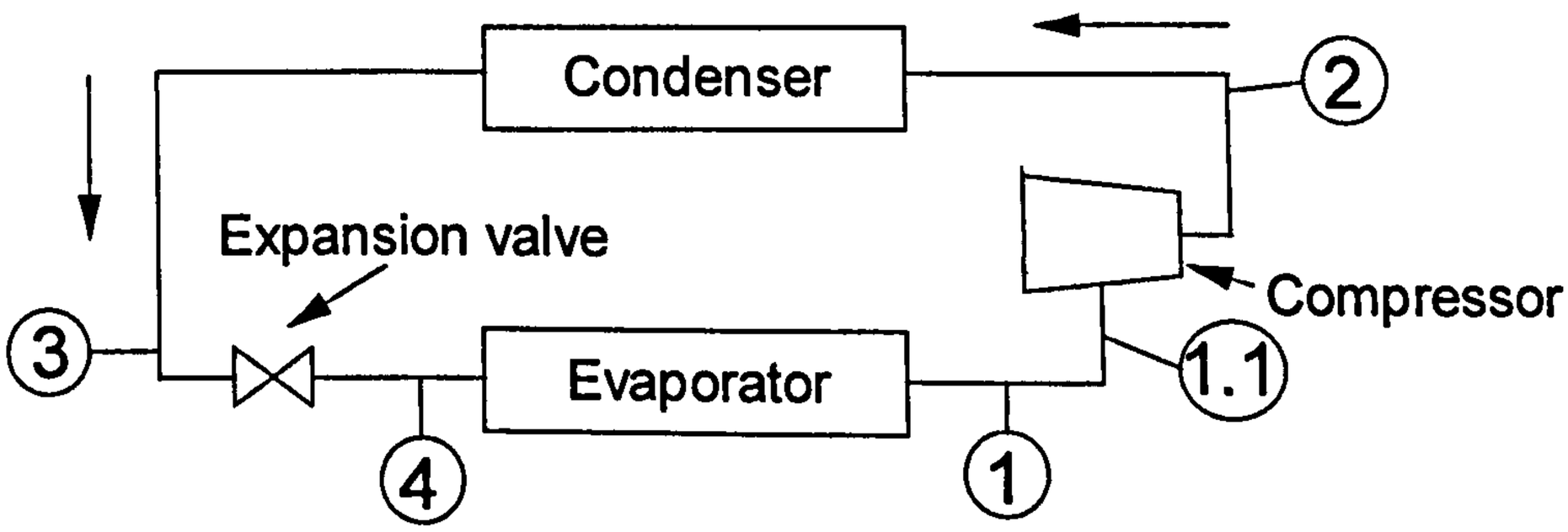


**Figure 3.3** Schematic of vapour compression system.

### 3.1.1 Description of vapour compression cycle

This consists of two coils for the evaporator and the condenser, an expansion valve and a compressor. It is considered that an irreversible and adiabatic compressor and an expansion valve connected through piping has pressure loss and heat transfer. Heat transfer and pressure loss also takes place in the condenser and evaporator with heat exchange with the surroundings. Figure 3.4

represents the vapour compression cycle. It can be seen that the line 2-3 represents the condensing phase where the refrigerant

moves from a superheated vapour to a sub-cooled liquid state. The line 3-4 represents the pressure drop as the refrigerant passes through an expansion valve. The line 4-1 depicts the refrigerant in the evaporator changing from a liquid-vapour mixture to a saturated vapour. The line 1-1a shows the heat gain in the suction line and the diagonal line 1-1b represents compression of the refrigerant gas from suction to the discharge pressure.

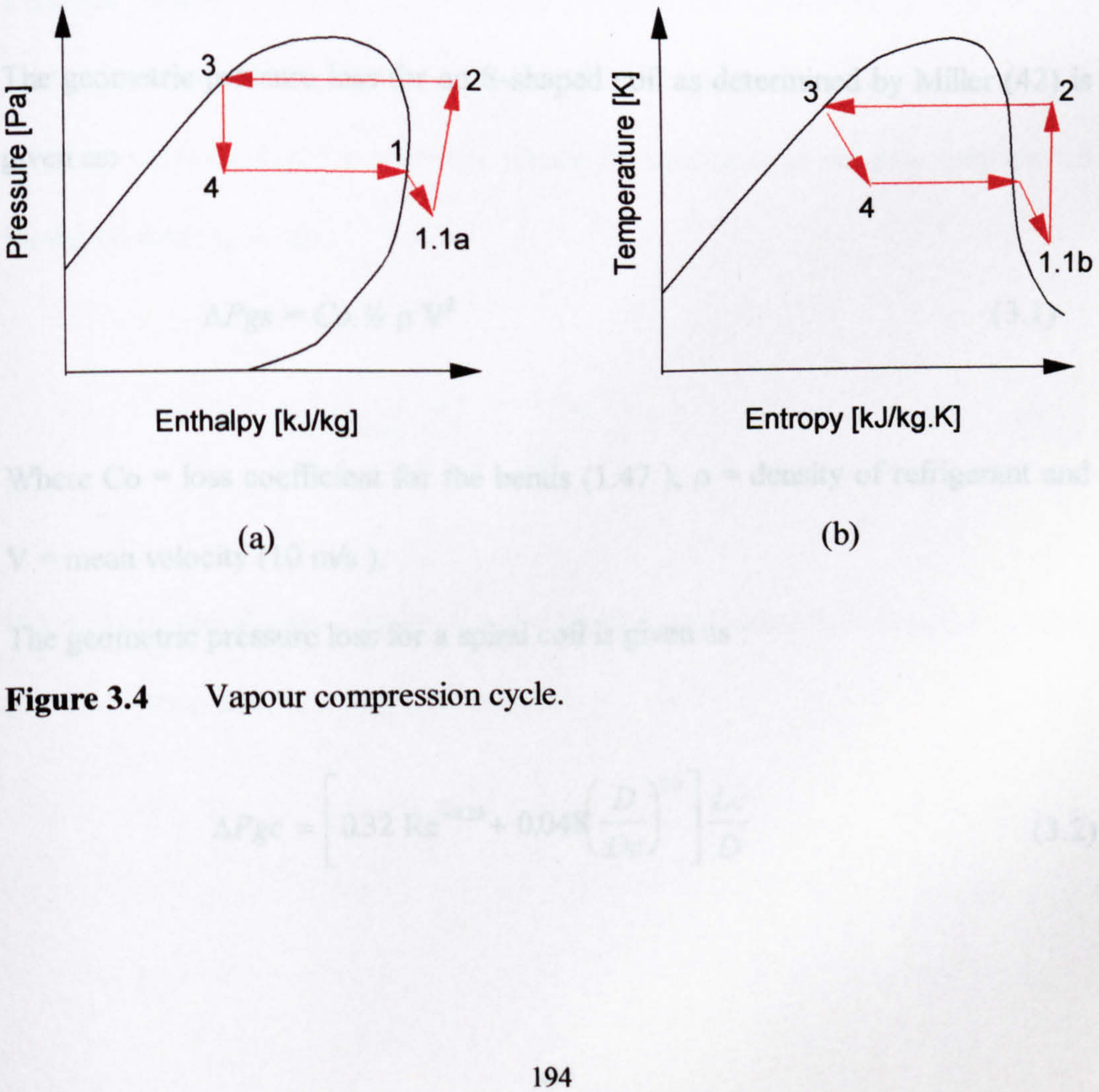


**Figure 3.4** Vapour compression cycle.

## 3.2 Pressure loss in coils

A theoretical analysis can be obtained from various sources of reference for both single-phase and two phase flow for S-shaped and spiral coils. Pressure loss in a coil for single-phase flow can be calculated by summing the frictional pressure loss and the geometric pressure loss. However for two-phase flow there is the additional sum of the pressure loss due to a change in momentum within the liquid/vapour mixture.

The geometric pressure loss for an S-shaped coil as determined by Miller (42) is given as:

$$\Delta Pgs = Co.\tfrac{1}{2}\,\rho\,V^2 \qquad (3.1)$$

Where Co = loss coefficient for the bends (1.47 ), ρ = density of refrigerant and V = mean velocity (10 m/s ).

The geometric pressure loss for a spiral coil is given as :

$$\Delta Pgc = \left[0.32\,\mathrm{Re}^{-0.25} + 0.048\left(\frac{D}{Dc}\right)^{0.5}\right]\frac{Lc}{D} \qquad (3.2)$$

Where D = pipe diameter (0.03 m), Dc = coil diameter (0.2 m) and Lc = length of spiral coil without upstream and downstream pipes (3.142 m). These values were taken as typical dimensions of evaporator and condenser coils found in heat pump systems.

### 3.2.1 Single phase flow

The pressure drop through an S-shaped coil is calculated by summing the frictional pressure loss and the geometric pressure loss of the bends. The friction coefficient is derived from the Colebrook-White equation as given in White (43) which requires an iterative solution. Hence for calculations we may only use an estimated form given as :

$$f = 0.25 / \left[ \log\left( \frac{k_r}{3.7D} + \frac{5.74}{\mathrm{Re}^{0.9}} \right) \right]^2 \qquad (3.3)$$

Where D = pipe diameter (0.015 m), f = friction coefficient, $k_r$ = roughness value (~ 0.0025 mm) and Re = Reynolds number.

The frictional pressure drop through bothe coils can be given as :

$$\Delta P_f = \frac{f L_{s,c} \rho V^2}{2D} \qquad (3.4)$$

Where the subscripts s and c refer to the S-shaped and spiral shaped coils respectively.

Using equations (3.1) and (3.4) the pressure loss through both coils can be estimated as :

$$\Delta P = \left( \frac{f L_{s,c} \rho V^2}{2D} \right) + \Delta P g_{s,c} \qquad (3.5)$$

Where $L_s$ = length of S-shaped coil wothout upstream and downstream pipes (5.6 m ).

### 3.2.2 Two-phase flow

The pressure drop across an S-shaped coil with two-phase flow is given by friction, momentum change within the liquid/vapour mixture and the geometric arrangement of the coil. The pressure loss due to the liquid/vapour mixture as

given in equation 3.6 correlates well with experimental results as given in Miyara (44).

$$\Delta P_m = -\Delta\left[\frac{G_r^{\,2}x^2}{\xi\rho_v} + \frac{G_r^{\,2}(1-x)^2}{(1-\xi)\rho_L}\right] \tag{3.6}$$

Where $\xi$ is the void fraction that can be calculated from Smith's (45) equation :

$$\xi = x\left[x + \frac{\rho_v}{\rho_L}(1-x)\left\{0.4 + 0.6\left(\frac{x\rho_L/\rho_v + 0.4(1-x)}{x + 0.4(1-x)}\right)^{0.5}\right\}\right]^{-1} \tag{3.7}$$

Where x = mixture quality, $G_r$ = mass velocity of refrigerant, $\rho_v$ and $\rho_L$ = density of refrigerant vapour and liquid, respectively.

Using Soliman et. al. (46) equation, the frictional pressure drop through both types of coils can be calculated by :

$$\Delta P_f = L(1+2.85X_t^{\,0.523})^2\left(\frac{dP}{dL}\right)_F \tag{3.8}$$

Where $(dP/dL)_F$ is the frictional pressure drop for the two-phase flow. The frictional pressure drop for the vapour flow $(dP/dL)_v$ is calculated by :

$$\left(\frac{dP}{dL}\right)_v = \frac{2 f_v G r^2 x^2}{D \rho_v} \tag{3.9}$$

and $$X_t = \left(\frac{1-x}{x}\right)^{0.9} \left(\frac{\rho_v}{\rho_L}\right)^{0.5} \left(\frac{\mu_v}{\mu_L}\right)^{0.1} \tag{3.10}$$

and $$f_v = 0.046 / Re_v^{-0.2} \tag{3.11}$$

Therefore from equations (3.1), (3.2), (3.5) and (3.7) the pressure drop across both types of coil with two-phase flow is given as :

$$\Delta P_{s,c} = \Delta P_{gs,c} + \Delta P_m + \Delta P_f \tag{3.12}$$

## 3.3 Comparison of CFD prediction and experimental theory

A comparative analysis of various refrigerants was carried out for single phase flow through the S-shaped coil and an analysis of various refrigerants for two phase flow through both S-shaped coil and spiral coil.

### 3.3.1 Single phase flow through S-shaped coil

Table 3.2 shows the relationship between theoretical pressure drop and predicted pressure drop using CFD when predicting liquid and vapour flows. It was found that CFD was able to predict the pressure drop to within 86 % accuracy on average, compared to theoretical analysis using equations verified by experiment. It can be seen that the newer refrigerants (R134a and R32) give a much higher pressure drop compared with the conventional refrigerants (R12 and R717). CFD however did on average slightly overestimate the pressure drop compared to theoretical values, which may be due to the fact that CFD takes into account more physical effects of refrigerant flow than is included in the theory.

**Table 3.2** Pressure drop through an S-shaped coil for single phase liquid and vapour, values given in kPa. Operating conditions are as given in section 3.0 .

| Refrigerant : | R12 | R717 | R134a | R32 |
|---|---|---|---|---|
| Pressure loss: | | | | |
| CFD vapour | 12.3 | 3.3 | 37.4 | 42.9 |
| Theoretical vapour | 11.8 | 2.9 | 25.1 | 32.1 |
| CFD liquid | 438.9 | 209.3 | 1036.0 | 736.0 |
| Theoretical liquid | 454.9 | 210.6 | 844.0 | 615.2 |

Figure 3.5 shows the pressure distribution through the S-shaped coil using ammonia (R717) as the refrigerant and comparing the liquid and vapour states. The linear pressure loss both before and after the coil can be clearly seen making an accurate evaluation of the pressure loss through the coil. The pressure loss for each bend of the coil an also be seen.

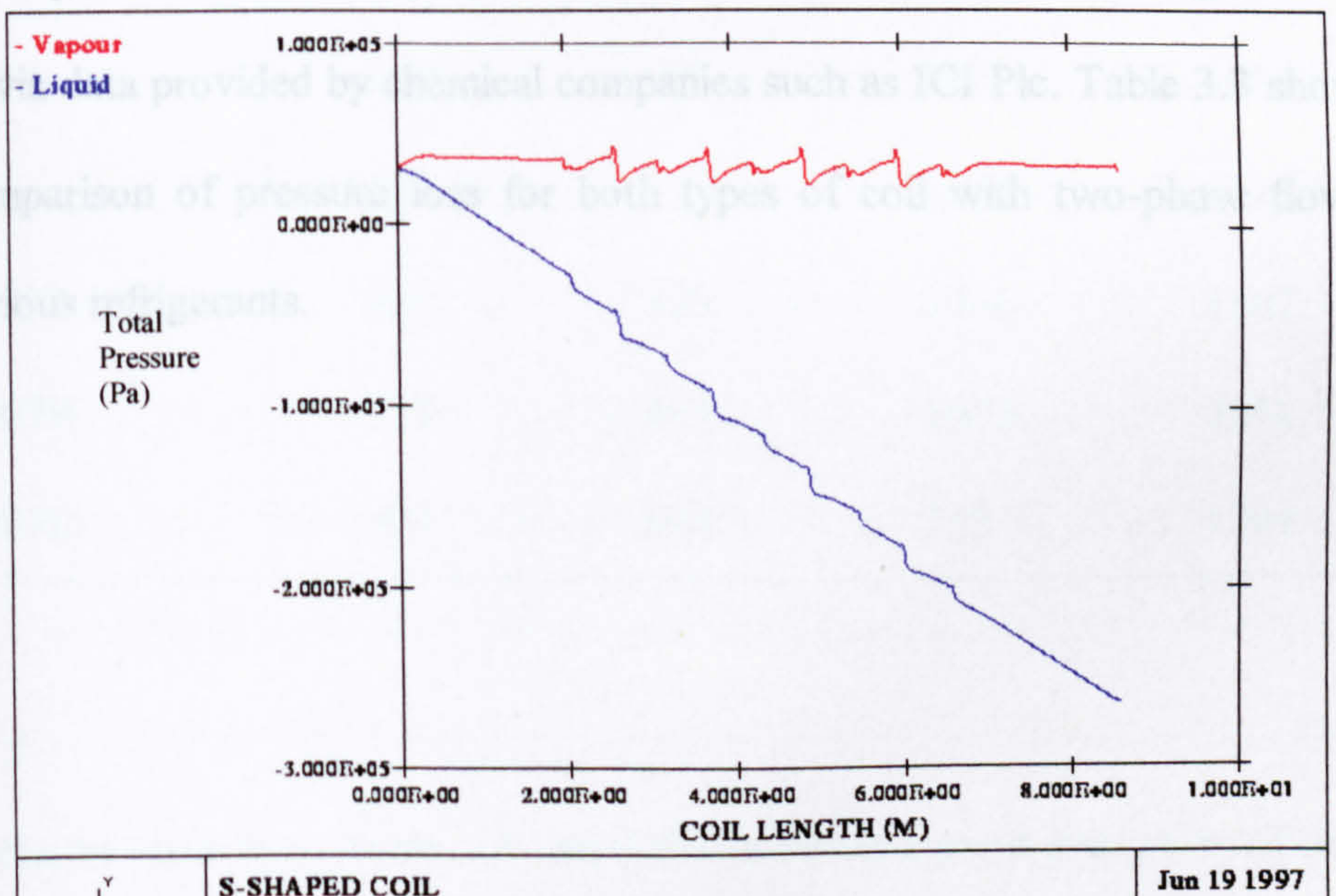


**Figure 3.5** Total pressure distribution for ammonia in single phase through the S-shaped coil.

### 3.3.2 Two-phase flow through spiral and S-shaped coils

Unlike single phase flow in CFD prediction where certain characteristics of the refrigerant remain constant including temperature, in two-phase flow the thermal equations are activated and the refrigerant variables such as density and viscosity change depending on the temperature. Instead of constant values these variables are expressed in terms of polynomial functions either obtained through data tables or via data provided by chemical companies such as ICI Plc. Table 3.3 shows the comparison of pressure loss for both types of coil with two-phase flow with various refrigerants.

**Table 3.3** Pressure loss comparison for two phase flow, values given in kPa.

Operating conditions are given in section 3.0 .

| Coil type: | CFD S-shape | S-shape theory | CFD spiral | Spiral theory |
|---|---|---|---|---|
| Refrigerant: | | | | |
| R717 | 164 | 42 | 354 | 322 |
| R12 | 451 | 332 | 2622 | 1950 |
| R134a | 1403 | 327 | 5891 | 1884 |
| R32 | 450 | 926 | 1216 | 1746 |
| R407A | 526 | 320 | 1440 | 1602 |
| R407B | 620 | 457 | 1673 | 2217 |
| R407C | 409 | 274 | 752 | 1394 |

It can be seen from Table 3.3 that CFD provides a good prediction of pressure loss for both types coil with different refrigerants when compared with theoretical values. CFD gave average predictions to within 53 % accuracy for the spiral coil

and to within 69 % accuracy for the S-shaped coil, indicating that CFD is 16 % more accurate for prediction of flow through the S-shaped coil compared with the spiral coil using the same refrigerants and operating conditions.

### 3.3.3 Pressure loss for conventional and more modern refrigerants

A CFD prediction of pressure loss for various refrigerants with both types of coils can be seen in Figures 3.6 and 3.7, which show the total pressure loss through the entire coil including the upstream and downstream pipes which are not included in the values given in Table 3.2 . In Figures 3.6 and 3.7 the order of pressure loss for the refrigerants used can be seen to be almost identical for both coils with the exception of refrigerant R12 which appears to have a much higher increase in pressure loss than the other refrigerants when comparing the spiral coil to the S-shaped coil. The results show an increase in pressure drop of more than 400 % on average when using one of the new refrigerant blends rather than the conventional refrigerants. This finding was also evident with theoretically evaluated values. The refrigerant that gave the highest pressure drop was R134a showing that the performance of the evaporator within the refrigeration cycle would depend very much on the refrigerant used. CFD was also shown to be 25 % more efficient when predicting single phase flow rather than two-phase flow.

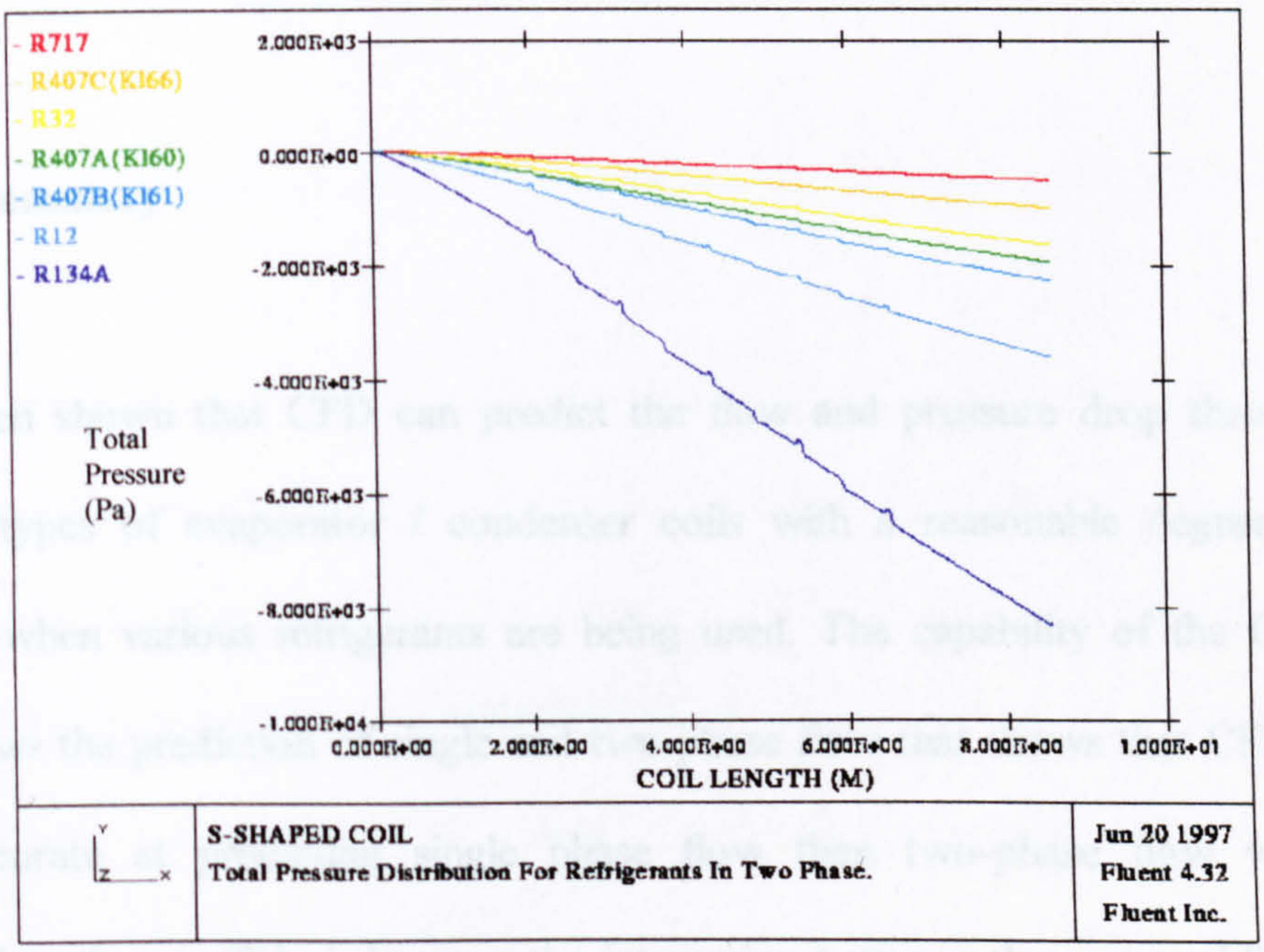


**Figure 3.6** CFD pressure distribution for various refrigerants in two-phase flow through the S-shaped coil.

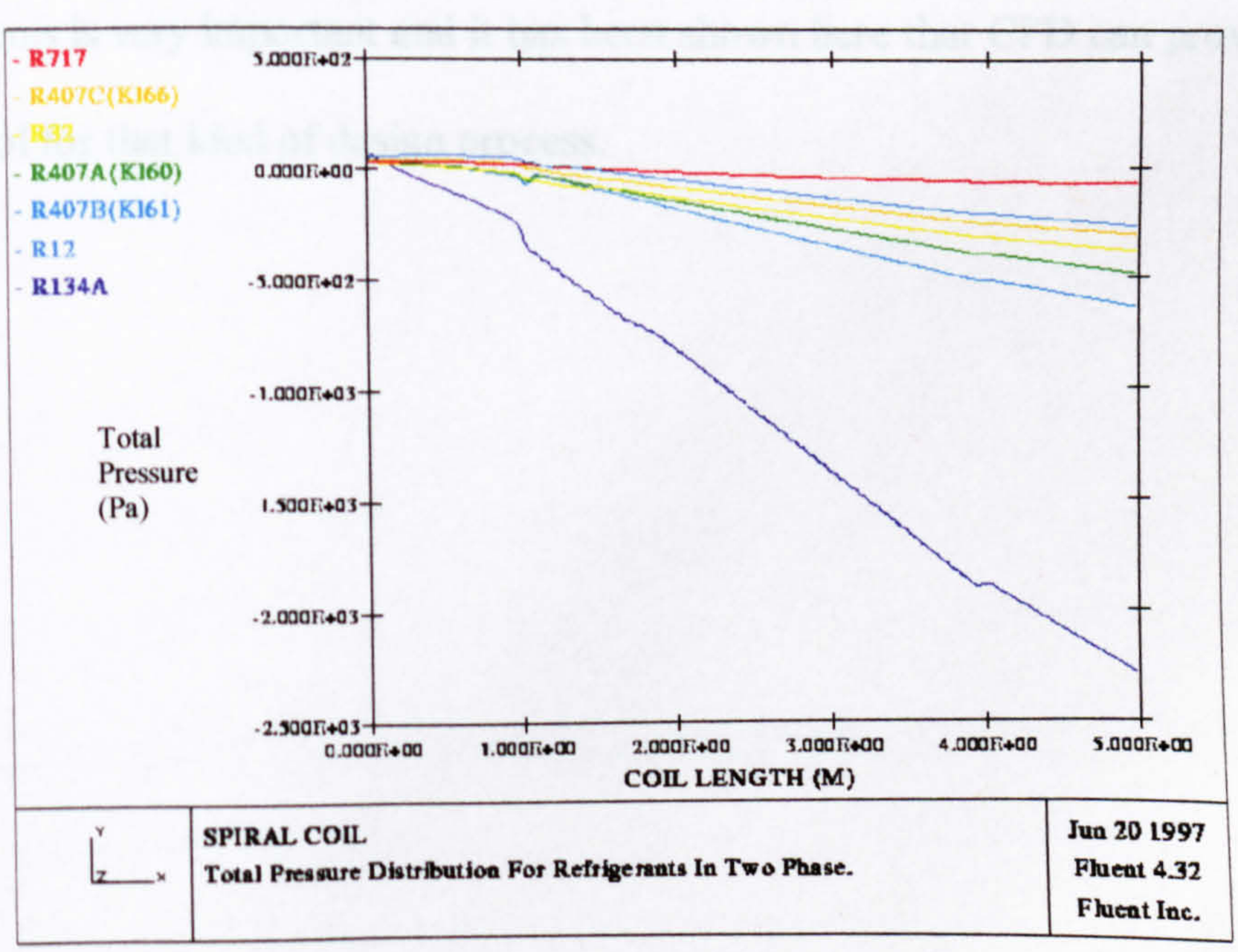


**Figure 3.7** CFD pressure distribution for various refrigerants in two-phase flow through the spiral coil.

## 3.4 Summary

It has been shown that CFD can predict the flow and pressure drop through different types of evaporator / condenser coils with a reasonable degree of accuracy when various refrigerants are being used. The capability of the CFD code allows the prediction of single and two-phase flow that shows that CFD is more accurate at predicting single phase flow than two-phase flow when compared to theory. This is because the interaction between the vapour / liquid state is very difficult to simulate. The optimum design of coils as used in heat-pump systems is very important and it has been shown here that CFD can provide a useful tool for that kind of design process.

Appendix 4

# Application of CFD to Specific HVAC Equipment : Ejectors

# Appendix 4 Application of CFD to specific HVAC equipment : ejectors

The usual application of using vapour compression systems for refrigeration and air conditioning has already been described in chapter 7. However, due to the inefficiencies in power generation and transportation, the overall efficiency and performance of vapour compression systems is considerably low. In addition these systems have moving parts which require constant maintenance. Other methods of refrigeration such as absorption systems do use " environmentally friendly " refrigerants, however, consequently are constructed with many bulky parts.

## 4.1 Heat pump system

Another type of system is known as the ejector heat pump. This is a heat operated cycle with the advantage of utilising various sources of energy such as solar, waste energy or natural gas. This type of refrigeration system can also incorporate hybrid energy use making it a very applicable system. In addition they have a long life and unlike vapour compression systems, produce no noise or vibration.

### 4.1.1 Literature search

Very little work has been carried out involving CFD prediction of ejectors and heat pump system components, however Hammer (47) has investigated the cooling effect of the ejector heat pump experimentally. Other work has been carried out by Korres (48) who studied the influence of the design on the coefficient of performance of a solar powered ejector heat pump whilst Thupvongsa (49) developed an analytical computer model to analyse an ejector heat pump. More recently, work on the advancement of ejector refrigeration has been investigated by Sokolov and Hershagal (50-52) .

### 4.1.2 Description of the ejector heat pump system

Figure 4.1 shows a schematic of the basic design of an ejector heat pump system. It consists of a generator, an ejector, evaporator, condenser, pump and an expansion valve. The dimensions of an ejector used in these investigations are given in Figure 4.2 . From Figure 4.2 it is shown that the ejector consists of a converging/diverging primary nozzle, a mixing tube and a diffuser. When the refrigerant (for example steam) is produced from the heat input to the generator it expands as it passes through the ejector causing entrainment from the evaporator due to the difference in pressure. The working fluid is then passed

through the diffuser into the condenser and is pumped back to the generator or expanded through a valve into the evaporator.

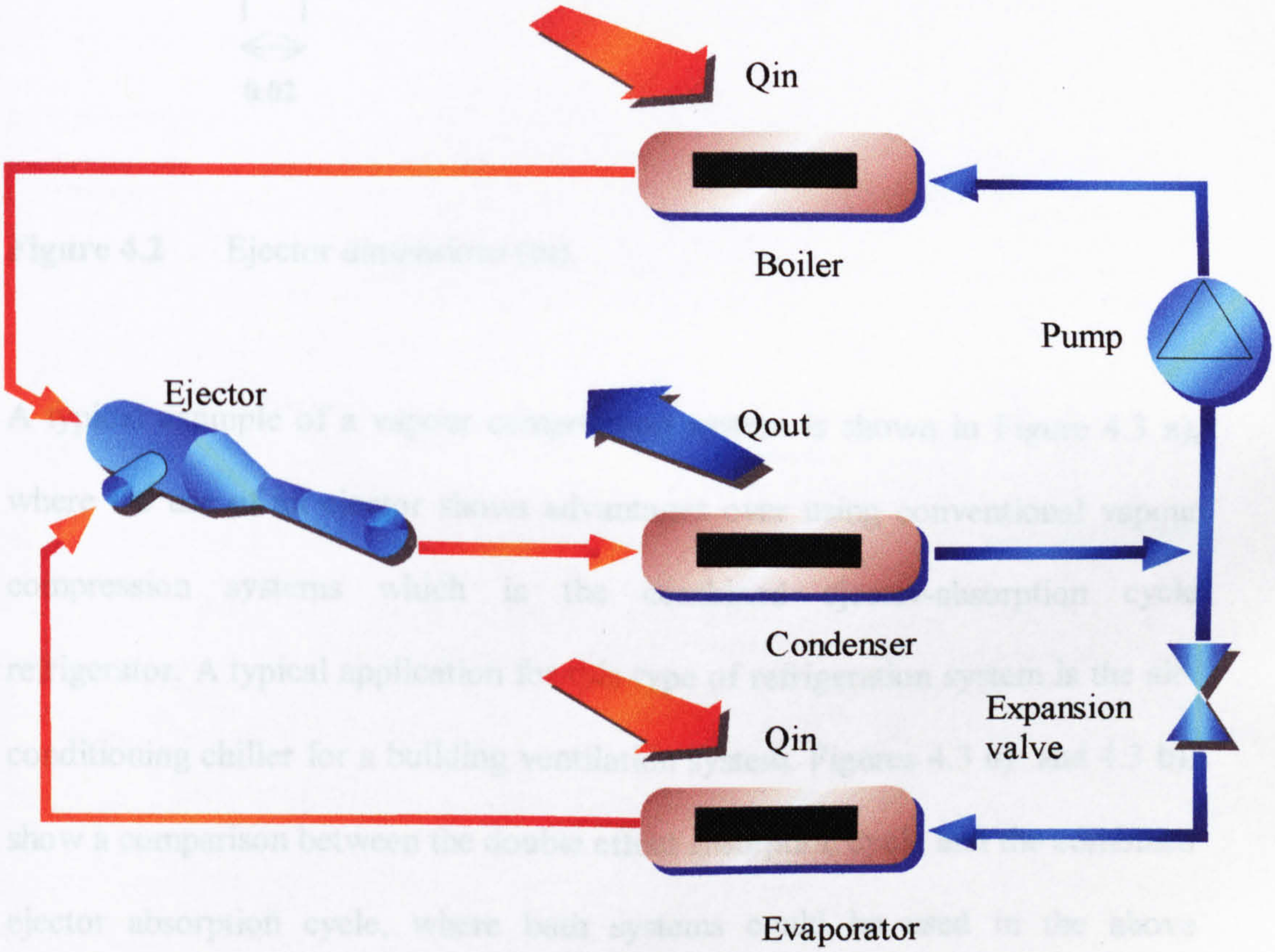


**Figure 4.1** Schematic diagram of a basic ejector heat pump system.

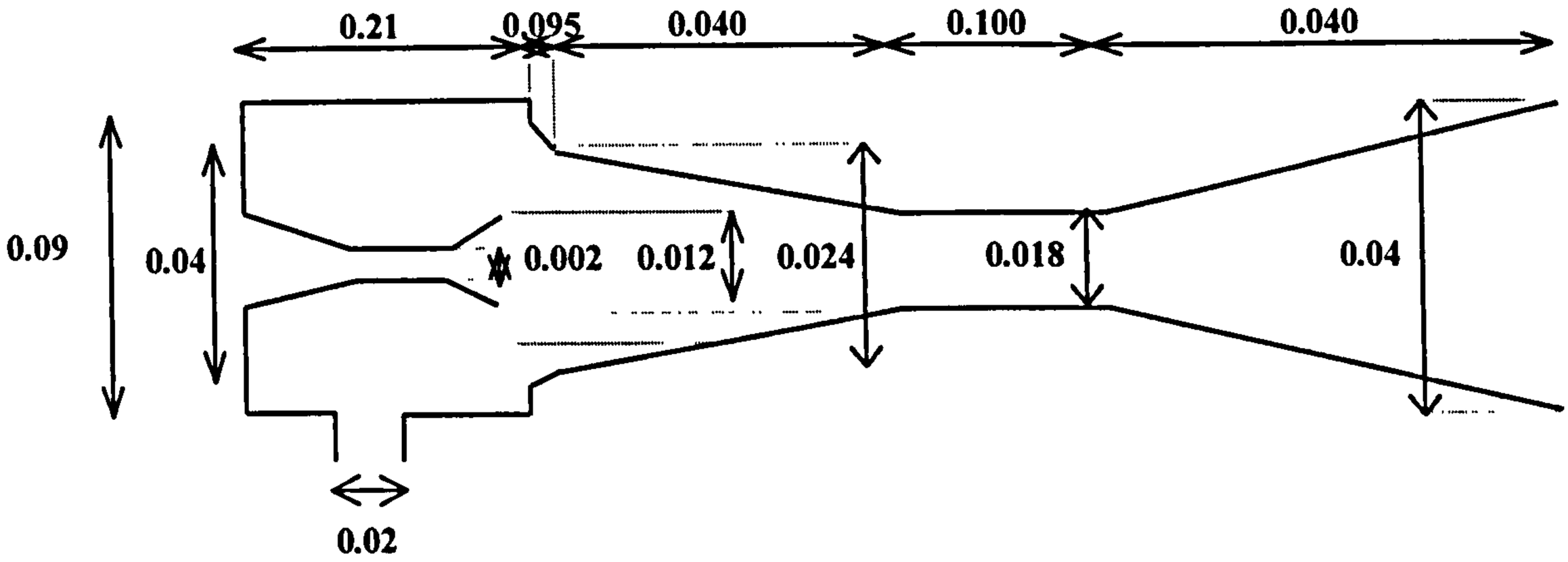


**Figure 4.2** Ejector dimensions (m).

A typical example of a vapour compression system is shown in Figure 4.3 **a)**, where the use of an ejector shows advantages over using conventional vapour compression systems which is the combined ejector-absorption cycle refrigerator. A typical application for this type of refrigeration system is the air-conditioning chiller for a building ventilation system. Figures 4.3 **a)** and 4.3 **b)**, show a comparison between the double effect absorption cycle and the combined ejector absorption cycle, where both systems could be used in the above mentioned example. This system uses a lithium bromide/water mixture for the main refrigerant, which is boiled in the generator. The high pressure water vapour is passed through the ejector causing entrainment of low pressure liquid water from the evaporator. This low pressure liquid water is taken from the exit of the ejector after condensation and expansion through a valve. The evaporation takes place at low temperature due to the low pressure and hence heat has to be

taken out of the supplied water from the supplied water within the building ventilation system, therefore cooling the water. The lithium bromide at high concentration is allowed to absorb water vapour in the absorber and is then fed back to the generator to be re-used.

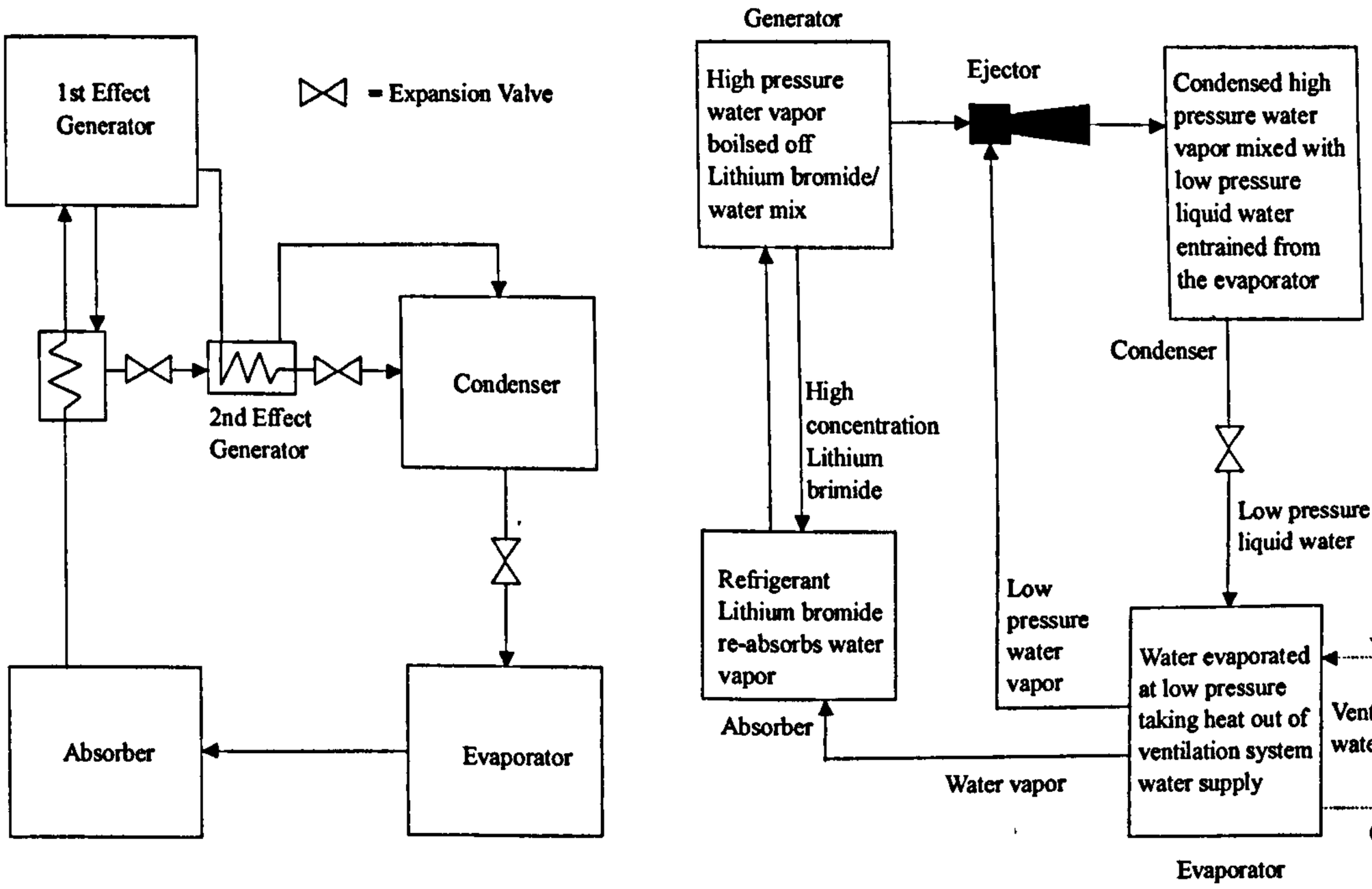


**Figure 4.3** Schematic diagram of a) Double effect absorption cycle and b) Combined ejector absorption cycle.

The schematic comparison shows that the ejector removes the requirement for the second effect generator and a combined ejector absorption cycle has the following advantages over the double effect absorption cycle :

- low running costs;
- simple cycle with few moving parts;
- low capital cost compared to a double effect chiller;
- minimal environmental impact:
  - no ozone depleting refrigerants;
  - clean combustion.

## 4.2 Scope for CFD modelling

The crucial part of the heat pump refrigeration system that makes it different from all other systems is the ejector and it is the performance of the ejector that is critical to the operation of the system. Some theoretical investigations of the parameters affecting the performance of ejectors have been carried out by Keenan and Neumann (53), however, with the advancement of computer technology it is now possible to predict the compressible flow through ejectors with a high degree of accuracy. In order to achieve optimum performance an accurate design technique would be necessary for the prediction of refrigerant flow patterns and pressure distribution through the ejector. CFD can be used as a

design tool to analyse the performance of ejectors either prior to construction or after construction to refine ejector performances or to solve unexpected performance problems.

### 4.2.1 CFD modelling approach

The FLUENT CFD code is used to predict the flow pattern and pressure distribution through an ejector using various refrigerants including steam, R134a and R12. The governing equations described in section 4.3.5 of Chapter 4 were used with the k-ε model and the Power Law discretisation scheme as mentioned in section 4.3.5.2 in Chapter 4. The ejector geometries and structured grids were constructed using the PREBFC pre-processor. In order to obtain an accurate prediction with the computing power available the model grids were of the order of 50,000 computational cells using a symmetrical boundary in the ejectors symmetric plane. Figure 4.4 shows an example of a surface grid for an ejector created using the PREBFC pre-processor. The surface grid is the external surface of the computational model showing where the physical boundaries are. All the computational calculations take place both inside and at this boundary surface. The dimensions for this ejector are given in Figure 4.2, where the actual ejector dimensions are superimposed on to a basic sketch of an ejector. The nozzle which cannot be seen in Figure 4.4 because it is placed within the chamber,

however the basic designs of nozzle used can be seen in Figure 4.5. A plane of symmetry is used to reduce the total number of computational cells, however due to the instability of the flow there will inevitably be small areas of asymmetric characteristics such as the area around the nozzle exit that may contribute to small errors in the prediction. The thermal heat transfer model was used with this prediction and the governing equations are described in section 4.3.5.1 . The experimental operating conditions were used to setup the boundary conditions for the computational inlets and outlet. Although the prediction is temperature dependant within the working fluid, hat transfer between the walls of the ejector and the refrigerant was not considered since the ejector in the laboratory is insulated so that very little heat exchange takes place through the walls. Therefore the CFD model wall boundaries were left with default characteristics since it was more important to model the refrigerant flow through the inside of the ejector.

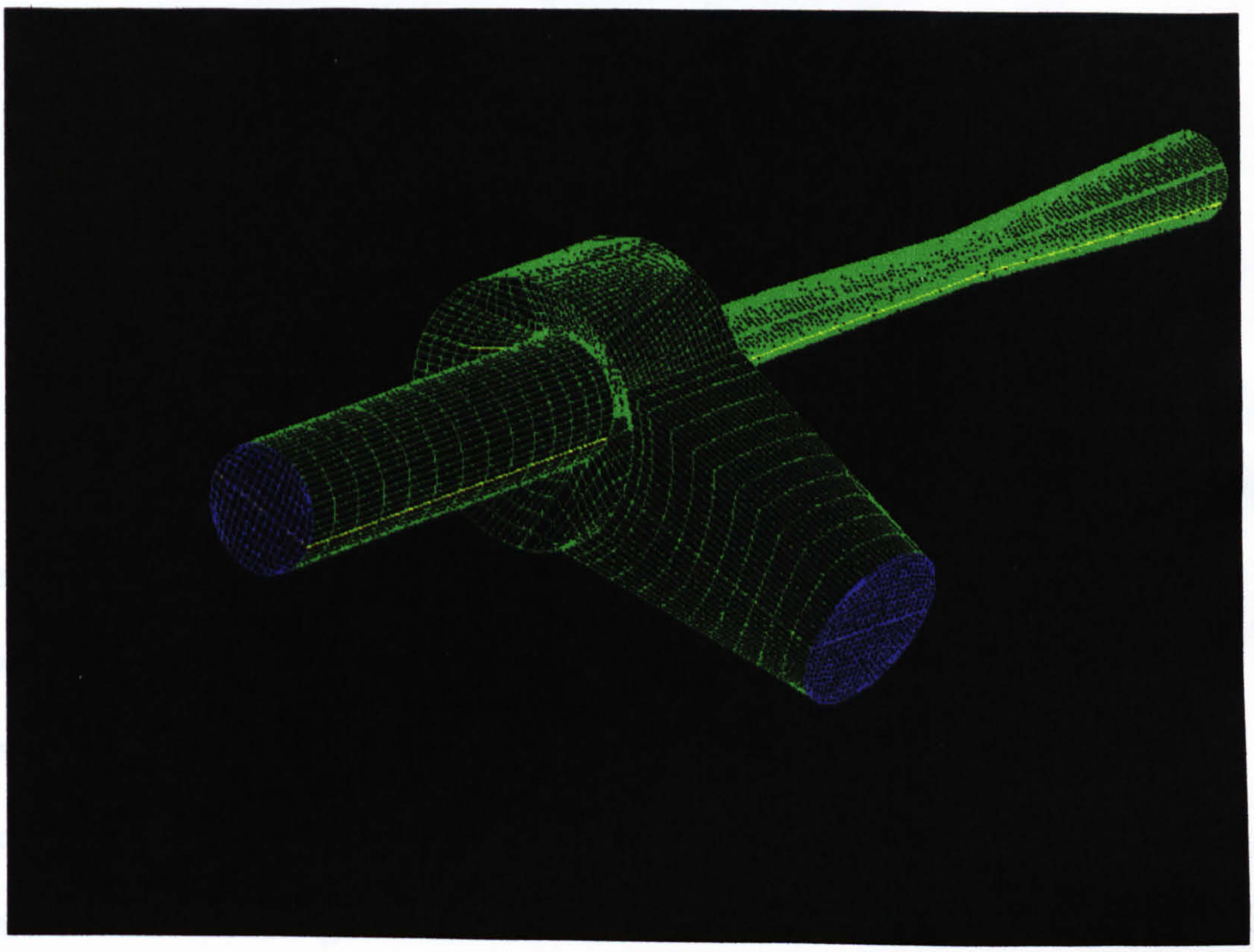

**Figure 4.4** CFD surface grid for an ejector.

## 4.3 CFD prediction of high pressure ejectors

It is discussed later in this chapter that the working pressures of the ejector play an important role in determining the stability of the computer model and therefore its accuracy. The working pressures relate to the pressure and therefore temperature of the refrigerant at the nozzle inlet (generator), the suction inlet (evaporator) and the diffuser outlet (condenser). Depending on the application the CFD predictions made in this investigation were divided into two categories,

that of high pressure ejectors (a generator pressure in the order of 20 bar) and low pressure ejectors (a generator pressure in the order of 0.5 bar).

### 4.3.1 Effect of refrigerants

The three refrigerants (ammonia, R134a and propane) were used to predict the flow through an ejector at high pressure using a converging/diverging nozzle as shown in Figure 4.2. Table 4.1 shows the refrigerant properties used for the predictions for saturated vapour, which is taken from the ASHRAE (54) Fundamentals reference guide.

**Table 4.1** Saturated vapour properties for various refrigerants.

| | Temperature (°C) | | | Pressure (MPa) | | | Density (kg/m$^3$) | | |
|---|---|---|---|---|---|---|---|---|---|
| Refrigerant: | Motive: | Suction: | Exit: | Motive: | Suction: | Exit: | Motive: | Suction: | Exit: |
| Ammonia | 50 | -9 | 22 | 2.03 | 0.30 | 0.91 | 15.73 | 2.47 | 7.10 |
| R134a | 62 | 2 | 22 | 1.76 | 0.31 | 0.61 | 91.79 | 15.37 | 29.35 |
| Propane | 62 | 2 | 22 | 2.20 | 0.43 | 0.88 | 51.95 | 10.95 | 19.05 |
| | Viscosity (kg/m.s)x10$^{-4}$ | | | | | | | | |
| Ammonia | 114 | 91 | 103 | | | | | | |
| R134a | 149 | 11 | 120 | | | | | | |
| Propane | 109 | 78 | 85 | | | | | | |

It is found from the prediction that the flow rate ratio ( coefficient of performance ) for ammonia is 0.17 and for propane it is 0.42 . The higher COP for propane is due to the higher motive pressure ratio, lower suction pressure ratio and also the higher density of the refrigerant has a significant effect on the performance of an ejector used in a heat pump. An ejector designed for a refrigerant with a low density such as ammonia may not function well for a refrigerant with a high density such as R134a.

### 4.3.2 Nozzle geometry and orientation

Another important aspect on the performance of an ejector is the nozzle geometric parameters and orientation. The nozzle is placed within the ejector chamber and is responsible for producing the suction effect from the evaporator. Using ammonia as the working refrigerant, three types of nozzle designs were incorporated into the simulations and a comparison of mass flow rate ratios were obtained. Furthermore, for each nozzle type two different positions were used and the data compared. Figure 4.5 shows the basic designs of the three types of nozzle used based on theoretical efficiency mentioned in Miller (55) .

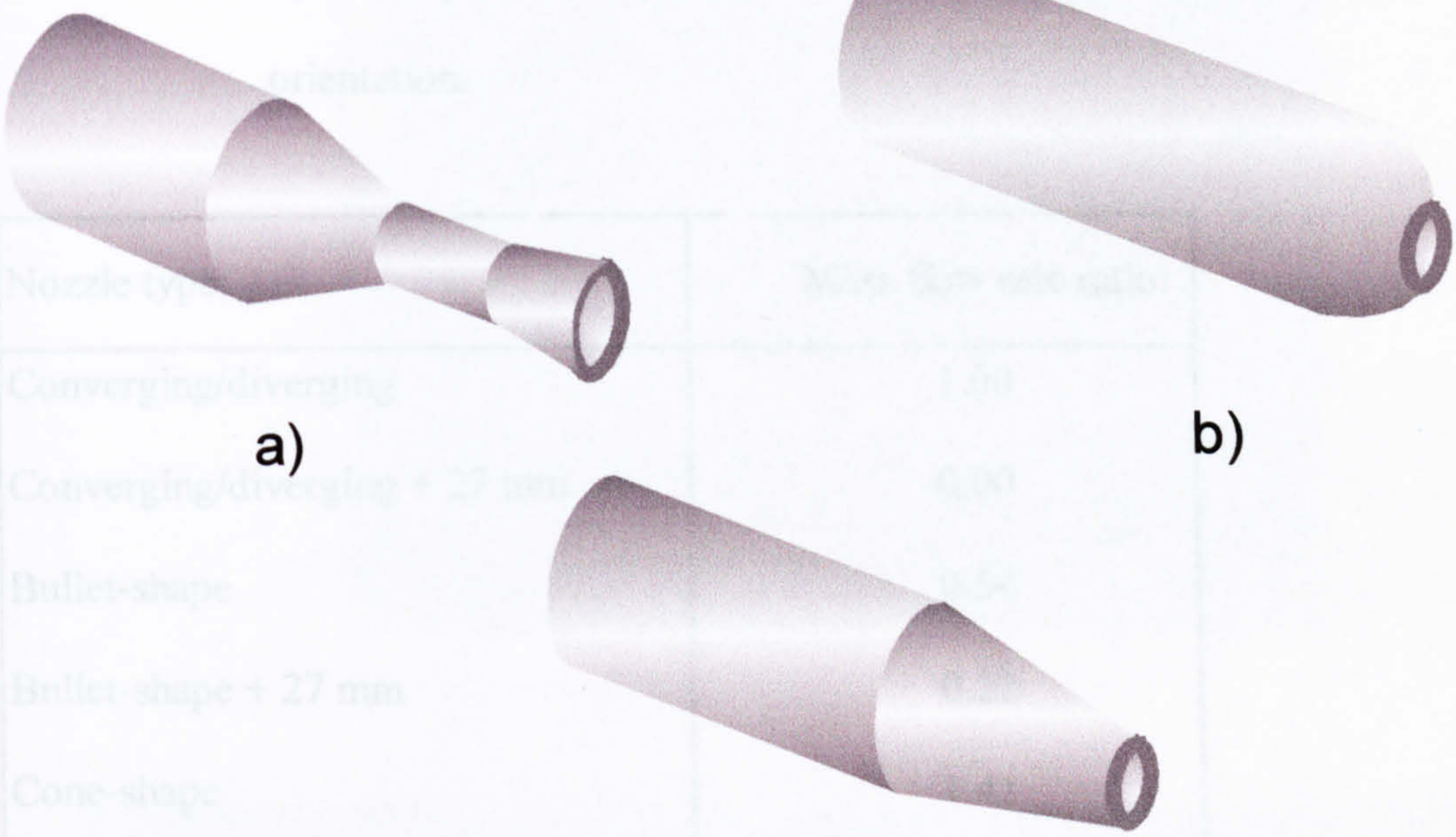


**Figure 4.5** Nozzle types a) Converging/diverging, b) Bullet-shape and c) Cone-shape.

Table 4.2 shows the comparison of mass flow rate ratio between the various nozzles with the addition of the converging/diverging nozzle and the bullet-shape nozzle being moved 27 mm further into the ejector to observe the effect.

**Table 4.2** Ejector performance with various nozzle geometry and orientation.

| Nozzle type: | Mass flow rate ratio: |
|---|---|
| Converging/diverging | 1.00 |
| Converging/diverging + 27 mm | 0.00 |
| Bullet-shape | 0.54 |
| Bullet-shape + 27 mm | 0.22 |
| Cone-shape | 1.41 |

If the mass flow rate ratio for the original converging/diverging nozzle is set at a reference value of 1.00 , then for comparative analysis it can be seen in Table 4.2 that moving the converging/diverging nozzle further into the ejector the motive suction is overcome with back pressure either developing in the chamber or the diffuser of the ejector, resulting in a negative entrainment and a zero mass flow rate ratio. A reduction in mass flow rate ratio is also evident for the bullet-shape nozzle when it is moved further into the ejector. According to prediction there is a 41 % increase in performance when the converging/diverging nozzle is replaced by the cone-shape nozzle. Figure 4.6 shows a CFD prediction of velocity vectors for the flow of ammonia through a high pressure ejector using the converging/diverging nozzle. Figure 4.6 shows the interior parts of the ejector which could not be seen from the exterior surface grid in Figure 4.4 .

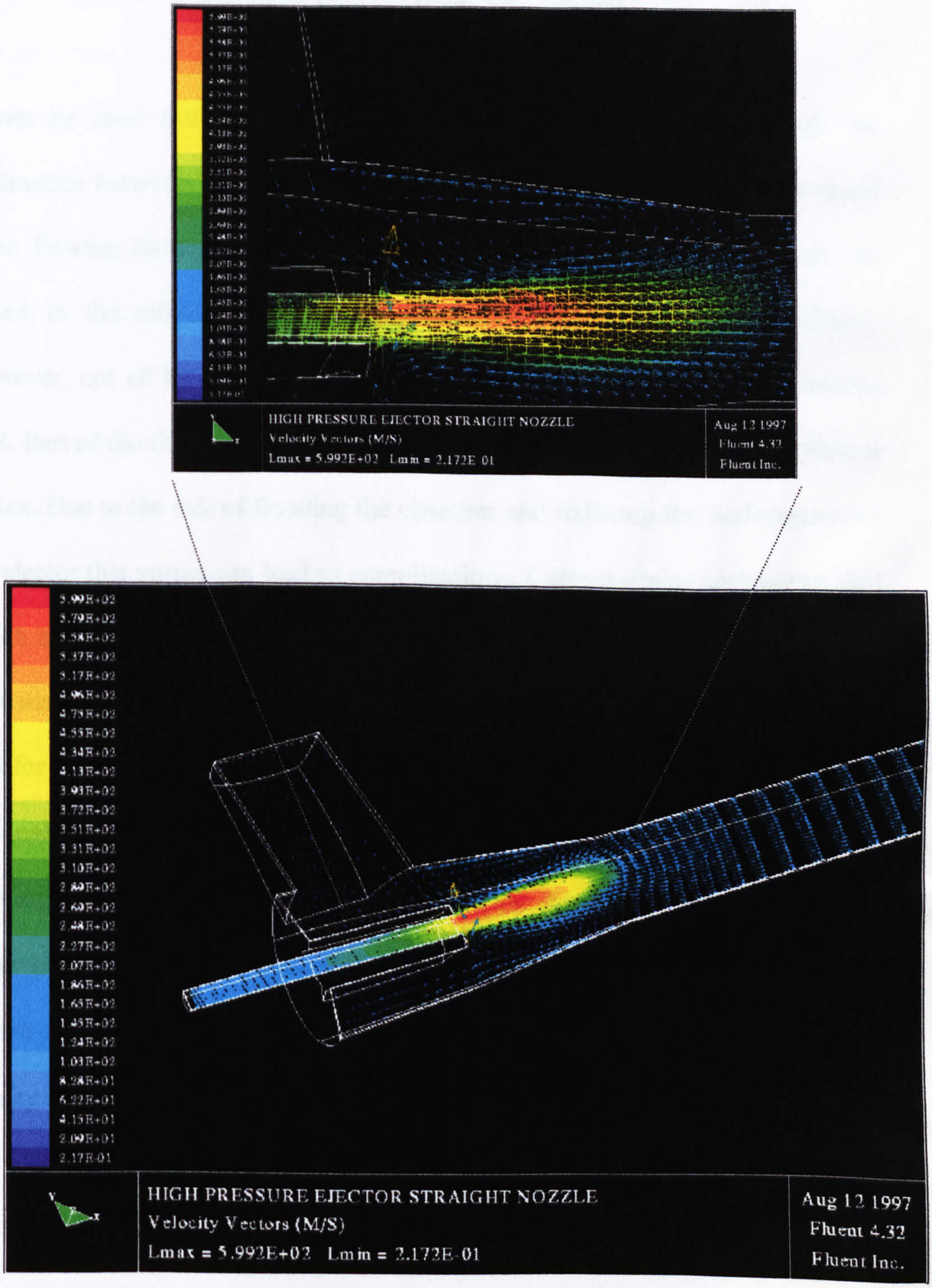


**Figure 4.6** CFD predicted flow through an ejector.

### 4.3.3 Flow characteristics

It can be seen from Figure 4.6 that the fluid is accelerated through the contraction between the motive inlet and the nozzle and reaches a sonic speed when flowing through the motive nozzle. The motive and suction fluids are mixed in the mixing duct and decelerated through the discharge diffuser. However, not all the fluid from the motive nozzle flows straight to the mixing duct. Part of the fluid expands in the suction chamber and recirculates to form a vortex. Due to the risk of flooding the chamber and reducing the performance of the ejector this vortex can lead to complications. Current design techniques (56) which are based on one dimensional constant area flow models do not take the formation of such vortices into account. This is why CFD can provide a useful tool for design and optimisation. It was found that when the refrigerant R134a was used as the working fluid, there was considerable back pressure in the diffuser leading to a negative entrainment. This shows that the fluid physical properties have a considerable effect on the performance of the ejector. The reason for this is that the pressure losses ($\Delta P$) are proportional to the fluid density ($\rho$) and the mean velocity (V) by :

$$\Delta P \propto \rho V^2 \qquad (4.1)$$

It can be seen in Table 4.2 that the density of R134a is approximately six times that of ammonia, therefore it follows that the excessive pressure loss in the chamber being less than that required to overcome the back pressure in the diffuser.

## 4.4 CFD prediction of low pressure ejectors

CFD is applied to the prediction of ejector performance in terms of entrainment ratio and velocity ratio relating to the evaporator and generator inlets, and a comparison is made to experimental results based on an identical ejector under the same operating conditions. The experimental results were obtained from laboratory tests carried out by Smith (57). This investigation uses steam as the working fluid passing through a converging/diverging nozzle with a 2 mm throat, and 12 mm exit diameters. The temperature is controlled and varied from 90 °C to 130 °C for the generator and from 5 °C to 15 °C for the evaporator. The experimental procedure included three variations of the nozzle dimensions as well as a variation of the condenser temperature.

### 4.4.1 CFD prediction and experimental comparison

The nozzle design optimised by experimental results is found to give satisfactory predictions using CFD when using steam as the refrigerant. The performance of the ejector is greatly reduced by the effect of back pressure causing a weak negative entrainment. It was found that this phenomena is caused by :

- changes in nozzle design creating a high pressure within the ejector chamber;
- increasing the condenser temperature higher than the optimum temperature of 22 °C;
- varying the generator temperature outside the optimum working range of 110 °C to 120 °C.

The average velocity readings for the CFD prediction were taken over the cross section of the nozzle inlet and a velocity ratio calculated with the evaporator inlet velocity. Figures 4.7 to 4.9 show a comparison of entrainment ratio, or coefficient of performance (COP) for the experimental results and the CFD prediction. The COP is measured as the motive flow rate to suction flow rate ratio. The graphical representation shows a good correlation between experimental results and CFD prediction with a 12.9 % difference on average. It can be seen that a characteristic optimum ejector performance occurs in the

generator temperature range of 110 °C to 120 °C for the range of evaporator temperatures used.

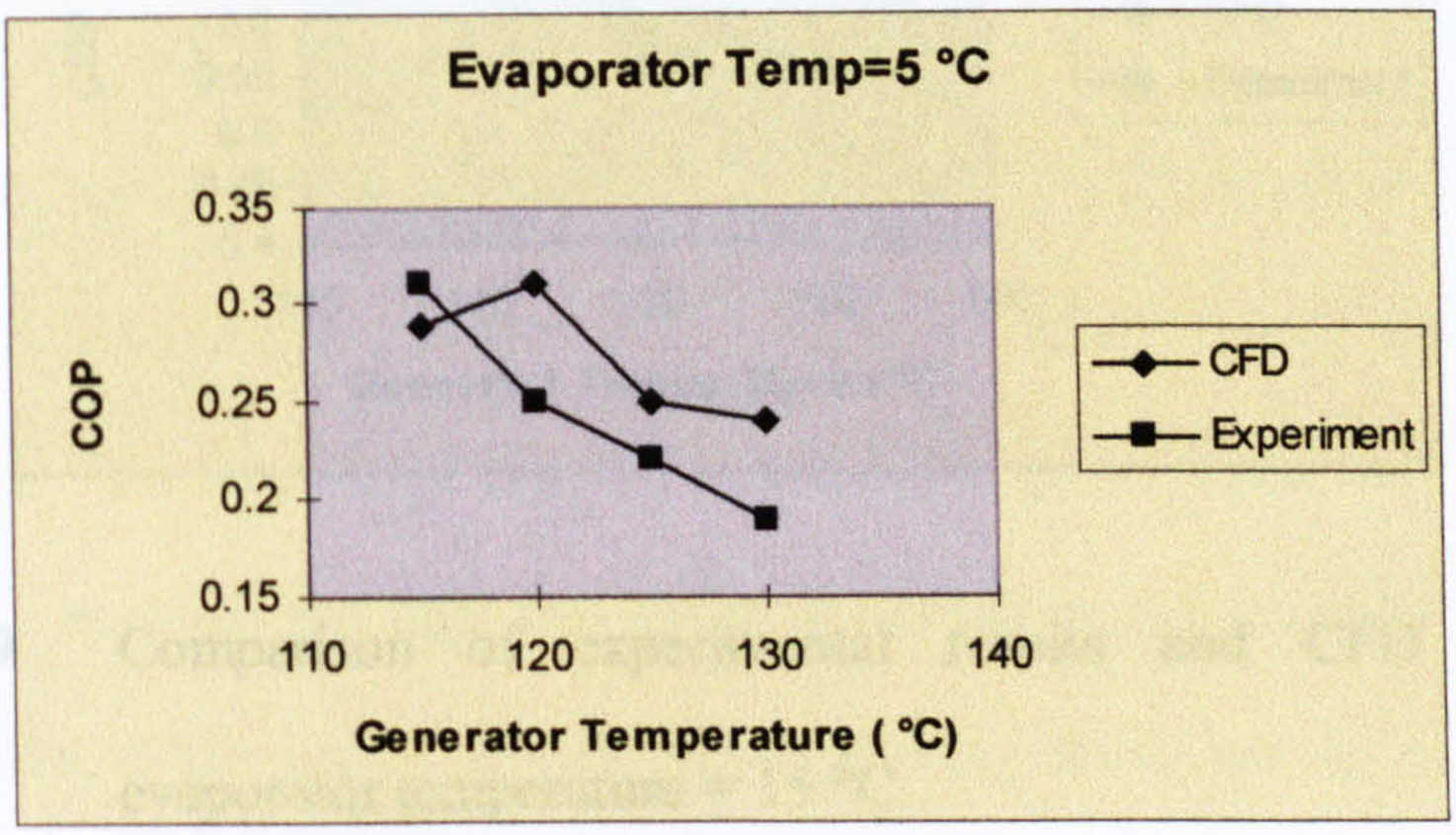


**Figure 4.7** Comparison of experimental results and CFD prediction, evaporator temperature = 5 °C.

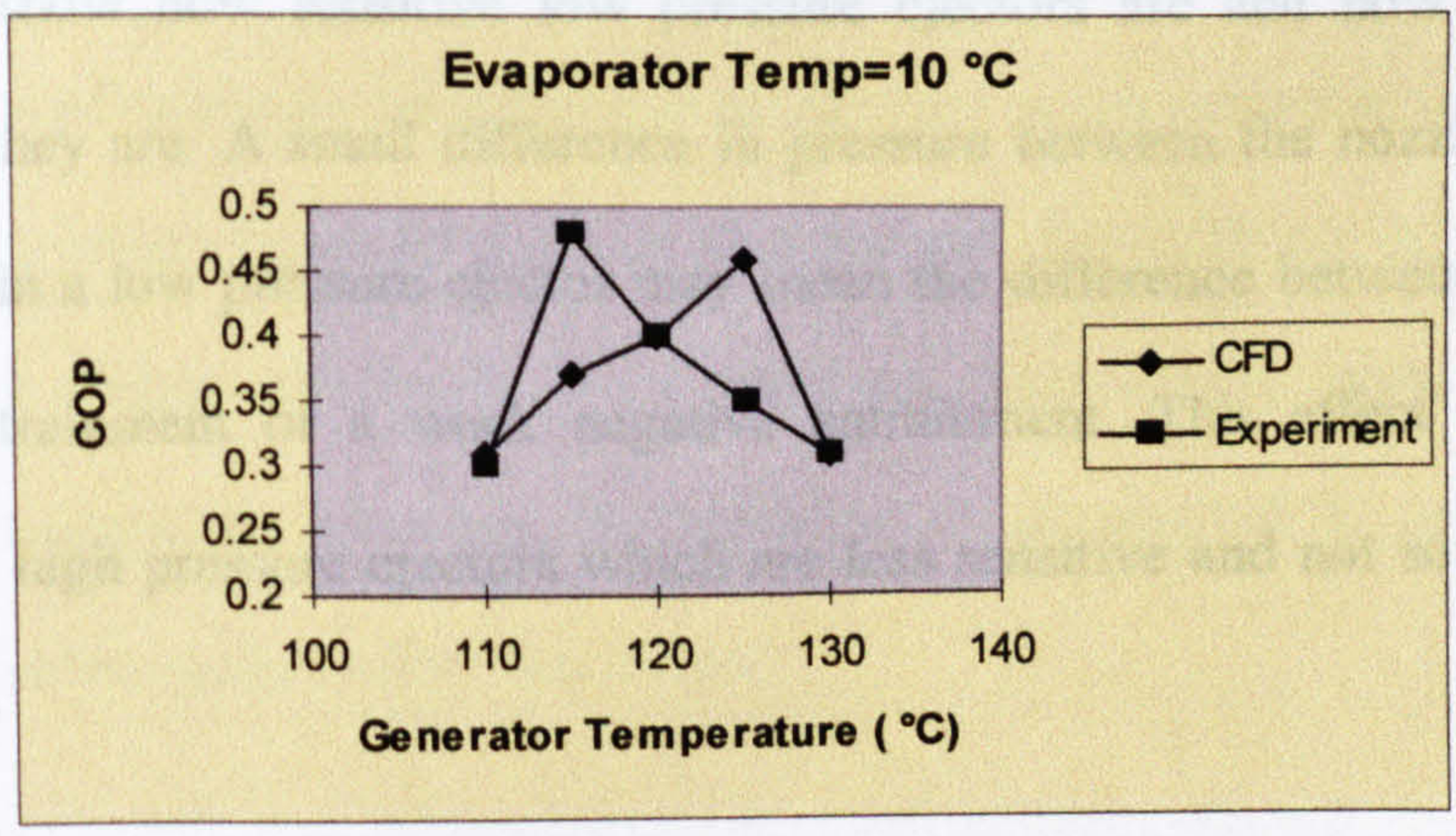


**Figure 4.8** Comparison of experimental results and CFD prediction, evaporator temperature = 10 °C.

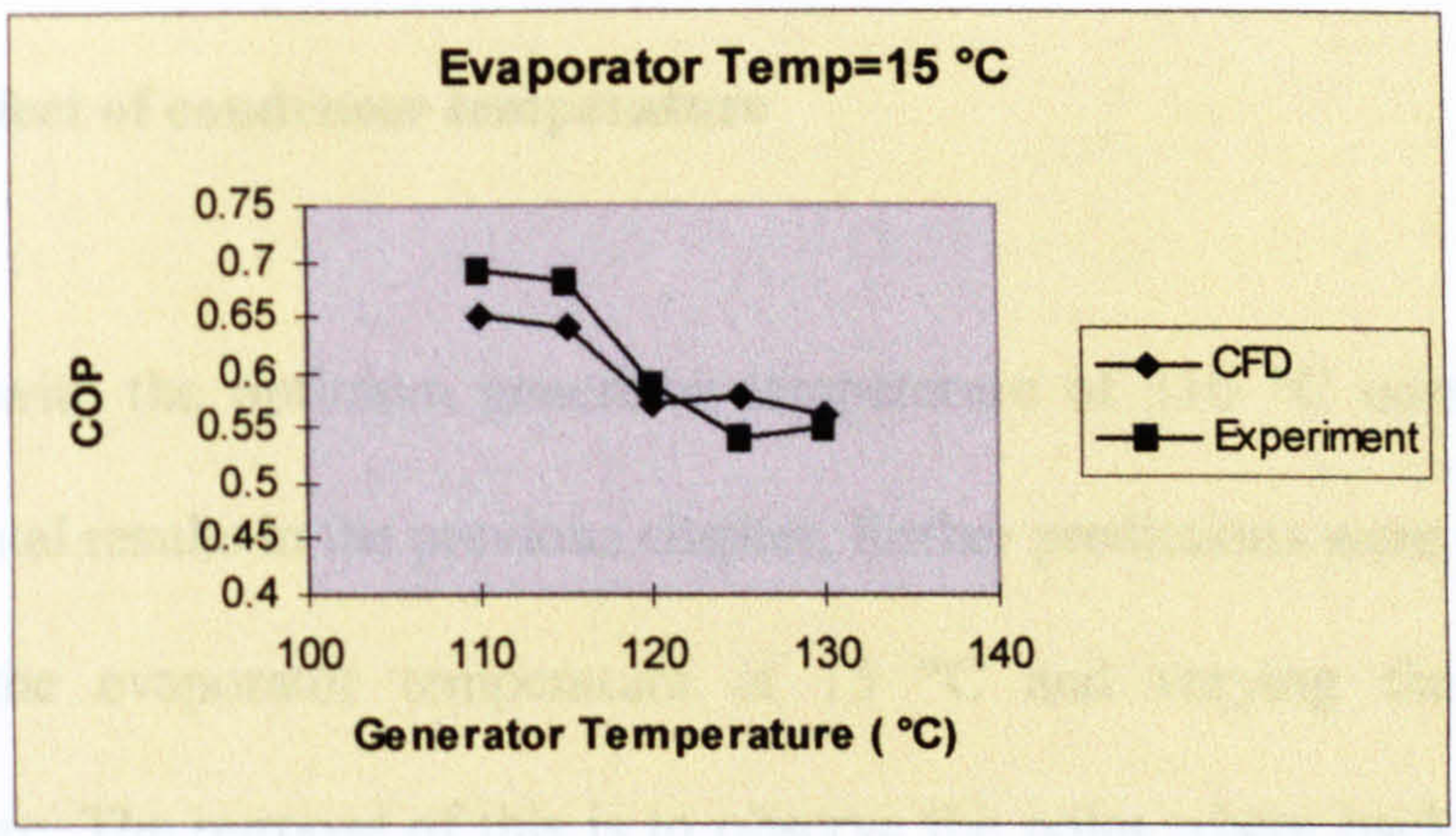


**Figure 4.9** Comparison of experimental results and CFD prediction, evaporator temperature = 15 °C.

The reduction in entrainment ratio previously discussed and observed in Figures 4.7 to 4.9 show how sensitive low pressure ejectors are and how geometry dependant they are. A small difference in pressure between the nozzle and the evaporator in a low pressure ejector may mean the difference between a strong positive entrainment or a week negative entrainment. This effect is not so apparent in high pressure ejectors which are less sensitive and not so geometry dependant.

### 4.4.2 Effect of condenser temperature

Working with the optimum generator temperature of 110 °C correlated with experimental results in the previous chapter, further predictions were obtained by keeping the evaporator temperature at 15 °C and varying the condenser temperature. The purpose of this is to observe the point where back pressure in the diffuser becomes too high and floods the chamber reducing the entrainment ratio to zero. This results in refrigerant moving from the condenser to the evaporator. Figure 4.10 shows the relationship between condenser temperature and the coefficient of performance (COP) for different generator temperatures. It can be seen that as the condenser temperature increases, the COP reduces slightly until at a certain temperature it quickly reduces to zero. This is evident for all values of generator temperatures except that as the generator temperature increases, the point of zero entrainment also reduces. The COP is reduced to zero because the ejector effectively stops working. This occurs because as the generator temperature increases, the pressure at the exit of the nozzle also increases and the suction effect is reduced.

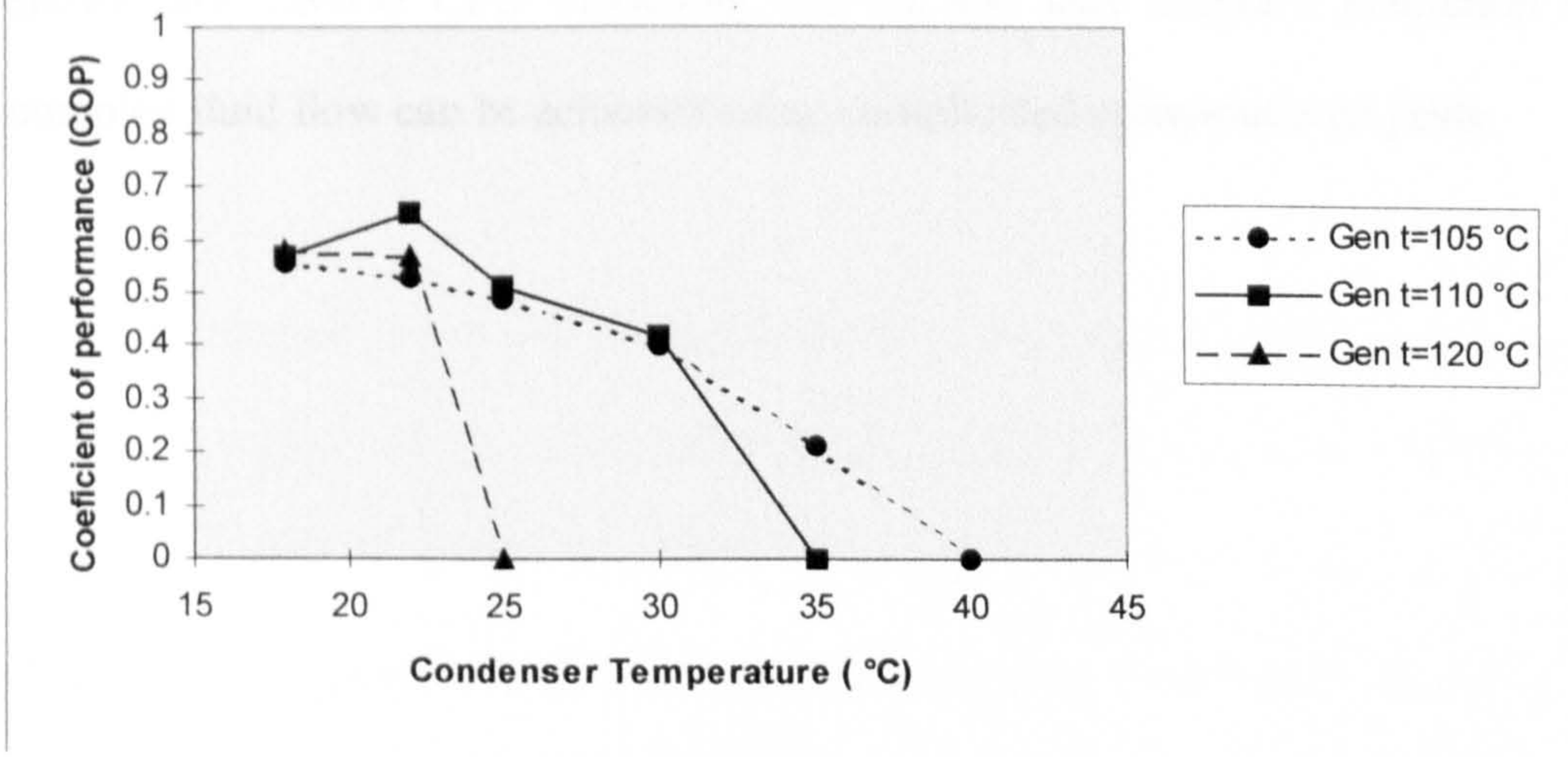


**Figure 4.10** Relationship of condenser temperature and COP for different generator temperatures.

## 4.5 Summary

The advantages of using CFD to predict the performance of ejectors become paramount when taking into account the importance of optimising the working conditions in ejector driven refrigeration cycles. It follows that if CFD models are callibrated with experimental results, that has been shown here, then benefits can be achieved through being able to visualise the flow of steam through the ejector. Furthermore changes to the geometric design can be easily employed and the corresponding coefficient of performance can be observed. This chapter

shows how diverse CFD modelling can be and that accurate prediction of complex fluid flow can be achieved using complicated computational grids.

# References

1. ASHRAE handbook of fundamentals, American Society of Heating, Refrigeration and Air Conditioning Engineers, Atlanta, GA. (1989).

2. CIBSE guide: reference data, The Chartered Institution of Building Services Engineers, London. (1986).

3. BSRIA guide : Heating and Ventilating Research Association, Engineering Abstract Vol. 101-102, (1975).

4. Fluent Inc. Fluent users guide, USA. (1993).

5. Dick, J. B., "Measurement of ventilation using tracer-gasses", Heat. Pip. Air Conditioning, Chp 22, pp 131-137, (1950).

6. I'Anson, S. J., Irwin, C. and Howarth, A. T., "A multiple tracer-gas technique for measuring air-flow in houses", Building Environment, Vol. 17, pp 245-252, (1982).

7. Harrje, D. T., Dutt, G. S. and Bohac, D. L., "Documenting air movements and infiltration in multicell buildings using various tracer-gas techniques", Preprint ASHRAE Trans. 91, HI-85-40, No. 3, (1985).

8. Niemela, R., Toppila, E. and Tossavainen, A., "A multiple tracer-gas technique for the measurement of air-flow patterns in large industrial premises", Building and Environment, Vol. 22, No. 1, pp 61-66, (1987).

9. Sherman, M. H., "On the estimation of multizone ventilation rates from tracer-gas measurements", Building and Environment, Vol. 24, No. 4, pp 355-362, (1989).

10. Persily, A. and Axley, J., "Measuring of flow rates with pulse injection techniques", American Society for Testing and Materials, Philadelphia, (1989).

11. Riffat, S. B. and Lee, S. F., "Turbulent flow in duct: Measurement by a tracer-gas technique", Building Services Engineering Research and Technology, Vol. 11, No. 1, pp 21-26, (1990).

12. Sateri, J., "PFT measurement in ventilation ducts", Proceedings 12th AIVC Conference, Canada, Vol. 1, pp 375-386, (1991).

13. Smith, S.J., Gan, G., Riffat, S.B. and Shao, L., "k-Factor Data of Duct Fittings Based on Measurement and CFD Modelling". CIBSE National Conference, Eastbourne, 1-3 October (1995). VII, p337-344.

14. Flovent, Flovent User Guide, Flomerics Inc., (1995).

15. Idelchik, I.E., Malyavskaya, G.R., Martynenko, O.G. and Fried, B. Handbook of Hydraulic Resistance, 2nd ed, New York : Hemisphere Publishing Corp., Subsidiary of Harper & Row, (1986).

16. Brooks, P.J., "New ASHRAE local loss coefficients for HVAC fittings", 1993 Annual meeting of ASHRAE Inc. 26-30 June (1993), Denver, USA, Vol 99, No. 2, pp 169-193.

17. BSR/ASHRAE Standards 120P , "Methods of testing to determine flow resistance of HVAC air ducts and fittings", (1995), Atlanta GA 30329.

18. Streeter, V. L., Wylie, E. B. and Bedford, K. W., Fluid Mechanics, Ninth Ed. McGraw-Hill, (1997). pp 456-479.

19. Sateri, J. O., "The development of the PFT-method in the nordic countries", NBS-I 1991. Document D9:1991, Swedish Council for Building Research (Distribution: Svensk Byggtjanst, S-17188 Solna, Swedan).

20. Dietz, R. N. and Cote, E. A., "Air infiltration measurements in a home using a convenient perfluorocarbon tracer technique", Environment International, Vol. 8, No. 1-6, pp 419-433, (1982).

21. Munson, B. R., Young, D. F. and Okiishi, T. H., "Fundamentals of fluid mechanics", J. Wiley & sons Inc. (1994).

22. Shao, L. and Riffat, S.B., "Accuracy of CFD for predicting pressure losses in HVAC duct fittings", Applied Energy, (1995), Vol. 51, No. 3, pp 233-248.

23. Lin, C.H., Han, T.Y. and Sumantran, V., "Experimental and computational studies of flow in a simplified HVAC duct", International Journal of Vehicle Design, (1994), Vol. 15, No. 1-2, pp 147-165.

24. Chen, Q.Y., "Computational fluid dynamics for HVAC : Successes and failures", 1997 Winter Meeting of ASHRAE 24-28 Feb., Philadelphia, USA, Vol. 103, No. 98, pp 178-187.

25. Shao, L. and Riffat, S. B., "Tracer-Gas Mixing with Air : Effect of Tracer Species", J. of Applied Energy, Vol. 49, pp 197-211, (1994).

26. Cheong, K. W. and Riffat, S. B., Thesis :"A Measurement Technique Guide on the Application of Tracer-Gas Techniques for Measuring Airflow in HVAC Systems", School of the Built Environment, University of Nottingham, (1994).

27. Miller, D.S. "Internal Flow Systems" 2nd Ed. BHRA (Information Services), Bedford, (1990), p81.

28. Fluent Inc. Fluent users guide, USA. (1993), Vol. 1, section 19.1-19.12.

29. Hinze, J.O., Turbulence, McGraw-Hill Publishing Co., New York, NY (1975).

30. Patankar, S.V., "Numerical Heat Transfer and Fluid Flow", Washington, DC : Hemisphere Publishing Corp., (1980).

31. Maruszuwski, J.P., Bounded QUICK Scheme in FLUENT, Fluent Inc. Technical Memo, TM-049, (1991).

32. Leanard, B.P. "A Stable and Accurate Convective Modelling Procedure Based on Quadratic Upstream Interpolation, Computer". Methods in Appl.Mech.Eng., V19, (1979), pp59-98.

33. Miller, D.S. "Internal Flow Systems" 2nd Ed. BHRA (Information Services), Bedford, (1990), p227, p297 and p300.

34. Tritton, D. J., Physical Fluid Dynamics, 2nd Ed., Oxford Science Publications, (1995), p 30.

35. Douglas, J. F., Gasiorek, J. M. and Swaffield, J. A., Fluid Mechanics, 3rd Ed. Longman Group Ltd. (1995). p 260.

36. Tritton, D. J., Physical Fluid Dynamics, 2nd Ed., Oxford Science Publications, (1995), p 139, p 146.

37. Ward Smith, A. J., Pressure losses in Ducted Flows, The Butterworth Group, (1971), p 142.

38. Sami, S.M. and Song, B. "Heat transfer and pressure drop characteristics of HFC quarternary refrigerant mixtures inside horizontal enhanced surface tubing", Applied Thermal Engineering, 16(6), 461-473, (1996).

39. Jones, R.A., Abu Madi, M. and Heikal, M.R. "Performance of non-ozone depletion refrigerants in condensers and evaporators", The Institute of Marine Engineers, Marine Refrigeration, 107(3), 31-48, (1996).

40. ASHRAE handbook of refrigeration, American Society of Heating, Refrigeration and Air Conditioning Engineers, Atlanta, GA. (1989).

41. ICI Plc Refrigerant Technical Information Database, ICI Inc. UK, (1995).

42. Miller, D.S. "Internal Flow Systems", 2nd Ed. BHRA (Information Services), Bedford, (1990).

43. White, F.M. "Fluid Mechanics" 3rd Ed. McGraw Hill Publishing, New Jersey, USA, (1994), p317.

44. Miyara, A., Koyama, S., Fujii, T. "Consideration on the performance on the vapour compression heat pump cycle using NARMs", Int.J.Refrigeration.

45. Smith, S.L. "Void fractions in two phase flow: a correlation based upon an equal velocity heat model", Heat and Fluid Flow, (1971), V1(1), pp22-39.

46. Soliman, M., Schuster, J.R. and Berenson, P.J. "A general heat transfer correlation for annular flow condensation", Journal of Heat Transfer, (1986), Vol. 90, No. 2, pp267-276.

47. Hammer, R. M., "An alternative source of cooling: The ejector-compression heat pump", ASHRAE Journal, July (1990), pp60-66.

48. Korres, C. J., Bardakas, F. E. and Koumoutsos, N. G., "Performance analysis of solar vapour thermal compression chiller", International Journal of Energy Research, (1989), V13, No. 2, pp243-253.

49. Thupvongsa, C., "Investigation of an ejector heat pump", PhD Thesis, University of N. Mexico, Albuquerque, USA, (1976).

50. Sokolov, M. and Hershgal, D., "Solar-powered compression enhanced ejector air conditioner", Solar energy, (1993), V51, No. 3, pp183-194.

51. Sokolov, M. and Hershgal, D., "Optimal coupling and feasinility of a solar-powered year-round ejector air conditioner", Solar energy, (1993), V50, No. 6, pp507-516.

52. Sokolov, M. and Hershgal, D., "Enhanced ejector refrigeration cycles powered by low grade heat, Part 1 : Systems characterisation", International Journal of Refrigeration, (1990), V13, No. 6, pp351-356.

53. Keenan, J. H. and Neumann, E. P., "Asimple air ejector", ASME Journal of Applied Mechanics, June (1942), A75-81.

54. ASHRAE handbook of refrigeration, American Society of Heating, Refrigeration and Air Conditioning Engineers, Atlanta, GA. (1989).

55. Miller, D.S. "Internal Flow Systems" 2nd Ed. BHRA (Information Services), Bedford, (1990), pp375-376.

56. "Ejectors and jet pumps - design and performance for compressible air flow", Engineering Sciences Data Unit, Data item no. 84029, (1984).

57. Smith, S.J., Riffat, S., Wu, S. and Eames, I. "Computer Modelling and Testing of Low Pressure Ejectors Applied to Refrigeration Cycles", CIBSE'97 National Conference, Eastbourne, October (1997).

**Published Papers by the Author**

1. "k-Factor Data of Duct Fittings Based on Measurement and CFD Modelling", CIBSE National Conference, Eastbourne, VII, pp337-344, 1-3 October (1995).

2. "Computational Fluid Dynamics Applied to Ejector Heat-Pumps", J. of Applied Thermal Energy, V16, No. 4, April (1996).

3. "k-Factor Data of Interacting Duct Fittings Based on Measurement and CFD Modelling", International Journal of Energy Research, V20, No. 12, pp1129-1137, December (1996).

4. "A Comparison using Computational Fluid Dynamics of Pressure Drops of CFC and HFC Refrigerants in Heat-Pump Coils", J. of Applied Energy.

5. "CFD Prediction of Low Pressure Ejectors", Building Services Engineering Research and Technology Journal, CIBSE, V18, No. 3, pp179-182, (1997).

6. "Efficiency Based on CFD Modelling of Extract Hoods and Diffusers used in HVAC Systems", Ventilation'97 Conference, Ottawa, Ontario, Canada, 14-17 September (1997).

7. "Computer Modelling and Testing of Low Pressure Ejectors Applied to Refrigeration Cycles", CIBSE'97 National Conference, Eastbourne, October (1997).

8. "Determination of k-Factors for HVAC System Components", CIBSE'97 National Conference, Eastbourne, October (1997).